Optimising Acoustic Cavitation for Industrial Application

Lukman Aminu Yusuf

Submitted in fulfilment of the requirements for the Degree of Doctor of Philosophy

School of Engineering

Department of electronics and electrical engineering

University of Glasgow

March 2022

Abstract

The ultrasonic horn is one of the most commonly used acoustic devices in laboratories and industry. For its efficient application to cavitation mediated process, the cavitation generated at its tip as a function of its tip-vibration amplitudes still needed to be studied in detail. High-speed imaging and acoustic detection are used to investigate the cavitation generated at the tip of an ultrasonic horn, operating at a fundamental frequency, f_0, of 20 kHz. Tip-vibration amplitudes are sampled at fine increments across the range of input powers available. The primary bubble cluster under the tip is found to undergo subharmonic periodic collapse, with concurrent shock wave emission, at frequencies of f_0/m, with m increasing through integer values with increasing tip-vibration amplitude. The contribution of periodic shock waves to the noise spectra of the acoustic emissions is confirmed. Transitional input powers for which the value of m is indistinct, and shock wave emission irregular and inconsistent, are identified through V_{rms} of the acoustic detector output. For cavitation applications mediated by bubble collapse, sonications at transitional powers may lead to inefficient processing. The ultrasonic horn is also deployed to investigate the role of shock waves in the fragmentation of intermetallic crystals, nominally for ultrasonic treatment of Aluminium melt, and in a novel two-horn configuration for potential cavitation enhancement effects. An experiment investigating nitrogen fixation via cavitation generated by focused ultrasound exposures is also described. V_{rms} from the acoustic detector is again used to quantify the acoustic emissions for comparison to the sonochemical nitrite yield and for optimisation of sonication protocols at constant input energy. The findings revealed that the acoustic cavitation could be enhanced at constant input energy through optimisation of the pulse duration and pulse interval. Anomalous results may be due to inadequate assessment for the nitrate generated. The studies presented in this thesis have illustrated means of improving the cavitation efficiency of the used acoustic devices, which may be important to some selected industrial processes.

Table of Contents

List of Figures

List of Tables

Acknowledgement

First of all, I would like to appreciate the Almighty Allah for sparing my life until now.

There are several people whom I would like to especially appreciate for their contributions towards the success of my PhD-thesis: Jae Hee Song; thank you for all the pieces of advice. Jack Stevenson, thank you for the fruitful discussion regarding the use of OnScale software.

I would like to appreciate my colleagues in the CavLab: Lisa McMenamin, Ben Jacobson, and Hilde Metzger, for their support.

I would also like to thank Marc Sorel for giving me a listening ear during the darkest period of my PhD.

I would like to appreciate my lovely wife for her support and encouragement towards the success of the PhD-thesis.

My special appreciation to my supervisor, Paul Prentice, for giving me hope where it seems there was none. Thank you for believing in me and for introducing me to the 'Cavitation's world' for all the help you provided throughout my PhD. I really appreciate you.

Lastly, I would like to appreciate the Nigerian government through the Petroleum Technology Development Fund (PTDF) for providing the funding for my PhD.

Declaration

The author carried out all work in this thesis unless otherwise explicitly stated.

List of symbols

$\bar{V}_{SW}$	Mean amplitude of shock wave
$\bar{V}_{rms}$	Mean time average shock wave content
V_{rms}	Time average shock wave content
P_a	Acoustic pressure
σ	Surface tension
R_m	Mean radius of bubble
R_{min}	Minimum radius of bubble
R_{max}	Maximum radius of bubble
P_o	Atmospheric pressure
f_r	Resonance frequency of gas bubble
f_0	Fundamental frequency of the source
T_0	Period of the source
T_c	Bubble's collapse time
T_∞	Ambient temperature of the host
γ	Ratio of heat capacities or adiabatic index
E	Energy
Z	Acoustic impedance
T_b	Beat's period
K	Duty cycle
f_s	Sampling frequency
c	Speed of sound
ρ	Density of water
t_{on}	Period when the transducer is excited

t_{off}	Period when the transducer is not excited

List of Abbreviations

- Cavitation laboratory (CavLab)
- Continuous wave (CW)
- Frames per second (fps)
- Field of view (FOV)
- Full width half maximum (FWHM)
- High intensity focused ultrasound (HIFU)
- High-speed imaging (HSI)
- High-speed camera (HSC)
- Hydrophone (HP)
- Lead zirconate titanate (PZT)
- National Physical Laboratory (NPL)
- Number of burst (#Burst)
- Polyvinylidene Flouride (PVdF)
- Peak-positive amplitude (PPA)
- Passive cavitation detector (PCD)
- Peak negative pressure (PNP)
- Pulse interval (PI)
- Pulse duration (PD)
- Pulse width modulation (PWM)
- Periodic shock wave (PSW)
- Rise time (RT)
- Shock wave PCD (swPCD)
- Signal to noise ratio (SNR)
- Shock wave (SW)
- Sum duration of non-shocking activity (ΣdNSA)

Overview of Thesis and Dissemination

Acoustic cavitation refers to driven bubble activity within a liquid host medium exposed to a sufficiently intense acoustic/ultrasonic exposure. As a compressible entity within an incompressible (to a first approximation) host medium, the bubble is highly sensitive to the pressure fluctuations of the ultrasonic exposure. The often-violent collapse phases of the bubble oscillations are associated with highly localised and transient temperatures in excess of 10000 K, at 100's of atmospheres of pressure, picosecond flashes of light (so-called sonoluminescence) and other energetic phenomena such as jet-formation and shock wave emission. The potential industrial applications for acoustic cavitation have long been recognised, including acoustic cleaning and sonochemistry, with the latter employed in sectors ranging from food production to pharmaceutical preparation. Industrial applications such as drying and defoaming with airborne ultrasound, emulsification and homogenization, green extraction methods and magnesonics (the use of high-frequency ultrasound) for separation of oil/water dispersions, degassing and separation of milk fat in dairy industries have all been established. Despite these established applications, it is generally recognised that significant up-scaling of the technology has yet to occur as optimisation of the processes is still much required. More so, there are still potential energy-saving avenues in these applications [1].

Reproducibility and efficiency of cavitation-mediated processes are commonly cited as preventing further development. Moreover, the mechanisms that underpin the vast range of cavitation-mediated sonochemical processes that have been reported are generally poorly understood. The research presented in this thesis mainly focuses on enhancing acoustic cavitation efficiency for industrial application, using ultrasonic fixation of nitrogen (i.e., sonochemistry fixation of nitrogen) as a case study. An overview of relevant sonochemical literature is given in Chapter 2 of this thesis.

The research was undertaken in the Cavitation Research Laboratory (CavLab), at the Centre for Medical and Industrial Ultrasonics (C-MIU), University of Glasgow. CavLab is dedicated to a fundamental understanding of acoustic

cavitation activity, with a view to optimising and refining applications. The laboratory is based on two high-speed cameras, described in Chapter 3, for imaging rapid cavitation bubble dynamics at high temporal and spatial resolution. A number of hydrophones and passive cavitation detectors (PCDs) are available for parallel acoustic detection, used for reconciling cavitation emission signals to source bubble dynamics. Previous CavLab research, salient details from which are reviewed in Chapter 1, has traditionally been motivated by medical therapy applications of cavitation, such as blood-brain barrier disruption mediated by contrast agent microbubble-cavitation, driven by focused ultrasound at several 100's of kHz.

The author of this thesis is the first CavLab PhD student to study acoustic cavitation activity in relation to industrial applications. This essentially means that an ultrasonic horn, or sonotrode, was used to generate the cavitation investigated, as featured in *Results* Chapters 4-6, which are briefly introduced below.

Chapter 3 describes the technical details of the essential devices and important algorithms that are used in the study of acoustic cavitation. Devices such as high-speed cameras and the shock wave passive cavitation detector (swPCD) are discussed.

Chapter 4 describes a detailed characterisation of the cavitation activity generated at the tip of a commercial ultrasonic horn, fig. 1, for varying tip-vibration amplitude sampled at fine increments. In particular, the periodicity of bubble-cluster collapse and shock wave generation is studied

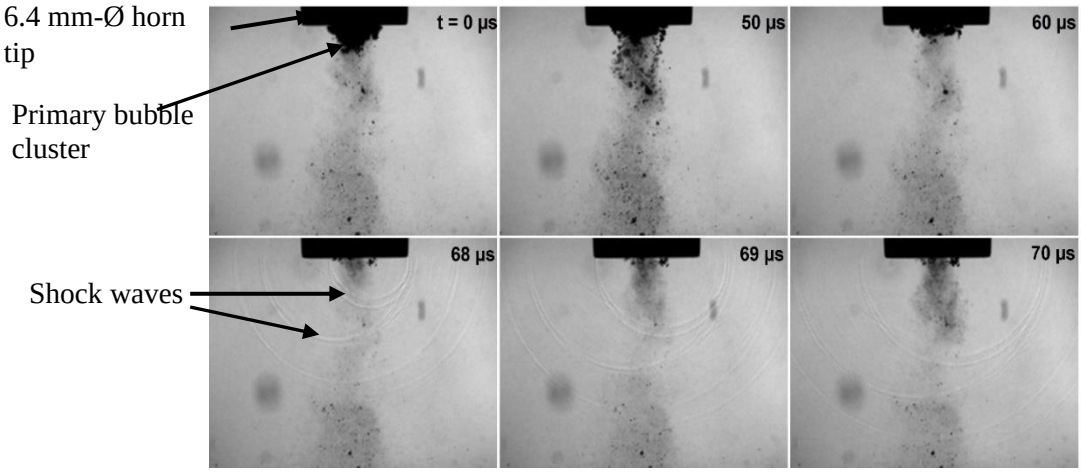

Figure 1: High-speed shadowgraphic (described in Chapter 3) imaging at 2 Mfps of the cavitation activity at the tip of an ultrasonic horn, vibrating with an amplitude of ~ 263 µm. Cluster collapse occurs at ~ 62 µs, generating multi-fronted shock waves that propagate through the field-of-view.

The data described in Chapter 4 was published as below:

Characterising the cavitation activity generated by an ultrasonic horn at varying tip-vibration amplitudes

Ultrasonics Sonochemistry, 70 (2021), 105273.

Lukman Yusuf, Mark. D. Symes & Paul Prentice

And disseminated at the following international conferences:

1. The 49th Virtual Annual Symposium of the Ultrasound Industry Association (UIA49 VIRTUAL) 26-28th of April 2021
2. ESS-JSS-AOSS 1st Joint Sonochemistry Conference (Online) 8-10th of November 2021- Oral presentation.

Chapter 5 reviews research undertaken in collaboration with the group of Prof Iakavos Tzanakis, at Oxford Brookes University. This work sought to develop an ultrasonic treatment of Aluminium melt for grain refinement. The author of this thesis contributed through direct observation of shock wave interaction with free-floating intermetallic crystals, in water host medium, as contributing to crystal fragmentation, fig 2.

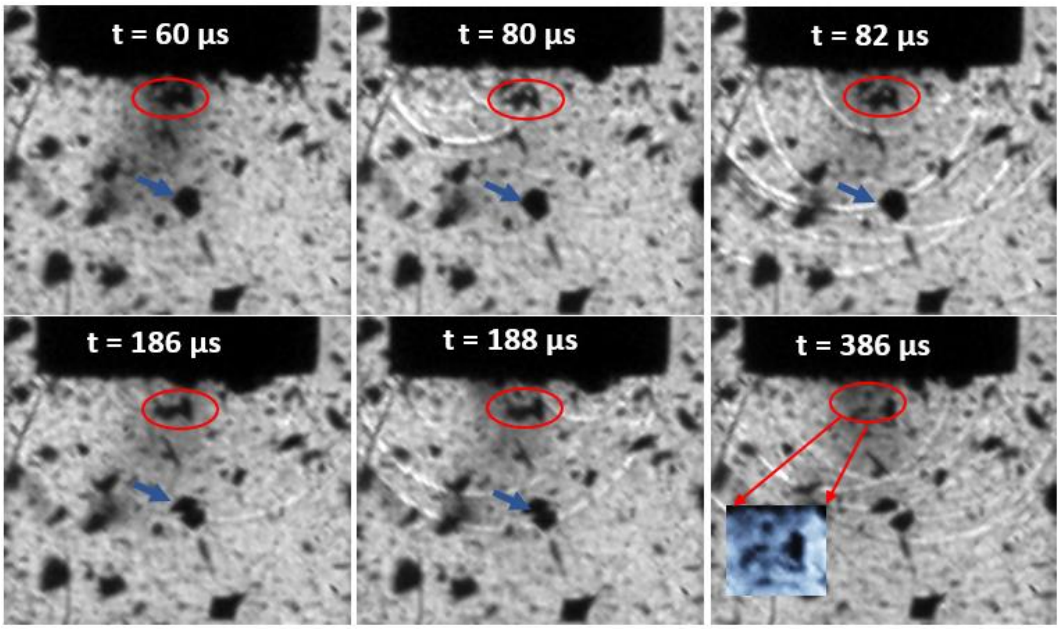

Figure 2: High-speed imaging at 0.5 Mfps of a tip vibrating with an amplitude of 219 µm, showing intermetallic crystals fragmenting. The red oval and the blue arrow indicate the fragmented crystal. The rectangle inset shows the enlarged fragmented crystals.

This data described in Chapter 5 was published as below:

In-situ observations and acoustic measurements upon fragmentation of free-floating intermetallics under ultrasonic cavitation in water

Ultrasonics Sonochemistry, 80 (2021), 105820.

Abhinav Priyadarshi, Mohammad Khavari, Shazamin Bin Shahrani, Tungky Subroto, **Lukman A Yusuf**, Marcello Conte, Paul Prentice, Koulis Pericleous, Dmitry Eskin & Iakovos Tzanakis

Chapter 6 investigates the cavitation activity generated between the tips of two ultrasonic horns, aligned in opposition, as a function of the relative phase of tip-vibration. I was particularly interested in identifying potentially enhanced cavitation activity generated from two horns configured in opposition, relative to

that generated by a single horn, in the case where the tips were thrusting and retracting simultaneously, around the central point, fig 3 (b). The findings in this chapter illustrate the potential of simultaneous operation of more than a single horn during sample processing.

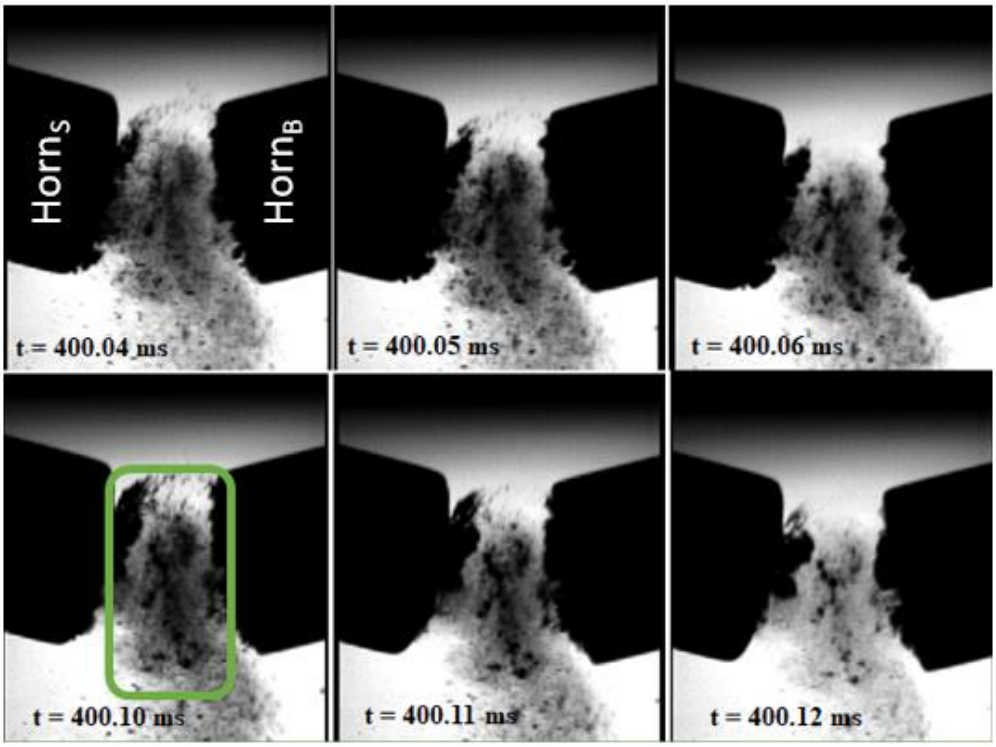

Figure 3: High-speed imaging at 100 kfps of the cavitation activity resulting from a two-horn sonication.

Finally, Chapter 7 employs a focused ultrasound transducer to investigate ultrasonic fixation of Nitrogen gas, sparged through a reaction vessel, in collaboration with colleagues at the School of Chemistry. Literature relevant to this Chapter specifically, is reviewed. The work sought to correlate the cavitation emissions to sonochemical yield and optimise in terms of the sonication parameters at the same input energy and constant sparged rate. Fig. 4 shows the effect of varying pulse intervals (PI) at constant input energy on the cavitation generated.

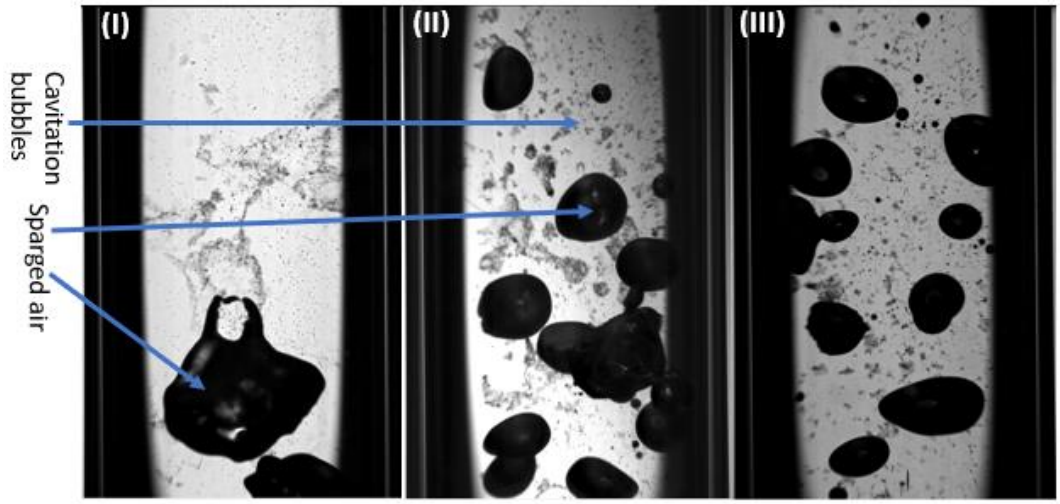

Figure 4: High-speed imaging at 20,000 fps of cavitation bubbles (smaller) generated by focused ultrasound in water sparged with air (bigger bubble) for investigating nitrogen fixation. (i) Observation collected at input pulse interval of (i) 10 ms, (ii) 40 ms, and (iii) 80 ms.

Chapter 1

An introduction to cavitation

This Chapter presents the necessary background on cavitation and methods used in studying it.

The Chapter is structured as follows: In §**1.1. A brief history of cavitation research**, the history of the emergence of cavitation as a research topic is described. §**1.2.** Acoustic cavitation presents the description of acoustic cavitation. Previous research from CavLab is presented in §**1.3. Previous research from CavLab**, and §**1.4. Conclusion** concludes the Chapter.

1.1. A brief history of cavitation research

Cavitation can be described as the rupturing of a liquid at a fairly constant temperature by an external pressure (P) that falls below the saturated vapour pressure of the liquid (P_v). The tensile stress (P_v-P) drags the molecules apart and creates a vacuum/void called a cavitation bubble. Cavitation is a nucleated process, meaning it is formed from a pre-existing 'weak point' in the liquid, such as an impurity/contaminant, dissolved gas or gas pocket. The nucleation can be homogenous if temporary microbubbles are formed due to thermal motion within the liquid, which serves as a point for the creation and growth of cavitation bubbles. Sometimes the nucleating point can be at a boundary between the liquid and solid particles or a solid wall called heterogeneous nucleation [2]. Cavitation is different to boiling in that the former takes place at a fairly constant temperature but under a decrease in pressure, whereas the latter occurs at constant pressure but through an increase in the temperature [2].

The first account of cavitation was reported in 1893 when two engineers, Thornycroft and Barnaby, discovered that part of the propeller of their submarine ship (HMS *Daring*) was eroded. They noticed an unexpected surge in the speed of the propeller, which they attributed to the rupture of the surrounding water due to the tension introduced by the rotating propeller. Froude suggested the term

"Cavitation" for this phenomenon, derived from the Latin word "cavus, -a, -um," meaning '*hollow*' [3]. Two years later (1895), an Anglo-Irish engineer, Parsons, reported a similar cavitation effect (propeller erosion) during the trial of his steam-operated ship (*Turbinia*). For this reason, he designed a novel steam turbine that mitigates the adverse effect of cavitation through the making of small cavitation tunnels. His work paved the way in understanding hydrodynamic cavitation [4]. He aimed to reduce the propeller's speed so that the developed pressure is reduced below the tensile strength of the liquid via the developed cavitation tunnel. As can be inferred from his statement, "…if the mean pressure of propulsion over the blade area exceeds $11\frac{3}{4}$ lbs/inch^2 then vacuum, or cavitation is set up". A modern cavitation tunnel is depressurised to allows the observation of cavitation flows at a much slower speed (i.e., at 1500 RPM instead of the normal operation around 12000 RPM). Photographing of the propeller cavitation is much easier at a slower rotation speed.

Swinton carried out the first photograph cavitation experiment in 1895. He took an image of water heated by a lamp, arranged below a tank, to a temperature just below the boiling point of water. However, this was not considered very successful due to poor photograph speed and resolution. Richardson, in 1911, produced another cavitation photograph by imaging a propeller rotating in water at moderated speed. This particular photograph was referred to as the copper tunnel [5]. The photograph was generated with an exposure of 10 s at *f*/16. The duration for the illumination of the propeller during each revolution was 1/3000 of a second. Following this development, effective photographing of cavitation activity was available. One of the most notable was made by Knapp and Hollander, when they used high-speed cinematography to monitor the life history of a cavitation bubble in 1948. They observed the presence of very large radial velocities and accelerations during the implosion period of the bubble. Their achievement made it possible to validate the early mathematical model described below. However, an understanding of the bubble dynamics was still unclear until the end of the 19th century.

The first mathematical model of a single cavitation bubble in an incompressible liquid was formulated in 1917 by Rayleigh. The model described the interaction of the surrounding host medium on a single spherical empty bubble. The bubble is assumed to expand under isothermal conditions and is compressed under adiabatic conditions. He estimated the collapse time (T_c) for a freely spherical bubble that has

reached a maximum size (R_{max}) to collapse to its minimum size (R_{min}), as expressed in equation (1.1).

$$T_c \approx 0.915 R_{\max} \left(\rho / P_0\right)^{1/2} \quad (1.1)$$

Where ρ and P_0 are the density of the liquid and the atmospheric pressure, respectively. Rayleigh's mathematical model did not consider the internal vapour pressure within the bubble, and the effect of surface tension was also neglected. Beeching modified Rayleigh's model in 1942 by including the possible effect of the bubble's internal vapour pressure and surface tension[6]. Plesset, in 1949, then modified Rayleigh's mathematical model by considering a vapour filled bubble subjected to an externally applied acoustic pressure field. The resulting model is commonly referred to as the *Rayleigh-Plesset* model. Analysis of this model demonstrated a firm agreement with Knapp and Hollander's imaging experiment results [7]. Although the Rayleigh-Plesset model remains the most popular for predicting the oscillations of a spherical bubble subject to external pressure fluctuations or acoustic cavitation, it is formulated on several assumptions. These assumptions include a constant bulk ambient temperature for the host medium, neglection of the compressibility of the liquid (i.e., assumption that the liquid density remains the same during compression), assumption that the dynamic viscosity of the liquid is constant, an assumption that the bubble's contents are homogeneous, and that the temperature and pressure within the bubble are always constant. In addition, the model predicts oscillations for a single bubble which is not representative of the majority cavitationing systems [8]. A single bubble may be used as a tool in understanding some fundamental aspects of cavitation bubbles. They are mostly created in a controlled environment like a laboratory for studying purposes. Most acoustic cavitation effects are due to a multi-bubble cavitation effect and not a single bubble event [9].

Two distinct classifications of cavitation are commonly reported: *inertial cavitation* occurs when the generated bubble or cavity undergoes rapid and violent collapse within a few acoustic cycles, generating extreme high physical conditions. *Non-inertial* (or *stable*) cavitation refers to the situation whereby the cavitating bubble undergoes oscillation in volume, or shape, due to input energy [2]. A third category, stable-inertial, has been suggested due to the generally inadequate

description of the complex features in cavitation emission spectra, using the common binary classification [10] [6].

Hydrodynamic cavitation[1], laser-induced[2] cavitation, and ultrasound (*acoustic cavitation)* are being studied by many researchers. In this thesis, we shall consider using ultrasound to generate cavitation.

1.2. Acoustic cavitation

Before cavitation occurs, a negative pressure must be applied to rupture the existing cohesive force in the medium. The minimum value of the pressure required to create observable cavitation in the medium is known as its *cavitation threshold* [11]. Therefore, for an ultrasound wave to produce an observable cavitating bubble in a liquid, its acoustic pressure should be greater or equal to the *cavitation threshold* of the liquid. The approximate acoustic pressure (P_a) required to create a bubble of radius R_m is given as in equation (1.2) [12].

$$P_a \approx P_0 + \frac{0.77\sigma}{R_m} \qquad (1.2)$$

Where; P_0 is atmospheric pressure under normal experimental conditions, σ is the surface tension of the liquid. Equation (1.2) is valid when $2\sigma/R_m \ll P_0$. For a large bubble where σ can be neglected, the size of the cavitation bubble generated depends on the resonance frequency (f_r) of a gas bubble, as approximated in equation (1.3) [12].

$$f_r \approx \frac{3}{R_m} \qquad ; f_r \text{ (Hz)}, \ R_m \ (m). \qquad (1.3)$$

Different liquids have distinct values for cavitation threshold, dependent on frequency and temperature [11]. For example, the cavitation threshold at 20 kHz for distilled water is estimated to be in the range of 0.06-0.1 MPa [13], 0.15 MPa

[1] Hydrodynamic cavitation refers to bubbles generated due to specific flow conditions and changes in ambient pressure. It is commonly encountered around in valves, propellers, and impellers. This can be generated in the laboratory using Venturimeter where flow is restricted for change in pressure.

[2] This technique generates cavitation at a specified location of choice by propagating a laser of a certain energy level through the medium. Once the energy introduced from the laser reaches or is greater than the breakdown threshold of the medium, the incident point nucleates and generate a plasma that rapidly expands to form a large bubble [45]

for liquid glycerine [14], and 0.7 MPa for molten aluminium [13]. When ultrasound is irradiated to a liquid, the rarefaction cycles exert negative pressures on the liquid, pulling the molecules away from one another. If the ultrasound pressure exceeds the value of the cavitation threshold for the host medium, the rarefaction cycle can create cavities in the liquid [15]. The rate at which gases diffuses in and out of a bubble cavity depends on the internal pressure of the bubble and the ambient pressure of the host medium. During expansion, the pressure inside the bubble is slightly higher than the ambient pressure surrounding it. The reverse is the case during the compression phase. The bubble oscillates in size over many acoustic cycles. The bubble changes in size/volume during different phases of the sound field such that the bubble is expanding during the rarefaction phase through a process known as *rectified diffusion.* The size of the bubble increases as a result of the net effect of *rectified diffusion* until the bubble reaches a size that can no longer sustain itself due to poor absorption of energy from the sound field; the bubble then collapses [16]. The collapsed bubble creates extreme physical (high temperature and pressure) and chemical conditions (radical generation). The process discussed so far is represented in fig. 1.1.

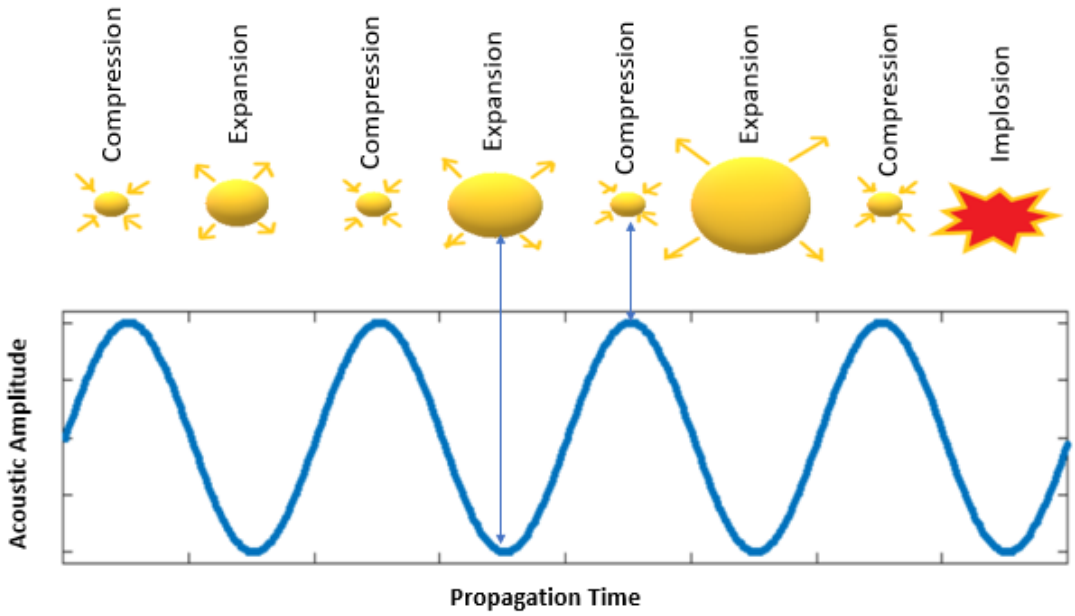

Figure 1.1: Behaviour of bubble generated in a host medium when exposed to ultrasound. Extreme high physical and chemical condition is generated when the bubble collapses.

Bubble formation is essential for most industrial applications during ultrasound exposure. For example, in sonochemistry applications, ultrasound wavelengths are not comparable with molecular dimensions. Therefore, the chemical effects of ultrasound cannot take place from direct irradiation of ultrasound with molecular species except when bubbles are generated [17]; this illustrates the importance of bubbles in the sonochemistry process. Cavitation leads to a huge concentration of energy that is much higher when compared with the energy density of the acoustic field that produces it. High temperatures (hotspots, described in §**2.2.1** Hotspot), pressure spikes (shock wave), and microjets, which are associated with the bubble's collapse, are responsible for most cavitation mediated applications [12][8]. Microjet formation is observed when the bubble collapses asymmetrically (especially in proximity to a boundary) due to a non-uniform fluid flow surrounding the bubble. The velocities of the microjet are in the order of 100 m/s [12]. All physical and chemical effects generated from acoustic cavitation are good candidates for industrial applications like Crude oil upgrading [18][19], biofuel production [20], sonochemistry [12][21], metallic alloy treatment [13], and food processing [22][23].

1.2.1 Methods of studying cavitation bubbles

The monitoring of cavitation bubbles is essential for studying and understanding the sonochemical and physical effects of cavitation. The following techniques can be used to study acoustic cavitation [24].

- Acoustic emission detection- cavitating bubbles act as secondary sources of sound, non-linearly scattering the primary field. These acoustic emissions can be detected and analysed for information about cavitation activity.
- Chemical detection- this is the measurement of radical generation via cavitation. The concentration of radicals generated is quantified using chemical dosimeters described in § 2.3.1 Chemical dosimetry.
- Light detection- measuring the light emission from the cavitating bubble (sonoluminescence) due to the radiative recombination of electrons and ions and electrons-atom (bremsstrahlung) [12]. The intensity of light emitted from the bubble can be enhanced by adding a small amount of luminol in aqueous alkaline solutions [12]. The generated hydroxyl radical will react

with the luminol during cavitation and generate an intense light. The region covered by these emitted lights is the active region in the sonochemistry, as shown in fig. 1.2. The figures show that the brightness of the emitted light was increased with the addition of luminol under the same sonication condition.

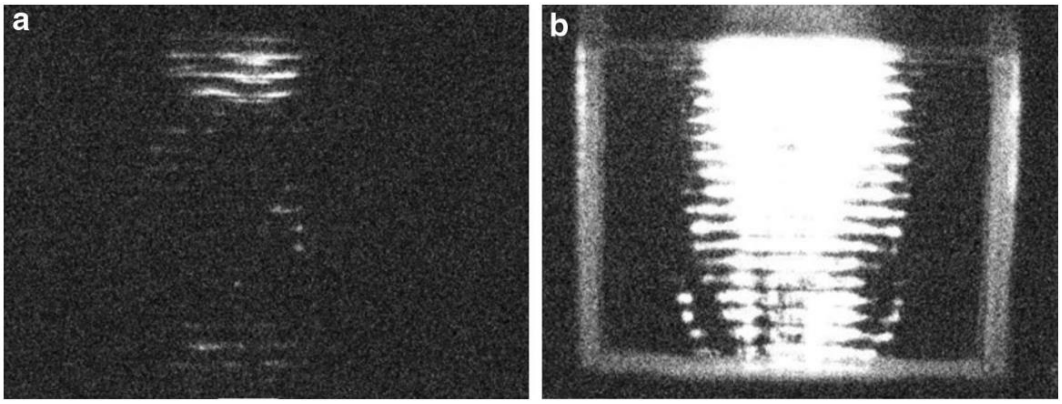

Figure 1.2: Sonoluminescence from (a) water and (b) an aqueous solution containing luminol; frequency = 170 kHz; power = 12 W [25].

- Mechanical detection- measuring the erosion of surface and material loss due to cavitation effect. This technique assumed that the cavitation takes place at the surface of a test material which then wears, deforms, cracks or break the material. A simple and popular method used for investigating the mechanical effect of cavitation is by placing a sheet of aluminium foil into a cavitating vessel for about 30 s and then examining the resulting perforations caused by the cavitation bubble [24]. There are erosion sensors developed to detect the mass defect after sonication
- Acoustoeletrochemistry- is the process by which mass flux reaction or erosion from acoustically induced liquid motion results in an electrochemical current that is sensed with an electrode. In the stagnant fluid, the electrochemical current is limited only by diffusion, but as soon as cavitation occurs, the liquid region close to the electrode tip becomes depleted of active species with time. Convection is thereby introduced to the system due to the disruption of the depletion layer by the liquid motion. This change in the depletion layer is sensed by the electrode (usually made

from metal like platinum covered with an insulator like glass or epoxy resin) as an enhancement of electrochemical current [26].

- High-speed imaging (HSI)- is the use of images to study cavitating bubbles. The dynamics of cavitating bubbles evolve within a fraction of a second. The high-speed camera deployed for studying or monitoring cavitation bubbles can record at a high number of frames within a second (i.e., capable of recording millions of frames in a second). Two such of such cameras are described in § **3.2 High-speed cameras**.

In this thesis, acoustic emission, chemical detection and HSI are the techniques used to study acoustic cavitation.

1.2.1.1 Acoustic emission

Acoustic emission is one of the most popular, accessible, and versatile tools for monitoring acoustic cavitation. The degree of information obtained in the detected acoustic emission depends on the cavitation sensor used. Acoustic data-rich in spatial and temporal resolution is obtained when an efficient sensor with high spatial sensitivity is used.

Acoustic emissions can be detected using the basic setup shown in fig. 1.3 (a) & (b), the nature of the ultrasound field source differs from the two acoustic transducer devices[3] used. The acoustic transducer device comes in different types, sizes, and geometries. The device is shown in fig. 1.3 (a) is a low-frequency high, power ultrasonic horn (the subject of investigation in Chapters 4-6). When operated, the tip of the horn vibrates, generating intense cavitation activity at the tip location. The acoustic device in fig. 1.3 (b) has a concave radiating surface that concentrates the ultrasonic waves to a specific point at some distance from the device (focus). This is the type used in Chapter 7 for the sonochemical experiment, and it is used generates cavitation bubbles at the focus of the transducer due to the intense acoustic field formed at this region.

[3] An ultrasonic transducer is an electromechanical transducer that converts electrical energy to sound energy at a designated frequency.

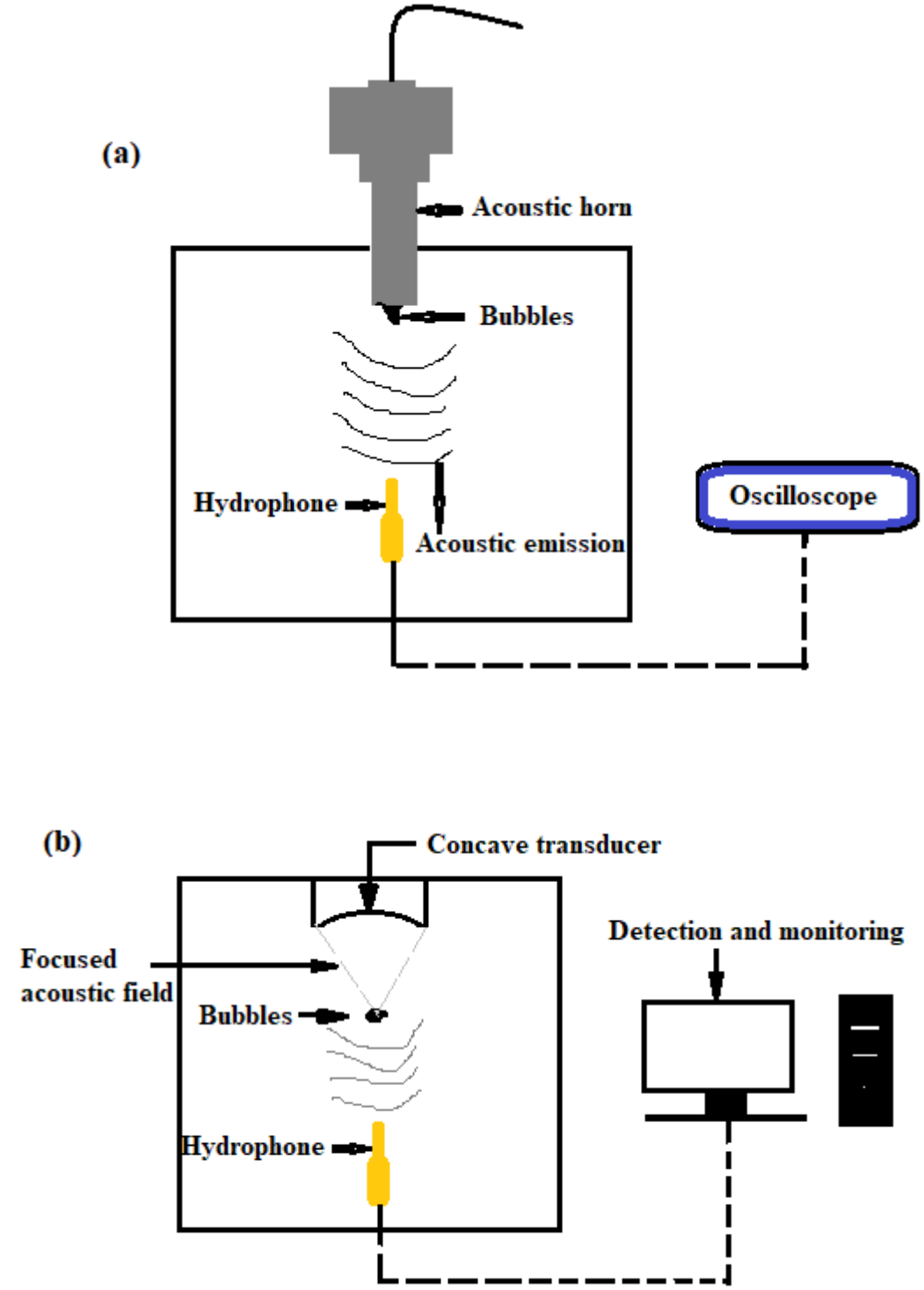

Figure 1.3: Basic cavitation detection experiment with (a) ultrasonic horn that has bubble generated at its tip (b) focused ultrasound transducer that nucleates cavitation activity in focus. The bubbles are forced to oscillate and generate acoustic emissions. A hydrophone measures the acoustic emissions, and some detection and monitoring protocol is used to classify and quantify the cavitation activity

The generated *acoustic emission* is collected by another transducer (hydrophone). A hydrophone converts the acoustic pressure data to electrical voltage data, which can then be post-processed to reveal information about the cavitation bubble. The collection of acoustic emission data may seem simple, as shown in fig. 1.3 (a) & (b) however, adequate precaution is required to avoid all possible complications, such as hydrophone damage and alignment problems where accurate measurement is required.

The acoustic emission spectrum mostly comprises frequencies related to the fundamental frequency of the ultrasound, f_0 (harmonics, subharmonics, and ultra-harmonics) [27] [28]. The origin of these frequencies from cavitating bubbles is suggested to either be from the collapse of specific-sized bubbles or from various non-spherical oscillations along with the bubble interface [29].

The harmonic (nf_0) components in the acoustic spectrum are due to the nonlinear oscillation of the cavitation bubbles [30]. The peaks at several harmonic frequencies appear more in the spectrum at high intensity when the bubble is no longer undergoing spherical oscillation [28]. The subharmonic, f_0/m (m is an integer), has been used to describe the inception of inertial cavitation and may also occur when a bubble that is twice as the resonance bubble's size was excited. Ultraharmonics, at nf_0/m (m, n are integers and $m > n$) are generated from the same bubbles as those producing subharmonics [30] [28]. The broadband signal is also known as *white noise* and may be sampled from between spectral peaks. It is thought to form from sources like the chaotic and nonlinear oscillation of the bubbles and shock waves generated from bubble collapse. Broadband signals in the acoustic spectrum indicate the bubbles underwent inertial cavitation [28] [31]. An alternative explanation for the bubble-based source for all of these features, based on recent CavLab research, is offered in §**1.3. Previous research from CavLab**.

Binary classification of cavitation using the acoustic spectrum is somewhat confusing. The presence of harmonics, sub, and ultraharmonics is sometimes used to describe stable cavitation or repetitive transient cavitation [31]. It has been suggested that both stable and inertial cavitation can occur together where there is broadband noise superimposed with harmonics [28] [32]. This is why a third category, *stable-inertial*, was necessary [6] [10].

An example of a cavitation emission spectrum obtained from a commercial ultrasonic cleaning bath, using a hydrophone (Reson TC4035) is shown in fig 1.4. The driving frequency (f_0) of the bath is 40 kHz; the spectrum shows that its frequency is not a single value but multi-frequency values. Frequencies such as the $f_0/2$ subharmonic at ~20 kHz, harmonics up to $6f_0$, and ultraharmonics ($3f_0/2$, $5f_0/2$, and $7f_0/2$), the broadband noise sample between the peaks are visible in the spectrum [24]. The curved shape of the spectrum with a local minimum at ~ 180 kHz is due to the hydrophone response.

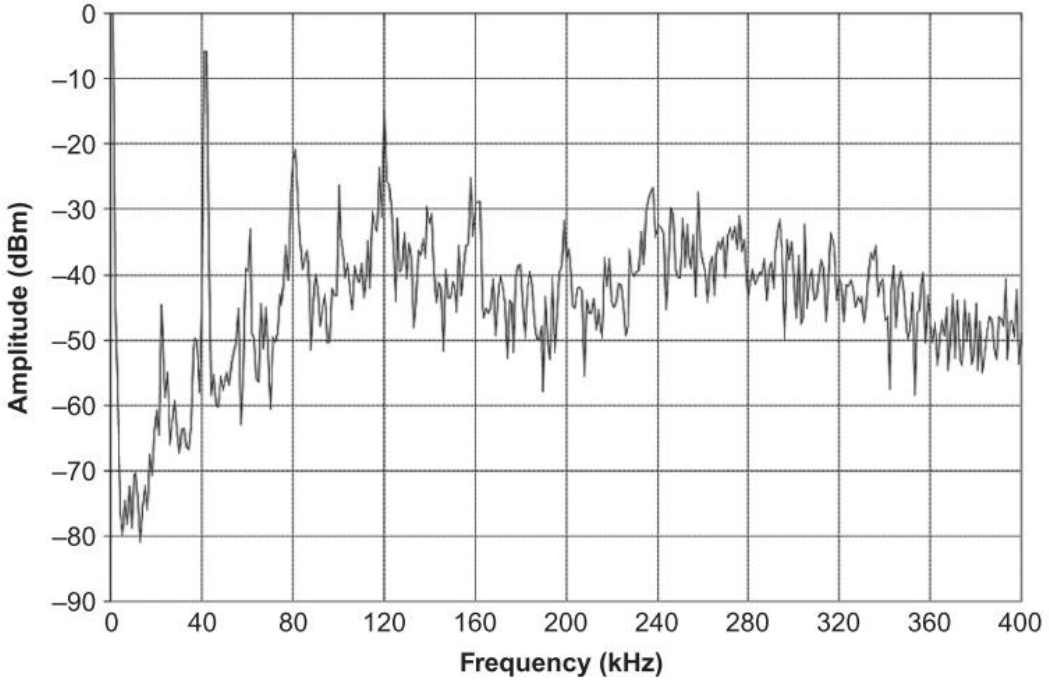

Figure 1.4: Hydrophone spectrum, measured in a 40-kHz commercial cleaner [24].

The energy distribution of the spectrum is highly nonlinear, especially at higher driving amplitude, where the inertial cavitation is expected to be high. A sensor of suitable bandwidth should be selected for representative acoustic data collection. In selecting the cavitation sensors for monitoring acoustic emission, there is a variety to choose from depending on the frequency bandwidth they operate and their tendency to resolve cavitation in a specific region of the fluid. Specialist suppliers, such as Sonic Concepts Inc., Precision Acoustics Ltd, and National Physical Laboratory (NPL), offer sensor devices, often with a stated

application and bandwidth. The sensors are commonly available as hydrophones [33][34], cavitometers [24] or passive cavitation detectors (PCD) [35]. Others are bespoke PCD that are manufactured in-house used for cavitation measurement [36][37][38] [39]. The most commonly used piezo-active materials for detectors are Lead Zirconate Titanate (piezoelectric ceramic material), PZT, and PVdF. Both PZT and PVdF are piezoelectric materials that generate charges when they are compressed, twisted, or distorted. PZTs are toxic, nonflexible, and brittle piezoceramics, thus are most suitable for flat surfaces. They exhibit very high dielectric and piezoelectric properties. They have large acoustic impedance (20-40 MRayl) due to their high material densities, hence matching layers are necessary for efficient utilisation of these materials in most liquid media. Their relatively large permittivities encourage electrical tuning and reduce their piezoelectric voltage coefficients. Also, their large mechanical quality factors demand the use of damping layers, to minimise ringing. PVdF, on the other hand is flexible, chemically inactive, tough, creep resistant, and stable when exposed to sunlight. More so, it has a relative low density as well as a low dielectric permittivity, hence possesses a very high voltage coefficient. However, PVdF requires a high electric field for poling, making the poling a slightly difficult. The type of piezoelectric materials used for fabricating acoustic detectors depends on the requirements of the target acoustic emission to be detected [40] [41].

For cavitation mediated applications, the detected acoustic emissions are often correlated with the effect they produce for the purposes of control and optimisation. For example, for some medical therapy applications, a certain spectral component of cavitation is used as a threshold for monitoring and controlling cavitation [42]. For industrial applications, the *arithmetic-mean power* over the active bandwidth of the sensor is used as a cavitation index to infer the 'strength' of the cavitation generated [36][29][24][43].

1.2.1.2 Chemical detection

The cavitation is studied or measured using the measurement of generated radicals. The generation of radicals via ultrasound is termed Sonochemistry, a review of which is the subject of Chapter 2. Description of how chemical detection is used for monitoring cavitation is discussed in § 2.3.1 Chemical dosimetry of this

thesis. Chapter 7 of this thesis also investigates the correlation between chemical detection (Chemical dosimetry) and acoustic detection.

1.3. Previous research from CavLab

CavLab is a research infrastructure dedicated to studying cavitation generated by a range of ultrasonic transducer and laser sources, based on high-speed imaging (as described in Chapter 3 and the Results Chapters) and acoustic detection. Previously in CavLab, fundamental research was motivated by therapeutic cavitation applications, using focused ultrasound transducers (also used in this work, **Chapter 7**) to cavitate contrast agent microbubbles and phase change nanodroplets [44]. This thesis marks the first time CavLab has turned its attention to industrial applications and sources of cavitation. The investigation carried out in the thesis are, however, based on the previous key findings from the CavLab. Therefore, this section briefly describes some of these findings related to the research presented in this thesis.

A key finding from the previous work on therapeutic cavitation was identifying the role of *periodic shock waves* (PSWs) generated from repeated bubble collapses and their contribution to features within the acoustic noise spectrum, fig 1.5, [45]. This work involved precision laser-nucleation [39] of a single cavitation bubble/bubble cloud at the focus of a transducer operating at 692 kHz at varying pressure amplitudes, in proximity to the tip of a 0.2 mm PVDF needle hydrophone (Precision Acoustics Ltd). The shadowgraphic high-speed imaging §3.2.1 Shimadzu High-speed camera) of the bubble activity, driven at an amplitude of 1.63 ± 0.12 MPa, is shown in fig 1.5 (a), (b) with the corresponding acoustic data collected, filtered for f_0, presented in (d). The PSWs emitted by the bubble respond in a *period-doubled*[4] regime, whereby strong collapses only occur for every other compressive phase of the driving.

[44] Period-doubled behaviour is a phenomenon that occurs dues to inertia of the host medium preventing collapse for every compressive phase in the ultrasound [44].

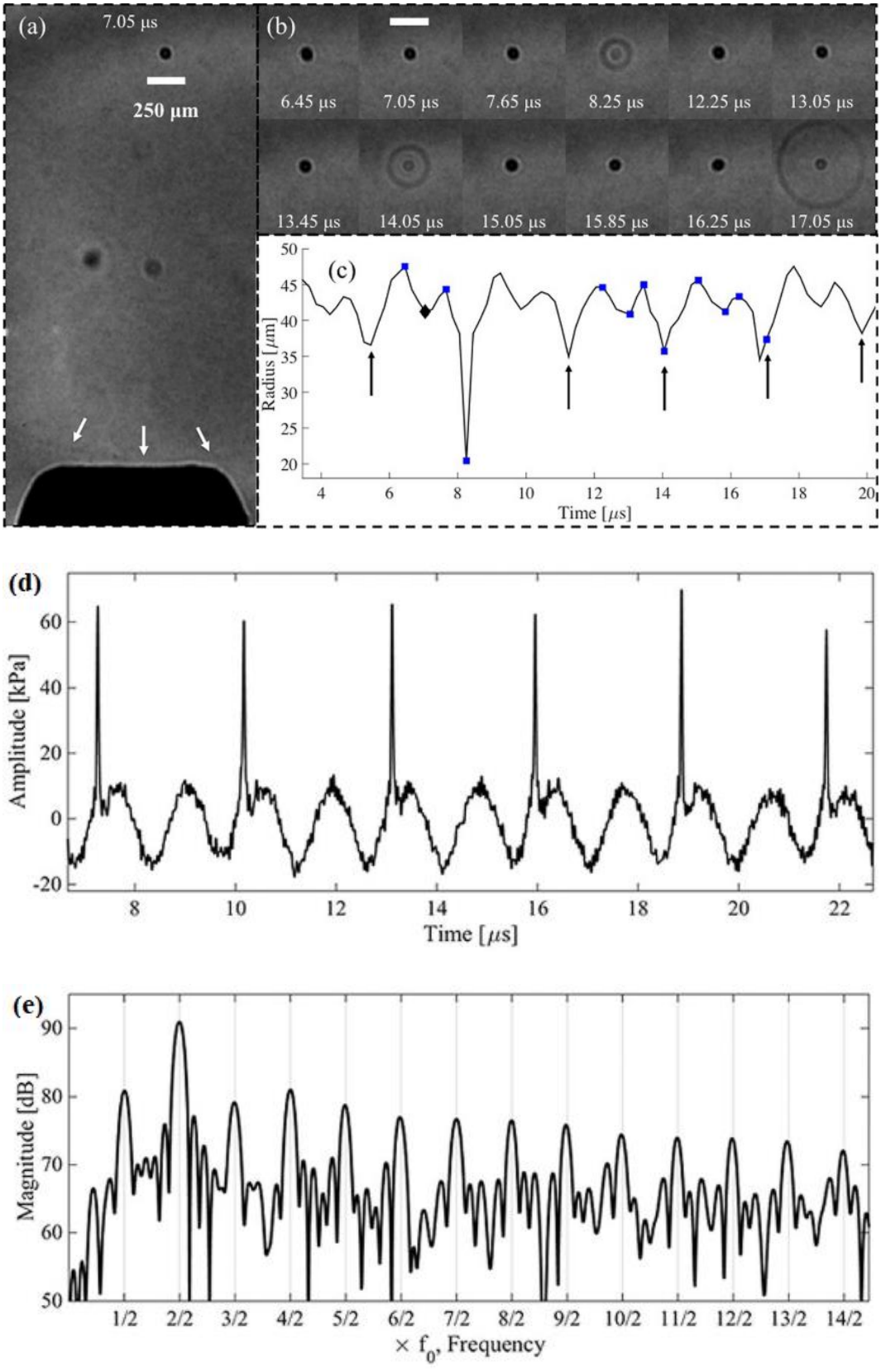

Figure 1.5: Images extracted from a high-speed sequence recorded at 5 x10^6 fps of cavitation activity in the $f_0/2$ regime. (a) The whole field of view, depicting the Hydrophone tip position relative to the activity, with a shock wave (arrowed white) incident to it. (b) Selected images representing the

cavitation oscillation dynamics, including three strong collapses and coincident shock wave emission. (c) Radius-time curve based on a dark pixel counting algorithm for the time interval under investigation. Diamond and squares indicate the specific images represented in (a) and (b), respectively. Scale bar represents 250 µm. (d) The experimentally detected acoustic emissions from a single cavitation bubble after subtracting a controlled exposure where no bubble was nucleated. The cavitation bubble was driven by a focused ultrasound field of f_0 = 692 kHz in the $f_0/2$ regime with the pressure amplitude PPA = 1.63 ± 0.12 MPa. (b) The corresponding acoustic cavitation noise spectrum from the measurement in (a) [45].

Careful analysis of this data, through the construction of a 'synthetic spectrum' and a spectral model developed for PSWs, confirmed that all features of the spectrum of the emission signal, fig 1.5 (e), can be attributed to the detected PSWs, and scattered components of the primary driving field. Essentially, PSWs at a given frequency ($f_0/2$ for fig 1.5) raise spectral peaks at integer values of that frequency, in the spectrum ($nf_0/2$, for all n, fig 1.5 (e)). This finding was further confirmed for cavitating contrast agent microbubble (SonoVue^{TM}), using the same focused ultrasound transducer. Moreover, microbubble-cavitation at a lower pressure amplitude of 385 kPa, for which bubble collapse occurred with every compressive phase, emitting PSWs at f_0 of the driving (and at much lower peak-pressure amplitudes), raised spectral peaks at nf_0 only [44].

This finding inspired the development of the shock wave passive cavitation detector (swPCD) device, optimised for the detection of bubble collapse shock waves [36]. The swPCD plays a prominent role in the current work, and a technical description is provided in § 3.3 Shock wave passive cavitation detector.

A key motivation for the work described in this thesis was to investigate if PSWs played an equivalent role in the emission signal from cavitation generated by a typical industrial source; the ultrasonic horn. A detailed account of this is provided in Chapter 4.

1.4. Conclusion

This chapter presented a general overview of cavitation methods available for studying cavitation activity, with an emphasis on those used within this thesis. Key research findings from CavLab directly related to the present research undertaken in this thesis were discussed.

Chapter 2

Sonochemistry

Sonochemistry refers to the use of acoustic cavitation to initiate and enhance chemical activities. The direct irradiation of sound field of any intensity may not initiate chemical activities except through bubble mediated action. For any active radicals to form, sufficient energy is required to dissociate the existing chemical bond and ionise them. Such needed energy is achieved during the collapse of the cavitating bubbles. The adiabatic compression of gases in the bubble leads to the generation of heat energy within the bubble. Since the discovery of sonochemistry in the early 19^{th} century, it has been deployed for many chemical processes and applications. Even though the use of ultrasound to enhance chemical reactions has been established, Neppiras was the first to mention *sonochemistry* in his review published on acoustic cavitation in 1980 [8][46]. Despite several research outputs on sonochemistry, the optimisation of the sonochemical yield at constant input energy, as a function of the acoustic parameters, is yet to be exploited. Particularly the use of a focused transducer as the source of ultrasound for a sonochemistry experiment, described in Chapter 7 of this thesis. The subsequent section reviews some relevant literature on the subject.

2.1. Historical background of sonochemistry

One of the interesting aspects of sonochemistry is how extreme temperature and pressure conditions necessary for some chemical reactions, albeit highly localised in space and time, can be generated under otherwise ambient conditions, simply through ultrasound exposure. The first known report on the chemical effect of a sound wave was in 1927 by Richards and Loomis [47]. They reported that certain chemical reactions, such as the hydrolysis of dimethyl sulphate in the presence of an indicator, and the reduction of potassium iodide (KI) by sulphuric acid, proceeded faster when reagents were exposed to an ultrasound at frequency 289 kHz under varying intensity. Brohult *et al* [48] in 1937 reported that an

ultrasound exposure at 250 kHz to a colloidal solution of haemocyanin was effective in cracking its molecule into three smaller molecules. Following this development, most sonochemical research was channelled towards synthetic polymer degradation until 1939 [8]. In the early 1950s, the field of sonochemistry witnessed several exciting developments. The first computations modelling of a cavitation bubble was carried out by Noltingk and Neppiras [12]. Schultz and Henglein reported the sonolysis of organic solvent in 1953. Microstreaming associated with cavitating bubbles was suggested by Elder *et al* in 1954 and 1959 as one of the mechanisms responsible for ultrasonic cleaning effects in heterogeneous systems. In the 1960s, most publications on sonochemistry focused on biological systems. Also, ultrasonic cleaning baths deployed in many chemical and metallurgical laboratories for cleaning glassware and forming dispersions were becoming popular during this era. The knowledge and understanding of the physical effects of ultrasound in the homogeneous liquid medium began to increase in 1961. In 1961, Naude and Ellis postulated the existence of microjets from the non-uniform implosion of the bubble (asymmetric collapse). This dynamic is now known to explain the pitting of solid surfaces and possible grain refinement. In 1963, Wessler published the first observation that showed the inverse relationship between sonochemical reactions and ambient temperature. He observed a decrease in the sonochemical reaction with an increase in the ambient temperature of the host medium. In 1964, Flynn first suggested the now popular terms *transient cavitation* and *stable cavitation*. In the 1970s, there was a drought in sonochemistry publications until the 1980s [8][49].

The surge in interest in sonochemistry in the late 80s and early 90s led to the first international conference on sonochemistry, held at the University of Warwick in 1986, organised by the Royal Society of Chemistry. The overwhelming success of the conference saw it established as an annual event. In 1987, the Royal Society of Chemistry founded a new sonochemical research group located at Harwell Laboratory in the UK. This group wanted to develop ultrasound-based research output that could be directly integrated into the industry. Similar efforts were made to facilitate the large-scale implementation of the sonochemical process in other countries. One such effort in France realises a sonochemical plant designed to convert cyclohexanol to cyclohexanone. The research was funded by the Electricite de France [47]. Another sonochemical plant was established in Germany, with a modular reactor capable of producing four metric tons of Grignard

reagent (EtMgCl and BuMgCl) per annum. Hoechst and others jointly constructed the plant at the Clausthal Technical University in Germany. Following the successful operation of the plant, ultrasound increases its production rate fivefold, and the induction time is reduced by 96.5% (i.e., from 24 h to 50 min) [47]. Following these developments, in the early 90s, the demand for acoustic devices rose correspondingly, and many companies specialising in producing these devices emerged. This development led to the production of several varieties of equipment made for sonochemical research to be readily available in the market. Therefore, the research output in sonochemistry experienced a boom, leading to establishing a dedicated scientific journal, *Ultrasonics Sonochemistry*, with its first issue in 1994 [8]. From this time, a substantial volume of literature is available on the chemical effect of an ultrasound, and these effects have since been deployed for several chemical applications such as; degradation of chemical and biological effluent in water treatment [50] [51], catalysis or improvement in the rate of chemical reaction [52] [53], polymer and material synthesis [54], electroplating processes [55], crude oil production [18].

Despite the development and advancement in the process and methods in sonochemistry research, the industrial application is still limited, owing partly to several reasons that include:

- Lack of detailed understanding of the correlation between the sonochemical output and the acoustic input/output parameters [8].
- Poor efficiency issue of the acoustic devices, which may lead to high operation costs.
- The issue associated with output measurement, failure to specify the actual exposure conditions, and reporting protocol may lead to difficulty reproducing the research results.
- An issue associated with upscaling of the research methodology for industrial applications. One of the fundamental issues is knowing the role of cavitation in sonochemical enhancement and improving it for maximum efficiency.

Quantification and correlation of the acoustic output and the chemical yield for a given process, information regarding the acoustic characteristic of the reactor to be used, and adequate driving conditions of the transducer required to produce optimum cavitation effect could significantly address a number of the issues

highlighted above. Monitoring the acoustic emissions generated by cavitation activity is a popular method used to quantify, categorise, and evaluate cavitation. If the acoustic emitted from cavitating bubbles is adequately monitored with the help of a suitable hydrophone (See Chapter 1 for discussion on hydrophone). The acoustic emitted associated with the bubbles is retrieved and evaluated after processing the signal to reveal the dynamic bubble behaviour. Hence, the chemical yield is then directly correlated with the acoustic emission for possible maximum chemical yield.

Price *et al* [28][56] suggested from two of their works that an increase in inertia cavitation was responsible for the increase in the sonochemical generation of hydroxyl radicals. The collected acoustic emission spectra contain harmonics, subharmonics, ultraharmonics of the driving frequency, and broadband noise. The harmonics are sourced from the nonlinear oscillations of the bubbles. In contrast, the broadband noise, the sub, and ultra-harmonics result from bubbles undergoing inertial cavitation, which may be better explained using periodic shockwaves generated from the bubble implosion [57], [58]. Therefore, for quantification and optimisation purposes, the cavitation produced during sonochemistry and the sonochemical yield should be monitored and studied in parallel for possible improvement in the sonochemistry efficiency.

Most research available on sonochemistry is primarily concerned with improving the sonochemical yield but pays little or no attention to the process's energy usage or overall efficiency [51], [55], [59]–[62]. Suslick *et al* [61] used ultrasound to enhance several sonochemical activities such as material synthesis, chemical synthesis and protein synthesis. Yao *et al* [62] achieved the degradation of a complex substance known as parathion[5] within 30 minutes of ultrasound exposure at a frequency of 600 kHz. The degradation rate was found to increase with increasing ultrasound intensity from 0.1 to 0.69 W/cm^2. Zupanc *et al* [51] reviewed several cavitation effects on microorganisms (Bacteria, Fungi, Viruses, Algae). They identified the mechanical, thermal, and chemical effects as agents responsible for microorganism destruction. Dheyab *et al* [55] used an ultrasonic horn operated at 20 kHz to effectively deposit some layer of gold nanoparticles onto a ferrite core. Similarly, sonochemical effect/yield improvement is the primary

[5] Parathion is an organophosphorus pesticide that is often used for agriculture activities which extremely dangerous when consumed from a contaminated water.

concern of many other research studies [63]–[65]. It can be seen from the above-reviewed literature that the authors are more concerned with the sonochemical yield/effect. Energy used or power delivered during these experiments were not monitored.

Below, the literature that mentions the power delivered from the acoustic device used during the respective experiments, but do not optimise the yield at constant input energy, is reviewed.

Mason *et al* [66] quantify the sonochemical efficiency of ultrasonic effect on the particle size reduction of copper bronze in liquid media under varying operating conditions. A special sonoreactor (Undatim Sonoreactor probe system) was designed to maintain constant acoustic power. The acoustic power of the reactor was estimated via a calorimetric method. N_2 and Ar gases were sparged into the heterogenous mixture (solid/liquid) during the ultrasound exposure, and their effects were investigated. A greater reduction in particle size was achieved with sparged gases, with much more reduction observed for Ar than when N_2 gas was used. It implies that monoatomic gas generates greater cavitation activity than polyatomic gas. Koda *et al* [67] provided a more elaborate method for categorising sonochemical efficiency. Seven different experimental setups were considered; see the table in fig 2.1 for detailed experimental conditions. Ultrasound of frequency range from 19.5 kHz to 1.2 MHz was exposed into the 50 cm^3 of distilled, ionised water, which was sparged with air for 30 minutes before the exposure. The calorimetry method was used to estimate the transducer's acoustic power (~ 6.5 W).

Apparatus and experimental conditions

Apparatus	Abbreviation	Configu-ration	Transducer		Fre-quency (kHz)	Load power (W)	Method				Thermo-couple
			Type	Diameter (mm)			Cal.	TPPS	KI	Fricke	
Honda Electronics HSC-01	Aist 25k	(B)	BLT	45	25	41, 55	○	○			(a)
Honda Electronics HSC-01	Aist 45k	(B)	BLT	45	45	110–220	○	○	○	○	(a)
Honda Electronics HUS-2	Aist 96k	(A)	BLT	45	96	50–150	○	○	○		(a)
Honda Electronics HUS-2	Nagoya 96k	(B)	BLT	45	96	50–100	○	○	○	○	(b)
Honda Electronics HUS-2	Nagoya 130k	(B)	BLT	45	130	50–200	○	○	○	○	(b)
Honda Electronics HSR-1	Nagoya 500k	(B)	PZT	50	500	10–40	○	○	○	○	(b)
Kaijo 4021	Shiga 20k	(C)	Ferrite	130 × 150	19.5	40–200	○	○	○	○	(a)
L&R Cleaning Bath T7B	Shiga 40k	(B)	Ferrite	110 × 100	40	35	○	○	○	○	(a)
Kaijo 4021	Shiga 200k	(C)	PZT	65	200	140–200	○	○	○	○	(a)
Kaijo TA-4015	Toyama 400k	(C)	Barium titanate	80	400	120	○	○	○	○	(c)
Kaijo TA-4015	Toyama 1200k	(C)	Barium titanate	80	1200	120	○	○	○	○	(c)

(a) Advantest S Theath thermocouple TR1101-1300 (K-type, 1.6 mm), (b) Takahashi Thermo Sensor Theath thermocouple (K-type, 1.6 mm), (c) Chino KT91A 5410N (K-type, 1 mm).

Figure 2.1: Apparatus and experimental conditions for each investigation [67].

The sonochemical efficiency (SE) was computed as a ratio of the sonochemical yield and the acoustic energy. The sonochemical yield of OH^- obtained using Fricke, KI, and 5, 10, 15, 20-TPPS[6] dosimetries depends on the frequency used. The sonochemical yield was maximum at a frequency of 300 kHz for all the dosimetries used, as shown in the table displayed in fig. 2.2. Their work suggests that sonochemistry yield could be improved in the range of 200-300 kHz. Although, the optimum frequency depends on other experimental aspects such as the nature of the host medium, the type of acoustic devices, and the sonoreactor used for the sonochemistry experiment.

[6] Tetrakis (4-sulfotophenyl) porphyrin($H2TPPS^{4-}$)

	kHz	SE_{KI} (mol J^{-1})	SE_{Fricke} (mol J^{-1})
Shiga 20k	20	$0.60 \pm 0.02 \times 10^{-10}$	$2.3 \pm 0.1 \times 10^{-10}$
Shiga 40k	40	0.60 ± 0.02	2.8 ± 0.1
Aist 45k	45	0.67 ± 0.06	3.7 ± 0.1
Aist 96k	96	4.5 ± 0.2	
Nagoya 96k	96	4.1 ± 0.2	16.8 ± 1.0
Nagoya 130k	130	5.6 ± 0.4	22.6 ± 1.6
Shiga 200k	200	8.3 ± 0.6	15.2 ± 0.9
Toyama 400k	400	7.8 ± 0.2	19.3 ± 1.2
Nagoya 500k	500	7.1 ± 0.2	20.3 ± 1.2
Toyama 1200k	1200	0.64 ± 0.3	2.6 ± 0.1

Figure 2.2: Frequency dependence of the sonochemical efficiency (SE-value) for KI oxidation and Fricke reaction [67]

Choi *et al* [68] considered the effect of air sparged rate on the oxidation rate during ultrasound exposure of water placed in a rectangular reactor. A plane transducer attached to the base of the reactor was the source of the 36 kHz ultrasound. The acoustic energy was estimated using a calorimetric method. The effects of sparged air gas and liquid height (42 mm to 333 mm) on the sonochemical yield of OH^- determined using both KI and luminol intensity dosimetries were investigated. The position of the air sparger, as well as its distance from the transducer, had a great effect on the generation of OH^-. For all the liquid heights and the gas flow rates, the concentration observed when the sparger was placed in the central position just below the transducer was higher than when it was placed at the corner within the reactor. The sonochemical yield was observed to increase with the flow rate of sparged air, due to the resulting higher mixing rate.

Even though the literature reviewed above stipulates the acoustic power used, it is equally important to quantify the amount of cavitation generated from the acoustic power or energy. The methods used to quantify the amount of cavitation generated in relation to the sonochemical yield are discussed in § **2.3.** Measurement techniques

2.2. Mechanisms of sonochemistry

As described in § **2.1. Historical background of sonochemistry,** that ultrasound exposure to the host medium can initiate, enhance, or generate chemical radicals

under suitable conditions. The radicals hardly form without cavitating bubbles being generated or when the reactant is not volatile enough to enter the cavitation bubble during its formation [8] [69]. A phenomenon known as the *ordering effect* was suggested to generate radicals during sonication even without cavitation bubbles. Though it has not been proved experimentally; thus, it may be considered just a hypothesis [70]. The actual mechanism responsible for generating radicals during cavitation remains a subject of research. However, the most widely accepted mechanism of sonochemistry is the local hotspot [8].

2.2.1 Hotspot

The hotspot is formed due to adiabatic compression of the cavitation bubble leading to high temperature and pressure developed in and around the gas bubble just before it collapses [69]. The collapsing bubble creates a short-lived localised high-temperature spot before the heat is effectively diffused to the bulk of the liquid via thermal transport [71]. Thermolysis often takes place within the bubble cavity and in the interfacial layer surrounding the cavity, and it is responsible for the production of free radicals. Even though the hotspot concept gained wider acceptance among researchers, it cannot explain polymer degradation from cavitation [69]. Besides the hotspot concept, electrical or corona discharges have also been suggested to enhance radicals generation during cavitation [61] [72] [73]. This concept suggested that fragmented bubbles carry charges whose nature depend on the host medium. The compression phase of an acoustic wave could produce transient solid-like structures within the solution. These structures would result in an *ordering effect* of the molecules in which electrical charges could develop. The movement of these charge carrying bubbles during cavitation could result in a chemical effect [74]. It is possible that the combined effects are present and linked with each other since both phenomena would depend on the gaseous mixture's transport properties in the bubbles.

2.2.2 Factors affecting sonochemical yield

It has been established in the preceding section that cavitation generates chemistry action; therefore, factors that affect cavitation generation would

consequently influence the sonochemical activity. This section identified the controllable variables that can affect the sonochemical yield during sonochemistry. Some of these controllable variables are used as optimisation parameters in the sonochemical fixation of nitrogen in chapter 7.

2.2.2.1 The sonication times

The length of sonication time is the period during which the sample is exposed to ultrasound. It is a control variable that can affect the use to enhance the sonochemical yield. The sonochemical yield is mostly increased in proportionality with the effective sonication time [75]. The sonication time is investigated for optimising the acoustic cavitation generated at constant input energy in Chapter 7.

2.2.2.2 Frequency

The ultrasound frequency used for the generation of cavitation has an inverse relationship with the critical size of the cavitation bubble (see equation (1.3)) [76] [77]. The cavitation effect is reduced at a very high frequency due to a very short time for rarefaction and compression cycle [8]. Driving frequencies in the range of 20 kHz are associated with larger and violently collapsing bubbles that are mostly responsible for the mechanical effect of cavitation, such as surface deformation, surface erosion, and fragmentation. In contrast, medium frequencies in the region of 100 kHz are associated with a shorter life cycle of smaller cavitation bubbles that promote chemical reaction and cleaning [78], [79]. Therefore, most sonochemistry experiments are often performed at a frequency range of 20 kHz and 900 kHz. There is no optimum frequency for all sonochemical yields. The optimum frequency depends on the type of reaction and reagent involved. The oxidation reaction is favoured at high frequency than at low frequency. Entezari *et al* [80] observed that the rate of sonochemical yield of KI was about 31 times greater at an operating frequency of 900 kHz compared to 20 kHz. Wayment *et al* [81] found that the alachlor oxidation rate was approximately 25 times faster at 300 kHz under argon saturation than at 20 kHz. A similar observation was found in [82], where they suggested that OH^- escaped the cavitation bubble to the bulk of the liquid due

to short lifetimes of the bubble, promoting further chain reaction. The optimum driving frequency needs to be determined for all reactions. Merouani *et al* [83] considered the effect of driving frequency on the amount of oxidant produced in sonochemical experiment, the production rates of H_2O_2 was found to be 2.5071, 4.2060, 3.4386 and 2.0960 μM/s at respective frequencies of 300, 585, 860 and 1140 kHz, which shown a nonlinear relationship. For the most sonochemical experiment, the optimum frequency for maximum yield was suggested to be 300 kHz [84] [85] [86].

2.2.2.3 Pressure amplitude

The amplitude of the acoustic pressure delivered into the reaction sample during sonochemistry significantly affects the rate of radical generations. The pressure amplitude of the ultrasound determined the ambient radius of the active bubble during ultrasound exposure [87], [88]. Most literature confirmed that increasing the acoustic pressure increases the sonochemical yield until it reaches a maximum value, decreasing with increasing acoustic pressure [89]. Merouani *et al* [86] show through simulation that the amount of the oxidants produced in the bubble at the end of the bubble collapse increases as the acoustic amplitude increases from 1.5 to 3 atm until it reaches a maximum at 2 atm. Similarly, the result obtained in [67] shows that sonochemical yield increases linearly with increasing ultrasonic power. The increase in the pressure amplitude results in an increase in the acoustic power, hence more input energy is used. The pressure amplitude is an important parameter for the sonochemistry experiment reported in chapter 7.

2.2.2.4 Ambient temperature

The temperature of the host medium generally has an inverse relationship with sonochemical yield [8]. Most sonochemical yields are favoured at a lower bulk temperature of the host (i.e., ambient room temperature) [90] [86]. When the bulk temperature is raised, the vapour pressure of the sample is also increased. Hence, the cavitation threshold of the medium is lower, and more cavitation is generated at a given pressure amplitude [61]. However, the formed cavitation bubbles contain

more vapour, thus reducing their cavitation effect. The values between 10°C and 20°C are considered optimum values for all the pressure amplitude in many sonochemical experiments [86]. Merouani *et al* [91] show that the amount of the oxidised KI produced during sonication decreases with increasing temperature from (25°C to 55°C). A similar finding in [92] was reported, where the yield of nitrite decreased with increased temperature. Since the temperature significantly influences acoustic cavitation and chemical yield during sonochemistry, the sonochemistry experiment presented in Chapter 7 was undertaken at approximately constant temperature to avoid any effect of temperature changes.

2.2.2.4 Nature of dissolved gases

Dissolved or saturation gases act as nucleation sites for cavitation. As gases are used up from the reaction sample because of the cavitation bubbles, initiation of new cavitation events becomes increasingly difficult. Sparging gases through the reaction sample replenished the used gas and facilitated the production of cavitation bubbles. The temperature attained by the cavitation bubble depends on the nature of the dissolved gases in the host medium, among other factors. The heat conductivity, the adiabatic index, and the thermal properties of the gas determined the temperature of the cavitation bubble.

Moreover, very soluble gases in the reaction sample may cushion the cavitation effect since the bubbles formed may redissolve before collapse occurs. The bubbles with insoluble gas often become so large (because of superficial diffusion of gas into the bubble) that they float to the surface and collapse [8]. If the bubble is assumed to undergo adiabatic collapse, the temperature attained can be expressed as given in equation (2.1) [93].

$$T = T_{\infty}\left(\frac{R_{max}}{R}\right)^{3(\gamma-1)} \qquad (2.1)$$

T_{∞} is the ambient temperature, R_{max} is the maximum radius reached by the bubble before the collapse, R is the mean radius of the bubble after the collapse, and $\gamma = C_p/C_v$ is the adiabatic index (ratio of heat capacities). Noble gas like Ar or neon (Ne) has a high adiabatic index, thus generating higher temperature than oxygen gas. The concentration of radicals generations was 2 times higher with Ar gas than

with N_2 used as sparging gas and 20 times higher than with methane used as sparging gas [15]. Considering the effects of the nature of sparged gas on the sonochemical yield and the type of products formed during a sonochemistry experiment, it is essential to choose a gas that enhances the sonochemical yield and generates the target product. For this reason, liquefied air was chosen as the sparged gas used in the sonochemistry undertaken in chapter 7.

2.3. Measurement techniques

There are several opportunities available for studying cavitating bubbles with their mediated effects. As discussed in § **1.2.1 Methods of studying cavitation bubbles**, during cavitation, bubbles usually emit sound (acoustic emission), light (sonoluminescence), and generate radicals, as depicted in fig. 2.3 [94].

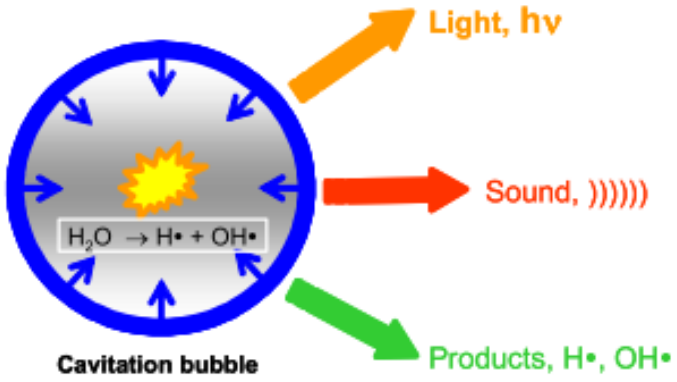

Figure 2.3: 'By-product' of a sonochemical active cavitation bubble that can be used for measuring or monitoring of processes [94].

As seen from fig. 2.3, the emitted light, the emitted sound (acoustic emission) and the radicals generated are used in studying cavitation and the effects it mediates. Therefore, acoustic emission and radicals generation were used in the study presented in chapter 7.

Both acoustic emission and sonoluminescence have been explained in § **1.2.1** Methods of studying cavitation bubbles, but the estimation of radicals generated during cavitation referred to as *chemical dosimetry* is briefly discussed in § **2.3.1**

Chemical dosimetry. After that, we shall consider literature that has used acoustic emission and sonoluminescence with radicals dosimetries in § **2.3.2** Sonochemistry studies using acoustic emission and sonoluminescence.

.

2.3.1 Chemical dosimetry

Chemical dosimetry is the technique used in quantifying radicals generated during sonochemistry. They are different types of dosimeters used for detecting different radicals. The most popular ones are KI, Fricke, Griess, and Terephthalate dosimeter.

The KI dosimetry is mostly used to quantify the OH^- radicals that are generated during sonochemistry. The oxidation reaction of the aqueous KI with OH^- to generate I_3^- which is then measured using a UV spectrometer [95].

The Fricke dosimetry comprises acidified iron II tetraoxosulphate VI salts ($FeSO_4$). It is also used for quantifying OH^- radicals generated during sonochemistry. The Fe^{2+} from the FeSO4 is oxidised to Fe^{3+} when reacted with OH^- or hydrogen peroxide (H_2O_2). Sometimes, Copper solution may be added (Copper-Fricke) for further radicals differentiation [8].

Griess dosimetry is used to quantify the presence of nitrite after sonication. This dosimeter was used in chapter 7, and a detailed description can be found in §7.3.4 Griess test

Terephthalate dosimetry makes use of the OH^- induced hydroxylation of the terephthalate ion. It was originally developed for the dosimetry of ionising radiation. They produced 2-hydroxyterephthalate after reaction with OH^- which is readily determined based on its fluorescence [60].

2.3.2 Sonochemistry studies using acoustic emission and sonoluminescence

Frohly *et al* [32] carried out the ultrasound water exposure at varying acoustic intensities ranging from 12-300 mW/cm^2 at a constant temperature. The acoustic emission is obtained using a hydrophone (DAPCO NP 10-3) from an experimental setup with a 6 cm by 6 cm piezoelectric transducer (PZT) operated at

1.075 MHz. The acoustic intensity was determined using the measured electrical input power and the acoustic efficiency of the transducer. They characterised the cavitations generated using acoustic spectra obtained from acoustic emission. Acoustic cavitation noise power (CNP) was used to quantify the inertial cavitation, whereas the spectra peaks at $f_0/2$ and $2f_0$ were suggested to be responsible for non-inertial cavitation. The CNP value was obtained from the numerical integration of cavitation spectra in logarithm scale, and only 10% was obtained from subharmonics, harmonic, and ultraharmonics peaks. The rest was from the acoustic noise (white noise). Fig. 2.4 presents the noise and peaks contribution in the spectrum, obtained at the 30 dB limit (the highest noise level observed from the acoustic emission). The contribution was evaluated by considering values above 30 dB to represent the contribution from the peaks and values below 30 dB to represent the contribution from the noise spectra.

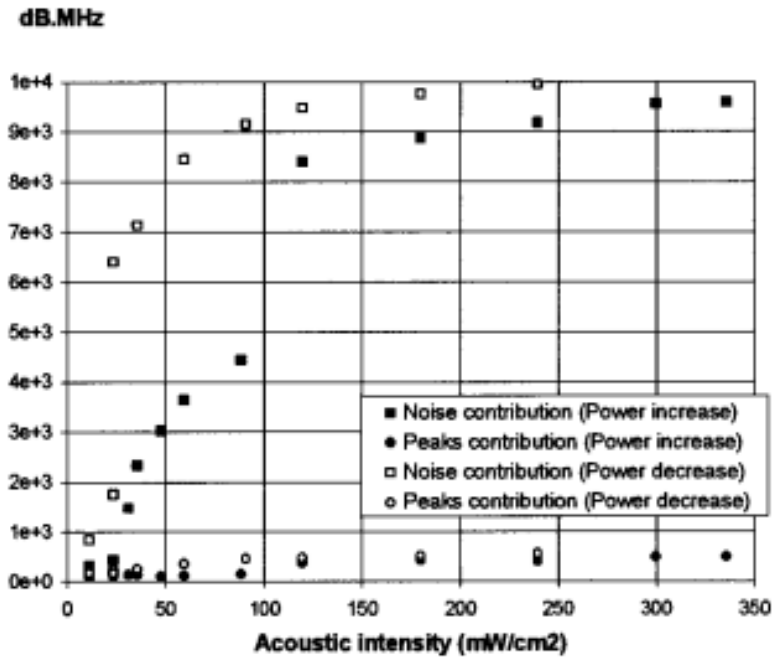

Figure 2.4: Comparison between noise and peak contribution to the cavitation noise power [32]

More so, the cavitation noise was observed to increase with acoustic intensity, as seen in fig. 2.5. The acoustic spectrum below 24 mW/cm^2 is an approximate lines spectrum comprising subharmonic, fundamental, harmonic, and

ultra harmonic components. Above 24 mW/cm^2, the line spectrum is superimposed with a broadband component referred to as acoustic noise.

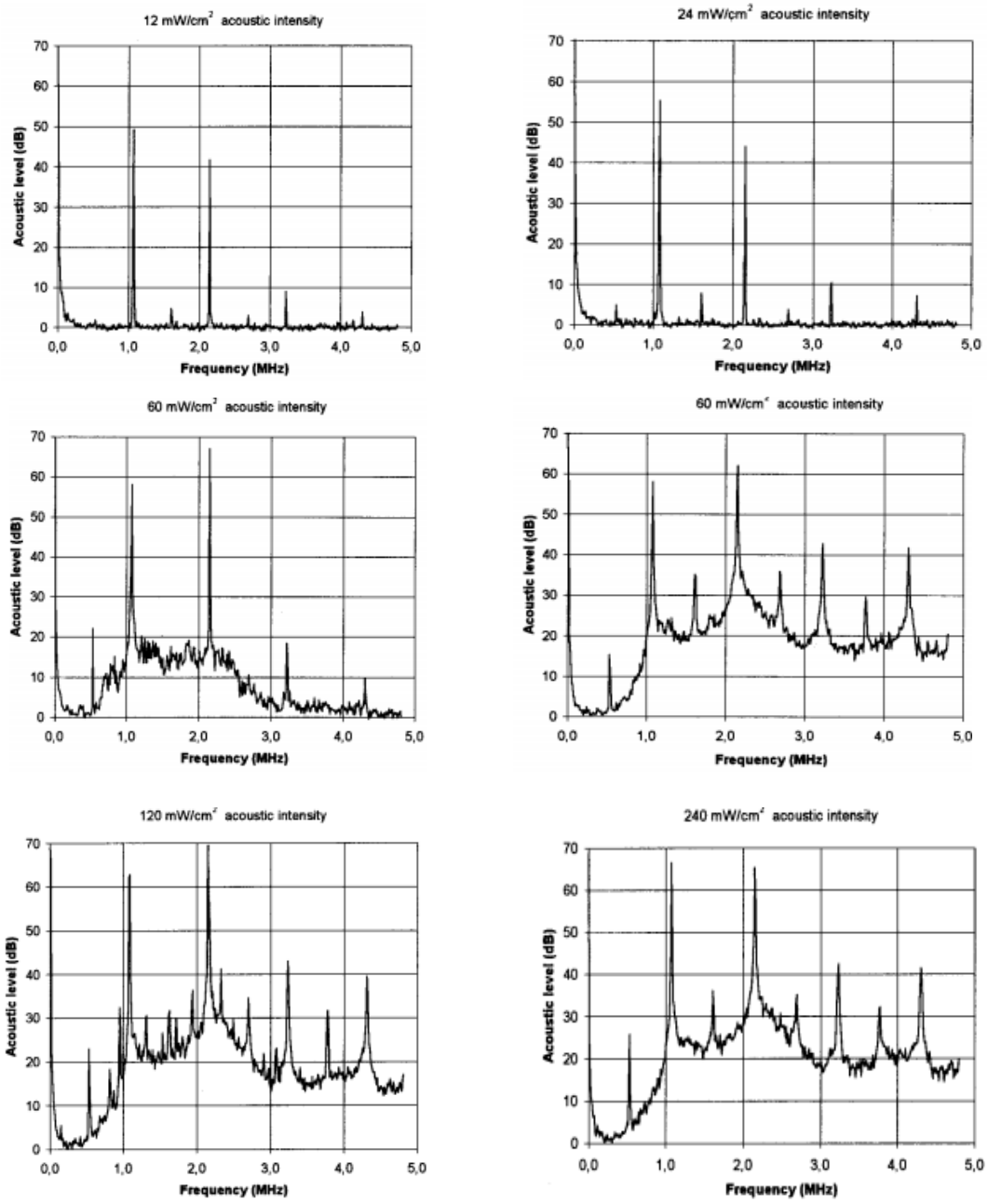

Figure 2.5: Cavitation noise spectra at different acoustic intensities transmitted to the liquid for increasing power [32]

The acoustic noise increases with intensity and reaches a maximum of around 30 dB. A phenomenon referred to as acoustic hysteresis was identified, which was defined as a phenomenon where acoustic cavitation intensity is sustained

at a much lower input power level than the initially established power. Specifically, for ultrasound exposure of 25 mL of iron II solution whose initial concentration is 2.2 x 10^{-2} M, the sonochemical yield estimated through the Fricke dosimetry increases with the electrical input power and the obtained CNP. The noise spectra and the sonochemical yield of oxidised OH^- shows a good correlation with respect to electrical power, seen in fig. 2.6.

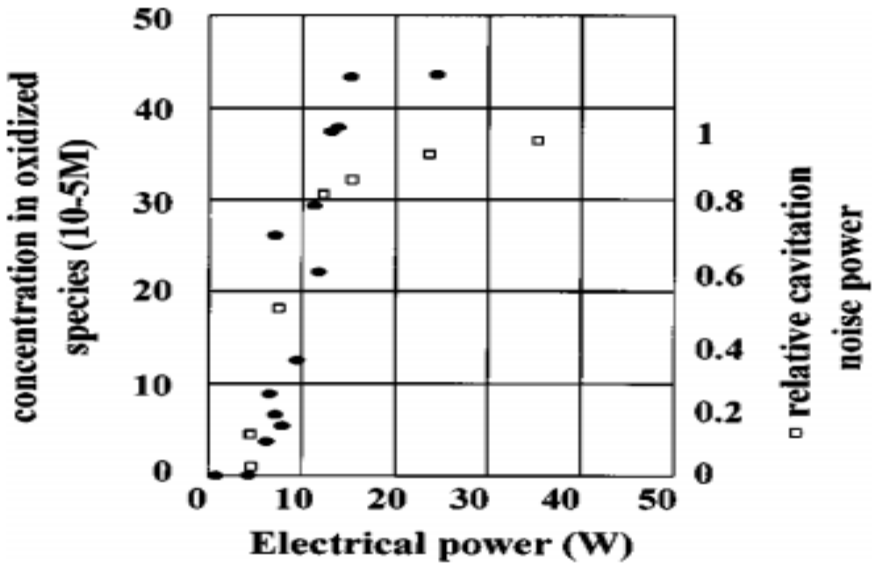

Figure 2.6: Experimental correlation between acoustic cavitation noise power (CNP) and sonochemical yield in an oxidation process [32]

Price *et al* [31] distinguished the cavitation from two different transducers using acoustic emission. The ultrasound exposure of water was carried out at two different frequencies of 20 kHz and 515 kHz at varying intensities. The acoustic emission signal was measured using a cavitation sensor made from a 110-µm-thick PVDF membrane sandwiched in polyurethane which is acoustically matched to water. A 350 cm^3 of pure water, with acoustic intensities in the range 0-120 W/cm^2, was used at 20 kHz whereas, at 515 kHz, a 130 cm^3 of solution with intensities in the range 0-8 W/cm^2 was used. The ultrasound exposure was limited to about 30s in each case to minimise temperature changes (23-26^oC). The spectral features at various intensities from the two frequencies were different. The spectra feature at 515 kHz comprises several high-intensity peaks up to 20th harmonics (20f_0). They are classified as stable cavitation; however, some broadband emission signified

inertial cavitation thus took place to some extent. This feature is attributed to the nonlinear oscillation of the bubbles. At 20 kHz, on the other hand, the acoustic spectra are featureless over the band of the hydrophone sensor (0-10 MHz) that was used. Only a very few low-intensity peaks of harmonics are observed up to $5f_0$. The rest of the spectra largely comprise broadband noise, subharmonics and ultraharmonics, representing the characteristic of transient cavitation as seen in fig. 2.7.

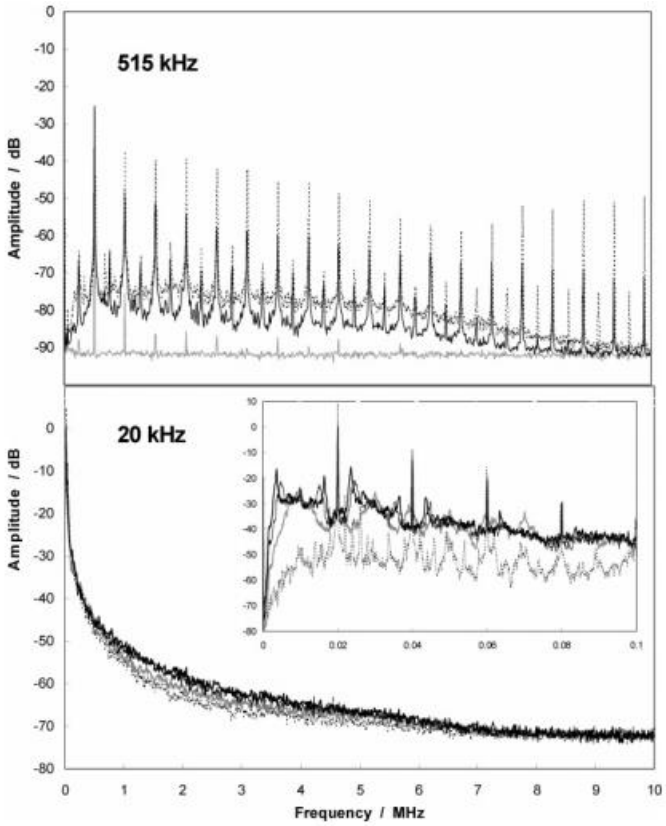

Figure 2.7: Acoustic emission from water sonicated at 515 or 20 kHz at various acoustic intensities. Inset shows emission between 0 and 100 kHz. For 515 kHz: (gray line) 0.90 W cm^{-2}, (black line) 2.1 W cm^{-2}, (dashed line) 6.5 W cm^{-2}. For 20 kHz: (dashed line) 10 W cm^{-2}, (gray line) 24 W cm^{-2},(black line) 70 W $cm^{-2,}$ (heavy black line) 120 W cm^{-2} [31]

The energy consumed is computed from the obtained spectra using equation (2.2). The concentration of OH^- was determined at different applied intensities using KI dosimetry. The results show a good correlation between the computed spectra energy and OH^- produced, as more yield is obtained at higher ultrasound intensity.

$$E = \int_0^{f_b} V(f)^2 df \qquad (2.2)$$

Where V(*f*) is the frequency dependent sensor voltage, and f_b is the upper bound of the sensor limit. The authors claimed that the spectrum under 515 kHz is dominated by non-inertial cavitation and that under 20 kHz is dominated by inertial cavitation. They expect the latter to generate a relatively higher sonochemical activity than the former, but this was not the case, as can be seen in fig 2.8. Even though the intensity used under 20 kHz was much higher than that for 515 kHz. It again substantiates that cavitation is not adequately represented through the popular binary classification of stable versus inertial.

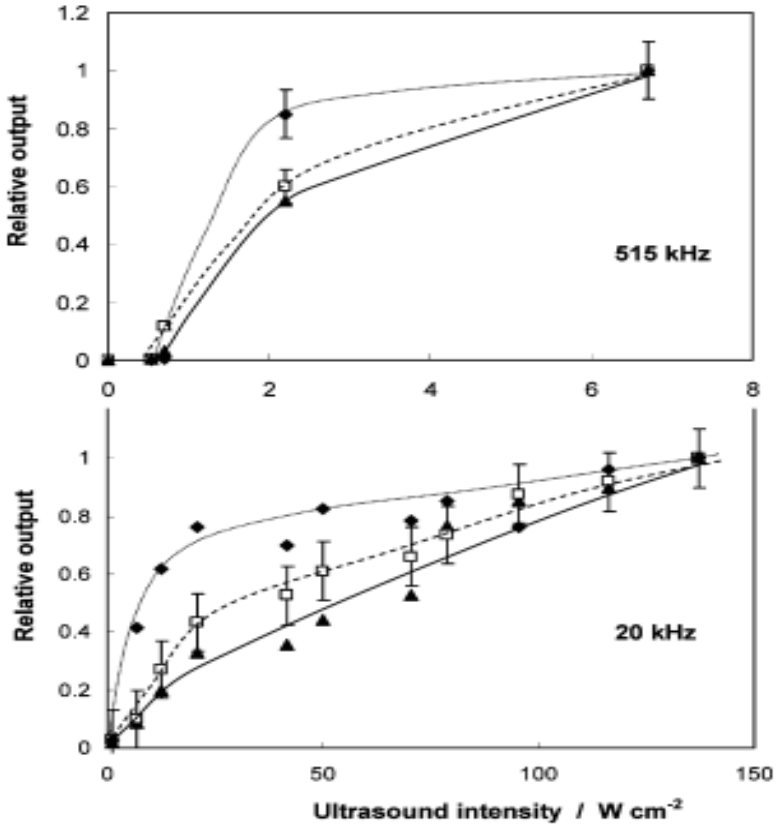

Figure 2.8: Comparison of acoustic emission (marked with diamond shape), sonoluminescence output (marked with square shape), and hydroxyl radicals production (marked with triangle shape). Values are relative to the output at the highest measured ultrasound intensity [31]

Beckett *et al*, [93] investigate the effect of frequency and sparged gas (Ar and O_2) on the sonoluminescence (SL) and sonochemical yield of H_2O_2 and 1,4-Dioxane decomposition. Four different ultrasound frequencies were considered (205, 358, 618, and 1071 kHz). The ultrasonic transducer used had an active vibrational area of 25 cm^3. Its output power is 128 W. It is important to note that the expected acoustic intensities (if calculated from power/area) will be different for the four frequencies studied due to the different modes of vibration for the piezoelectric crystal at these frequencies. All SL emission data was collected using a monochromator which is spectrally calibrated with the help of a NIST-traceable standard mercury Ar lamp, and the spectral response was calibrated in the range of 200-600 nm using a QTH source (Oriel Instruments). The 500 mL of pure water contained in a 700 mL capacity reactor was sparged with gas for 30 minutes before the start of sonication, continually sparged at a constant rate of 100 mL/min. The sample was maintained at a temperature of 25°C. The SL spectra of luminescence obtained from all the frequencies under investigation showed a similar pattern except for a different degree of broadness and intensities, as seen in fig. 2.9. The optimum frequency for the sonochemical yield was at 358 kHz with the SL spectra, where both the broadness and intensity were maximum. The sonochemical yield was minimum at the frequency of 1071 kHz.

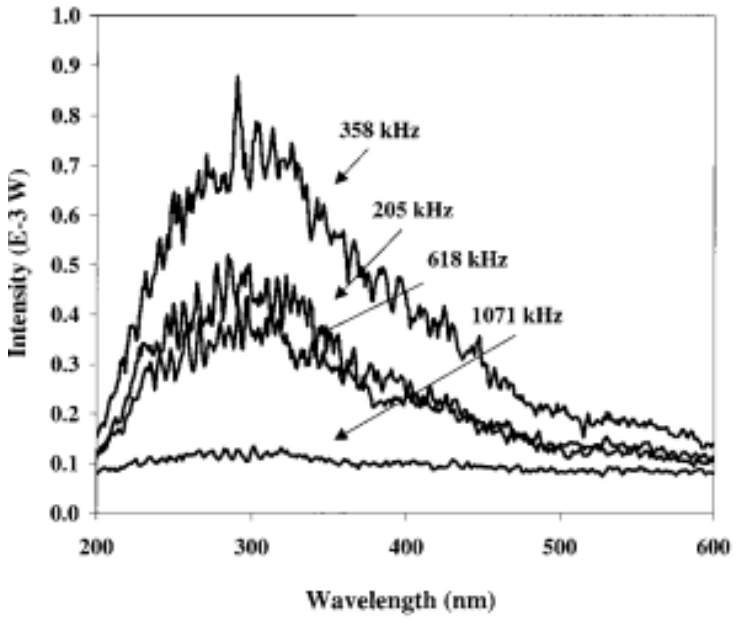

Figure 2.9: SL spectra at four discrete ultrasonic frequencies. Sparge gas 100% Ar [93].

After that, a detailed investigation was carried out with ultrasound at 358 kHz with a different sparged ratio of Ar and O_2 gas. They found that the spectral intensity increases with the increase in the percentage of sparged Ar, as shown in fig. 2.10. More so, no SL spectrum was observed when the only sparged gas was O_2, implying that oxygen is the quencher of luminescence.

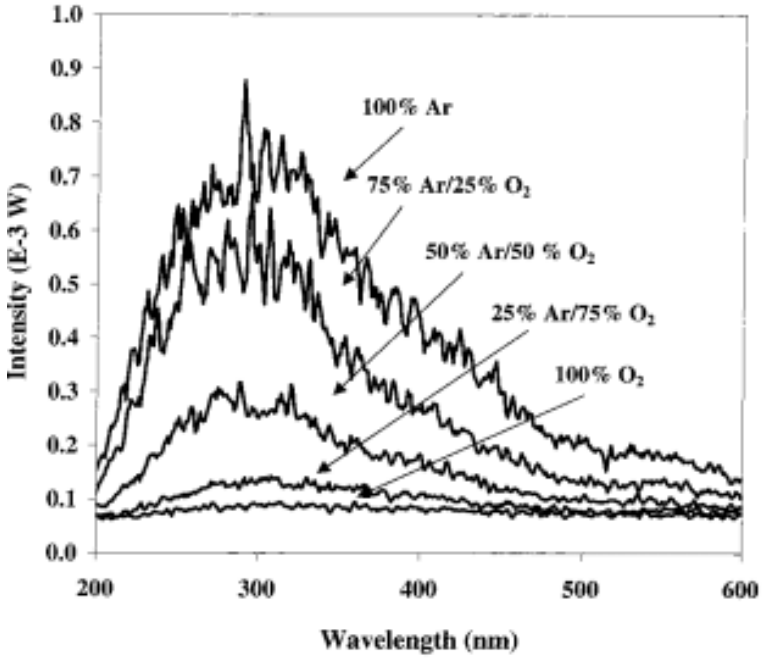

Figure 2.10: SL spectra at an ultrasonic frequency of 358 kHz [93]

Hadi *et al* [96] studied the cavitation activity using both sonoluminescence and acoustic emission in a sonochemical setup operated at a frequency of 1 MHz. The ultrasound source had an effective active area of 5 cm^2 and acoustic intensity of 2.03 W/cm^2 estimated using radiation force balance. A 25 mm PVDF-type HP with a calibration range of 20 kHz-1 MHz was placed at a vertical distance of 5 mm from the transducer was used to collect the acoustic emission. A fresh solution of terephthalic acid was prepared, and the solution was exposed to ultrasound for 20 minutes. The fluorescence intensity of the sample was determined using a spectrofluorometer (Shimadzu, ModelRF-1500, Japan). The solution of a 2-hydroxyterephthalic acid (HTA) was used as dosimetry to estimate the OH^- concentration. A linear relationship (a straight-line graph with a positive slope) was observed between the fluorescence intensity and the concentration of HTA, as shown in fig. 2. 11. It translates to the concentration of OH^- produced as a function

of a fluorescence count. This indirect method was used to quantify the inertial cavitation.

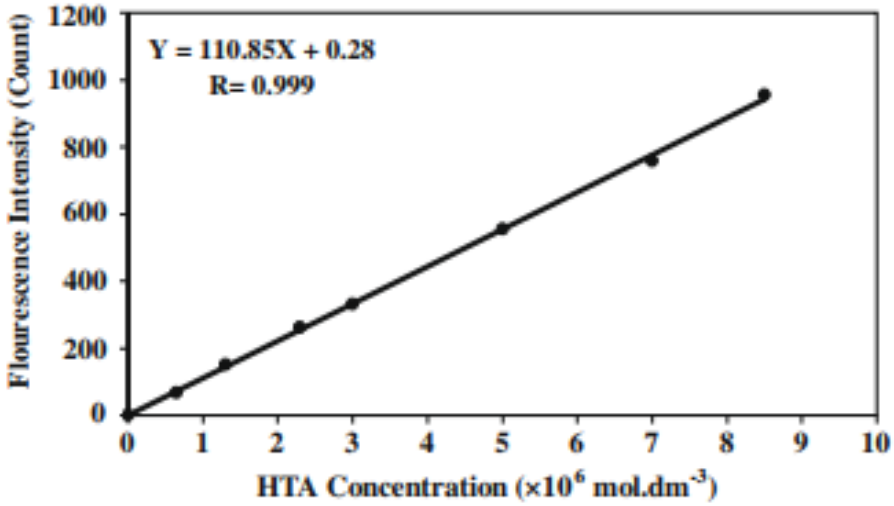

Figure 2. 11: Calibration curve for the dosimetry solution [96]

The effects of the ultrasound intensity on the sonochemical yield of OH^- was investigated using subharmonic spectral feature and fluorescence intensity. The OH^- concentration was found to increase linearly with increasing ultrasound intensity. Also, both the fluorescence and subharmonics intensities were observed to increase with an increase in the intensity of the ultrasound. Overall, a good correlation (see fig. 2.12) was found between the subharmonic and fluorescence intensities indicating that subharmonics can be used to monitor/evaluate the chemically active cavitation activity.

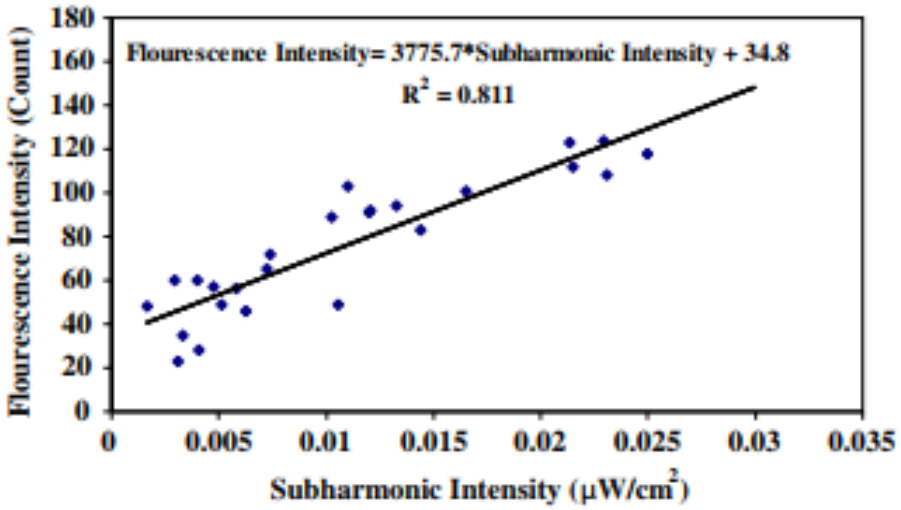

Figure 2.12: Pearson correlation and linear regression analyses between subharmonic intensity (W/cm^2) and fluorescence intensity (count) in different irradiation conditions [96].

Table 2.1 summarises the relevant papers reviewed above, detailing the acoustic parameters used in each case.

Table 2.1. Summary of the selected review papers detailing the acoustic parameter used.

Author(s)	Transducer types	Acoustic power /Intensity	Frequency	Products investigated
Yao, *et al* (2010) [62]	Planar	0.1-0.69 W/cm^2	1 MHz	Hydroxyl radical
Dheyab, *et al* (2019) [55]	Planar	—	20 kHz	Gold deposit
Mason *et al* (1992) [66]	Planar	96, 26, 11W	20, 40, & 60 kHz	Size reduction of copper-bronze
Koda *et al* (2003) [67]	Planar	6.5 W	19.5 – 1.2 MHz	Hydroxyl radical
Choi *et al* (2019) [68]	Planar	190 – 260 W	36 kHz	Hydroxyl radical
Wayment *et al* (2002) [81]	Planar	2 – 3 W	20 kHz & 300 kHz	Alachlor
Merouani *et al* (2015) [83]	Planar	2 W/cm^2	300, 585, 860, & 1140 kHz	Hydroxyl radical
Merouani *et al* (2010) [91]	Planar	13.7 – 25.6 W	300 kHz	Hydroxyl and hydrogen peroxide radical
Frohly *et al* (2000) [32]	Planar	12 – 300 mW/cm^2	1.075 MHz	Hydroxyl radical
Price *et al* (2005) [31]	Planar	0 – 120 W/cm^2	20 kHz & 515 kHz	Hydroxyl radical
Beckett *et al* (2001) [93]	Planar	128 W	205, 358, 618, & 1071 kHz	Hydrogen peroxide
Hadi *et al* (2010) [96]	Planar	2.03 W/cm^2	1 MHz	Hydroxyl radical

2.3.3 Estimation of acoustic power

The acoustic power delivered by the transducer into the host medium is mostly estimated using the *calorimetry* method, especially for low-frequency

transducers. This method relies on the heat dissipated in the host medium from the acoustic power delivered by the transducers. The power dissipated in the host medium is given as equation (2.3) [97].

$$P_{diss} = \left(\frac{dT}{dt}\right)_{t=0} mC_p \qquad (2.3)$$

Where *m* and *Cp* are the respective mass and heat capacity of the host medium, and $(dT/dt)_{t=0}$ is the initial slope of temperature rise of the host medium against the exposure time of the ultrasound. Using the expression in equation (2.3) to estimate the dissipated power in the host medium is inefficient as it is predicted that only 33% of the source power from the transducer is dissipated as heat [8]. The method is improved if the heat dissipated by the sonoreactor is considered. Other methods have also been used to estimate the power delivered to the host medium. The method like chemical dosimeters where known heat for a particular reaction was used to estimate the power used for generating the radicals. The power may still be estimated through measured acoustic pressure and the surface area of the source, as discussed in §7.3.5 Estimation of acoustic energy.

2.4. Conclusion

This chapter has considered the historical background on sonochemistry and how the understanding of cavitation has been developed over the years. The hotspot concept during cavitation may be considered the generally accepted mechanism through which radicals are formed during sonochemistry. Other possible mechanisms such as electrical discharge and ordering effects have also been suggested and developed. Qualitative measurement of parameters that are of particular interest, using suitable measurement tools is paramount for achieving scale-up methodology. More so, understanding the role of cavitation in enhancing the sonochemical process, and finding means of improving it, would go some way to addressing the scale-up issue for industrial application.

Chapter 3

Principal experimental instrumentation

This Chapter provides brief technical descriptions of the essential devices used throughout the results Chapters 4-7 and algorithms used to analyse the experimental data reported in this thesis. CavLab has dedicated state-of-the-art devices for research related to cavitation.

The Chapter is structured as follows: In §**3.1**, the Sonoptic chamber is described. §**3.2** presents the descriptions of the high-speed camera (HSC) used in the research. §**3.3** presents the description of the bespoke shock wave passive cavitation detector (swPCD) used to collect the acoustic emission from the cavitating bubbles. Finally, a filter description is presented in §**3.4**, and §**3.5** concludes the Chapter

3.1. The Sonoptic tank

The Sonoptic chamber is an open-architecture customised chamber designed for effective cavitation studies, as shown in (labelled as **i** in fig. 3.1 (a)). The tank measuring 420 × 438 × 220 mm^3 has two tunnels on opposing walls (labelled as **ii** in fig. 3.1 (a)) into which imaging optics can be placed in proximity to the intended location of the bubble activity to achieve high spatial resolution imaging. It was built such that the focused ultrasound transducers (described in fig. 1.3 (b) of chapter 1), such as that used in Chapter 7, formed at the centre, for which the imaging can be accessed through the tunnel. Moreover, the field generated can propagate through this region unperturbed by the tank geometry, such that cavitation response to well-characterised pressure fluctuations can be observed. The Sonoptic chamber is also equipped with two x, y, z manipulators (labelled as **iii** in fig. 3.1 (a)) for precision mounting of components within the tank. Although it was initially built to study laser nucleated bubbles in close proximity [6], it was used for several investigations involving cavitation studies reported in this thesis. Fig. 3.1

(b) shows the Sonoptic tank used to study the cavitation generated from the tip of the ultrasonic horn, **Chapter 4**. Fig. 3.1 (c) is the photograph of the Sonoptic tank in use for the sonochemistry experiment of **Chapter 7**. It is understood that there will be reflections within the tank for the longer duration used in Chapter 7, but the divergence of the field at the far-field is expected to minimise it.

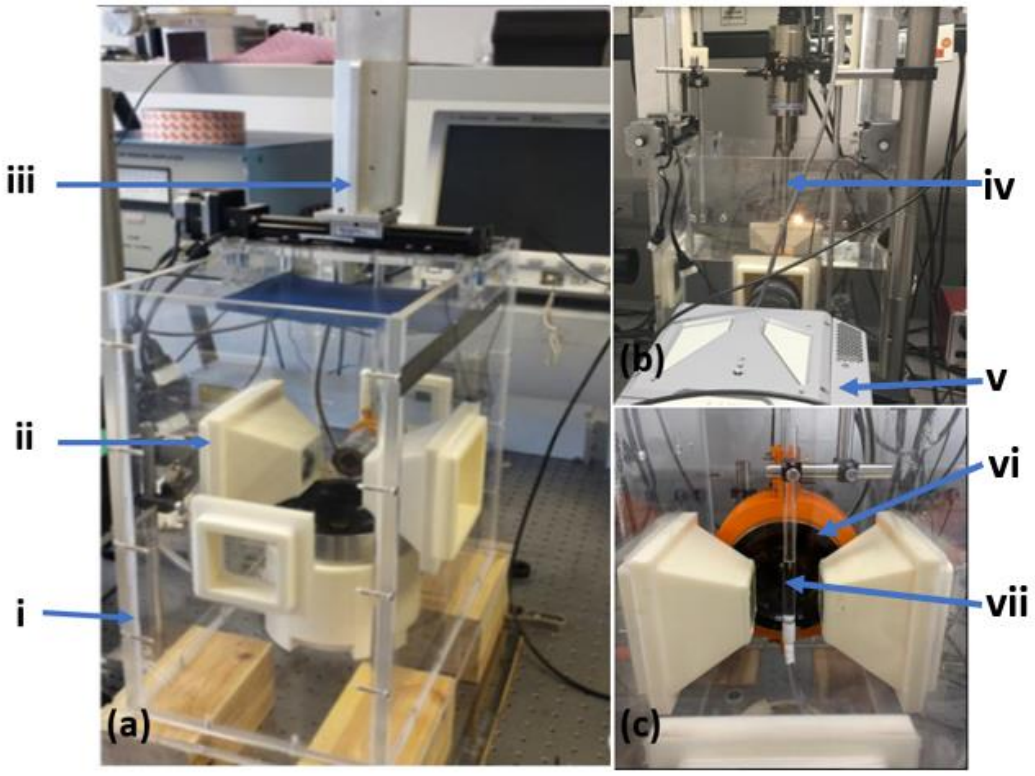

Figure 3.1: Image (a) of Sonoptic tank: (i) Plastic tank (ii) Two opposite tunnelling (iii) x, y and z manipulator (b) Sonoptic chamber adapted for studying cavitation at the tip of the ultrasonic horn: (iv) The sonotrode (v) The Photron camera (c) Sonoptic tank adapted for sonochemistry experiment: (vi) focussed transducer (vii) Sonoreactor.

3.2 High-speed cameras

The choice of a high-speed camera is primarily determined by the frame rate and the recording length required to observe a particular cavitation-related phenomenon. The results presented in this thesis are obtained with at least one of the high-speed cameras or a combination of the Shimadzu HPV-X2 (Shimadzu,

Kyoto Japan) and the FASTCAM SA-Z 2100 K (Photron, Bucks UK, 128 GB of RAM).

3.2.1 Shimadzu High-speed camera

The Shimadzu camera (Hyper Vision) is capable of acquiring high-speed imaging of up to a maximum framerate of 10×10^6 frames per second (fps) for 256 frames per sequence, each with 400 × 250 pixels. Illumination is provided by synchronous 10 ns collimated laser pulses (632 nm, red) (CAVILUX Smart, Cavitar, Finland), which both facilitates shadowgraphic imaging and provides effective temporal resolution.

These short illumination pulses allow direct visualisation of pressure transients (including shock waves) via slight refractive index fluctuation imposed to the host medium as the wave propagates, commonly known as shadowgraphic imaging [98]. This has been critical to realising and investigating the previously under-appreciated role of periodic shock waves within the signals emitted by acoustic cavitation, as described in fig 4.7 of **Chapter 4**. The Shimadzu camera-Cavitar illumination system is ideally suited to highly detailed cavitation imaging over shorter durations.

Figure 3.2: Image of the Shimadzu camera [99]

3.2.2 FASTCAM Photron High-speed camera

The FASTCAM Photron high-speed camera has 128 GB of RAM, making it suitable for longer recording durations (depending on the frame rate and pixel resolution setting). It is capable of imaging up to a maximum frame rate of 2.1 x 10^6 fps and has a maximum resolution of 1024 × 1024 pixels. In this thesis, the Photron camera was used to record the whole sonication process with a 159 ns shutter time, and other available shutter times range from 1 ms to 1 μs. The shutter time measures how long the camera shutter is open while exposing light onto the camera sensor. A shorter shutter time exposures require higher intensity illumination for adequate imaging but deliver imaging at higher temporal resolution. The Photron camera is shown in fig. 3.3. A continuous 150 W halogen bulb source (Thorlabs, Ely UK) coupled to a liquid light guide provided the required illumination at the shutter time of 150 ns.

Figure 3.3: Image of the Photron camera [100].

The lenses used together with the HSCs will be described in the relevant Materials & Methods sections for each results chapter.

3.2.3 Dark pixel counting algorithm

Dark pixel counting is a basic technique of image processing applied to estimate the occupied area of the cavitation bubble in the frames collected by the high-speed camera. This technique is based on subtracting areas whose light intensity value is greater than a set threshold (area without bubbles) from the selected area of investigation [49]. The dark pixel counting algorithm was formed as follows:

- Read all the images in the file.
- Select a section of interest within the image to be analysed.
- Defining the threshold based on the light intensity value, and this threshold should differentiate pixel with bubble from pixel without bubble. Each part of the image is continuously compared with the reference (selected threshold), and a decision is made on whether to include or exclude the tested part.
- The dark pixel area is estimated by counting all the dark pixels.
- The dynamic oscillation of the size of the bubble can then be plotted against time determined from the frame rate.

- The dark pixel counting algorithm was created in Matlab®, 2016b (The MathWorks, Inc., Natick, MA, USA). The dark pixel counting algorithm script can be found in A.2 Dark-pixel Algorithm codes.

3.3 Shock wave passive cavitation detector

Since most industrial cavitation-mediated applications require intense cavitation to generate high-intensity shock waves, available commercial HPs are unsuitable for collecting such acoustic emissions. Therefore, the acoustic data collected in this thesis was undertaken by a bespoke shock wave passive cavitation detector (swPCD) previously built in-house by CavLab.

The swPCD was initially designed for detecting periodic shock waves (PSW) in acoustic emission. In the design of the swPCD, polyvinylidene difluoride (PVdF) was used as the active material, and its thickness was selected based on the power spectrum of the bubble collapse shock wave (BCSW) generated from laser nucleation as described in [36]. The final realised swPCD has a high acoustic impedance Tungsten-Epoxy (> 10 MRayl) backing layer to adjust the resonance of 110 um PVdF film (~ 4.56 MRayl) towards sensitivity for the target bandwidth (i.e., MHz and sub-MHz). This bandwidth covers many commonly reported cavitation emission frequencies and higher values of f_0 driving.

Fig. 3.4 (a) is a photograph of the final stage swPCD. Fig 3.4 (b) depicts a schematic cross-section of the device showing the PVdF-film, backing, and matching layers.

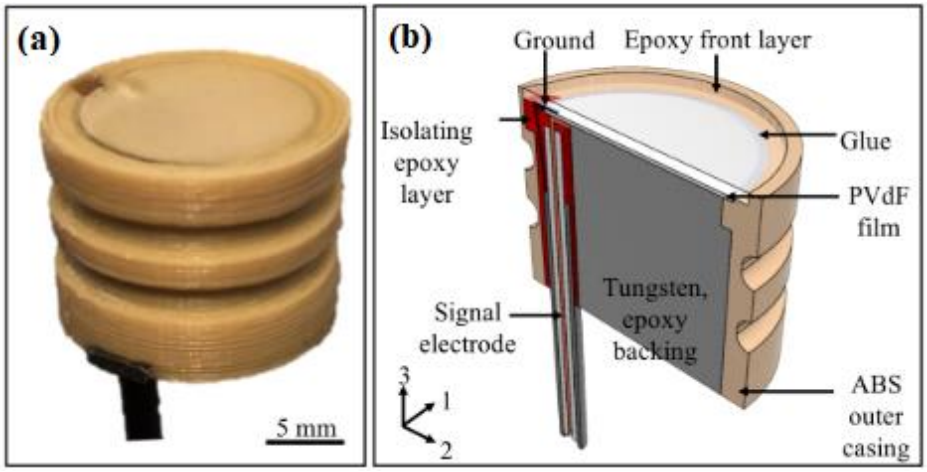

Figure 3.4: (a) Photograph of final stage swPCD, (b) schematic cross-section of the swPCD [36].

For performance evaluation, the developed swPCD was used to collect an acoustic cavitation cloud generated from laser nucleated single cavitation cloud but driving with a burst of high-intensity focus ultrasound at 220 kHz, comparable to the frequency used in Chapter 7 for the sonochemistry experiment. The HSI, the acoustic emission collected with both swPCD and commercial PCD (Y-107) during the investigation, is shown in fig. 3.5. The Y-107 has an active diameter of 17.5 mm and is geometrically focused to 68 mm. It has a stated bandwidth of 10 kHz–15 MHz, and its construction, as supplied by the manufacturer on request, is described as a "0.2 mm thick piezo-polymer stack, with high acoustic impedance backing material >4 MRayl and an EMI (electromagnetic interference) shielded plastic outer casing (20 mm OD × 40 mm length) to optimize the operating bandwidth and signal-to-noise ratios"[101].

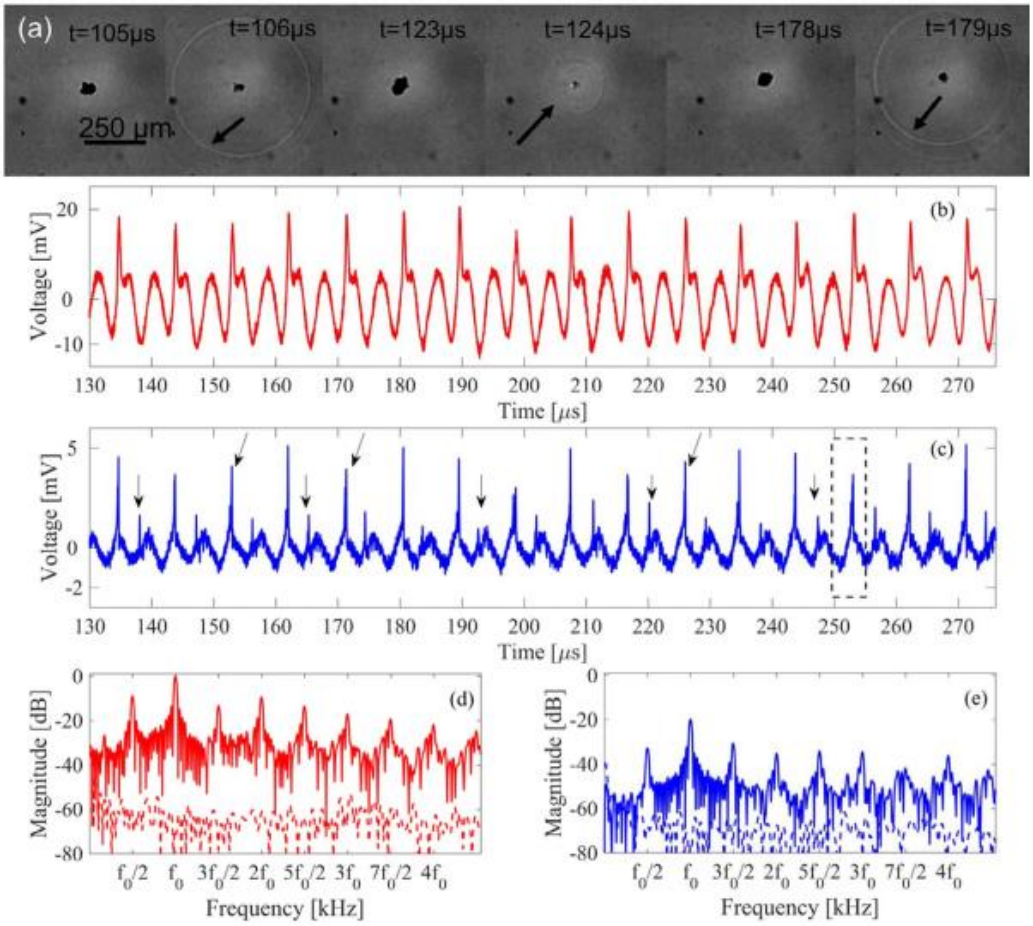

Figure 3.5: (a) Showcases a section of the high-speed shadowgraphic imaging of the cavitation cloud taken with the Shimadzu camera. The acoustic data in time and frequency for the swPCD (b, d) and Y-107 (c, e) detected from the bubble collapse of (a) shown, respectively. The black slanted arrows indicate the periodic shock waves, and the vertical black arrows indicate the reflected SWs from the lens-casing [36].

The high-speed imaging confirmed that the bubble cloud underwent strong collapses and PSW emissions at $f_0/2$, as arrowed in fig 3.5 (a). The $f_0/2$ regime was also observed in the acoustic data collected by the swPCD, fig 3.5 (b), and the acoustic emission collected simultaneously by a commercial PCD (Y-107, Sonic Concepts Inc) indicated with arrows in fig. 3.5 (c). The corresponding acoustic spectrum from the swPCD is well above the noise level within the target frequency band. Also, the sensitivity of the swPCD was high, which is an added advantage for the detection of weak shock waves.

The final developed swPCD performed better at the frequencies of interest than a commercially available PCD, characterised by a ~30 dB higher signal to noise ratio (SNR) at $f_0/2$ and greater sensitivity up to ~ 3MHz, as seen in fig. 3.6 [36]. The swPCD sacrifices temporal resolution for magnitude sensitivity, although a geometrically focused swPCD may be expected to improve the temporal resolution (the time resolution for the device was not specified; however, it is in the range of one-tenth of a microsecond). Moreover, its large active area will endow the swPCD with poor directivity, which was necessary for the comparison to Y-107. Therefore, the swPCD is a suitable detector for the driving frequencies (20 kHz and 200 kHz) used in this thesis.

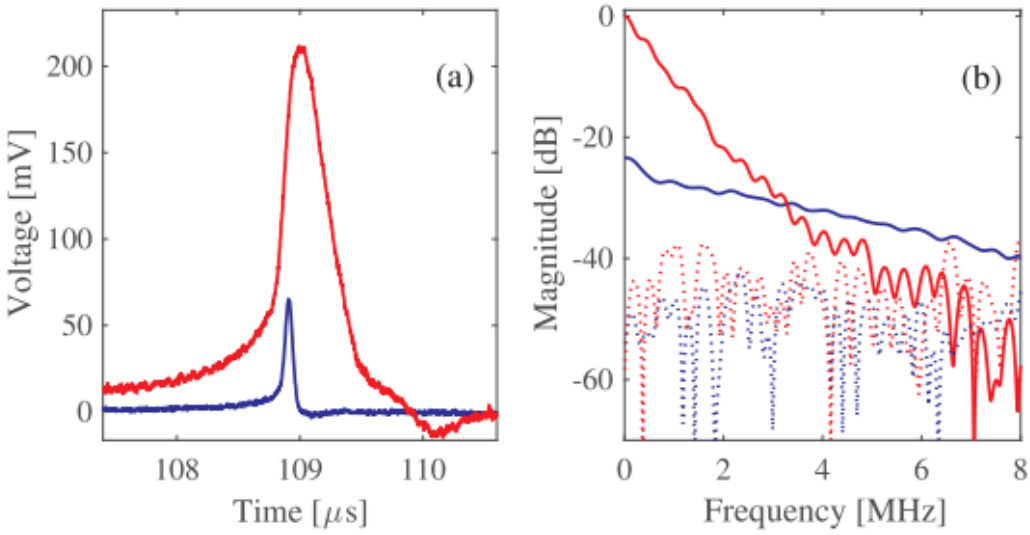

Figure 3.6: (a) Voltage-trace comparing final stage swPCD (solid red) and Y-107 (solid blue) for detection of a BCSW. (b) Spectra of shock waves in (a), where stapled data (Shown with dotted red and blue spectra below the -40 dB) represents the noise floor [36].

3.3.1 Filters used for acoustically detected data

Filtering is a common process used in both analogue and digital signal processing. Filtering is the deliberate passing or rejection of part of a signal associated with a specific frequency or frequency band. Digital filters are the most commonly used in signal processing because of several advantages that include higher reliability, accuracy, and less sensitivity to noise and ageing [102]. The

common filter types are low-pass filter, high-pass filter, band-pass filter, and band-reject filter.

A high-pass filter attenuates signal below the specified f_c and allows frequencies above the f_c to pass through unaffected, as shown in fig. 3.7 (a). A low-pass filter allows low-frequency signals below the specified cut-off frequency (f_c) to pass through unaffected, but blocks/attenuates signals above the f_c, as shown in fig. 3.7 (b). The band-pass filter allows signals within the frequency band specified by f_{c1} and f_{c2} to pass unaffected but attenuates every other signal outside the band, as shown in fig. 3.7 (c). The band-reject filter, also known as a notch filter, allows signal passage outside specified frequency bands f_{c1} and f_{c2} but attenuates the signal within the frequency band, as shown in fig. 3.7 (d).

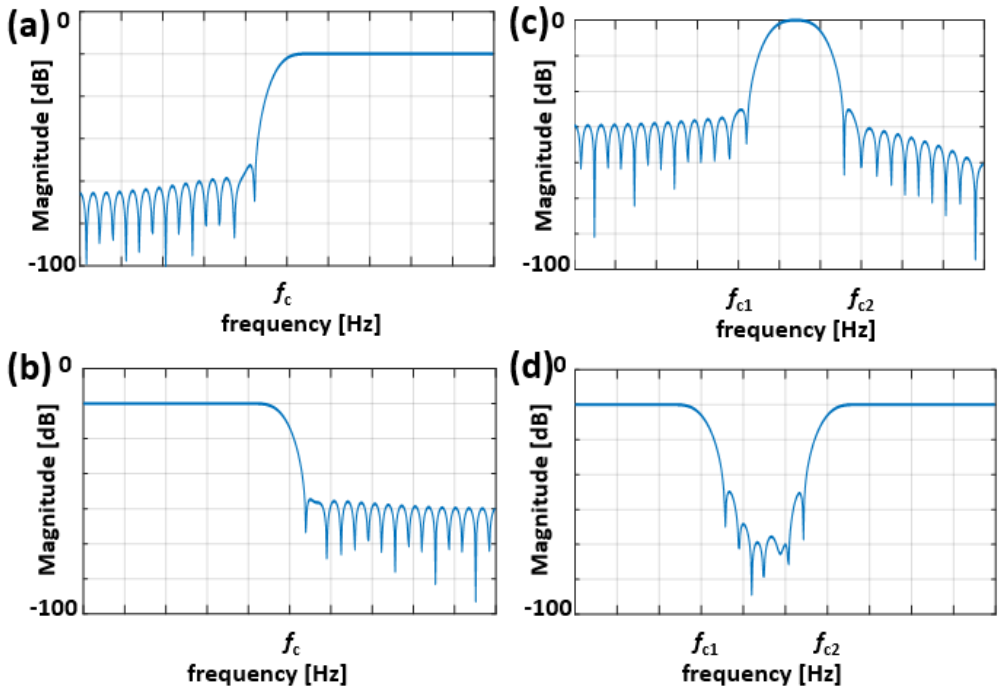

Figure 3.7: Showing magnitude response for (a) high-pass filter (b) low-pass filter (c) band-pass filter, and (d) band-reject filter.

Two concepts of digital filter design are commonly used, namely, the finite impulse response (FIR) and the infinite impulse response (IIR) filters. The FIR is used in the thesis because it is more stable as it requires no feedback. The FIR filter is an inbuilt function in Matlab®, 2016b MathWorks written as 'firl'. The FIR used in this thesis was designed with a Hamming window method. The basic elements

in the filter are the filter order (N), the f_c frequency, which must be greater than zero, and less than half the sampling frequency (f_s) ($0 < f_c < f_s /2$) [103]. The following two-step algorithm is used in realising the choice of filter desired.

- Create the filter coefficient using h = firl (N, f_c, 'filter type'). Depending on the requirement, filter types can be a low, high, band or stop filters. The filter h returned has an N+1 real vector and has a linear phase response.
- The filter is then convolved with the raw data to obtain the desired output.

The filter algorithm script can be found in the A.1 Matlab filtering and frequency codes.

3.5 Conclusion

This Chapter has described the key devices/equipment and the algorithms used in each of the experiments reported in this thesis.

Chapter 4

Characterisation of the cavitation generated by an ultrasonic horn

Efficiency and reproducibility are the key important factors required for any device to be deployed for use in manufacturing. Acoustic devices are no exception, and their efficiency should be of interest when they are deployed for bubble mediated applications. The ultrasonic transducer comes in different forms and shapes and has been classified using different taxonomy such as low/high frequency and low/high power acoustic devices. The most common acoustic devices are the ultrasonic bath and acoustic horn; the former is low intensity while the latter is high intensity [51]. Both are low-frequency devices. For efficient utilisation of these acoustic devices, it is important to characterise the cavitation that is produced from these devices as a function of input power for identifying process mechanisms and optimising applications [104]. More so, an understanding of the cavitation generated from the device may guide the selection of an application to which they are deployed. Surprisingly, the detailed characterisation of the cavitation generated by the ultrasonic horn as a function of tip-vibration amplitudes has not been previously carried out before now. Therefore, the characterisation of an ultrasonic horn is presented in this Chapter. The acoustic characterisation is motivated by the knowledge gained from the CavLab research group published literature, which are described in §1.3. Previous research from CavLab of this thesis, specifically regarding the dependence of subharmonic bubble response on input power, as well as the contribution of the periodic shock wave to nonlinear emission signals.

4.1. Introduction

The ultrasonic horn, also known as the sonotrode, is one of the most popular commercials and laboratory-based acoustic devices. Yet, its process mechanism is not fully understood due to the lack of adequate performance characterisation through the various parameter spaces offered (frequency, tip-vibration amplitude,

tip-diameter (Ø), and geometry). During operation, mechanical vibrations from a piezoelectric element within the main housing of the device, generally at a fundamental driving frequency (f_0) between 20-30 kHz, are transmitted and amplified through a tapered or stepped metallic rod, such that the (usually planar) tip vibrates with a displacement amplitude in the range of several 10's to several 100's of microns, depending on the input power setting. The ultrasonic horn used for the work[7] described in this Chapter (Branson Digital Sonifier 450, Branson Ultrasonic Corporation, 41 Eagle Road, Danbury, Connecticut, USA) comes with various attachment options ('horns' and 'output tips', fig 4.1a) according to the treatment volume and vibration amplitude/sonication intensity required for a particular application. Generally, smaller tips will oscillate with higher vibration amplitudes than larger tips at the same input power, as shown in the table obtained from the manufacturer user's manual in fig 4.1 (b).

The intensity/power of the horn or any other acoustic device is mostly reported using the rating power quoted by the manufacturers from which the corresponding intensity is computed by division with the radiating surface area of the acoustic device since acoustic devices are not lossless devices, which implies that not all the electrical input power is completely transformed to acoustic power. Others estimate the actual acoustic power transmitted to the system from the acoustic device using the calorimetry approach where the principle of heat transfer is employed [66], or calibrated hydrophone for directly measuring the acoustic pressure from which the acoustic intensity is computed. The latter approach should be carried out at a very low power input to prevent damage to the delicate hydrophone [105].

[7] The author is very grateful to Dr Mark Symes, of the School of Chemistry, University of Glasgow, for provision of the ultrasonic horn used to generate the data described in this Chapter

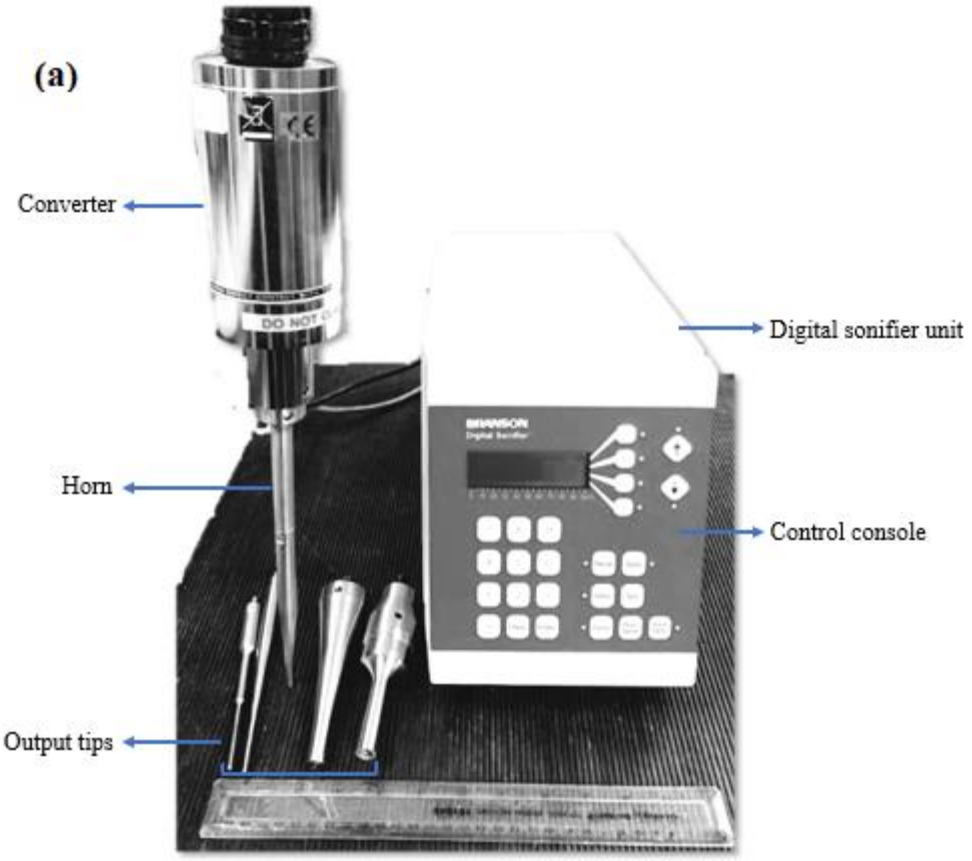

(b)

Horn EDP No.	Description	Amplitude Control Settings		
		10%	40%	70%
101-148-062	1/8" Diameter Tapered	116.0* 0.0046"	306.0* 0.0122"	494.0* 0.0194"
101-148-069	3/16" Diameter Tapered	59.5* 0.0023	183.0* 0.0072"	302.0* 0.0119"
101-148-070	1/4" Diameter Tapered	59.5* 0.0023"	151.0* 0.0059	247.0* 0.0097"
101-063-212	Double Step	64.0* 0.0025"	173.8* 0.0068"	274.0* 0.0108"

* All measurements in microns unless otherwise specified

Figure 4.1: (a) The Branson 450 Digital Sonifier system, comprising the control console for setting the input protocol, the converter housing and various attachment options; (b) Approximate Microtip Amplitudes as obtained from user's manual [106].

Horn-type devices over a range of powers and tip diameters have been reported as being utilised for processes such as cell disruption or lysis [107][108], preparation and dispersion of emulsions [109], nanoparticles [110], and the precipitation of 'sonocrystallisation' [111], for applications ranging from

pharmaceutical and food sciences to biodiesel production [112] and water treatment [50], [113]. Applications based in the medical sector, at various stages of development, include enhanced tissue dissection for surgery [114], transdermal drug delivery [115] and the generation of (ultrasound contrast agent) microbubble suspensions [116].

In applications during which the tip is immersed in liquid, it is generally accepted that cavitation in the region of the tip makes a significant contribution to the desired effect of the sonication [117]. Intuitively, frequency of operation, tip-size, and input power, which determines the amplitude of tip-vibration for any given attachment configuration, may be expected to significantly influence the characteristics and behaviour of the cavitation generated. Other factors known to affect bubble activity include the properties of the liquid host medium, such as dissolved gas content and viscosity [118]. Accordingly, there is significant interest in characterising the cavitation activity generated by horns, both for identifying process mechanisms and optimising applications [104]. As reviewed below, optical imaging and acoustic detection of the emission signal generated by the cavitation activity have underpinned much of this research effort.

Moussatov *et al.*[119] identified a cone-like bubble structure (CBS) at the tip of a 20.7 kHz horn for three different tip diameters (20, 80 and 120 mm-Ø). An example of the CBS formed under the tip of an ultrasonic horn is shown in fig. 4.2 from [120]. They attributed the formation of CBS to the reversal of the primary Bjerknes force[8] at the high-pressure zone just a few centimetres below the tip of the horn. This reversal of primary Bjerknes force creates a repulsive tension at this zone so that bubbles are repelled from this zone but pass around it through other paths where the pressure is comparatively low, and the vector sum of the primary Bjerknes forces is zero. The coverage of this repulsive zone decreases as the bubble moves further away from the tip of the horn (i.e. further below the horn's tip), resulting in the formation of CBS. Furthermore, bubbles were observed to move from the top of the cone to the tank's base via a narrow path formed. The smaller bubble clusters are combined within the channels to form larger ones due to

[8] Primary Bjerknes force is the average effective force that is experienced as a result of temporal and partial variation of acoustic pressure, medium density, and particle velocity from their equilibrium values [17].

secondary Bjerknes force[9]. This process is primarily responsible for the smooth physical structure (fine microstructure) observed in the CBS [119]. The observed CBSs were found to depend on the intensities of the source sound (the intensity of the source is obtained through the division of electrical power with the radiating surface area of the horn's tip). At low intensities of 1-2 W/cm^2, no CBS was formed except oscillating clusters of bubbles that move away from the radiating surface as soon as they are formed. When the intensity was raised to the range of 3-6 W/cm^2, the bubble gained more speed, the number of the clusters increased and become larger due to coalescence of several smaller clusters. At these levels of intensities, the CBS is formed, and bubbles move from the top of the cone to the bottom of the tank through a path. A full-blown and stable CBS was observed at a much higher intensity of 8 W/cm^2 in all the used tips. Strong sonochemical activity was also confirmed within the cone, via chemiluminescence observation in luminol, in agreeance with the study in [121], investigating chemiluminescence around tips of different shapes.

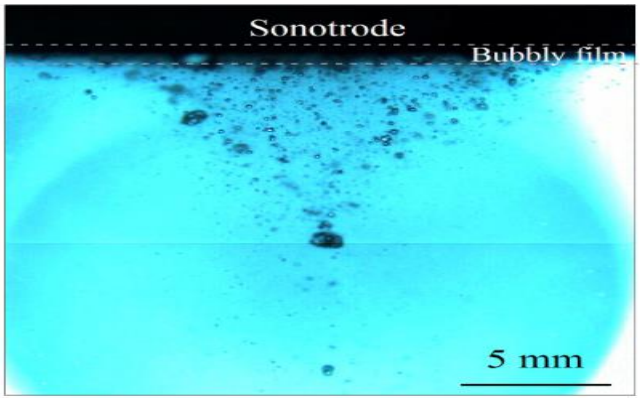

Figure 4.2: Cone like bubble structure (CBS) obtained from horn tip 20 mm-Ø at a high vibration amplitude in freshwater, captured with a high-speed camera at a frame rate of 5000 frames per second (fps) taken from [120].

Other studies have sought to further characterise the dynamic cavitation activity at the vibrating tip based on high frame rate imaging, often in conjunction with hydrophone measurements of the acoustic emissions. Birkin *et al.* [26] studied

[9] Secondary Bjerknes force is similar to the primary Bjerknes force, but it generated from the scattered sound field from a neighbouring bubble instead of the incident sound field which effect is attractions when the bubble cluster is of comparable sizes, and repulsion if otherwise [17].

the primary cavitation cluster beneath a 3 mm-Ø titanium tip at f_0 = 23 kHz and a single intensity of ~50 Wcm^{-2} (measured via the calorific technique but determined by the tip-vibration amplitude) using multiple sensing approaches, including; a small hydrophone with cylindrical active element used for detecting the acoustic emission; a photomultiplier tube (PMT) for temporal characterisation of multi bubble sonoluminescence (MBSL); a laser diode and photodiode for measuring the level of laser scattering by the bubbles via the electrical voltage output from the photodiode; and a passivated electrode coupled at the base of the electrochemical cell, below the tip of the horn at an adjustable distance, which was used for monitoring surface erosion effect. The horn-tip was submerged 15 mm below the surface of 0.75 $moldm^{-3}$ Na_2SO_4 solutions (to achieve a certain level of conductivity), contained in a 3.5 dm^3 vessel, and both PMT and the hydrophone were placed at a vertical distance of 15 mm from the tip of the horn. Finally, the bubble activity was captured using a high-speed camera (Phantom V7), imaging at 100,000 fps. A principal finding was that the bubble cluster underwent periodic collapses at subharmonic frequencies ($f_0/3$ and $f_0/4$), which corresponded to detecting pressure spikes in the acoustic measurements and correlated well with the bubble images obtained with a high-speed camera. It was further shown that surface erosion effects (detected via a passivated electrode located at the tip) and sonoluminescence also correlated temporally to the cluster collapses, pointing to the importance of the bubble-cloud collapses in cavitation-mediated processes.

Žnidarčič *et al.* [122] made observations of the cavitation bubble activity around a 3.2 mm-Ø tip, operating at 20 kHz with tip-vibration amplitudes of 100, 132 and 164 μm. The horn tip was submerged 10 mm below the surface of the water within a rectangular glass (5 x 5 x 5 cm^3) container. The bubble activity was filmed with a high-speed camera (Photron FASTCAM SA5 model 1000K-M1) at 100,000 fps. The acoustic pressure was measured for variations of several parameters, including liquid temperature, viscosity, level of air saturation, and surface tension, with a 3 mm-Ø calibrated hydrophone (Reson TC4038) placed at a horizontal distance of 7 mm away from the horn. The authors distinguished the large vaporous bubble activity they observed, attached to, and covering the tip as 'acoustic supercavitation'. Nonetheless, pressure spikes at $f_0/3$ and $f_0/4$, reminiscent of those described by Birkin *et al*, were reported for the lowest and highest tip amplitudes, respectively, corresponding to subharmonic oscillations of the bubble activity. At an intermediate value for tip vibration, it was noted that the cavity oscillation period

shifted irregularly between 3 and 4 cycles of the tip-vibration, or that cavity oscillation frequency was not clear. It was also shown that the variation of liquid parameters had no significant effect on the cavitation generated. These studies provided insight into the cavitation dynamics at the horn's tip, however the full characterisation was limited by short sampling durations of 3 ms (compared to a typical exposure of several seconds or more), and a limited number of input powers, or tip-vibration amplitudes, investigated.

More recently, Tan & Yeo [123] investigated a 20 kHz horn with a 12.62 mm-Ø tip, submerged 15 mm into deionised water within a customised tank (200 x 150 x 150 mm^3). The bubble activity was captured with high-speed camera (FASTCAM SA4, Photron) imaging at 100,000 fps, for a duration of 1.8 s within a 5 s sonication period. The acoustic emission was monitored with a calibrated hydrophone (Brüel & Kjær, 9.5 mm-Ø) placed at a 25 mm vertical distance below the horn tip. Although the main objective of the study was to investigate bubble dynamics within mm-sized channels under the horn, free-field characterisation at tip-vibration amplitudes of 6, 30, 60 and 120 μm was also provided. The authors presented spectra < f_0 for the acoustic signal collected, which featured subharmonic peaks at f_0/m, with m increasing for larger amplitudes, up to $f_0/8$. The authors speculated that the shift to larger m at higher power could be due to a decrease in bubble resonance at higher tip-vibration amplitudes.

Although the literature described reports rather different bubble characteristics observed via direct imaging, the subharmonic collapse behaviour with corresponding pressure spikes in the acoustic data appears to be consistent. In the current research, a study based on dual-perspective high-speed imaging of cavitation at the tip of a horn and parallel acoustic detection, capturing data for the duration of 2 s exposures, over ultimately twenty-five input powers, is reported. It is desirable to seek a detailed characterisation of the subharmonic response with tip-vibration amplitude and demonstrate the contribution of periodic shock waves to nonlinear features within the noise spectrum of the cavitation emission signal.

4.2 Materials and Methods

4.2.1 The experimental arrangement

The results described below were obtained with a commercial Branson 450 W Digital Sonifier, operating at 20 kHz through a 230 mm long tapered *Ti* probe, with a ¼″ tip diameter (6.4 mm-Ø), setup as shown in fig 4.3. Input power is entered as a percentage value at the control console, fig 4.1, with a minimum of 10% and programmable in 1% increments. All data were collected over 2 s sonications, initiated manually via a dedicated button on the front panel of the control console, fig. 4.1.

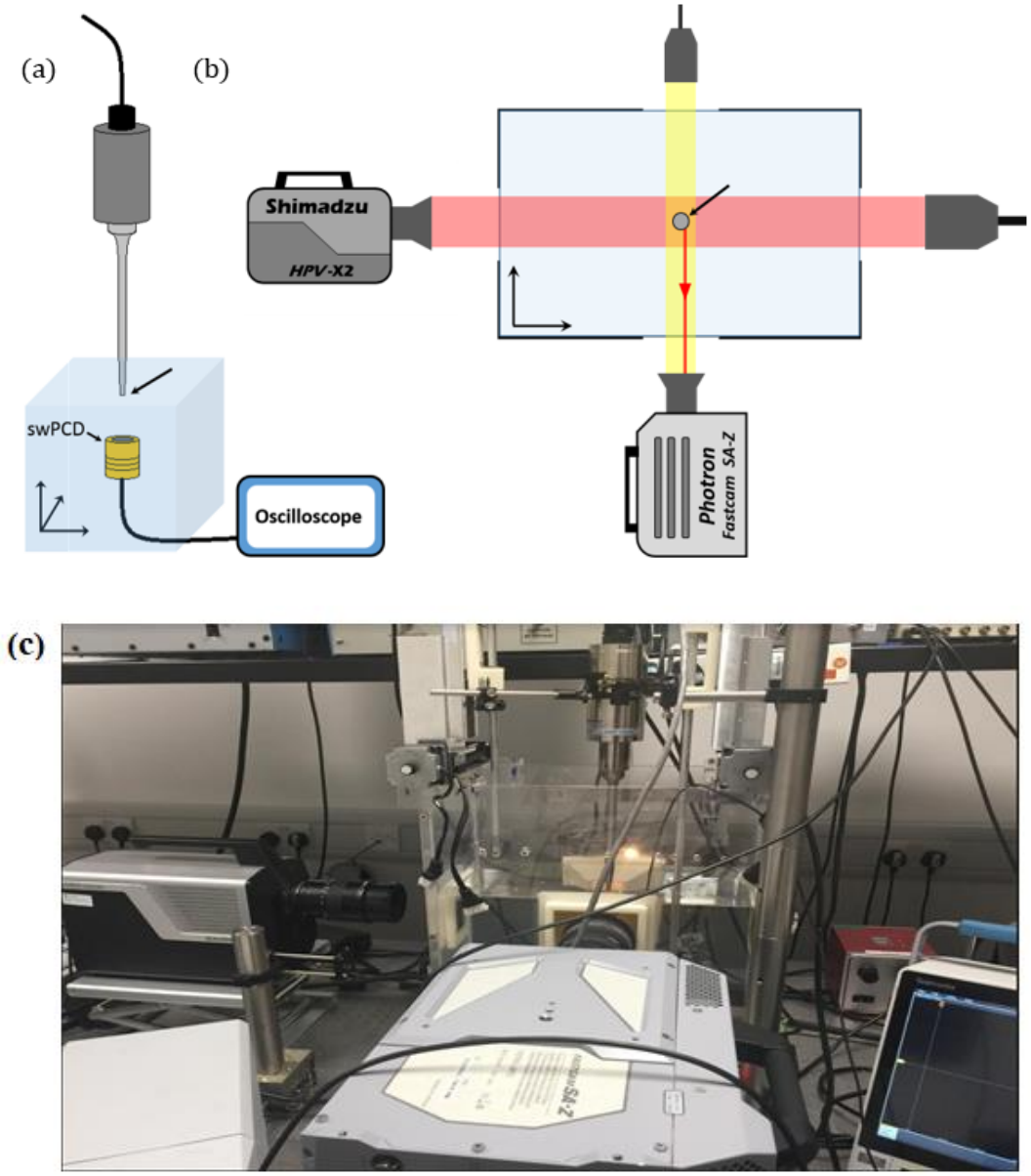

Figure 4.3: Schematic representations of the experimental arrangement (a) the ultrasonic horn and swPCD. (b) top-down view of the dual-perspective high-speed imaging configuration. The horn-tip is arrowed in both representations. (c) Image of the experimental setup of the ultrasonic horn experiment: the orthogonal arrangement of the two cameras in (c) is represents the schematic diagram in (a), and the top-down view of the Sonoptic tank with horn inserted vertically in (c) is represented with the schematic diagram in (b)

The horn was mounted such that the tip was submerged 25 ± 1 mm below the surface of de-ionised water, within a tank measuring 420 × 438 × 220 mm^3, fig. 4.3, refer to the detailed description of the Sonoptic tank in §3.1 of Chapter 3. As described in §4.2.2, high-speed imaging was conducted through glass windows embedded within the walls of the tank, fig. 4.3 (b). The picture of the experimental setup is shown in fig. 4.3 (c).

4.2.2 Dual perspective high-speed imaging

High-speed imaging of the cavitation at the tip during a sonication was undertaken simultaneously with the two high-speed cameras described in Chapter 3, from orthogonal perspectives in the horizontal plane, fig. 4.3 (b). The FASTCAM SA-Z 2100 K (Photron, Bucks UK, 128 GB of RAM) recorded the bubble activity for the entire 2 s duration of each sonication reported at 1×10^5 fps, with a 159 ns shutter time, through a macro-lens (EX DG, 24-70 mm 1:2.8, Sigma, Hertfordshire UK) and a 36 mm extension tube. At this frame rate, imaging was achieved over 384 × 256 pixels, with a resolution of 25 $\mu m pixel^{-1}$. Illumination was provided by a continuous 150 W halogen bulb source (Thorlabs, Ely UK) coupled to a liquid light guide and a collimating lens. The Shimadzu HPV-X2 (Shimadzu, Kyoto Japan), imaged at a higher temporal resolution of 2×10^6 fps (Mfps), but over a shorter duration of 128 μs. A spatial resolution of 65 $\mu m pixel^{-1}$ was achieved over 400 × 250 pixels through a macro-lens (Milvus 100 mm f/2M, Zeiss, Oberkochen, Germany). Illumination was provided via synchronous (to frame capture) 10 ns laser pulsed at 640 nm (CAVILUX Smart, Cavitar, Tampere Finland), coupled to a liquid light guide and a collimating lens. The shadowgraphic imaging capability described in **Chapter 3**, § 3.2.1, is used to identify the SWs generated by any bubble cluster within the field-of-view (FOV), that collapses sufficiently for the SW to be imaged. As will be shown in the results figures below, propagation of the higher amplitude SWs can be tracked through the image sequence, recoding incidence to the front face of the swPCD (the location for which is described below), such that it can be directly correlated to the corresponding feature in the voltage output.

4.2.3 Acoustic detection and filtering protocol

Acoustic detection was undertaken with the swPCD (described in §**3.3 Shock wave passive cavitation detector**) connected to an oscilloscope (Tektronix 5 series, Berkshire UK), and data sampled at 25 MSs^{-1}. For all data presented, the swPCD was located at 15 ± 1 mm from the tip of the horn. It should be noted that in this position, the swPCD will have a poor temporal resolution for the detection of shock wave emissions from tip-cavitation. The location does, however, put the front-face of the swPCD within the FOV of the Shimadzu imaging, such that individual shock wave incidence can be observed and used to identify corresponding features in the swPCD data. Preliminary tests with the swPCD ~ 10 cm from the horn-tip indicated that the positioning at 15 ± 1 mm did not influence cavitation dynamics within the vicinity of the tip, and shock wave periodicity, as reported below, was unaffected.

The output voltage signal from the swPCD, on detection of the acoustic emission signal generated by the cavitation at the horn-tip, is subjected to a filtering protocol designed using finite impulse response (FIR) as described in detail in §**3.3.1 Filters used for acoustically detected data**. The different stages of the filtering protocol are as follows:

- The voltage signal is first subjected to a high-pass filter with a cut-off frequency of 50 Hz to remove possible line noise.
- The resulting signal is then subjected to a low-pass filter of 10 MHz cut-off frequency to remove system noise.
- Finally, the resultant signal is subjected to a bandpass filter with cut-off frequencies [20 kHz 4 MHz]; the lower bound is guided by the horn driving frequency, and the upper bound is guided by the sensitivity bandwidth of the swPCD, above the noise level, [36].

Fig. 4.4 illustrates the effect of each filtering stage of the protocol, on sample swPCD data collected of the acoustic emissions generated by the cavitation at the horn-tip, for an input power of 40% (extended data for which is presented in fig 4.11 below, within the context of varying input power/tip-vibration amplitude measurements).

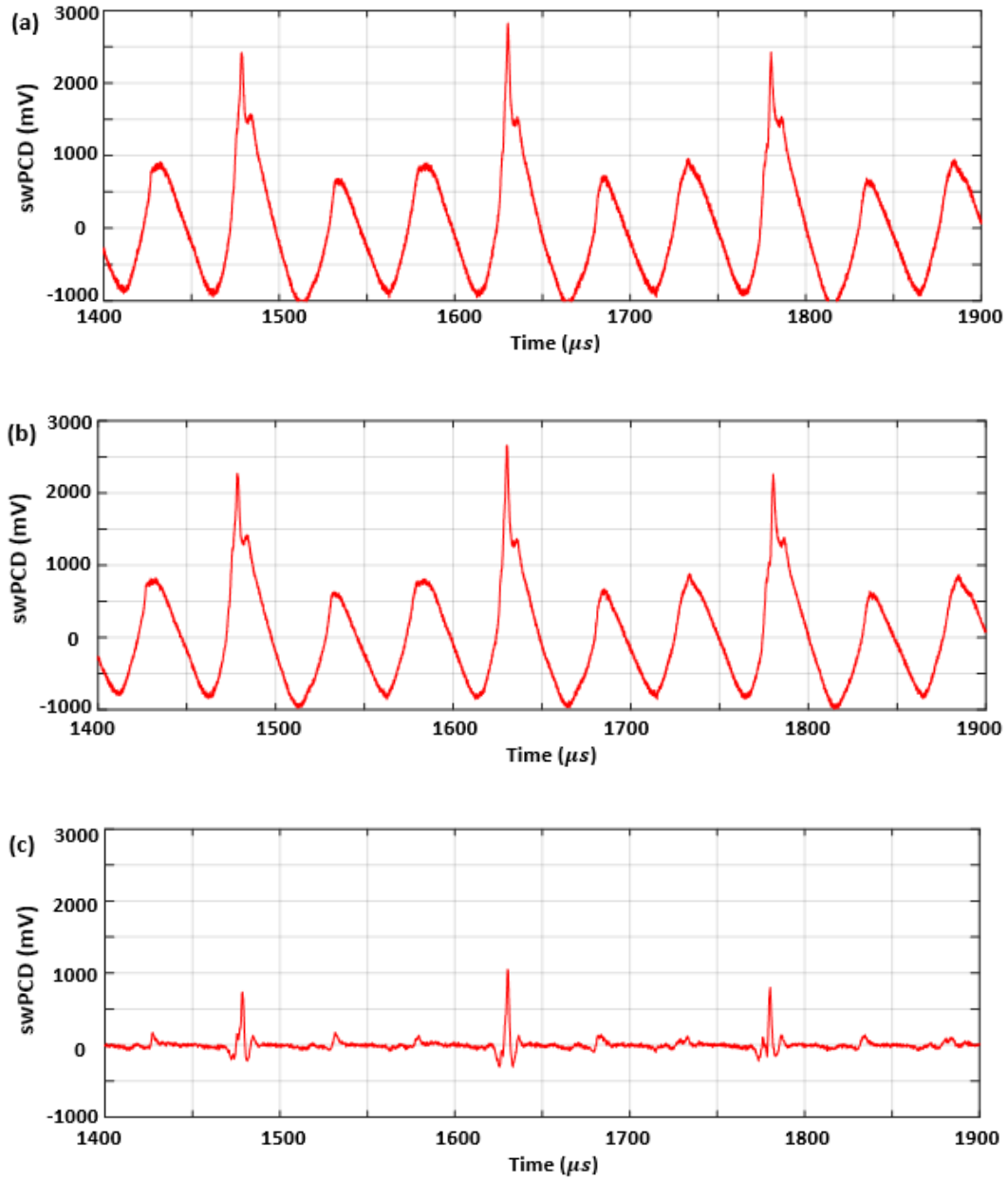

Figure 4.4: Illustration of the filtering protocol applied to sample swPCD data, collected from the acoustic emissions generated by the horn-tip 40% input power (a) Raw voltage data direct from the swPCD; the small positive feature that occurs on the trailing edge of each main peak in the figure (at ~1480 µs, ~1640 µs, ~1780 µs) was due to the response of swPCD used, (b) after the removal of line noises (50Hz) and system noise above 10 MHz, (c) after the application of bandpass filter removing the driving signal, (f_0).

The raw acoustic emission in fig 4.4 (a) is composed of driving signal at f_0, SWs signal, and possible noise associated with channel/lines and system noises. First, these noises are removed as described in steps 1 and 2 above, fig. 4.4 (b).

Finally, a bandpass filter is applied to remove the driving signal, revealing the SWs as shown in fig. 4.4 (c). The Matlab codes for these procedures are provided in Appendix **A.1 Matlab filtering and frequency codes**.

4.3 Data collection

Sonications were initiated manually from the control console of the ultrasonic horn at prescribed input powers. The rest of the instrumentation was synchronised via electronic triggering from a delay generator (DG535, Stanford Research Systems, Sunnyvale USA). Any datasets for which the Photron imaging did not capture the initiation of bubble activity beneath the tip were discarded. At lower input powers < 20%, cavitation occurrence was inconsistent. Results below are therefore limited to the range of 20 – 100%.

4.4 Preliminary overview of cavitation activities

The main research findings of this Chapter relate to the subharmonic response of the cavitating bubble-cloud at the tip of the ultrasonic horn, and the dependence on input power, as described in §**4.5.1 - 4.5.4**. The section is intended to see the nature and development of the primary bubble cluster formed as a function of input power over the sonication period. It was revealed that the primary cavitation bubble cluster that is formed at the tip of the ultrasonic horn needs some time before it attains a stable phase, hence it was decided that the cavitation at the horn's tip during the stable phase of the cavitation should be studied.

In this section, observations from an initial pilot study are presented to characterise the overall cloud development throughout the chosen 2s sonication duration at various input powers. For this purpose, data were collected with the Photron high-speed camera and the swPCD, as presented in figs 4.5 and 4.6, respectively, below. Indeed, a key objective from this pilot study was to determine when the limited duration shadowgraphic imaging provided by the Shimadzu perspective might be most usefully deployed. Input power was initially sampled at 10% increments, between 20 - 100%, with representative data provided at 20, 40, 60, 80 and 100%. Each row of fig 4.5 are selected frames from a Photron image sequence of the cavitation below the horn-tip, at the input power and time indicated.

It should be noted that each bubble-cloud is continuously oscillating in response to tip-vibrations throughout the sonication, and the dependence of these oscillations on input power, as a key finding, is described in §**4.5.2 Main cluster shock wave periodicity at selected input powers**. Here, the overall development of the bubble cloud with time, at each given input power is determined. The frames of fig 4.5 are thus selected as representing *maximum inflations phases* for the bubble-cloud within an oscillation, at around the time during the sonication indicated.

Fig 4.5 indicates that at all input powers, the bubble-cloud requires some time to 'grow' to the stable[10] size that is relatable to the input power for the observation. The growth of the bubble cloud towards a stable size associated with each input power is being referred to as the *proliferation phase*. Mechanisms for cloud growth likely include fragmentation of individual bubbles within the cloud with each collapse, each forming multiple daughter-bubbles, and rectified diffusion, which will gradually increase the overall gas phase within the cloud. Fig. 4.5 further suggests that the duration of the proliferation phase also depends on the input power, with larger clouds at higher power requiring longer to reach the characteristic stable size. It was observed that the point of formation of the primary bubble cluster at lower amplitudes was not specific but randomly changed for each experimental run. For this reason, it cannot be suggested that the position observed, for example, at 20% input power, was due to changing modes of vibration of the ultrasonic horn. However, it may be due to the random nucleation point and size of the bubbles.

[10] Stable size is referred to when the size of primary cluster (at maximum inflation) remains fairly constant during the sonication period. The primary cluster reaches the stable size approximately 750 ms into sonication for all amplitudes.

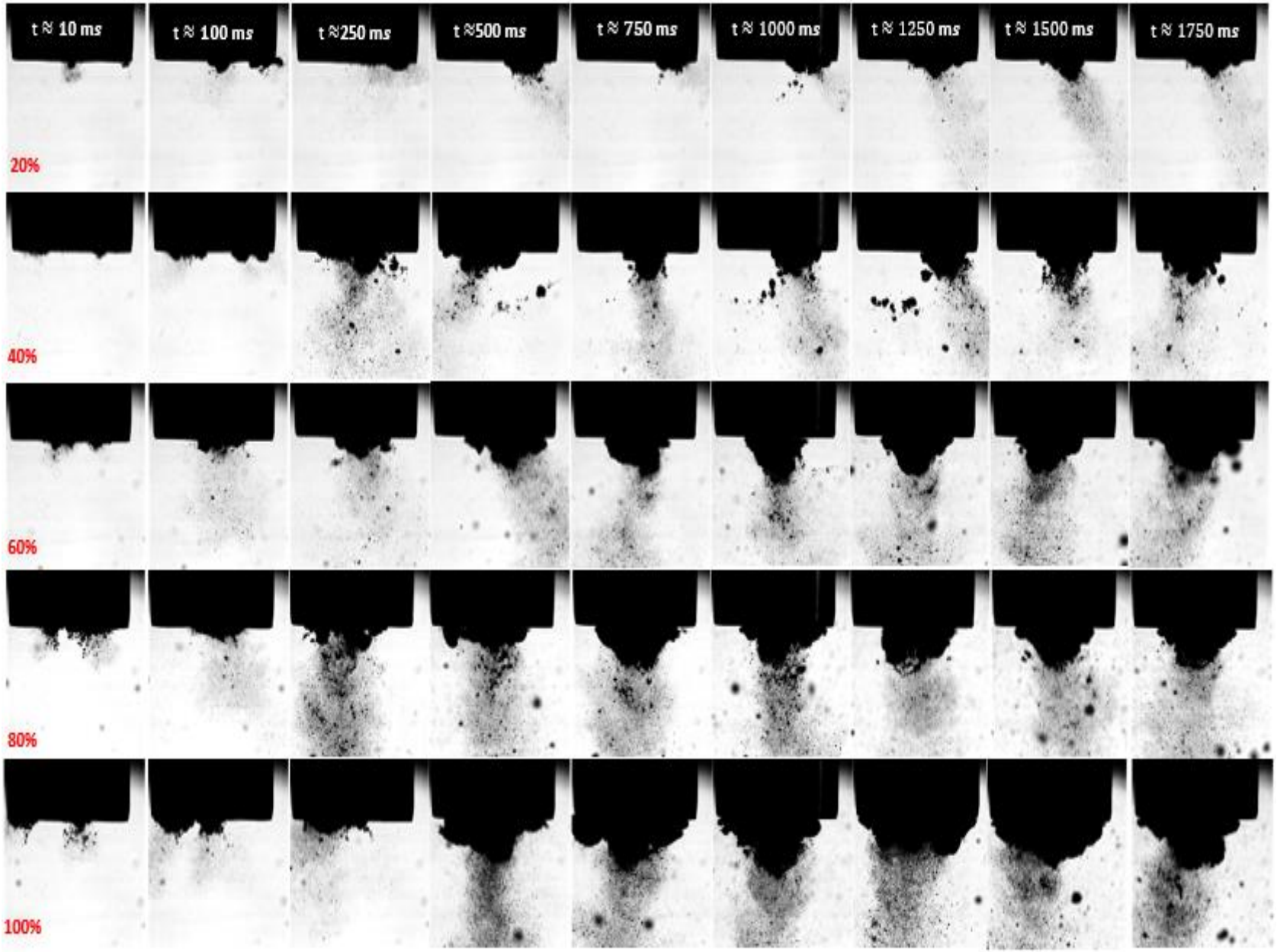
t ≈ 10 ms
t ≈ 100 ms
t ≈250 ms
t ≈500 ms
t ≈ 750 ms
t ≈ 1000 ms
t ≈ 1250 ms
t ≈ 1500 ms
t ≈ 1750 ms
20%
40%
60%
80%
100%

Figure 4.5: Selected frames from Photron high-speed image sequences collected at 1 × 10^5 fps, for input powers of 20, 40, 60, 80 and 100%, representing bubble-cloud development over a 2s sonication. Frames capturing maximum inflations within cloud-oscillations around the times indicated allow comparison of the bubble-cloud size at each input power. Higher input powers exhibit longer proliferation phases, whereby the cloud is building up to its stable[4] state, with clouds at all powers achieving this by ~ 750 ms. Scale is provided by the 6.4 mm-Ø tip.

Fig. 4.6 (a)-(e) represents swPCD data collected during the observations of fig 4.4, at input powers of 20, 40, 60, 80 and 100%, respectively. The figures show the filtered swPCD voltage signals (ii-iv), representing three different sections of 1.5 ms within the entire 2s sonication period. Evidently, features within the data are occurring on a much shorter timescale, such that this representation is not particularly informative. As an example, Fig 4.6 (a) reveals the trend in the acoustic data corresponding to the *proliferation* and *stable phase* identified for the high-speed imaging of fig. 4.5. Similar trends can be seen in figs. 4.6 (b)-(e). The periodicity and the magnitude of the SWs keep changing, most notably during the *proliferation phase*, until the bubble-cloud reaches its stable state, an investigation of which comprises the main research results of this Chapter.

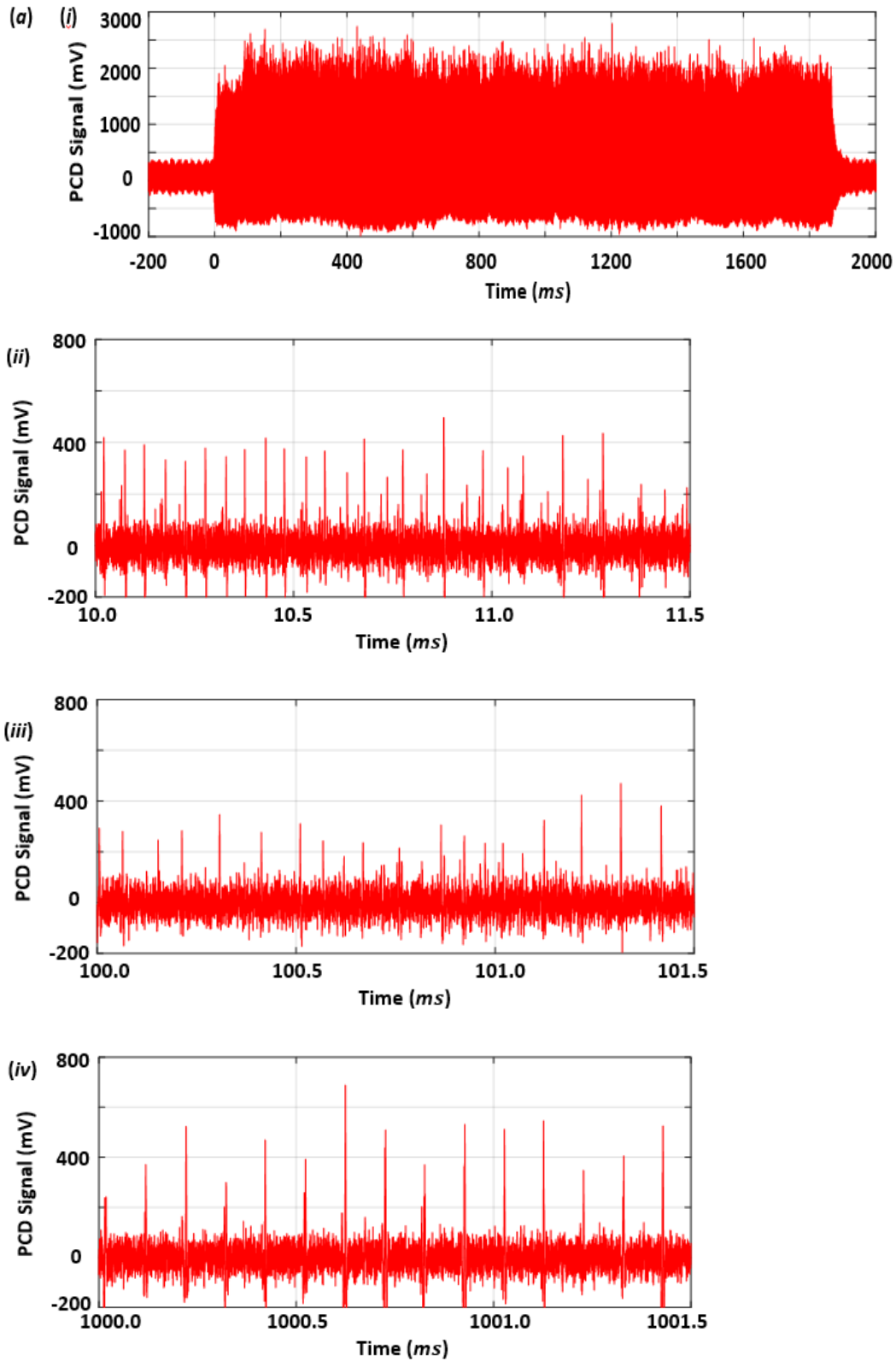
(a)
(i)
PCD Signal (mV)
3000
2000
1000
0
-1000
-200
0
400
800
1200
1600
2000
Time (ms)
(ii)
PCD Signal (mV)
800
400
0
-200
10.0
10.5
11.0
11.5
Time (ms)
(iii)
PCD Signal (mV)
800
400
0
-200
100.0
100.5
101.0
101.5
Time (ms)
(iv)
PCD Signal (mV)
800
400
0
-200
1000.0
1000.5
1001.0
1001.5
Time (ms)

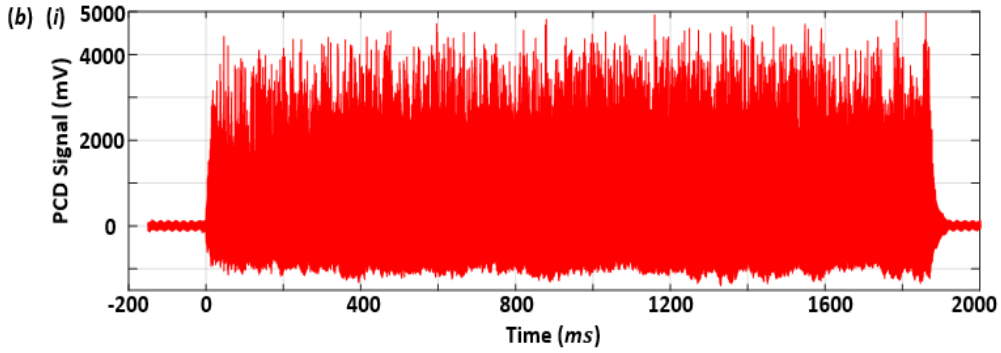
(b) (i)
PCD Signal (mV)
5000
4000
2000
0
-200
0
400
800
1200
1600
2000
Time (ms)

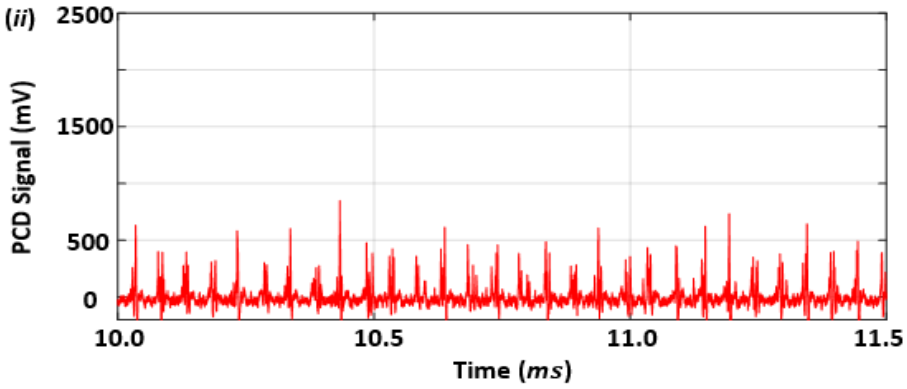
(ii)
PCD Signal (mV)
2500
1500
500
0
10.0
10.5
11.0
11.5
Time (ms)

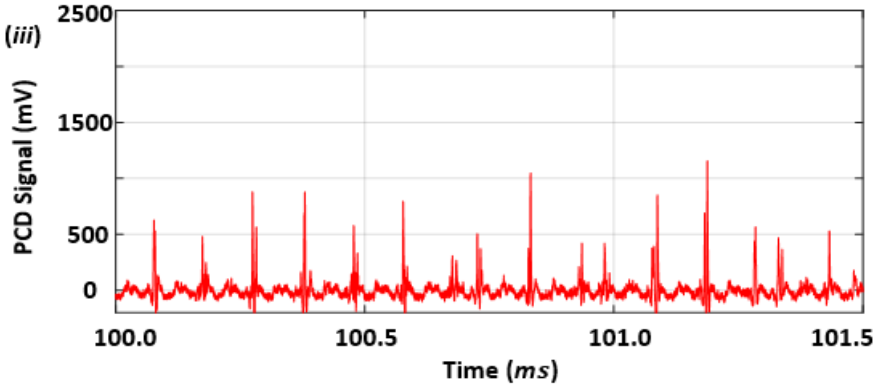
(iii)
PCD Signal (mV)
2500
1500
500
0
100.0
100.5
101.0
101.5
Time (ms)

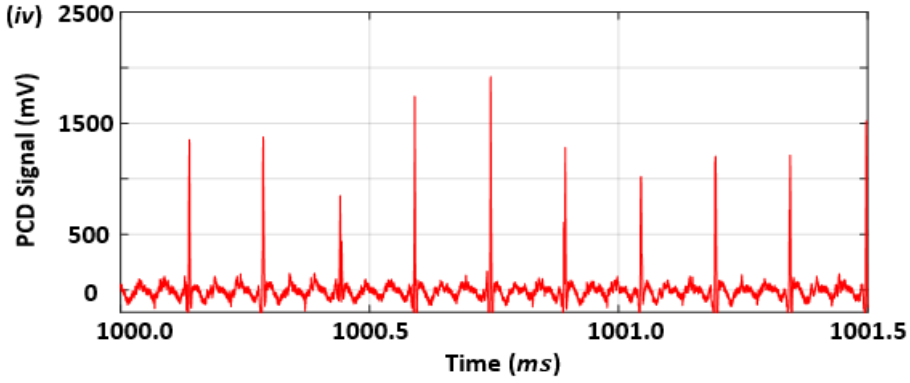
(iv)
PCD Signal (mV)
2500
1500
500
0
1000.0
1000.5
1001.0
1001.5
Time (ms)

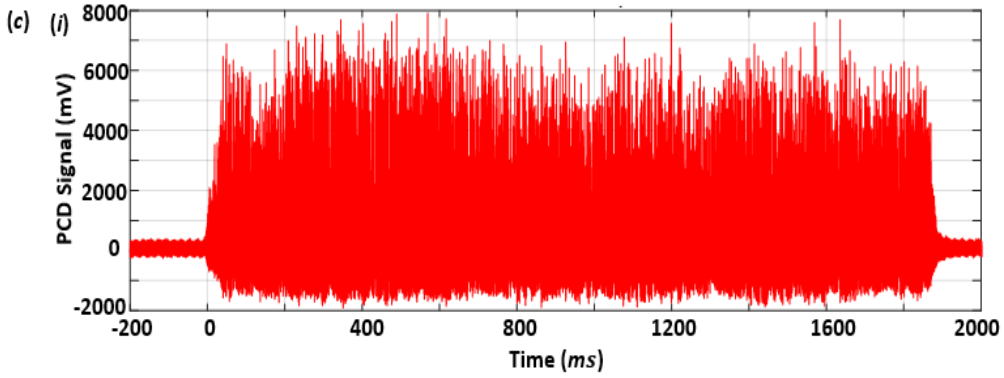
(c) (i)
PCD Signal (mV)
8000
6000
4000
2000
0
-2000
-200
0
400
800
1200
1600
2000
Time (ms)

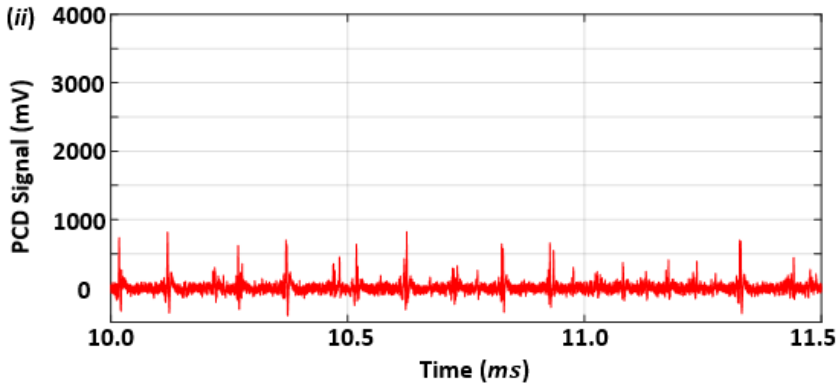
(ii)
PCD Signal (mV)
4000
3000
2000
1000
0
10.0
10.5
11.0
11.5
Time (ms)

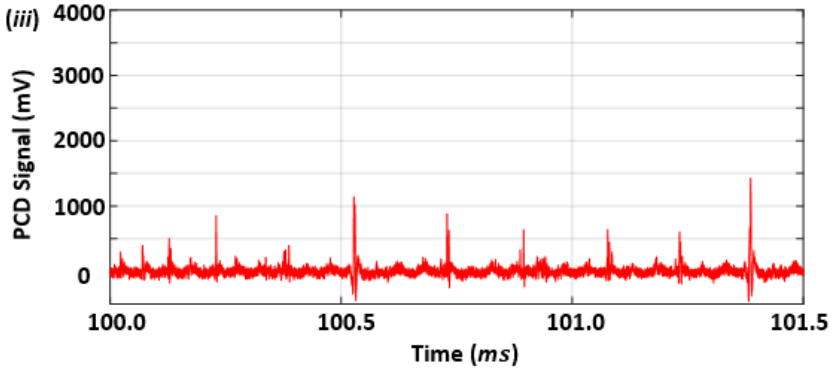
(iii)
PCD Signal (mV)
4000
3000
2000
1000
0
100.0
100.5
101.0
101.5
Time (ms)

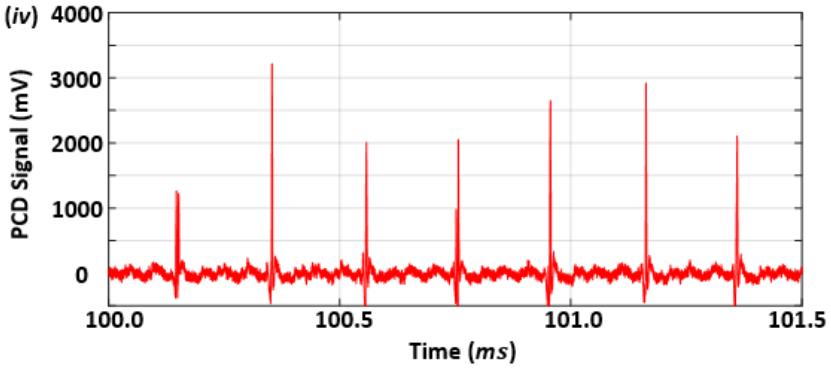
(iv)
PCD Signal (mV)
4000
3000
2000
1000
0
100.0
100.5
101.0
101.5
Time (ms)

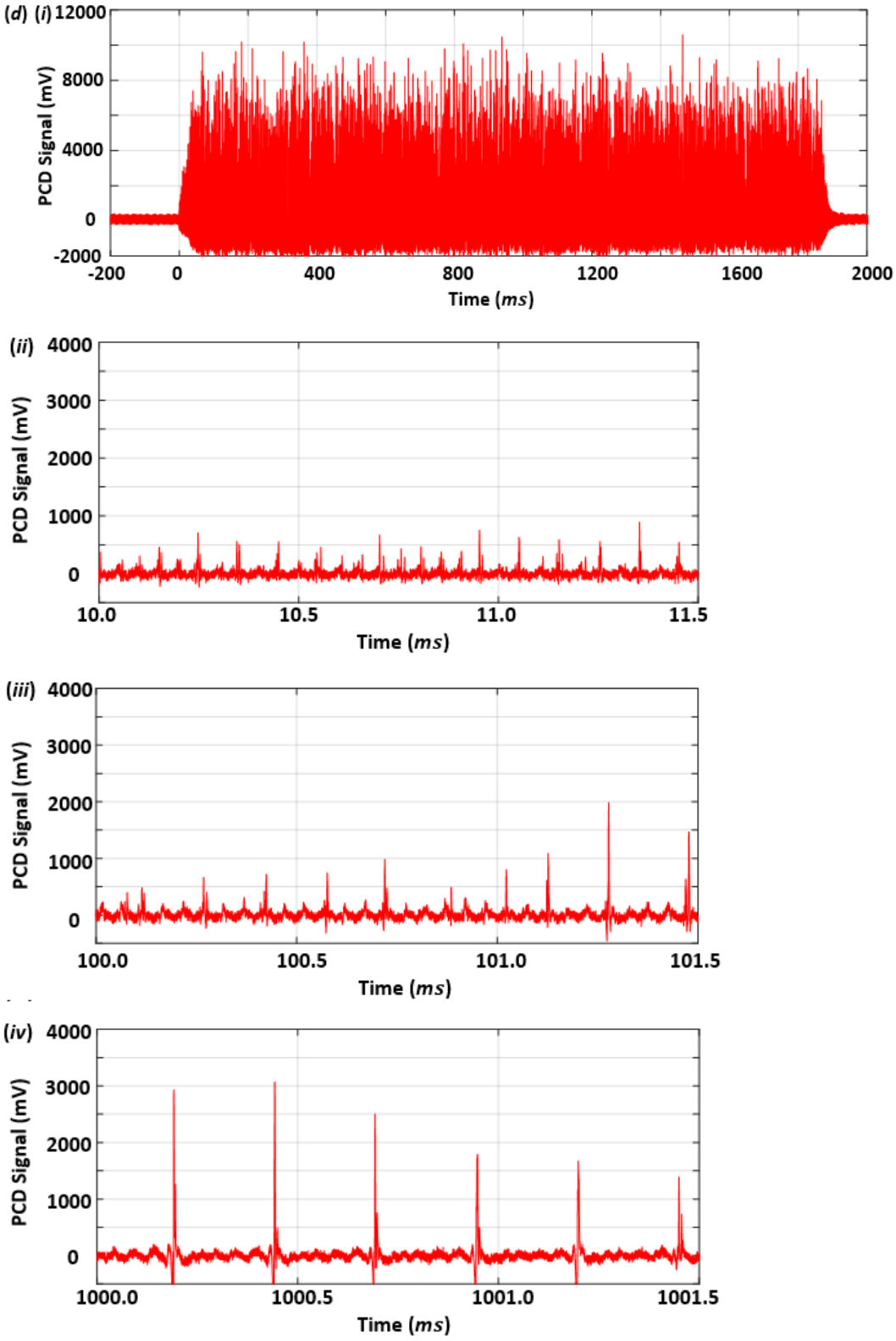
(d) (i)
PCD Signal (mV)
Time (ms)
(ii)
PCD Signal (mV)
Time (ms)
(iii)
PCD Signal (mV)
Time (ms)
(iv)
PCD Signal (mV)
Time (ms)

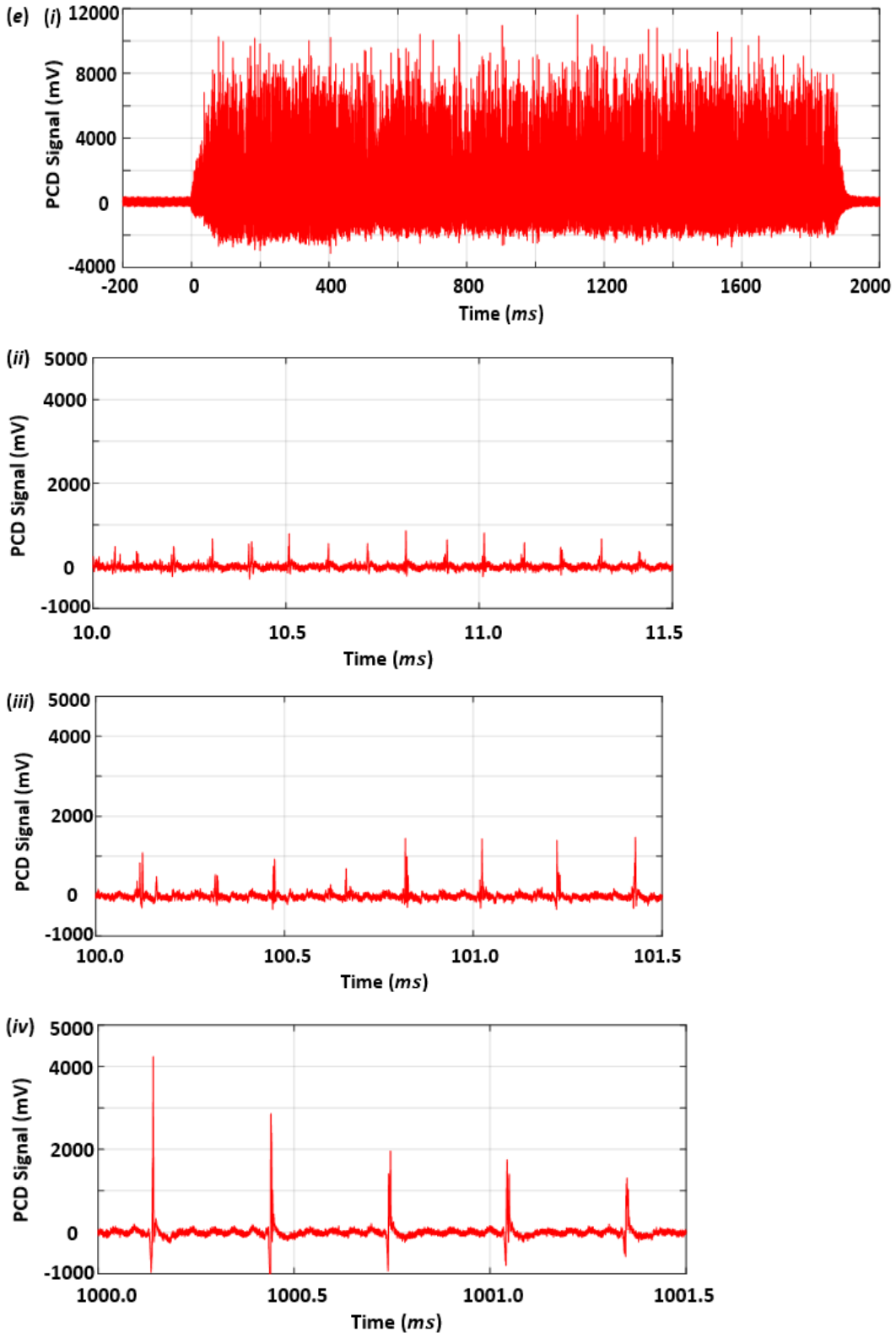

Figure 4.6: The representation of three different section of 1.5 ms from a filtered swPCD data within the sonication period of 2 s for the following input power: (a) 20%, (b) 40%, (c) 60%, (d) 80%, (e) 100%. (i) 2 s filtered swPCD data, (ii) 10 – 11.5 ms section of the filtered swPCD data, (iii) 100 – 101.5 ms section of the filtered swPCD data, and (iv) 1000 – 1001.5 ms section of the filtered swPCD data.

4.4.1 Conclusions from preliminary overview

The pilot study revealed that the bubble cloud under the tip of the ultrasonic horn undergoes a *proliferation phase* of growth, following the initiation of a sonication, to a stable size that is characteristic of the input power of the sonication. The duration of the proliferation phase also depends on the input power, with larger clouds at higher power taking longer to reach the stable size. The higher the input power, the higher the tip-vibration amplitude as would be shown in the later part of this chapter. Although, the mode of vibration in some sonotrode may change with tip-vibration amplitude or frequency depending on the design. The acoustic emissions detected from the cloud also vary considerably during proliferation, stabilising once the cloud has ceased growing. Longer sonication times of up to 10 s did not appear to result in further growth of the bubble clouds, beyond the stable sizes represented in fig 4.4, at each input power.

The following results sections report on the subharmonic oscillations of the bubble clouds during the *stable*[10] *phase* of sonications. As the proliferation phase appears to have ceased by 750 *ms*, including for the highest powers, the shadowgraphic imaging of the Shimadzu perspective, fig. 4.3 was set to trigger at 1 s into a 2 s sonication, to capture cloud collapse and shock wave generation at high temporal resolution.

4.5 Results

The results sections below are organised as follows: §**4.5.1 Data registration and cavitation characterisation** presents the details of dual-perspective imaging and swPCD data over a short 300 µs duration, from approximately 1 s into a 2 s sonication at a single input power of 33%. A dark-pixel counting algorithm (MATLAB, MathWorks) described in §**3.2.3 Dark pixel counting algorithm**, is used to quantify the oscillation behaviour of the 'summed bubble area' throughout a sequence of images. However, some care should be taken in interpreting the dark-pixel counting data presented, not least as the cavitation at the tip extends through 3-dimensions. The simplistic approach is, however, sufficient for identifying cloud-ensemble oscillations and collapse times [122],[124]. The purpose of this section is

to characterise the various cavitation behaviours in the vicinity of the tip, and justify the approach adopted for analysis of the subsequent *Result* section. §**4.5.2 Main cluster shock wave periodicity at selected input powers** presents dark-pixel counting from the Photron imaging, with the corresponding swPCD data, over representative 2.5 ms durations, at selected input powers (justified later, §**4.5.4**). Here, we seek to highlight differences in cavitation behaviour at the selected input powers. Table 4.1 extends the findings, via analyses of 200 ms sections of swPCD data, from five sonications at each of the selected input powers. §**4.5.3 Cavitation emission noise spectra at selected input powers** consider the noise spectra of the emission signal collected by the swPCD, for representative sonications at each of the selected input powers, for both the 200 ms section, and the entire signal collected over the 2 s sonication. This section confirms that the differences in the oscillation behaviour of the cavitation identified in §**4.5.2** are also manifested in the acoustic emission signal generated by the cavitation at each input power. Finally, §**4.5.4 Shock wave content within the emission signal over twenty-five input powers** presents the average root mean square of the swPCD signals collected over five 2 s sonications, at twenty-five input powers. This graph is interpreted in terms of the findings of the previous sections.

4.5.1 Data registration and cavitation characterisation

Fig. 4.7 presents sample data at a horn input power of 33%, approximately 1 s into a sonication, as collected by (a) the Photron at a relatively high spatial resolution, (b) the Shimadzu over a larger field-of-view (FOV) but at a high temporal resolution, and (c) the swPCD, the front face of which is visible at the bottom of the Shimadzu FOV.

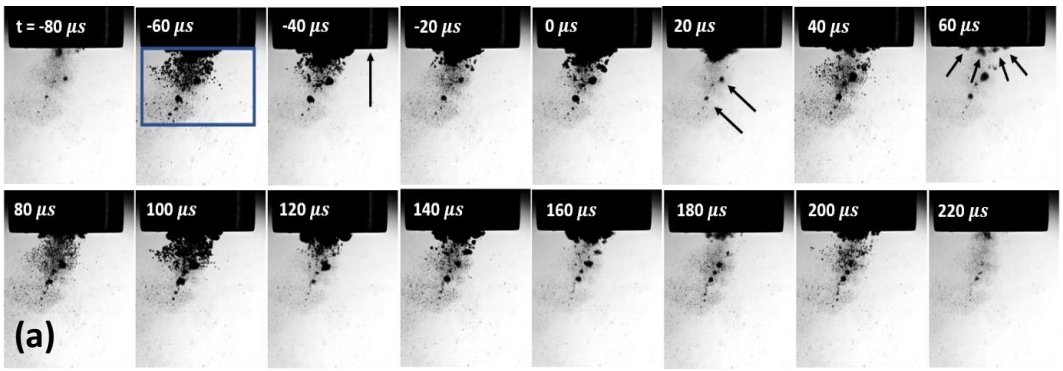

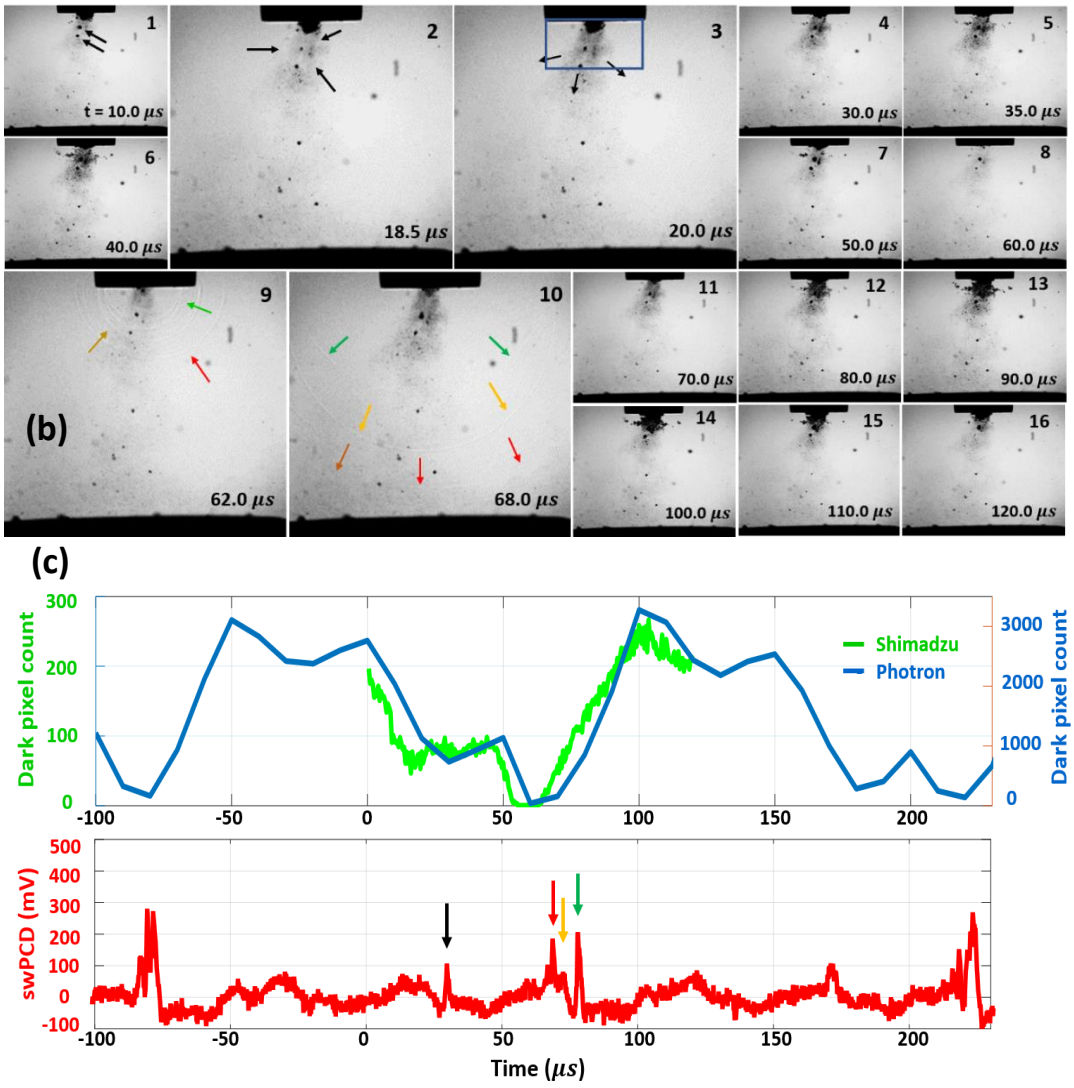

Figure 4.7: Sample data representing cavitation characterisation and data-registration between: (a) Photron imaging at 1×10^5 fps, (b) shadowgraphic Shimadzu imaging at 2 Mfps. The same two satellite clusters are arrowed in (a) at 20 µs and (b) at 10 µs, with the shock wave generated by the upper cluster also arrowed at 18.5 and 20.0 µs. Coloured arrows at 62.0 and 68.0 µs track shock wavefronts generated by primary sub-cluster collapses as they propagate through the FOV. Scale in both imaging data perspectives is provided by the 6.4mm-Ø of the horn-tip, and t = 0 µs is determined by the start of the Shimadzu imaging. (c) dark pixel counting for both imaging sequences and swPCD measurements.

Both imaging perspectives reveal cavitation activity that is generally consistent with many previous reports [26],[122],[123]; a primary bubble cluster that remains effectively in contact with the horn-tip throughout, 'satellite' clusters

that are detached from the tip, and a cloud of smaller bubbles that are not always well resolved, extending to several mm below the tip making up the cavitation zone. The Shimadzu imaging of fig. 4.7 (b) further reveals distal clusters > 5 mm from the tip, including along the front face of the swPCD. Overall the observations made in this study show that a shock wave was never detected from a distal cluster (either via the shadowgraphic imaging perspective or within the swPCD data), suggesting they cavitate non-inertially [125].

The Photron data of fig. 4.7 (a) is presented over ~300 μs and thereby captured six full tip-oscillations. The dark-pixel counting algorithm provides an overview of '*summed bubble area*' behaviour over this duration, fig 4.7 (c, blue), sampled from the region represented by the box below the tip, fig 4.7 (a) at -60 μs. It should be noted that this region includes the primary cluster, satellite clusters and some of the extended small bubble clouds. The primary cluster, however, which represents the largest and most dynamic of the bubble structures, will dominate the dark-pixel counting curve. Two peaks in the curve, at -50 and 100 μs, representing frames of maximum inflation as captured by the Photron camera, follow minima in the curve when the summed bubble area was close to zero at -80 and 60 μs (with a subsequent minimum apparent at 220 μs). The frames associated with these summed bubble area minima are presented in fig 4.7 (a), at the respective timings. These images suggest the primary cluster has just collapsed or is about to collapse, with the exact timing not precisely identified at the 1×10^5 fps temporal resolution of this perspective. Note that the two satellite clusters, arrowed at t = 20 μs, are inflating as the primary cluster deflates into a collapse, around t = 60 μs.

The Shimadzu data of fig. 4.7 (b), recorded at 2 Mfps from t = 0 – 128 μs, probes the activity around the Photron dark-pixel counting minimum at t = 60 μs with higher temporal resolution and shadowgraphic imaging, facilitated by the pulsed laser illumination described previously in §4.2.2. The illumination for the Shimadzu imaging axis, which is triggered in advance to sequence capture, is faintly apparent within the Photron imaging as some laser light is reflected orthogonally from the horn tip, arrowed at -40 μs, fig. 4.7 (a), and represented schematically in fig. 4.3 (b). The two satellite clusters identified in the Photron imaging at t = 20 μs, fig 4.7 (a), are also arrowed in the Shimadzu imaging of fig 4.7 (b), at t = 10 μs, for registration between the perspectives. Images 2, 3, 9 and 10 have been enlarged as they feature various cluster collapse shock waves (the

propagation of which are generally better perceived in the movie version of the data. The green curve of fig. 4.7 (c) represents the output from the dark-pixel counting algorithm applied to the Shimadzu image sequence.

Image 2 of fig. 4.7 (b), at 18.5 µs, captures a shock wave generated from the collapse of the upper satellite cluster, the propagation of which is still faintly apparent at t = 20 µs. The Shimadzu dark-pixel counting curve capture this collapse, with a local minimum of ~ 30 dark pixels at around 18 µs, and this shock wave is acoustically detected by the swPCD, arrowed black fig 4.7 (c), after a propagation time of ~ 10 µs. Images 9 and 10 capture the shock wavefronts generated by the prominent collapse of the primary cluster around 60 µs. The shadowgraphic imaging allows three main shock fronts to be identified along with the corresponding acoustic detections (arrowed red, orange, and green, fig 4.7 (b) and (c) respectively). The multiple fronts of this shock wave indicate that the primary cluster has not collapsed uniformly, but as several sub-clusters, each collapsing at slightly different times. This may be verified in the Photron imaging at t = 60 µs, where four clusters are apparent within the region occupied by the primary cluster (arrowed black, fig 4.7 (a)). The µs and sub-µs differences in the collapse timings of these sub-clusters explain why the minimum of the Shimadzu dark-pixel counting curve around this time is somewhat U-shaped. The movie version of this data reveals that as one sub-cluster collapses, the others are either still deflating into collapse or rebounding from it, such that there is not a well-defined minimum. It was noted that the extended cloud of smaller bubbles is at its most prominent after excitation via the propagation of a shock wave from the collapse of either the primary sub-clusters or a satellite cluster. The dark-pixel counting from both imaging perspectives register this excitation as local peaks, with shock waves either detected by the shadowgraphic imaging or acoustically by the swPCD after a propagation delay.

Another feature of fig 4.7 is the partial, non-collapsing deflations captured by the Photron imaging at t = -20, 30, 130 and 180 µs. Taken along with timings of the collapses at t = -80 and 60 µs, main cluster deflations generally occur approximately at the 50 µs period of the tip-vibration (T_0), with variations in the precise timings attributable to host medium inertia effects retarding the bubble dynamics according to the degree of the cluster deflation/inflation. The swPCD data

of Fig 4.7 (c) indicates primary cluster collapse and shock wave generation at $3T_0$ (or $f_0/3$) for the sampled duration.

To summarise, the cavitation in the region surrounding the tip comprises at least four distinct types of cavitation activity; the primary cluster, satellite clusters, an extended cloud of smaller bubbles and distal clusters. The first two are capable of shock wave generation. The primary cluster generates periodic multi-fronted shock waves at subharmonic values to the tip-vibration and satellite clusters generating shock waves independently of the main cluster oscillations. Both high-speed imaging perspectives and the parallel acoustic detection of this experimental configuration are required to characterise and distinguish between the behaviour of these cavitation categories. However, the Photron imaging in conjunction with swPCD detection is sufficient to interrogate the subharmonic collapse dynamics of the primary cluster over an extended sonication duration, as described in the following section.

4.5.2 Main cluster shock wave periodicity at selected input powers

Having established the utility of the experimental configuration represented in fig 4.3, results are now presented from an investigation to assess the periodicity of primary cluster collapse and shock wave emission across some selected key input powers of 20, 25, 33, 40, 50 and 60%. The justification for selecting these key powers will be given in §4.5.4, where data from twenty-five input powers across the full available range are considered.

Fig. 4.8 (a) is the Photron dark-pixel counting and swPCD data, equivalent to fig. 4.7 (c), but over a 2.5 ms duration approximately halfway through a 2 s sonication, at 20%. Fig. 4.8 (b) are the source images corresponding to the minimum of the dark-pixel counting curve at 1250 μs, with a corresponding shock wave detected by the swPCD. We note that the cavitation activity is not always centrally located with respect to the horn-tip, which was commonly observed for lower input powers below 30%.

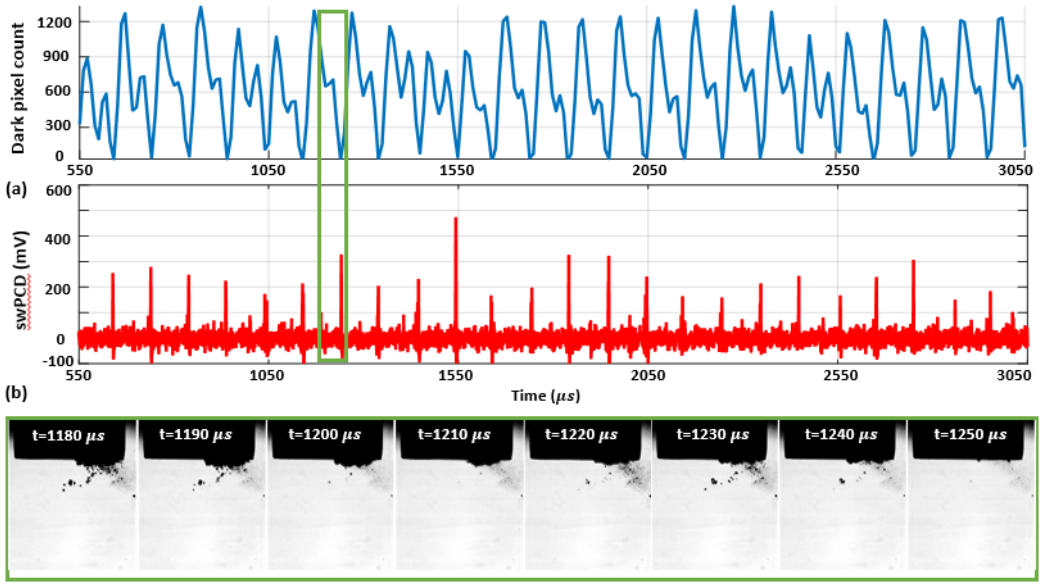

Figure 4.8: (a) Dark-pixel counting and swPCD data over ~2.5 ms duration from within a 2 s sonication at 20% input power. (b) Representative Photron imaging from within the duration, corresponding to the green box of (a). Scale is provided by the 6.4 mm-Ø tip.

The data of fig 4.8 reveals primary cluster collapse and shock wave detection at a regular periodicity of ~100 µs, or $2T_0$ of the tip-driving. In between each collapse, there is typically a single non-collapsing deflation, captured in fig. 8 (b) around 1220 µs.

Cavitation activities similar to that obtained at 20% input power was observed at 25% input power, as shown in fig 4.9. Part (a) is the Photron dark-pixel counting over 2.5 ms at 25%, and part (b) of the figure are the source images corresponding to the minimum of the dark-pixel counting curve at 1555 µs, with a corresponding shock wave detected by the swPCD. There is, however, a notable increase in the bubble-cloud size and the amplitude of the SWs generated at 25% input power.

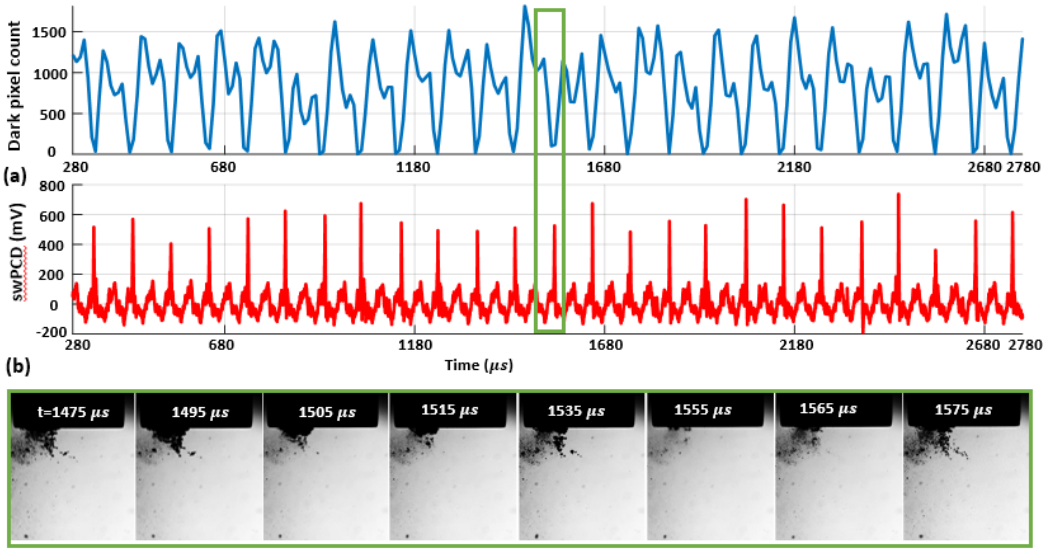

Figure 4.9: (a) Dark-pixel counting and swPCD data over a ~2.5 ms duration from within a 2 s sonication at 25% input power. (b) Representative Photron imaging from within the duration, corresponding to the green box of (a). Scale is provided by the 6.4 mm-Ø tip.

Fig. 4.10 presents data at an input power of 33% (as for fig. 4.7), but in a format equivalent to fig. 4.8 and 4.9, with fig.4.10 (b) displaying the source images over two sections of the 2.5 ms duration, according to the black and green boxes. The frame at 5090 µs was taken around a moment of primary cluster collapse, with the resulting shock wave clearly detected by the swPCD.

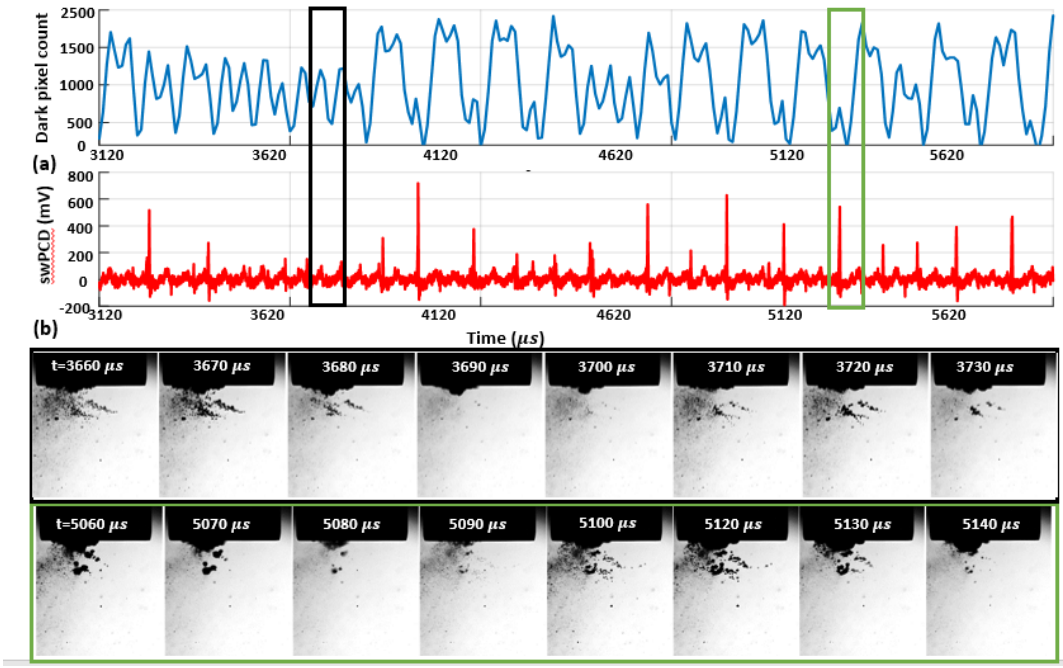

Figure 4.10: (a) Dark-pixel counting and swPCD data over a ~2.5 ms duration from within 2 s sonication at **33%** input power. (b) Representative Photron imaging from within that duration, corresponding to the green and black boxes of (a). Scale is provided by the 6.4 mm-Ø tip.

The two preceding shock waves detected by the swPCD, with corresponding minima in the dark-pixel counting curve, were emitted at ~150 µs intervals, or $3T_0$. The shock waves following the one highlighted, however, are closer to the $2T_0$ periodicity that characterised the cavitation behaviour at both 20% and 25%, fig. 4.8 & 4.9. earlier. In the data represented by fig. 4.10, between 3400-3800 µs, there appears to be an extended sequence of non-collapsing deflations, with no prominent shock wave typical of a primary cluster collapse, detected by the swPCD.

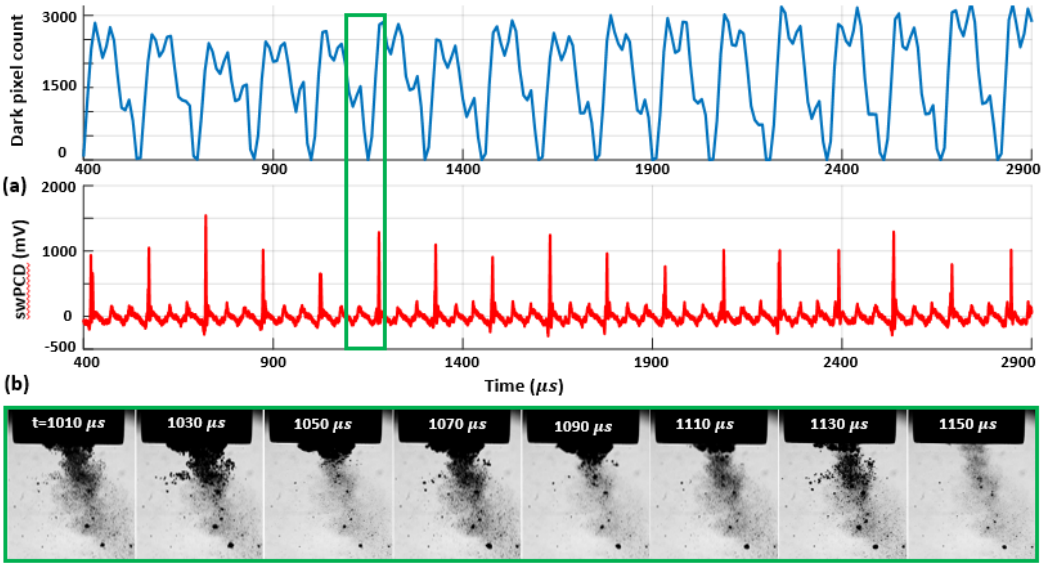

Figure 4.11: (a) Dark-pixel counting and swPCD data over a ~2.5 ms duration from within 2 s sonication at **40%** input power. (b) Representative Photron imaging from within that duration, corresponding to the green box of (a). Scale is provided by the 6.4 mm-Ø tip.

At a higher input power of 40%, fig. 4.11, a larger cluster exhibits regular $3T_0$ collapse behaviour throughout the 2.5 ms duration. The dark-pixel counting curve of fig. 4.11 (a) indicates that every collapse, confirmed via the detection of a shock wave in the swPCD trace, is followed by an inflation, a partial deflation, a re-inflation, then a stronger but still non-collapsing deflation before the next successive collapse. The source images of fig. 4.11 (b) indicate that satellite clusters and the extended small bubble cloud will be making contributions to the dark-pixel counting curve, although these will be somewhat limited by the region sampled below the horn, fig. 4.7 (a) at -60 μs. The prominent shock waves in the swPCD data of fig. 4.11 (b), confirm $3T_0$ collapses for the primary cluster.

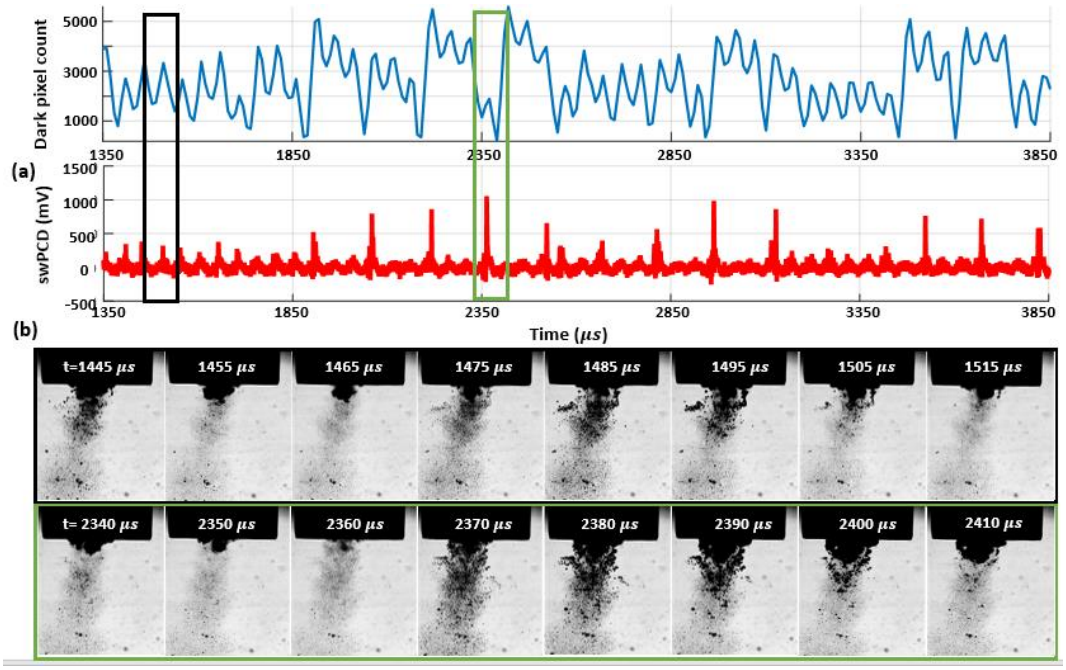

Figure 4.12: (a) Dark-pixel counting and swPCD data over a ~2.5 ms duration from within 2 s sonication at **50%** input power. (b) Representative Photron imaging from within that duration, corresponding to the green and black boxes of (a). Scale is provided by the 6.4 mm-Ø tip.

Fig. 4.12 reveals a mixture of $3T_0$ and $4T_0$ behaviour at 50%, with the latter behaviour incorporating an additional non-collapsing deflation phase. As for an input power of 33%, fig. 4.10, fig. 4.12 also exhibits extended durations without any strong collapse shock waves, such as that for which source images are provided within the black box of fig. 4.12 (b). The low amplitude (< 400 mV) features that are detected by the swPCD suggest that these shock waves may have originated from satellite cluster collapses.

Finally, fig. 4.13 at an input power of 60% suggests that regular periodic behaviour has been resumed, but with a periodicity of $4T_0$, such that three non-collapsing deflations now occur between each collapse. As with fig. 4.11 at 40%, the final deflation before the collapse of each cycle appears to be the lowest minima of the non-collapsing deflations.

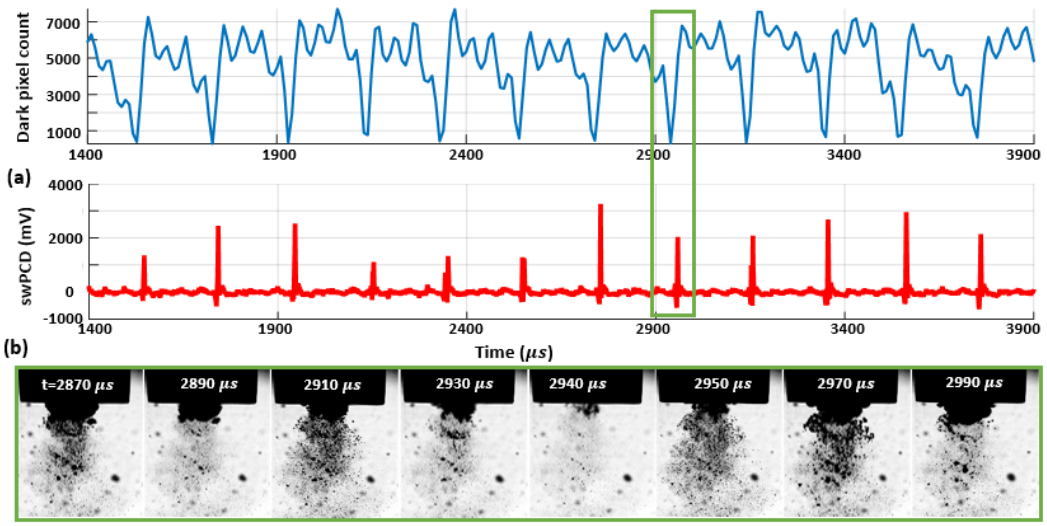

Figure 4.13: (a) Dark-pixel counting and swPCD data over a ~2.5 ms duration of a 2 s sonication at **60%** input power. (b) Representative Photron imaging from within that duration, corresponding to the green box of (a). Scale is provided by the 6.4 mm-Ø tip.

The results in figs 4.8 to 4.13 show sample raw imaging data obtained for cavitation activity from single sonications at each of the selected input powers. To demonstrate the behaviour identified as representative of the cavitation at these powers, 200 ms sections of swPCD data were analysed from data collected over five separate 2 s sonications at these powers, Table 4.1. Specifically, shock wave periodicity was assessed for the 200 ms section, from t = 0 μs (the start of the Shimadzu imaging) approximately 1 s into each sonication, with the number of shock waves at periodicities of mT_0 (for m's between 1 and 6), expressed as a percentage of the total ± the standard deviation across the five data sets collected, at each power. The average value of the shock wave amplitude, $\bar{V}_{SW}$ (mV), across the five sections at each input power, are also given (± the standard deviation). Only shock waves within 5% of the mT_0 timings and of amplitude > 20% of $\bar{V}_{SW}$, were considered to discount shock waves generated by satellite clusters.

Table 4.1. mT_0 periodicity of primary cluster collapse shock waves, as a percentage of the total number of shock waves detected, from the 200 ms sections sampled. Average shock wave amplitude, $\bar{V}_{SW}$, and total duration over which no shock waves were detected, ΣdNSA, are also given, for each of the selected input powers.

Input Power [%]	Tip-vibration [µm]	T_0 [%]	$2T_0$ [%]	$3T_0$ [%]	$4T_0$ [%]	$5T_0$ [%]	$6T_0$ [%]	$\bar{V}_{SW}$ [mV]	ΣdNSA [ms]
20	105 ± 25	2.80 ± 0.90	97.20 ± 0.90	—	—	—	—	410.72 ± 24.15	1.12 ± 0.33
25	130 ± 25	1.15 ± 0.43	98.88 ± 0.43	—	—	—	—	585.07 ± 5.63	0.96 ± 0.31
33	155 ± 25	19.08 ± 1.02	35.38 ± 1.88	41.54 ± 1.60	4.00 ± 2.39	—	—	680.38 ± 19.77	10.95 ± 0.51
40	175 ± 25	0.48 ± 0.55	6.02 ± 2.71	93.70 ± 2.79	—	—	—	1083.40 ± 22.35	4.28 ± 0.79
50	219 ± 25	13.30 ± 3.11	30.86 ± 2.30	16.92 ± 3.93	38.92 ± 1.70	—	—	1108.20 ± 53.00	13.02 ± 2.21
60	265 ± 25	0.08 ± 0.11	3.42 ± 2.18	32.92 ± 2.12	62.98 ± 2.79	—	—	1400.80 ± 44.07	8.52 ± 2.11
70	290 ± 25	5.28 ± 3.58	4.46 ± 2.65	37.80 ± 2.33	45.42 ± 5.45	7.04 ± 2.58	—	1850.79 ± 16.06	12.12 ± 4.09
75	—	9.66 ± 2.25	4.54± 1.37	8.64 ± 1.65	26.4 ± 2.90	50.76 ± 1.70	—	2241.21± 51.24	16.32 ± 0.38
80	325 ± 25	0.38 ± 0.65	1.42± 1.07	14.94 ± 2.53	31.98 ± 3.85	51.28± 1.35	—	2455.35± 36.12	19.39 ± 0.61
85	—	5.70 ± 2.38	2.02 ± 1.34	15.06 ± 1.51	28.94 ± 5.22	47.94 ± 3.59	0.34 ± 0.34	2505.15± 86.12	29.22 ± 2.53
90	390 ± 25	2.70 ± 1.96	1.84 ± 0.86	11.40 ± 1.40	41.18 ± 1.86	41.04 ± 2.07	1.84 ± 0.48	2812.54± 12.12	18.19 ± 1.58
100	435 ± 25	6.12±3.44	2.48±0.74	6.28±1.31	40.38±2.01	29.42±6.41	13.32±3.34	2986.91± 5.41	21.12 ± 1.81

The final column of Table 4.1 contains the summed durations within which no prominent shock waves were detected by the swPCD, representing the intervals of extended non-collapsing deflations identified in figs 4.10 and 4.12, over the five 200 ms sections at each power. This is referred to as the *summed duration of non-shocking activity,* ΣdNSA (*ms*).

To summarise, the dark pixel counting curves of figs 4.8 to 4.13 (b) indicate that all general oscillations (non-deflating collapses and collapses) occur on a 50 µs timescale, in accordance with T_0 of the tip-vibration. Table 4.1 reveals a trend for mT_0, the time between consecutive collapses to increase through integer values, with m = 2, 3, 4, and 5 dominating for input powers of 25, 40, 60, and 80%, respectively. Practically, this manifests as an additional non-collapsing deflation between consecutive collapse phases, as the power is increased from one of these values of the input, to the next. At the intermediate values of 33 and 50%, m is less distinct. Notably, at 33% input power, more collapses occur at T_0, than at 25%. Similarly, more collapses occur at $2T_0$ for 50%, than at 40%. The ΣdNSAs are also significantly longer at these powers, reflecting the swPCD data presented in Figs 4.10 and 4.12.

4.5.3 Cavitation emission noise spectra at selected input powers

The spectra of the swPCD data were obtained using frequency function ('freqz') with Blackman window approximation to reveal the frequency content of the time domain acoustic signal expressed in natural frequency unit (Hertz); see appendix A1 for Matlab code.

In this *results* section, data from the swPCD at the six input powers are presented in spectral form. Song *et al* [45] provide a model for determining the contribution of periodic bubble-collapse shock waves to the noise spectrum of the emission signal, whereby the frequency of shock wave emission, f_{sw} generates spectral peaks at nf_{sw}, for all n. For shock waves emitted at subharmonic values of the fundamental driving frequency, f_0, spectral peaks are therefore raised at nf_0/m. Scattering of the primary field contributes further to the f_0-peak, and nf_0 peaks in the case of nonlinear propagation.

Fig. 4.14 (a-f) provides representative noise spectra of the signal collected by the swPCD, during a sonication at each of the selected input powers in §**4.5.2 Main cluster shock wave periodicity at selected input powers**, for both the 200 ms duration of signal analysed for Table 4.1 and the entire 2 s sonication (insets). The similarity between the 200 ms spectrum and the whole-signal spectrum at each power may be taken as an indication that the 200 ms section is representative of the stable bubble cloud phase of the sonication.

At 20% fig. 4.14 (a), the lowest of the input powers, the spectrum exhibits clear peaks with $m = 2$ at $nf_0/2$, for all n. The spectral model of [45] suggests that the $2T_0$ periodic shock waves generated by the main cluster collapses, fig. 4.6 (a) and Table 4.1, raise these peaks, with additional contributions to nf_0 (with n = 2 within the presented bandwidth), arising from the primary field. Fig. 4.14 (b) is the spectra observed at 25% input power, which is similar to that of 20%; however, the peaks at $f_0/2$ are higher as expected from the SW characteristics of Table 4.1. Specifically, the percentage value of the SWs observed at $2T_0$ is higher at this input power than at 20% input power. The peaks at 20% are broader than that observed at 25% due to the higher number of f_0 contributing to this effect. Equivalently, the $3T_0$ shock waves of fig. 4.8 (a), at 40% input power, raise the clear $nf_0/3$ peaks of fig. 4.14 (d). At the intermediate power of 33%, the periodicity of shock wave emission is less distinct, and accordingly, the spectral peaks are not so well-formed, fig 4.14 (c). The small peaks of several dB at $nf_0/3$ are attributable to the > 40% shock wave emission at $3T_0$, Table 1. We introduce the term *transitional input power* to describe tip-vibrations that generate main-cluster oscillations *transitioning* between subharmonic orders of m.

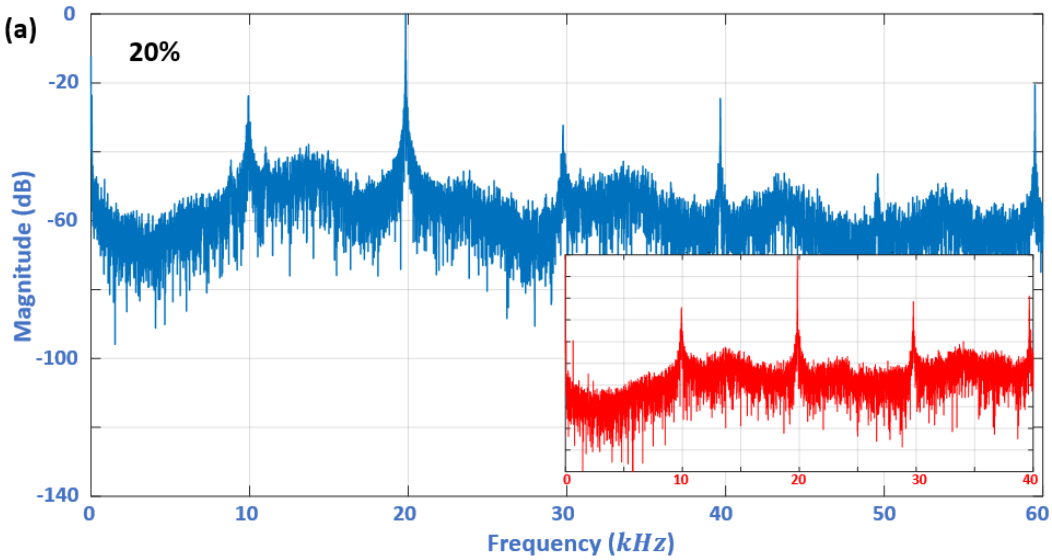

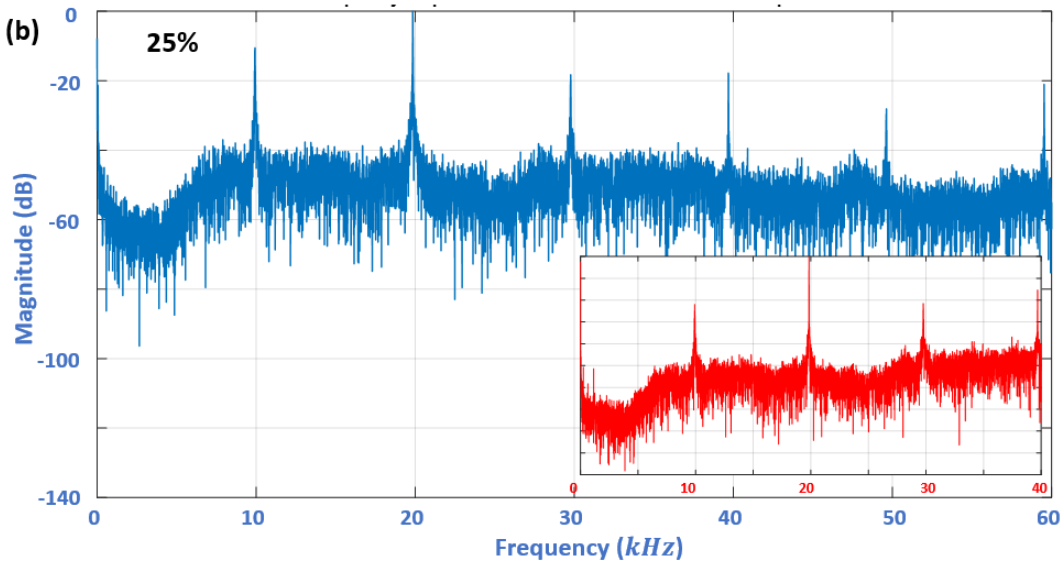
(b)
25%
Magnitude (dB)
0
-20
-60
-100
-140
0
10
20
30
40
50
60
Frequency (kHz)

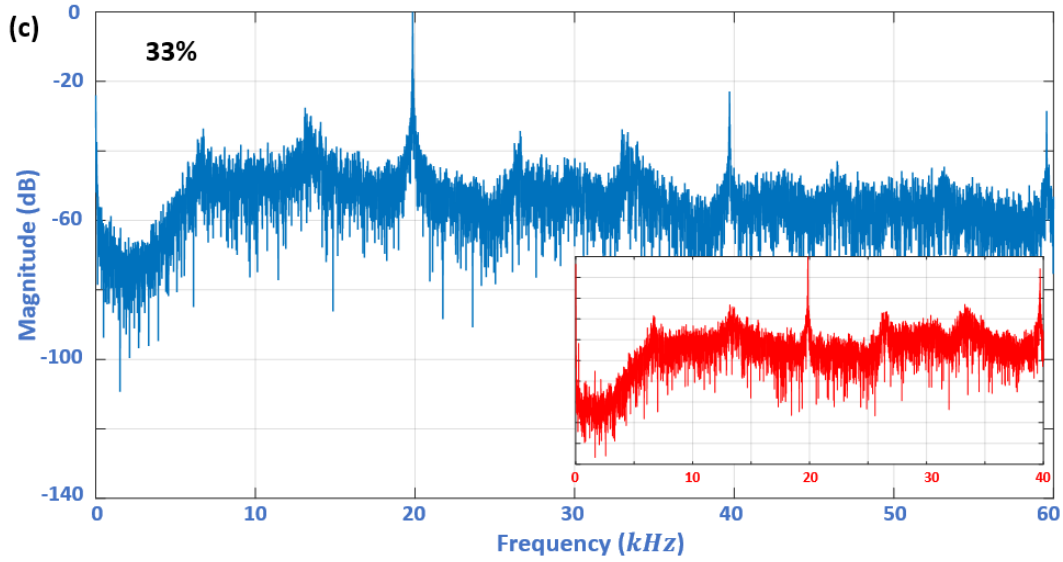
(c)
33%
Magnitude (dB)
0
-20
-60
-100
-140
0
10
20
30
40
50
60
Frequency (kHz)

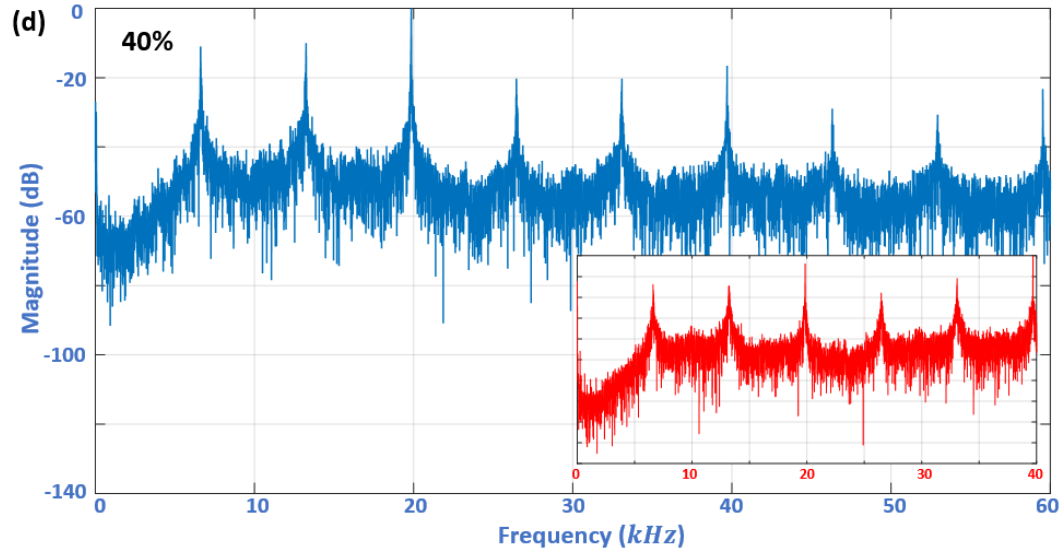
(d)
40%
Magnitude (dB)
0
-20
-60
-100
-140
0
10
20
30
40
50
60
Frequency (kHz)

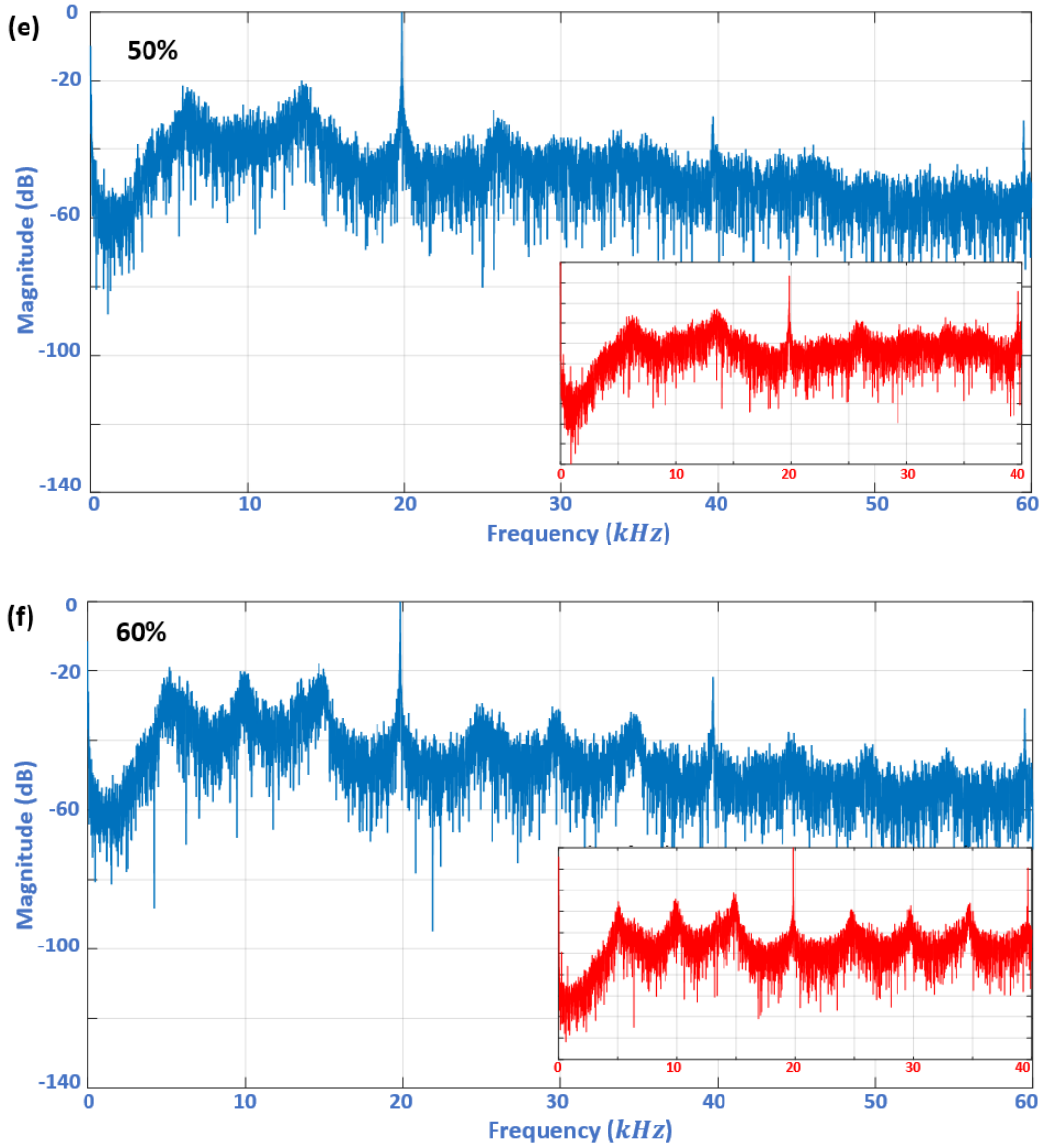

Figure 4.14: Cavitation emission noise spectra for the sampled 200 ms section of the signal, at the selected tip-vibration amplitudes of (a) 20 (b) 25, (c) 33, (d) 40, (e) 50 and (f) 60%. The insets depict the spectrum for the entire 2 s sonication.

This trend repeats for the higher input powers, with *m* transitioning between 3 and 4 at an input power of 50%, and *m* = 4 emerging at 60%, equivalent to the periodicity of $4T_0$, see Table 4.1. It should be noted that at the higher input powers, any given shock wave periodicity appears to be less dominant, even at non-transitioning tip-vibration amplitude. Therefore, the increment in the value of *m* as the input power is increased is due to the contribution of the periodic shockwaves and not a shift in the bubble resonance at higher input power as suggested in [123].

As discussed in §**1.3. Previous research from CavLab**, Song *et al* [126] extended the spectral model of periodic shock waves, [45] to demonstrate experimentally that for contrast agent microbubbles driven to cavitate by focused ultrasound, the spectral floor (over instrumental noise) is determined by variations in the amplitude of the shock waves generated, and the precise timings of shock wave emission. These variations redistribute power that would otherwise be contained within the frequency peaks to broadband components. Figs 4.8-4.13 and Table 4.1 of §**4.5.2 Main cluster shock wave periodicity at selected input powers** reveal the amplitude variance in the detected shock waves is disproportionately higher at the transitional input powers, than those of the non-transitional powers. Moreover, Fig. 4.15 (a-e) represents the general trend for primary cluster collapse shock waves at higher input powers, to consist of a higher number of component shock-fronts, across the full range of powers available (20-100%). Complete image sequences are available in movie format as *Supplemental Materials*. As described previously, §4.5.1, each shock-front is generated by the individual collapse of a sub-cluster within the primary cluster. Larger primary clusters at higher powers will contain more sub-clusters, generating more component shock-fronts.

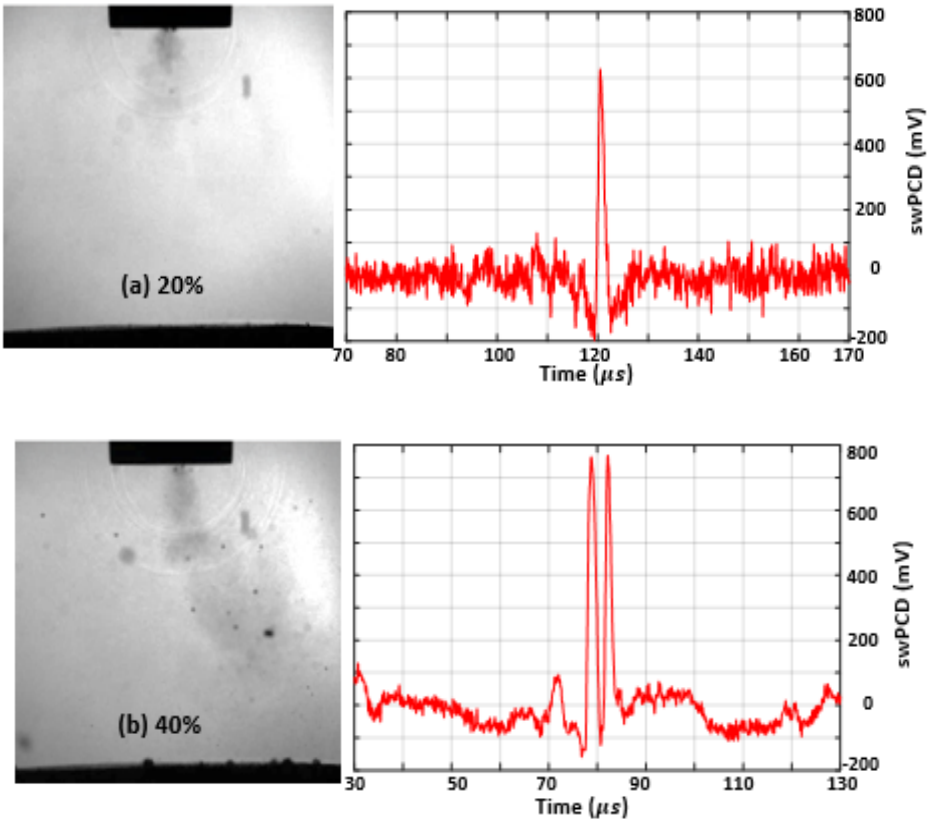

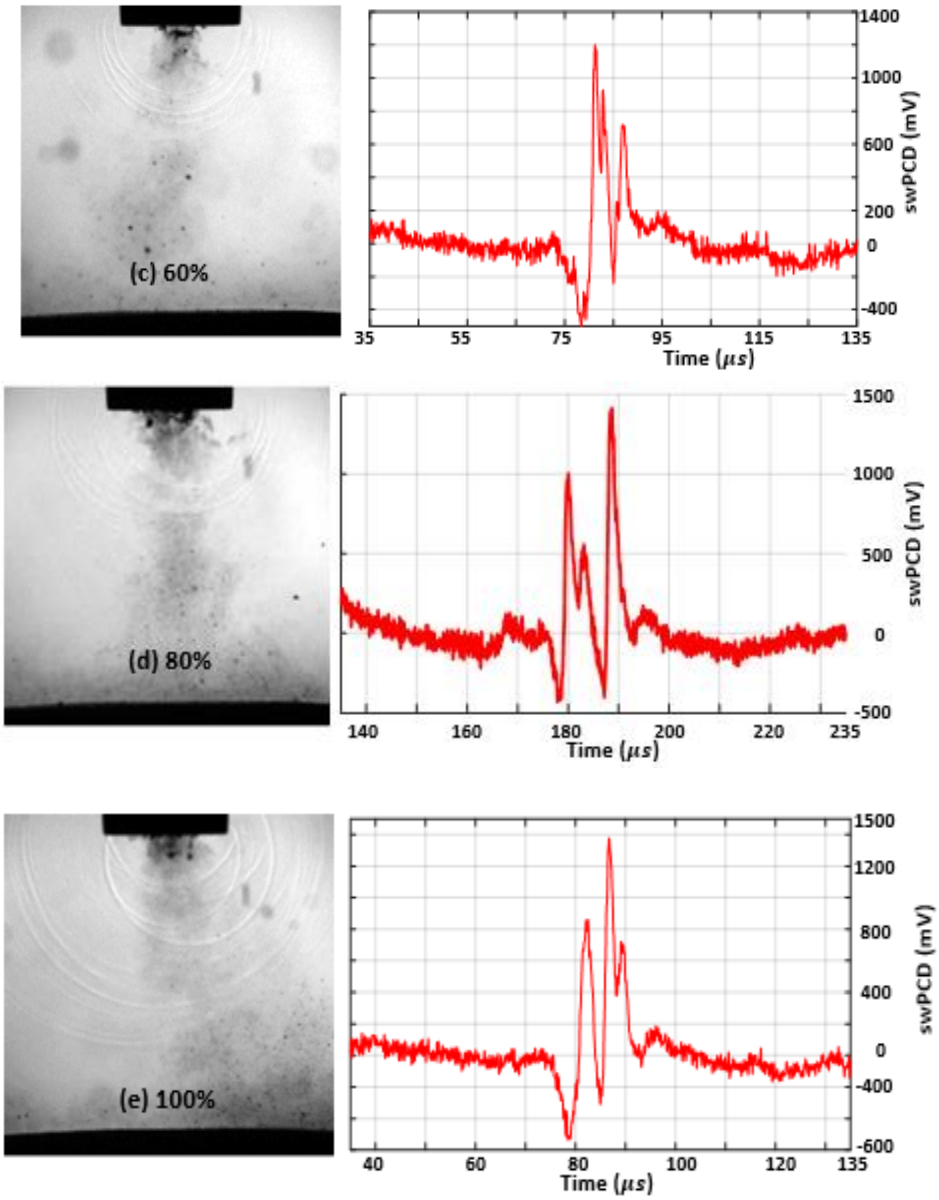

Figure 4.15: Single Shimadzu frames capturing a shock wave generated by a primary cluster collapse at increasing input powers of (a) 20, (b) 40, (c) 60, (d) 80 and (e) 100%, representing the tendency for higher numbers of component shock-fronts at higher powers.

Note that not all shock wavefronts apparent in the high-speed image of fig. 4.15 are resolved by the swPCD in this position due to its temporal limitation and the geometrical focus of the swPCD, as described in *§***4.2.3 Acoustic detection and filtering protocol.** For the noise spectra of the acoustic emission signals, fig. 4.14 (a-f), the increased variance in shock wave amplitudes at the transitional input powers and multi-fronted shock waves generated at higher input powers, will both

contribute to raising the noise floor of the spectrum. These effects are perceptible above the lower threshold apparent for swPCD sensitivity, at 3-4 kHz.

4.5.4 Shock wave content within the emission signal over twenty-five input powers

This final result section presents swPCD data at twenty-five input powers between 20 and 100%. The cavitation emission signals collected for five 2 s sonications were initially considered at input powers of 5% increments. The root mean square of the voltage, V_{rms}, of the filtered acoustic emission at each of the tip-vibration amplitudes was obtained. The mean of V_{rms} from each of the five sonications is taken to quantify the time-averaged shock wave content within the signal. Fig. 4.16 represents the mean V_{rms}, ($\bar{V}_{rms}$), over the five sonications, with error bars representing the standard deviation. Extra data were subsequently collected around 'input powers of interest' in terms of the structure of the plot. Since both the tip-vibration amplitudes of the horn and the sizes of the observed primary bubble clusters increases with the input power, it is expected that the $\bar{V}_{rms}$ should also increase. This is true for this particular sonotrode whose mode of vibration does not change with input power.

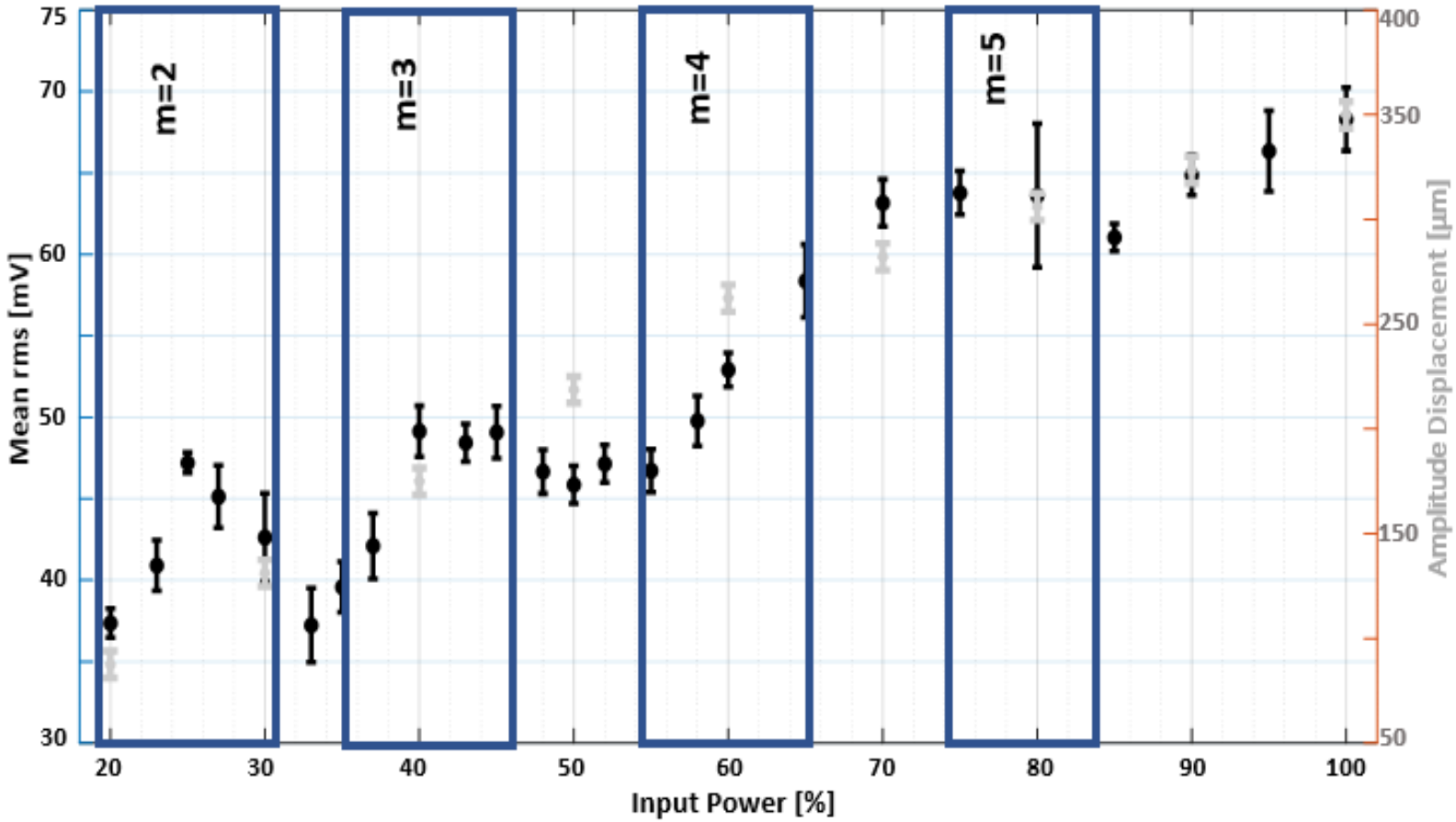

Figure 4.16: The mean V_{rms}, over five 2 s sonications at each input power, of the signal collected by the swPCD, over twenty-five input powers. Error bars represent the standard deviation over the five data sets. The peak-to-peak tip-vibration amplitude, estimated from the Photron imaging data, is also presented, ± 25 µm (the pixel resolution for this imaging perspective).

To remove the possibility that any interpretation of fig. 4.16 may be due to the nonlinear response of the acoustic element driving the tip-vibration or amplification of the vibration through the tapered rod of the horn, values for the tip-displacement amplitude at 10% input power increments are provided (grey data, fig. 4.16), estimated from the Photron imaging, with an accuracy primarily limited by the pixel-resolution of this imaging perspective. It should be noted that a more accurate amplitude measurement of the tip-vibration of the horn can be undertaken with a laser Doppler vibrometer.

Fig. 4.16 reveals local minima in $\bar{V}_{rms}$, at the transitional input powers of 33 and 50%, corresponding to the indistinct values of *m*, or orders of subharmonic collapse, consistent with those identified in §4.5.2 and 4.5.3. The behaviour at higher input powers appears to be indistinct as 70% and 85% input power appear to be transition input values for *m* from 4 to 5 and 5 to 6, respectively. Though the former does not clearly show a dip in $\bar{V}_{rms}$, as observed in the latter. This observation may be due to the data being much noisier because of the higher translatory speed possessed by these bubbles at higher input power. The minima are attributable to extended periods of non-collapsing deflations, ΣdNSA Table 4.1, in comparison to the regular, concerted, and periodic shock waves generated by primary cluster collapses, at the input powers with distinct *m*. Similarly, the value of ΣdNSA observed at 70% input power explained why local minima in $\bar{V}_{rms}$ was not observed at this input power. More so, fig. 4.16 also indicates the different mapped regions for the value of *m* when we apply the 50% criterion on the results in Table 4.1. The 50% criterion is defined as mapping input power to a regime of *m* if and only if the mean percentage value of *m* is greater than or equal to 50%. At input power above 85%, the mean percentage value of m = 6 increases from 0.3% at 85% until it reaches a value of 13.32% at 100% input power.

4.6 Discussion

The results presented indicate that oscillations of the primary cluster at the tip of the ultrasonic horn progresses through orders of subharmonic response, with *m* increasing through integer values as the amplitude of tip-vibration (input power) increases. In practice, this means the cluster undergoes *m* – 1 non-collapsing

deflations between each collapse cycle. The $2T_0$ subharmonic behaviour of the primary cluster at an input power of 20 and 25% (peak-to-peak tip-vibration amplitude of 130 ± 25 µm), figs 4.8(a) and 4.9(a), is generally known as *period-doubling* [127]. This effect is attributed to the inertia of the host liquid preventing bubble structures from inflating to a sufficient size during a tension phase, undergoing full deflation-to-collapse with every compressive phase of the driving. The progression through the Integer values of *m* exhibited by the primary cluster is analogous to that reported for a single cavitation cluster is driven by 220 kHz focused ultrasound, at increasing values of pressure amplitude [58]. Regimes of indistinct *m* at intervening values of pressure amplitude were also reported.

The progression with increased driving, in terms of subharmonic components in the spectrum of the acoustic emission signal, has been recognised for some time [128]. The dual perspective high-speed imaging and acoustic detection configuration described here, in conjunction with the spectral model for periodic shock waves [45], [126], confirms that the subharmonic emission components are mediated via the shock waves generated by the primary cluster collapses at increasing *m* for higher input powers, §**4.5.2 Main cluster shock wave periodicity at selected input powers**. The shadowgraphic imaging component at high temporal resolution was required to characterise the cavitation in the general vicinity of the tip §**4.5.1 Data registration and cavitation characterisation**, particularly to distinguish the shock waves generated by the primary cluster from those emitted by proximal satellite clusters.

As reviewed in *§***4.1. Introduction**, the cavitation at the tip of an ultrasonic horn has received significant research attention. Although many studies have investigated cavitation at different tip-vibration amplitudes, most are limited to a small number of amplitudes or power values. Fig. 4.14, over 25 input power values, is the most comprehensive investigation over the range of powers available for a given horn configuration to date. Crucially, this parameter space is sampled sufficiently to reveal the transitional input powers as *m* switches from 2 to 3 at 33% **(**155 ± 25 µm**)**, and 3 to 4 at 50% **(**219 ± 25 µm**)**, in terms of time-averaged shock wave content in the emission signal, $\bar{V}_{rms}$. The transitioning can then be linked to the cavitation behaviour observed over shorter durations within each sonication, Figs 4.10 and 4.12 of §4.5.2, and the shock wave characteristics of Table 4.1.

Žnidarčič *et al* [122] previously reported on high-speed observations and acoustic detection of tip-cavitation, at a single value of input power, that is reminiscent of what we have observed at the transitional input powers. The authors describe 'irregular cavitation dynamics' with an 'inability to lock to either 3 or 4 acoustic cycles', with the acoustic data revealing durations of reduced amplitude shock wave emissions, of no discernible periodicity. Our results indicate that this study identified transitional cavitation behaviour at just one of the input powers for which it will occur.

A number of other studies have presented acoustic emission data in terms of a measurement representing the intensity or energy detected during a sonication as a function of input power or tip-vibration amplitude. Tzanakis *et al.* [129], reporting on the use of a novel high-temperature 'cavitometer' for measuring cavitation in molten metal, presented V_{rms} from the detection of sonications generated by a 20 kHz sonotrode, with a 15 mm-Ø tip in water. Data was provided for tip-vibration amplitudes from 0 – 45 µm in ~5 µm increments, analogous to fig. 4.16 above, which featured a local minimum at an amplitude of 18 µm, as shown in fig 4.17.

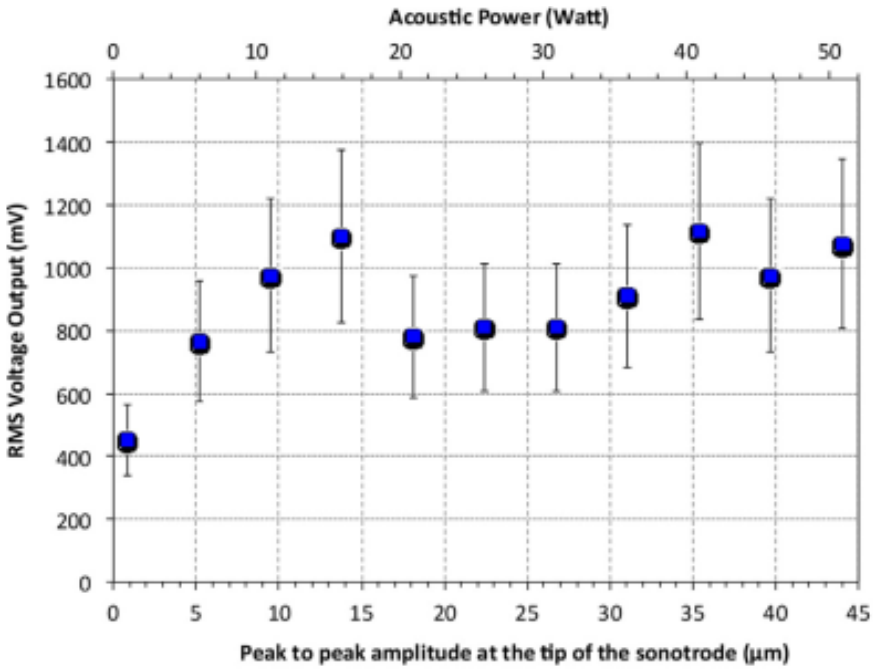

Figure 4.17: Variation of voltage output as a function of sonotrode tip displacement [129]

Hodnett *et al.* [130], using the same Branson Sonifier 450 horn that we have used for this study fig. 4.1, but with a 12.7 mm-Ø tip, measured sonications with a cavitation sensor developed at the National Physical Laboratory (NPL). This sensor, [131], [132] is constructed from 110 µm PVdF film, which also provides the active element of the swPCD, but in a cylindrical geometry such that the tip of the horn can be located centrally within the device. Broadband energy from the spectra of sonications was presented as a function of 'output setting' (equivalent to input power, for this Chapter) in 10% increments, with a local minimum detected only at high amplitude (80%). None at lower amplitudes, as shown in fig 4.18, most likely because the input power was not finely sampled enough. Both reports suggest the reduction in intensity or energy may be due to cavitation shielding (where bubbles located between the source cavitation intended for detection, and the detector, attenuate and scatter the source cavitation emissions) at the particular power/tip-vibration amplitude in question.

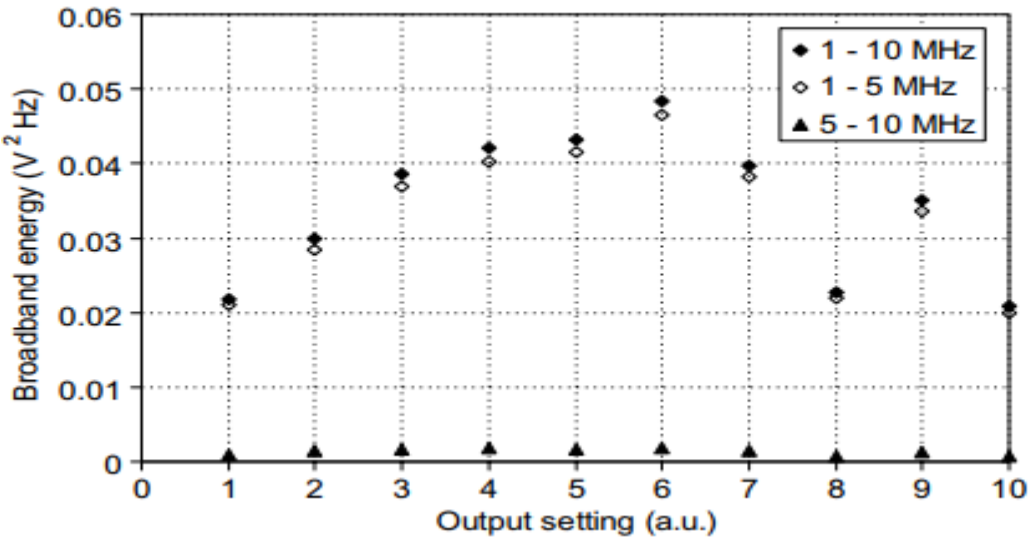

Figure 4.18: The variation of Broadband integrated energy as a function of input setting as obtained using rho-c sensor data evaluated over varying frequency bandwidth. A dip in the broadband energy was observed at input setting of 8 (equivalent to 80%) over the bandwidth of 1-10, and 1-5 MHz. It also shows that most of the energy was measured within the frequency bandwidth of 1-5 MHz, taken from [130].

The results described from the current work suggest that these measurements may have been taken at transitional amplitudes, as an alternative

explanation. Indeed, no perceptible cavitation shielding effects were observed, influencing the shock waves generated by periodic primary cluster collapses. As a further note, full identification of all the transitional input powers associated with any particular ultrasonic horn configuration, would require sampling at sufficiently fine increments of tip-vibration amplitude, across the full range of input powers available. Hodnett *et al* [130], used a sampling increment of 10 % (which is not fine enough) in the input power, which is most likely to detect a single local minimum in their work.

For the diverse range of ultrasonic horn applications, and of acoustic cavitation generally, sonications at transitional input powers may be expected to generate spurious results in terms of application 'yield'. Fig. 4.16 indicates that increasing power to the piezoelectric transducer does not necessarily translate to an increased intensity of cavitation activity, as determined by the level of detectable shock wave content within the emission signal. This may be particularly the case for applications such as sonochemistry, thought to be mediated by the energetic conditions generated during cavitation collapse [133],[134]. Also, in an application where an ultrasonic horn is used to homogenise milk, yoghurt, or ice cream where high pressure is required from ultrasound-induced cavitation bubbles [135], the transitional input power may be avoided for maximum yield.

4.7 Conclusion

The cavitation generated by an ultrasonic horn is investigated as a function of input power, with dual-perspective high-speed imaging and detection of the acoustic emissions. The main cavitation cluster directly underneath the tip, collapses subharmonically at f_0/m, with m increasing through integer values for increasing tip amplitude. Transitional input powers, where m is not well defined, are identified via the V_{rms} of the acoustically detected signal and its spectrum. The transition amplitudes should be avoided for applications such as disruption of biomass, food processing (where physical and chemical change are required), and sonochemistry, where high amplitude shock waves are desired for higher efficiency.

Chapter 5

Application of the ultrasonic horn in the fragmentation of primary intermetallic crystals

Ultrasonic melt treatment (UST) refers to the application of ultrasound (administered with horn-type sources) to a molten alloy of metal like magnesium (Mg), zinc (Zn) and aluminium (Al) alloys for grain refinement. Finer grain structure is well recognised as an essential approach to improving the thermo-mechanical performance (such as strength-to-weight ratio and corrosion resistance) and morphology of many metals and metal-alloys [136]. UST potentially offers both environmentally-friendly and energy-saving alternatives to existing methods [137], reviewed briefly below.

The work described in this chapter was undertaken as part of a collaborative effort with the group of Prof. Iakovos Tzanakis at Oxford Brookes University (OBU) and others at Brunel University, London. They have a long-standing research interest in developing UST of Al-melt, including studies based on X-ray imaging [138], and acoustic cavitation measurements with a high temperature 'cavitometer' probe [139] in real melt systems, and high-speed imaging of primary intermetallic crystals under sonication, in water [140].

This collaboration has resulted in the published article in *Ultrasonics Sonochemistry*, entitled 'In-situ observations and acoustic measurements upon fragmentation of free-floating intermetallic under ultrasonic cavitation in water', currently under review. The manuscript details observations of acoustic streaming and crystal fragmentation in the vicinity of the tip of a horn, at frames rates from $3 \times 10^3 - 1 \times 10^5$ fps, as summarised in §**5.2 Results from OBU**. My contribution is based on a short experimental programme on shadowgraphic imaging at 0.5 Mfps for direct observation of shock wave interaction with free-floating intermetallic crystals. Other results from the paper, originating from the OBU group, are described here for context.

5.1. Introduction

Some industrial sectors, such as aerospace, automotive, and defence, drive demand for materials of higher strength-to-weight ratio and corrosion resistance, which may not be achievable with as-cast metals or an alloy of metals except via post-processing through grain refinement. The grain refinement of Al melt to achieve commercial purified Al could be achieved via inoculation, i.e., treating Al melt with only grain refining master alloys[11] (Al-Ti-B) or (Al-Ti-C) [141] as shown in fig. 5.1.

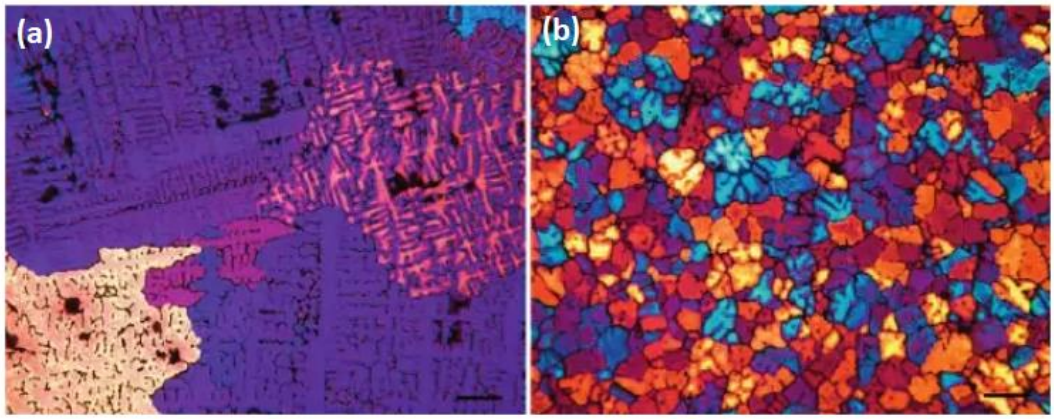

Figure 5.1: The Al alloy 6082: (a) not grain refined (b) grain refined with a 0.005 wt.% addition of an Al–3Ti–1B master alloy and a 0.02 wt.% addition of Ti solute [142].

When the master alloys are added to Al melt, it releases numerous potent particles like TiB_2 and Ti that are dispersed into the melt; less than 1% of TiB_2 nucleates the Al grain [143]. Both forms of Ti are beneficial to realising fine grain size [141]. In general, grain refinement using only master alloys requires the nucleant particles and the solute. The nucleant particles (B) create heterogeneous nucleation sites for the primary solid phase, while the solute element (Ti) moderates and inhibits the growth of grains and assists nucleation [144]. Issues such as the

[11] Grain refining master alloys is a mixture of Titanium (Ti), Aluminium and Boron (B) or Carbon (C) which is used as a chemical method in refining Al for improved mechanical features such as enhanced microstructure, finer equiaxed grain[142].

optimum quantity and type of grain refiner that are required to achieve the desired grain size in a particular alloy, the effect of the rate of adding nucleant particles, the content of solute that is required to achieve desired grain size and morphology in any casting for any alloy grain, and the temperature at which the refiner should be added, are the common problems associated with using grain refining master alloys. These problems have been well researched, with different levels of success achieved. For instance, Easton *et al* [145] study the effect of alloy content on grain size for a fixed particle addition, and the nature and function of the nucleant particles in a grain refiner are well studied [146][147]. UST techniques offer alternative methods, including in combination with master alloy techniques [148]–[150].

UST is the application of ultrasound of sufficient amplitude and at the optimal frequency for a liquid metal (melt) such as Al alloy resulting in the generation of acoustic cavitation, which refines the microstructural grain of the melt for performance enhancement. UST has been found very useful in treating as-cast Al alloys by improving the properties of the alloys through grain refinement, melt degassing, and improved structure uniformity, as seen in fig. 5.2 [136].

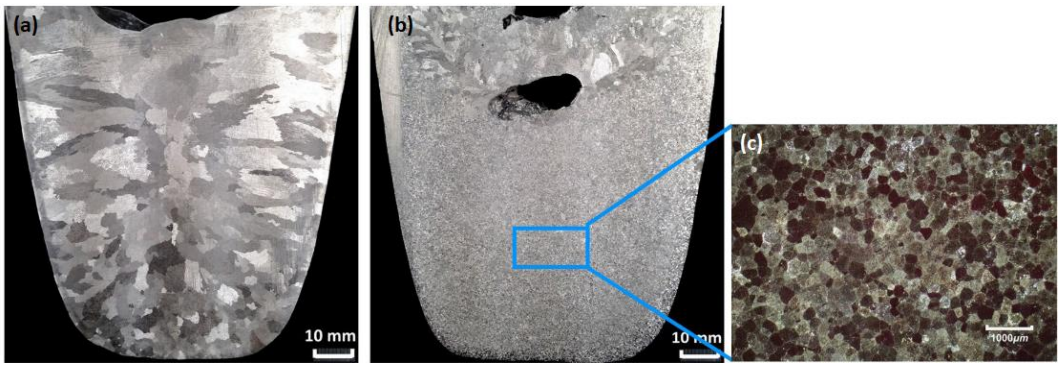

Figure 5.2: Showing macrostructure of the commercial cast purity Al ingots (a) without UST (b) with UST applied from 40 °C above the liquidus temperature for 4 minutes during cooling and solidification; (c) the magnified portion of (b) [136].

The combination of UST with conventional solidification processes like direct-chill casting offers an environmentally friendly and cost-effective process

[151][152]. Despite the advantages offered by this method, the actual mechanism used in the fragmentation of the crystal with UST is still a subject of investigation and in need of verification. Mechanisms such as crystal-ultrasonic horn collision, crystal-wall collision, jetting (where the crystals are very large), acoustic streaming, and shock waves have been suggested as responsible for the sono-fragmentation of the metallic crystal during UST of liquid metal alloys. However, acoustic streaming and shock waves are the two most commonly recognised mechanisms of sono-fragmentation in UST [150]. Cavitation-induced shock waves are believed to fragment the crystal via the tiny crack already present in the crystal during the UST, and the resulting fragmented particles provide more nucleation sites [153]. In contrast, the acoustic streaming distributes nuclei throughout the melt, thereby improving heterogeneous nucleation [154]. Han *et al* [155] investigated the effect of ultrasound on the distribution of solid phases in remelted Al-5Ti-B master alloy, and suggested that cavitation and acoustic streaming speed up the dissolution of the coarse $TiAl_3$ phase, leading to a uniform distribution of Ti solute and TiB_2 particles in the melt. Recently, a number of studies have investigated the sono-fragmentation dynamic of various fixed dendrites and crystals using in-situ synchrotron X-radiography imaging [153][156][157][158][159], including by the OBU group [138][160]. However, it is almost impossible to properly study and capture in real-time the interaction of cavitation bubble dynamic with solid phases in actual melt systems because of its high working temperature, opacity, and temporal and spatial limitations of X-ray imaging.

For this reason, an alternative approach is to create a milder scenario equivalent to the melt where the study of cavitation dynamics interacting with intermetallic crystals can be recorded and resolved in-situ. Water shares almost similar cavitation behaviour, in terms of the acoustic spectrum, with liquid aluminium in addition to the similarity in their transparent nature [78]. Numerous studies [136], [140], [161], [162] have successfully deployed water or other transparent organic solution to monitor the fragmentation process of solid phases. It was suggested that shock waves and oscillating bubble clouds are the primary mechanisms responsible for sono-fragmentation. However, these studies were

based on fixed[12] intermetallic or dendrite, which may not reflect the actual scenarios for UST of real melt. More so, the limitation of X-ray radiography is a concern if floating intermetallic or dendrite fragmentation is to be studied due to its low temporal and spatial limitations.

This research uses water as the host medium to investigate and identify the fragmentation mechanism in the case of free-floating crystals within the dynamic cavitating environment generated by an ultrasonic horn using high-speed cameras.

5.2 Results from OBU

The results presented under this section are those obtained from the OBU research group. They used a high-speed camera at frame rates between 3000 and 1 $\times 10^5$ fps to monitor the sono-fragmentation process of a free-floating intermetallic crystal (Al_3Zr) in water. The approximate dimension of the intermetallic crystal is L: 5.2 mm × H: 4.1 mm × W: 0.06 mm, as seen in fig. 5.3. The ultrasound source is a 200 W piezoelectric ultrasonic horn transducer (Hielscher UP200S) with titanium tapered sonotrode of tip diameter (3 mm-Ø), operating at a frequency of 24 kHz and at a fixed peak-to-peak tip-vibrating amplitude of 210 μm.

[12] A 'fixed' intermetallic crystal experiment is when the sample crystal is fixed at a particular position with respect to the ultrasonic source within the host medium. Many studies have used this method of experiment [153][140] to investigate the mechanisms of fragmentation for intermetallics or dendrites for identifying the fragmentation mechanism, and generally characterising the processes. However, this approach may not fully represent what might be expected in actual melt and thus research findings should be treated with caution.

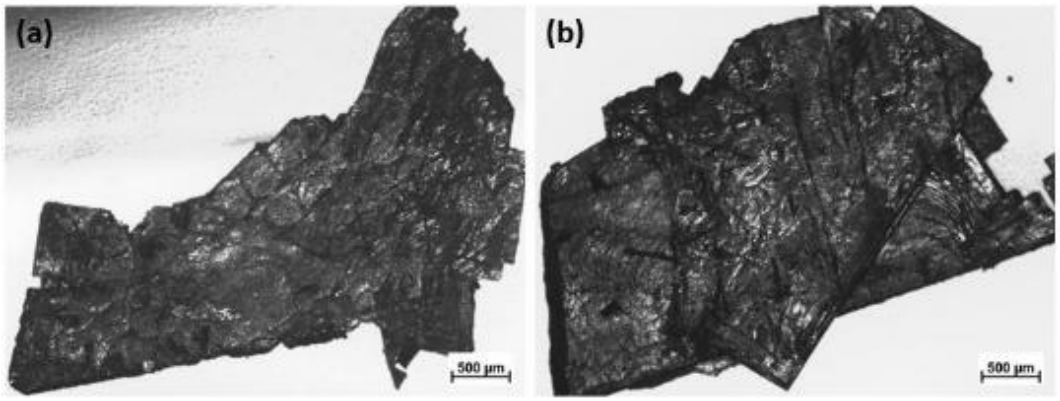

Figure 5.3: Optical micrographs of typical extracted primary Al_3Zr crystals.

5.2.1 Observation of free-floating crystal breakdown capture at 3000 fps

Fig. 5.4 is an observation at 3×10^3 fps and the following keynotes can be made. The floating intermetallic crystal is forced into motion by the induced acoustic flow at the time, t = 0 ms. The big crystal breaks into smaller fragments as soon as it comes into contact with the primary cavitating cluster at a time, t = 36 ms. The crystal fragments are subsequently subjected to the recirculating streaming paths indicated with red and blue arrows in the frame at t = 66.33 ms. One of the fragmented crystals within the green circle comes into contact with the primary bubble cluster at a time, t = 178 ms, where it also breaks, as seen in the inset at t = 181.33 ms. This motion of the fragmented crystals continues and ensures that the crystals recirculate through the cavitation zone (defined as the region below the tip of the horn, up to 11 mm away from the centre of the sonotrode) speeds in the of range 1-2 m/s. Depending on the path taken by the fragmented crystals, the average time for the crystals to return to the cavitation zone was found to be in the range of 17 – 120 ms, which fell within the range reported independently [163]. The OBU group suggests that vortices formed at the sides of the main cavitation flow stream help to restore the fragments back towards the sonotrode tip, also in agreement with previous observations [163], [78]. Therefore, it was suggested that the combination of primary bubble cluster oscillation and collapse could be responsible for the fragmentation of intermetallic crystals.

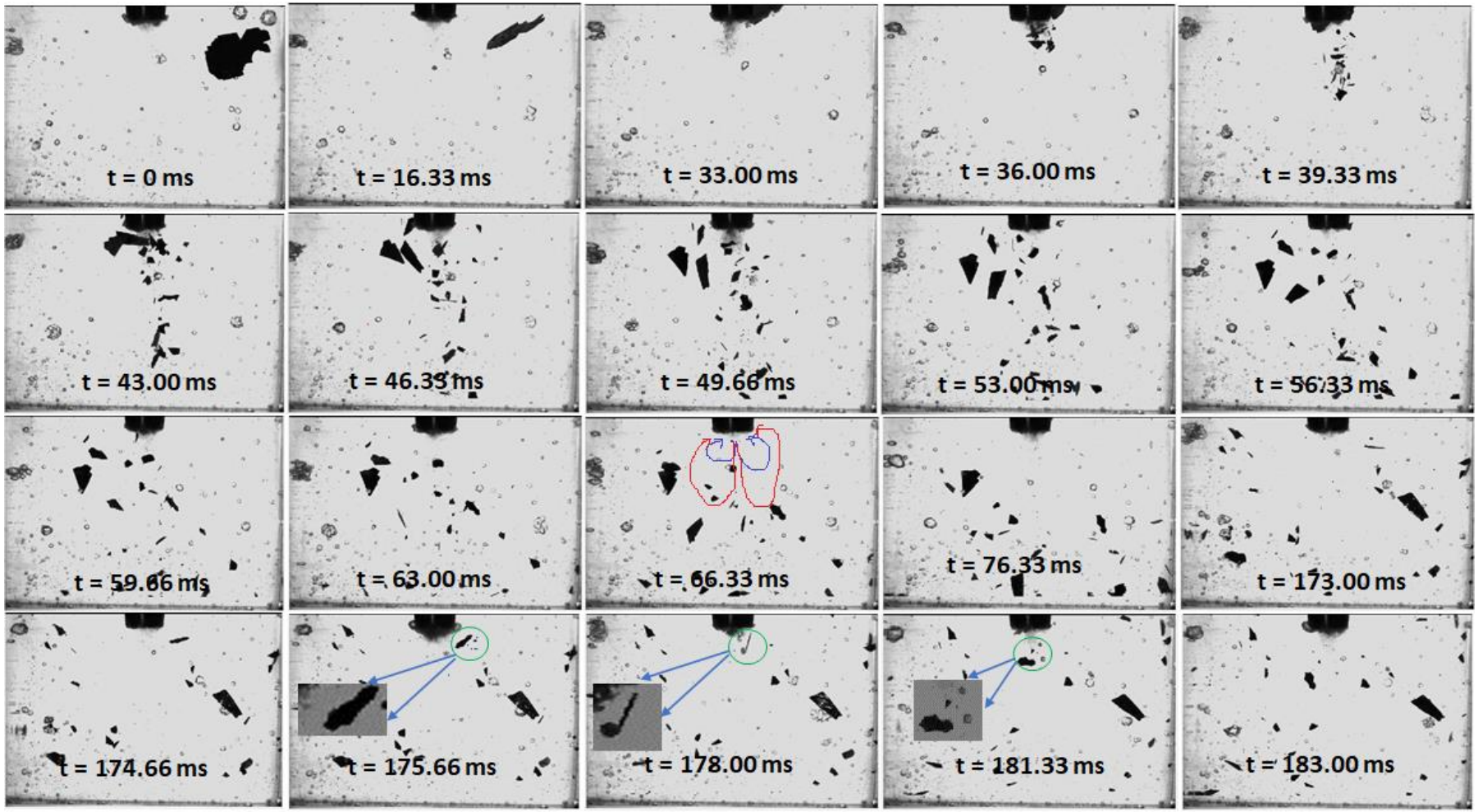

Figure 5.4: Selected frames from Photron high-speed image sequences collected at 3×10^3 fps, for tip-vibration amplitude of 210 μm, showing the break-up mechanism of free-floating primary crystal. Scale is provided by the 3 mm-Ø tip. High-speed imaging data credited to Abhinav Priyadashi at OBU.

5.2.2 Observation of free-floating crystal breakdown capture at 1×10^5 fps

Fig. 5.5 is a sequence of the sono-fragmentation processes of a larger floating intermetallic crystal in water observed at 1×10^5 fps. The crystal approaches the tip of the horn at the time, t = 0 ms. The crystal is seen close to the vibrating tip of the horn at the time, t = 1.2 ms, and the primary bubble cluster is not well developed until t = 2.2 ms, where a large primary cluster is formed. The primary cluster collapses at the time, t = 2.29 ms. The OBU group speculated that the shock waves generated induced the visible opening within the crystal (indicated with green circle). At t = 2.36 ms, the primary cluster is undergoing an inflation phase, visibly growing and in contact with the intermetallic crystal. The primary cluster grew to a maximum size at the time, t = 2.44 ms. The crystal was observed to crack at the time, t = 2.5 ms indicated with the red arrow (inset), and a further widening of the earlier crack (green circle). At the time, t = 2.58 ms, the faint crack now appears more visible, possibly due to the interaction of intermetallic crystal with the oscillating primary bubble cluster. The collapse of the next primary cluster at t = 2.84 ms completes the fragmentation process.

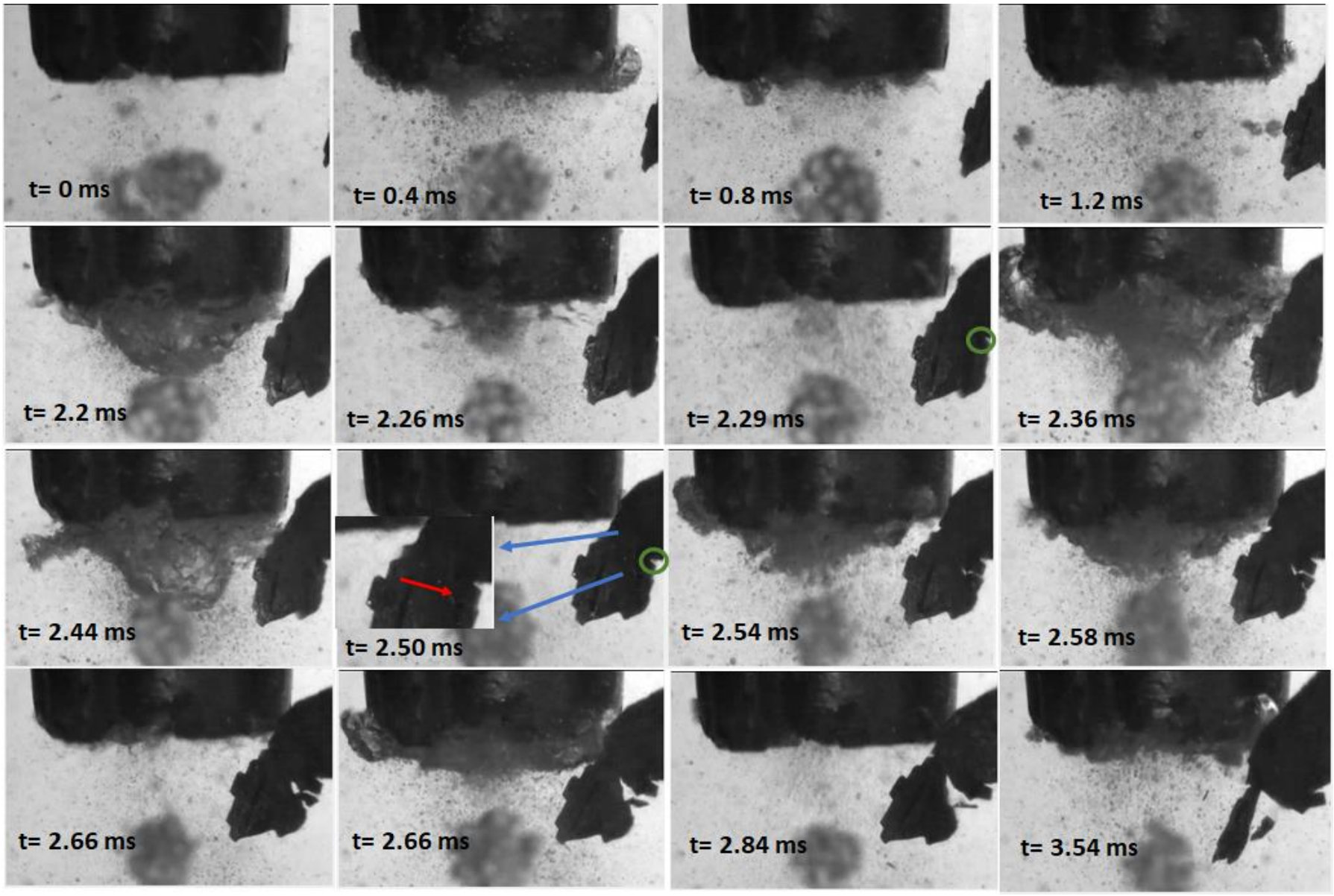
t= 0 ms
t= 0.4 ms
t= 0.8 ms
t= 1.2 ms
t= 2.2 ms
t= 2.26 ms
t= 2.29 ms
t= 2.36 ms
t= 2.44 ms
t= 2.50 ms
t= 2.54 ms
t= 2.58 ms
t= 2.66 ms
t= 2.66 ms
t= 2.84 ms
t= 3.54 ms

Figure 5.5: Selected frames from Photron high-speed image sequences collected at 1×10^5 fps, for tip-vibration amplitude of 210 μm, showing the break-up mechanism of free-floating primary crystal. Scale is provided by the 3 mm-Ø tip. High-speed imaging data credited to Abhinav Priyadashi at OBU.

As the data generated by the OBU group is suggestive of a prominent role for shock waves generated by primary cluster collapse in the sono-fragmentation process, they approached CavLab to conduct complementary experiments, utilising our shadowgraphic imaging capabilities to observe shock wave-intermetallic crystal interaction directly.

5.3 Materials and Methods

5.3.1 Sample preparation

The OBU group prepared the samples and sent them to Glasgow, as shown in fig 5.6, photographed on receipt. For the sake of clarity, a brief explanation of sample preparation at OBU is described.

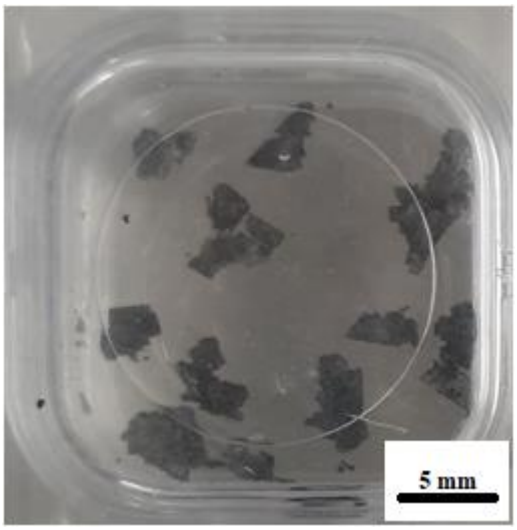

Figure 5.6: Image of intermetallic crystal (Al_3Zr) alloy received at Glasgow.

The sample (Al-3 wt% Zr alloy) was prepared from a pure commercial Al (99.97%) smelted with a master alloy (Al-5 wt% Zr) and cast into 350 g ingot. An electric furnace was used for remelting the ingot and transferred into a graphite crucible (50 mm diameter, 150 mm height) within the furnace where it was allowed to cool slowly to room temperature, with temperature accuracy of about 3 K. Multiples cubes of 5 mm^3 were cut from the solidified ingot using a rotating silicon carbide blade. These cubes were then placed in 15% dilute sodium hydroxide (NaOH) for 24 hours for the cubes to dissolve. After that, primary intermetallic (Al_3Zr) crystals were extracted from the alloy. The solution was filtered to collect the intermetallic crystals, which were then thoroughly rinsed in ethanol and allowed to dry for microscopic observation, as shown in fig. 5.3. The prepared samples are not perfectly solid but consist of pre-existing sub-micro cracks or faults.

5.3.2 The experimental arrangement

The results described below were obtained with the commercial Branson 450 W Digital Sonifier, operating at 20 kHz, described in chapter 4. The experimental arrangement is shown in fig. 5.7. Single input power of 50%, equivalent to peak-to-peak tip-vibration amplitude ~ 219 µm[13] , was used.

A transparent cuvette of dimensions 10 x 10 x 45 mm^3 and whose thickness is 2 mm was ¾ filled with de-ionised water. An extracted primary Al_3Zr crystal was placed at the bottom of the cuvette, and the ultrasonic horn was mounted such that the tip was submerged by 3 ± 1 mm.

[13] It is recognised, from the data of chapter 4, that this is a *transitionary* input power for the CavLab ultrasonic horn. Nonetheless, the OBU group requested that a comparable tip-vibration amplitude was employed, for consistency with the data generated at OBU, §5.2, despite the different tip diameter.

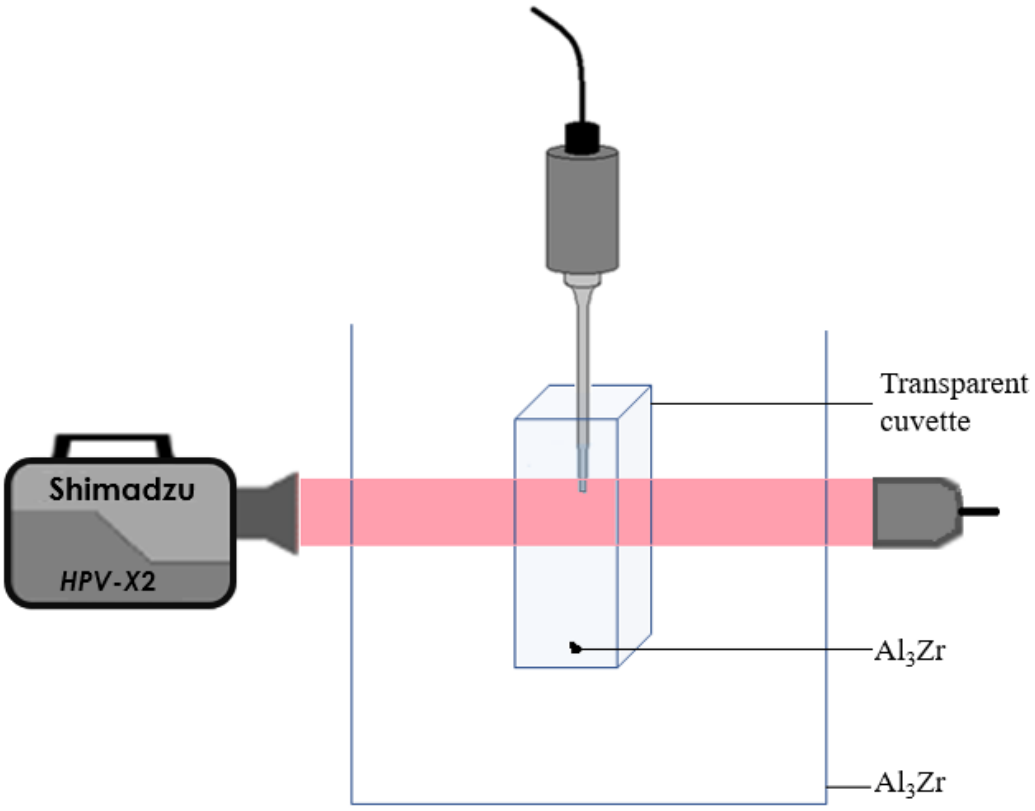

Figure 5.7: Schematic representation of the experimental arrangement.

The cuvette was placed in the customised tank described in chapter 4 (measuring $420 \times 438 \times 220$ mm^3), which was ¾ filled with de-ionised water. This arrangement maintained the temperature of the host medium (water in the cuvette) at room temperature condition during sonication. Three 1 s sonications were applied to each crystal, with HSI at the parameters described below, manually triggered once the sonication was initiated. Further sonications, after the initial three, did not produce any verifiable sono-fragmentation observations, as fragments were typically sub-millimetre by this stage.

5.3.2.1 High-speed imaging

The in-situ fragmentation of the free-floating intermetallic crystals during sonication was captured using Shimadzu HPV-X2 (Shimadzu, Kyoto Japan), imaged at a temporal resolution of 0.5 Mfps, but over a duration of 512 µs. This was deemed an acceptable compromise between sampling enough sonication to

opportunistically capture a sono-fragmentation event yet achieve a temporal resolution that would meaningfully contribute to the OBU work at lower frame rates (and without direct shock wave imaging). Time t = 0 μs for the HSI data presented below is arbitrarily defined as the start of the imaging, with the 1s sonication described above. A spatial resolution of 55 μmpixel^{-1} was achieved over 400 × 250 pixels through a macro-lens (Milvus 100 mm f/2M, Zeiss, Oberkochen, Germany). Illumination was provided via synchronous 10 ns laser pulses at 640 nm (CAVILUX Smart, Cavitar, Tampere Finland), coupled to a liquid light guide and a collimating lens. The shadowgraphic imaging capability was used to observe the interaction of shock waves with intermetallic crystals.

5.4 Results

5.4.1 Observation of free-floating crystal breakdown using Shimadzu

Figs 5.8 and 5.9 are representative of shadowgraphic HSI sequences captured opportunistically, revealing distinct sono-fragmentation processes – or parts of the process – within the limited imaging duration for the configuration described.

The sequence of fig. 5.8 was captured during the first sonication of one of the original crystals delivered from OBU, fig. 5.6. The crystal, arrowed red at time t = 0 μs and not fully within the FOV, is likely rising from the bottom of the cuvette for the first time, under the streaming action of the sonication. Two multi-fronted shock waves, with a $3T_0$ interval, due to primary cluster collapse are captured at 40 and 194 μs, respectively. Neither of these outwardly appear to have an observable effect on the intermetallic crystal. Following the generation of a third shock wave, captured at 284 μs, a dent-like structure begins to emerge, which appears to enlarge on the propagation of a fourth shock wave at 358 μs, arrowed red at 400 μs. The features of this sequence are reconcilable to those captured around 2.50 ms, in fig. 5.5 of the OBU data, and likely capture the initial crack formation of the sono-fragmentation of this original crystal.

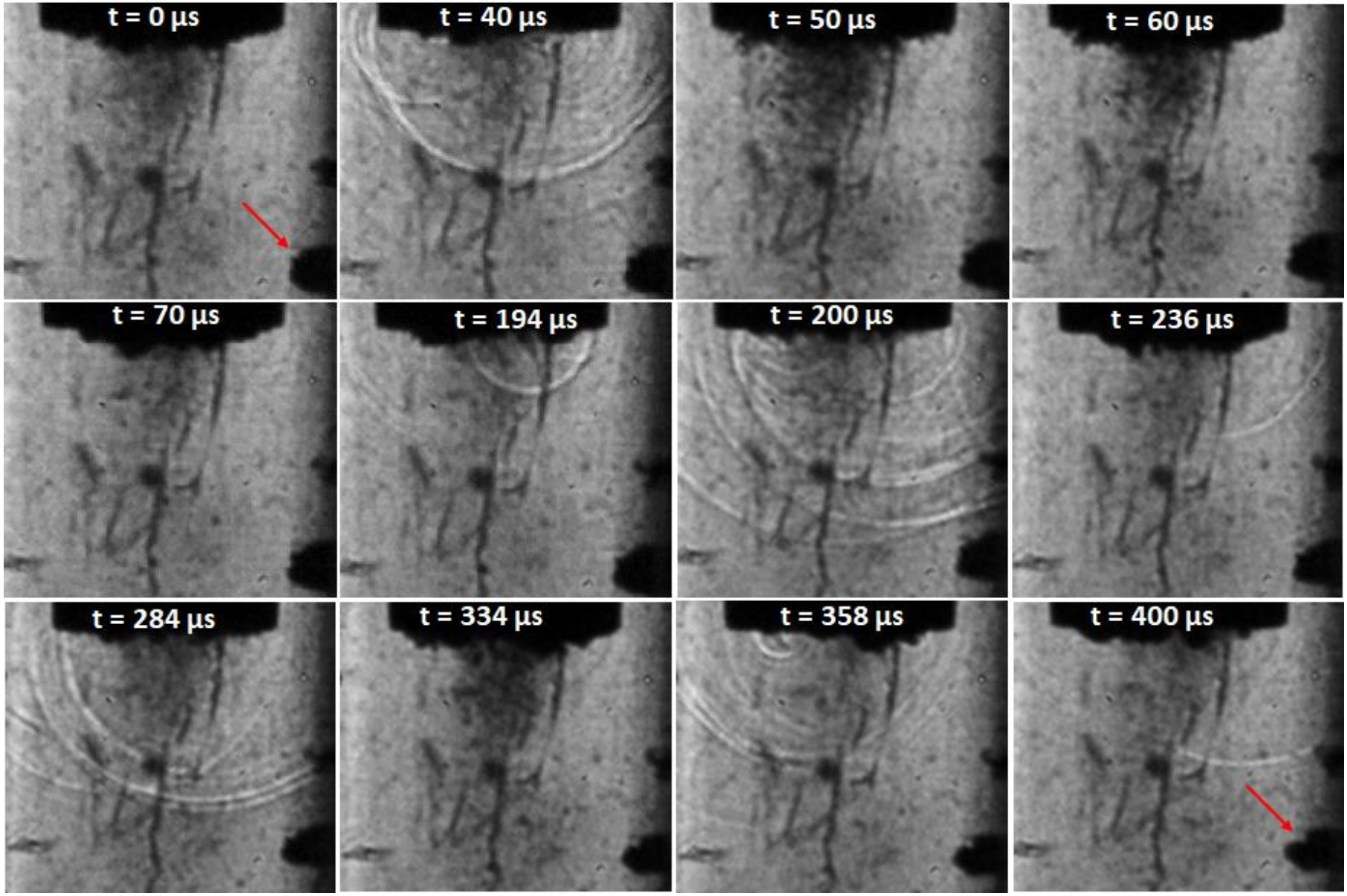
t = 0 µs
t = 40 µs
t = 50 µs
t = 60 µs
t = 70 µs
t = 194 µs
t = 200 µs
t = 236 µs
t = 284 µs
t = 334 µs
t = 358 µs
t = 400 µs

Figure 5.8: Selected frames from a Shimadzu high-speed image sequence captured at 0.5 Mfps, during a sonication with a tip-vibration amplitude of 219 μm, showing crack inception within an original, free-floating intermetallic crystal. Scale is provided by the 6.4 mm-Ø horn's tip.

Fig 5.9 represents the HSI sequence captured during the third 1s sonication of another original crystal. The sono-fragmentation of the previous sonications is evident through the reduced size of the crystal fragments within the FOV, compared to the original crystal in the first sonication sequence of fig. 5.8. Two larger fragments are identified as A and B at t = 0 μs and circled red and arrowed blue throughout, respectively. Fragment A appears to be in contact with the primary bubble cluster during an inflation phase at t = 0 μs. Following deflation, 60 μs, collapse and shock wave generation at 80 μs, further fragmentation of crystal A is apparent, exacerbated by further shock waves generated at 188 μs, before disintegration into multiple sub-fragments, as highlighted by the inset at 386 μs.

Crystal fragment B is located ~ 5 mm from the tip, does not make direct contact with the primary cluster throughout the duration of the HSI sequence, and exhibits a somewhat distinct sono-fragmentation process to that of fragment A. Crystal fragment B appears to be intact for the first 80 μs of the HSI sequence. At 82 μs, a multi-fronted shock wave is generated by a primary cluster collapse. This may initiate a crack in the fragment that is 'gradually' revealed over the following ~100 μs. By 186 μs, it is evident that the crystal has broken into two, approximately equal-sized sub-fragments, which become separated within the FOV at 260 μs.

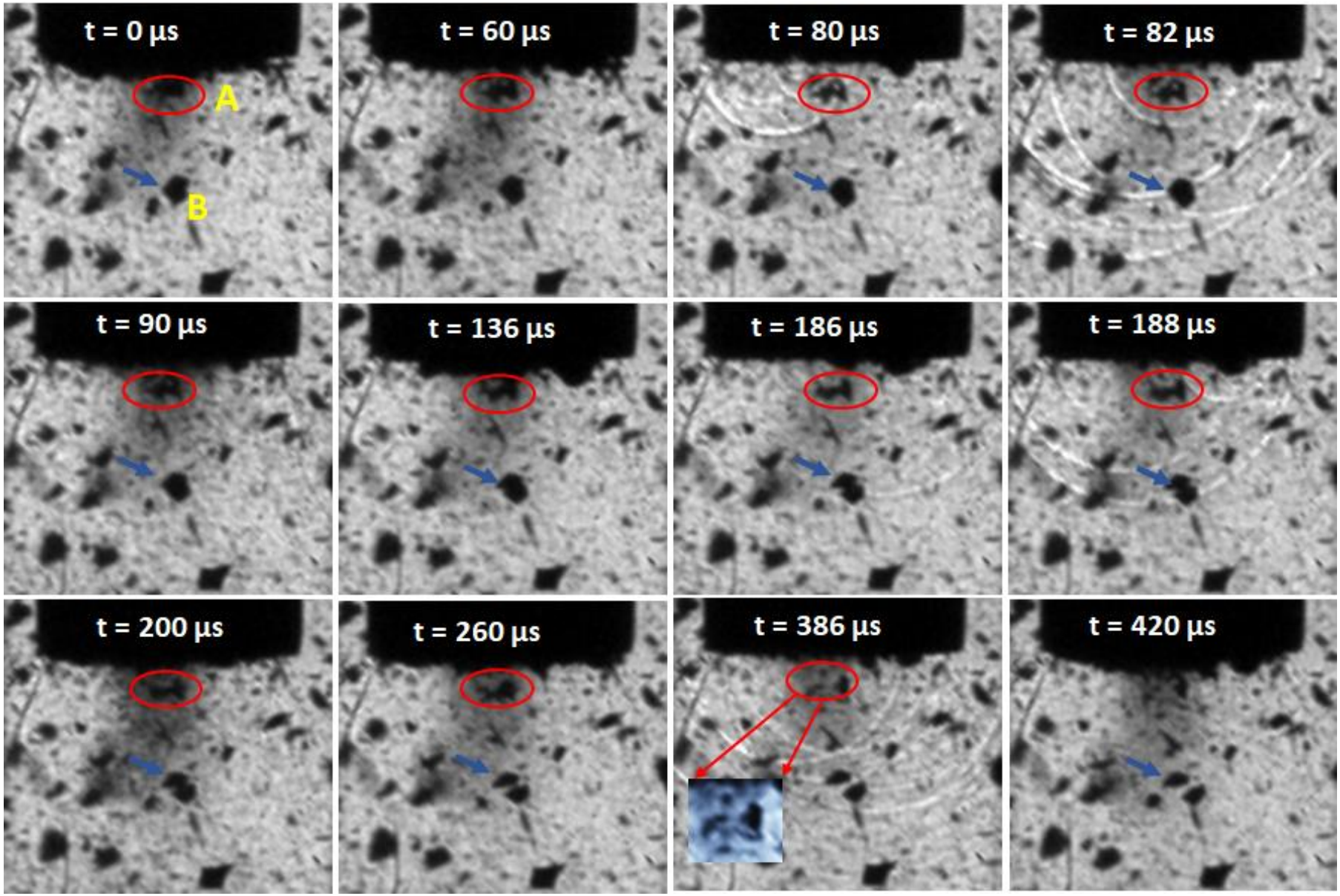
t = 0 µs
A
B
t = 60 µs
t = 80 µs
t = 82 µs
t = 90 µs
t = 136 µs
t = 186 µs
t = 188 µs
t = 200 µs
t = 260 µs
t = 386 µs
t = 420 µs

Figure 5.9: Selected frames from a Shimadzu high-speed image sequence captured at 0.5 Mfps, with a tip-vibration amplitude at 219 μm, showing crystals fragmented through previous sonications. Fragments A and B exhibit distinctive continued sono-fragmentation processes, distinguished by their proximity to the tip, interaction with the primary cluster and the shock waves generated on collapse. Scale is provided by the 6.4 mm-Ø tip.

5.5 Discussion

The OBU data at lower frame rates and over the extended imaging durations indicate the role of acoustic streaming in the recirculation of the intermetallic crystals through the 'cavitation zone' generated by the vibrating tip of their ultrasonic horn. The vortex flows bring the intermetallic crystals back to the cavitation zone for repeated sono-fragmentation treatment, consistent with observations previously reported [78] [137].

Fig. 5.5 from OBU captures sono-fragmentation of an original crystal, which is complementary to data generated at CavLab, Glasgow, capturing crack inception in an original crystal, as the initiation of the first sono-fragmentation process, with shock waves generated by primary cluster collapse revealed via the shadowgraphic imaging capability capture sono-fragmentation. The interaction of the oscillating primary bubble cluster with the crystal may also contribute to the breaking of the crystal by causing inherent fatigue or possible delamination through wetting [136][150]. However, research from [164][165] rules out the possibility of fragmentation due to bubble-crystal, horn-crystal, and crystal-crystal interactions. Their claims were based on a different experimental condition which is not like this present scenario. From fig. 5.8, it was observed that the inception of the fragmentation process was due to the repeated interaction of the crystal with the propagating shock waves. The direction of the propagating shock waves with respect to the crystal also plays a significant role in its impact on the cracking response of the intermetallic crystal. The intermetallic crystal in fig. 5.8 has shown the response of deformation/fragmentation that would possibly occur after more shock waves-crystal interaction. More so, the pre-existing micro-crack in the intermetallic crystal may contribute to its fragmentation response. From fig. 5.9, a strong fragmentation (breaks up to 3 fragments) of the intermetallic crystal A, closer

to the oscillating primary cluster, was observed, which repeated interaction of the crystal with the high-amplitude shock waves, close to the location of bubble collapse beneath the tip of the horn. Wang *et al* [153] also indicate that the combination of high acoustic flow and the collapse of the primary bubble cluster is very efficient in breaking up Zn alloy, both in solidifying phases and liquid-solid interface during the melt treatment. It seems highly likely that crystal fragments exposed to periodic shock waves generated by repeated primary cluster collapse throughout a sonication contribute to 'preparing' each crystal fragment for a further sono-fragmentation event, as captured for crystal B, in fig. 5.9. This is the subject of an ongoing modelling effort at OBU, based on intermetallic crystal structure and properties, incorporating the shadowgraphic imaging data generated in Glasgow.

5.6 Conclusion

This collaborative research studied the fragmentation mechanisms for a free-floating intermetallic crystal during UST with an ultrasonic horn in a water environment. Shadowgraphic HSI captures the interaction of the floating intermetallic crystal with propagating shock waves generated by primary cluster collapse, allowing the contribution to the sono-fragmentation process to be assessed. For the applicability of this contribution to real Al-melt, the observations of streaming-based flow in recirculating crystal fragments through the cavitating region in proximity of the horn-tip in real Al-melts requires further study. Nonetheless, these preliminary observations highlight the prominent role that propagating shock waves and the primary cluster collapses that generate them can have in industrial applications of cavitation. A thorough assessment of the ultrasonic source, the cavitation it generates, and the cavitation-mediated effect mechanisms are required for an application's efficient and effective development.

Chapter 6

Investigating the acoustic cavitation generated between the tips of two ultrasonic horns

Upscaling ultrasonic procedures for industrial application will almost certainly require a configuration involving more than one transducer [166]–[168]. In some cases, two or more transducers may be used at different operating frequencies to improve the efficiency of a sonochemical process, especially in the cleaning process where high and low-frequency transducers are operated together for effective cleaning [169]. In addition, multiple transducers in an ultrasonic bath may result in a uniform distribution of cavitation activity [22]. Whilst it is reasonable to assume in an ideal situation that an ultrasound-mediated effect should scale linearly with the number of transducers employed, there should be scope for considering transducer configurations that are more effective or efficient in terms of the yield for at a given total input power. It would also seem reasonable to speculate that the 'amount' of cavitation generated will be relevant to the ultrasonically mediated effect. These assumptions may not hold if the physical properties of the host change with a slight rise in temperature during sonication.

This chapter investigates the cavitation activity generated between the tips of two ultrasonic horn$_S$[14], for comparison to that generated by a single horn, described in Chapter 4. The hypothesis underpinning the work is that for two-horn sonications, where the tip-vibrations are in phase such that both tips approach a central point and retract from it simultaneously, an enhanced cavitation effect may be generated. Specifically, if both tips are retracting at the same time, the liquid between the tips should be subject to a greater tension than in the case of a single tip, and perhaps the resulting cavitation may be at a 'higher level' than the cavitation generated by two horns, operating independently, or sufficiently spaced that there is no interaction between the two.

[14] I wish to thank Dr. Andrew Feeney for the provision of the second ultrasonic horn (horn$_S$) used in this work.

6.1. Introduction

To the best of our knowledge, there are no reports investigating possible enhanced cavitation effects from combined sonications of two or more ultrasonic horns, specifically, in the literature. However, there are published reports that have considered the use of multiple sources of transducers for cavitation enhanced improvement. For instance, Asekura *et al* [166], developed a large sonoreactor measuring 508 x 508 x 672 mm^3 fitted with two units of transducers, each unit consisting of 6 PZT transducers, operating at a frequency of 500 kHz for oxidation of aqueous potassium iodide (KI) to iodine (I_2). The total electrical power applied to these transducer units is changed from 0 to 600 W. The two units of transducers were configured in two ways: at the bottom of the reactor and placed on opposite sides. The sonochemical luminescence from the 12 PZT transducers reveals their sonochemical reaction fields were independent of each other because of the high directivity of ultrasound propagated at 500 kHz. Also, a higher production rate of I_2 was achieved when the two transducer units faced each other, which the authors attributed to the standing wave phenomenon. Hodnett *et al* [170], characterised the acoustic cavitation generated from 30 transducers operating at 25 kHz fitted in a bespoke 1.8 kW, 25 L cylindrical vessel. The transducers, each 50 mm in diameter, were epoxy-bonded to the vessel wall arranged in three horizontal rows of 10 transducer units, with the middle row positioned at 'half the height' of the cylindrical part of the vessel. With this arrangement, the acoustic radiation is directed to the centre volume. The acoustic emission was collected with a hydrophone (Bruel and Kjær type 8103) fixed at the centre of the vessel. The analysis of rms value of the voltage output from the hydrophone during both line and X-Y raster scans showed a reasonable agreement; the rms voltage was observed to increase with the increasing input power to the vessel, though not linearly. The rms voltage increased by a factor of 3 when the input power is increased from 20 W to 100 W, and a factor of 1.7 when the power is increased from 100 W to 500 W. The authors attributed this nonlinearity behaviour to two reasons; first, as the input power is increased, greater fractions of the applied energy are transferred into higher frequency components in the spectrum outside the acquisition band of the hydrophone used. The second, at higher input power levels, the shielding effect of the cavitating bubbles limits the transmission of the ultrasound from the transducer

to locations beyond a few centimetres away. It should be noted that the cylindrical vessel approach is different from having multiple separate transducers operating together. The former operates via bulk cylindrical modes rather than from the summation of the sources.

A detailed characterisation of the cavitation generated from a single ultrasonic horn was presented in chapter 4, where the dependence of time average shock wave content ($\bar{V}_{rms}$**)** of swPCD output on the tip-vibration amplitude of the ultrasonic horn was established. We, therefore, seek to investigate the behaviour of the cavitating bubbles generated from two ultrasonic horns that are operated simultaneously at a number of tip-separation distances. The two ultrasonic horns are the Branson Digital Sonifier 450 as described in §**4.1. Introduction** (hereafter referred to as horn$_B$), and a Sonic Ultrasonic Processor 500, Sonics & Materials Inc. (hereafter referred to as horn$_S$)[1], shown in fig. 6.1. As with horn$_B$, horn$_S$ has a nominal operating frequency of 20 kHz, with a power rating of 500 W. A 6.4 mm-Ø tapered Ti tip is attached to horn$_s$, matching that of horn$_B$.

Figure 6.1: The Sonic 500 ultrasonic processor system comprises the control console for setting the input protocol, the converter housing, and the 6.4 mm-Ø Ti tip.

The experiment and data described in this chapter are in many ways directly comparable to those described in Chapter 4 – the Branson 450 Digital Sonifier with the same tip diameter (6.4 mm-Ø) as horn$_S$, the same high-speed camera with similar imaging parameters is used, and the swPCD provides acoustic detection; however, there are some important differences, that should be emphasised. To accommodate the same volume of liquid with the tips of two ultrasonic horns, the swPCD is orientated orthogonally to both horns' axis, as depicted in fig. 6.3, rather than along the axis of the single horn, as shown in fig. 4.3 of Chapter 4. However, the acoustic data should still be comparable to a first approximation, as the shock waves propagate radially from the cavitation collapse, as seen in fig. 4.15 of Chapter 4. Indeed, any shielding effects from satellite clusters or the cloud of smaller bubbles extending beneath the horn tip, §**4.5.1 Data registration and cavitation characterisation**, may be reduced when acoustic detection is undertaken from the orthogonal direction. The proximity of a second horn-tip also introduces a surface

closer to the cavitation activity generated by the other horn, than the front-face of the swPCD in the single horn experiment [171]. This may also have an influence on the cavitation activity itself, even when the second horn is not operating.

The chapter is structured as follows: the two-horn experiment is described in §**6.2**, with §**6.3** describing the rationale behind parameter selection. The results sections of §**6.4** present a characterisation of both horns operating individually in the two-horn configuration, in terms of the order of subharmonic emissions, and observations taken with the horns operating simultaneously. §**6.5** offers a discussion of the results, with §**6.6** concluding the chapter.

6.2 Materials and Methods

6.2.1 The experimental arrangement

The results described here are obtained with $horn_B$ and $horn_S$, both with a nominal operating frequency of 20 kHz, and fitted with 6.4 mm-Ø Ti tips. The input power for both horns is entered as a percentage value at the control console, and sonication is initiated manually. The maximum input power that can be entered from the control console of $horn_S$ is 40%, whereas it is 100% for $horn_B$ as described §4.2.1 The experimental arrangement. As stated previously, the general hypothesis motivating this work is that the two tips, vibrating in phase, may generate enhanced cavitation. Since neither horn accepts a trigger pulse, the two horn sonications were repeated until observations with the required relative phases of vibration were obtained.

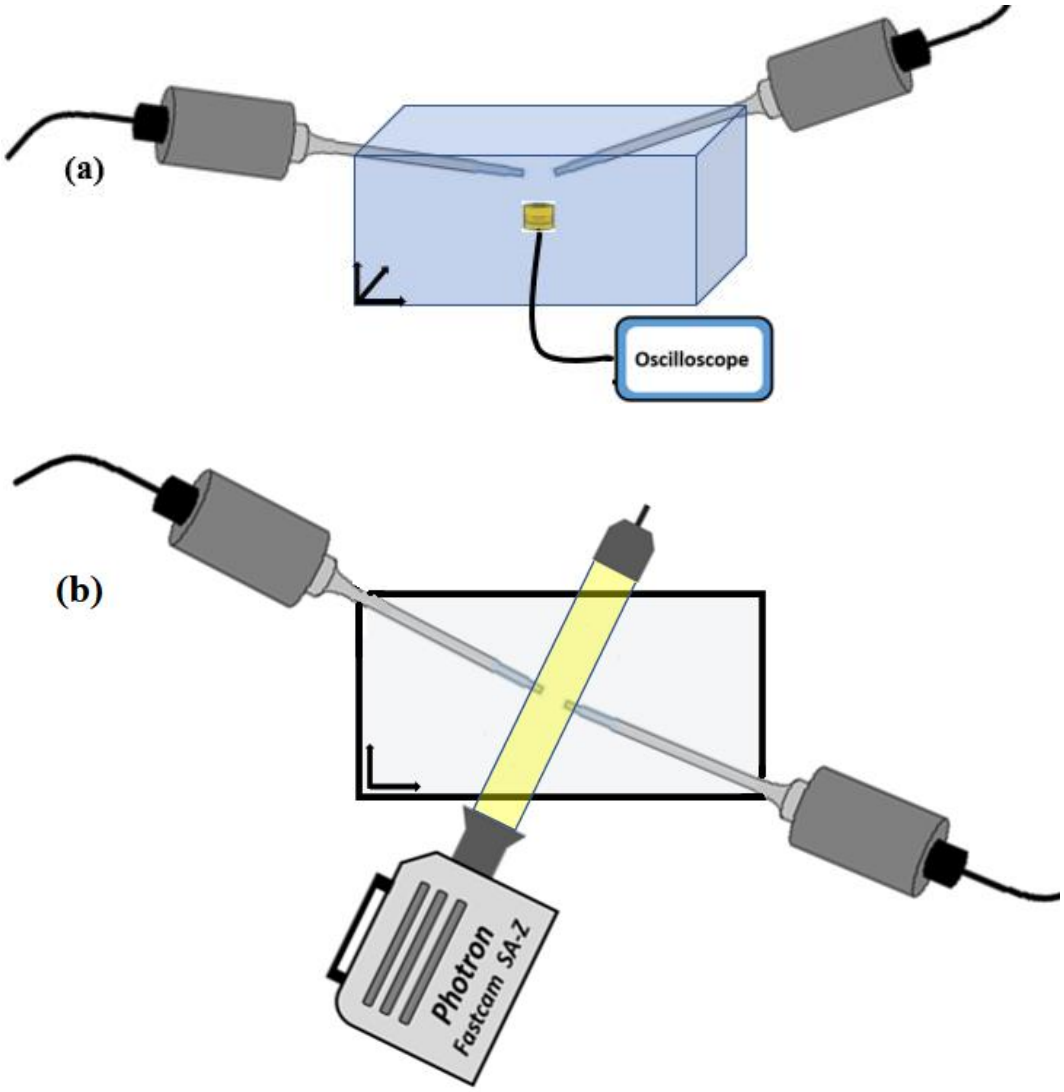

Figure 6.2: Schematic representations of the experimental arrangement (a) the ultrasonic horns and swPCD. (b) top-down view of the high-speed imaging configuration.

The two horns were mounted within a Perspex tank measuring 360 × 200 × 200 mm^3, filled with de-ionised water, such that the tips were submerged approximately 30 mm below the surface. The swPCD was placed at a vertical distance of ~ 20 mm below the centre point between the horn tips. The experiment is set up as shown in fig. 6.2, with the separation between the horn tips taken from the centre of the tip surfaces. The tip separation distance is limited to 7.5 mm (i.e., a wavelength for a sound wave propagating in water), recognising that the cavitation activity from an ultrasonic horn is localised to the tip. Other reports of

ultrasonic horn cavitation also note that the field decays strongly with distance from the tip, reaching nearly zero at 2-5 cm away from the tip of the horn [172], [173].

6.2.2 High-speed imaging and acoustic data acquisition

High-speed imaging of the cavitation between the tips was undertaken with the FASTCAM SA-Z 2100 K (Photron, Bucks UK) camera set such that an adequate FOV is captured. The camera recorded the bubble activity for part of 2 s duration of each sonication period at 1×10^5 frames per second (fps), with a 159 ns shutter time, through a macro-lens (Milvus 100 mm f/2M, Zeiss, Oberkochen, Germany) and a 32 mm extension tube. At this frame rate, imaging was achieved over 280 x 640 pixels, with a resolution of 38 μmpixel^{-1}. Illumination was provided by a continuous 150 W halogen bulb source (Thorlabs, Ely UK) coupled to a liquid light guide and a collimating lens.

Sonications were initiated manually for both horns from the control consoles at prescribed input powers. The oscilloscope and the camera were triggered simultaneously, approximately 1 s following the initiation of a sonication (defining t = 0 ms for the results presented below), from a signal generator, to avoid the proliferation phases of cloud growth for each horn, as observed for the Branson horn, §4.4 Preliminary overview of cavitation activities. Acoustic detection was undertaken with the swPCD at a sample rate of 25 MS/s. Five acoustic data sets were collected for each tip-vibration amplitudes investigated, with results presented as mean ± standard deviation. The collected acoustic signal is processed following the procedure described in § 4.2.3 Acoustic detection and filtering protocol.

6.3 Experimental rationale

Parameters were selected for the two-horn experiment to maximise the chances of observing an enhanced cavitation effect. According to the previous hypothesis, relative input powers were used as any enhanced cavitation would seem more likely to be detected for larger tip-vibration amplitudes. The larger primary bubble clusters associated with higher input powers should also increase the chance of cavitation interaction from both horns. Moreover, the cavitation at the tip of one

horn should not dominate the cavitation generated by the other. For these reasons, the cavitation generated by each tip, operating individually without the presence of the other in the two-horn configuration of fig. 6.3, were characterised in terms of the order of the subharmonic emissions at varying input power.

6.4 Results

6.4.1 Individual characterisation of the ultrasonic horns

HSI in fig. 6.3 (a) shows the cavitation generated from the two horns when operated separately undergo $f_0/5$ regime (i.e., collapse at every $5T_0$ at tip-vibration amplitude of approximate ~ 330 µm). Fig. 6.3 (b, c) are the filtered swPCD data collected over 2 s, and the insets also show that the generated SWs, at this tip-vibration amplitude, have a periodicity of $5T_0$. Fig. 6.3 (d, e) are the noise spectra of the cavitation emissions generated by the two horns at three selected input powers in the two horns configuration. The primary cluster collapsed subharmonically (f_0/m) with m increasing with an increase in the input power. As per the spectral model of Song *et al* [45], this manifests as spectral peaks at nf_0/m, for all n, with m increasing with increasing tip-vibration amplitude. The spectra of the emissions from each of the two horns operated separately show similar progression in m (where mT_0 is the time between successive primary cluster collapses, translating to f_0/m peaks in the emission spectra, as defined in **Chapter 4**) value, with the only difference being the input power at which they occur. The spectral features from $horn_B$, when operated alone at an input power of 40, 50, and 80% without the other tip, are shown in fig. 6.3 (d). The spectra content from $horn_B$ is similar in terms of subharmonic regimes with those observed in § 4.5.3 Cavitation emission noise spectra at selected input powers, which confirms that the position of the swPCD in relation to the tip of the horn does not significantly affect the features within the spectra.

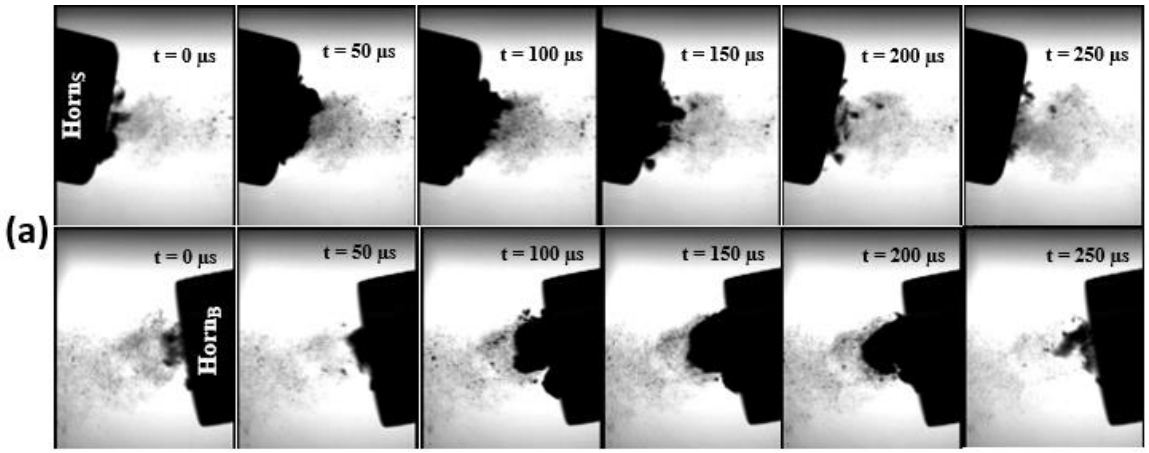
(a)
Horn S
Horn B
t = 0 µs
t = 50 µs
t = 100 µs
t = 150 µs
t = 200 µs
t = 250 µs

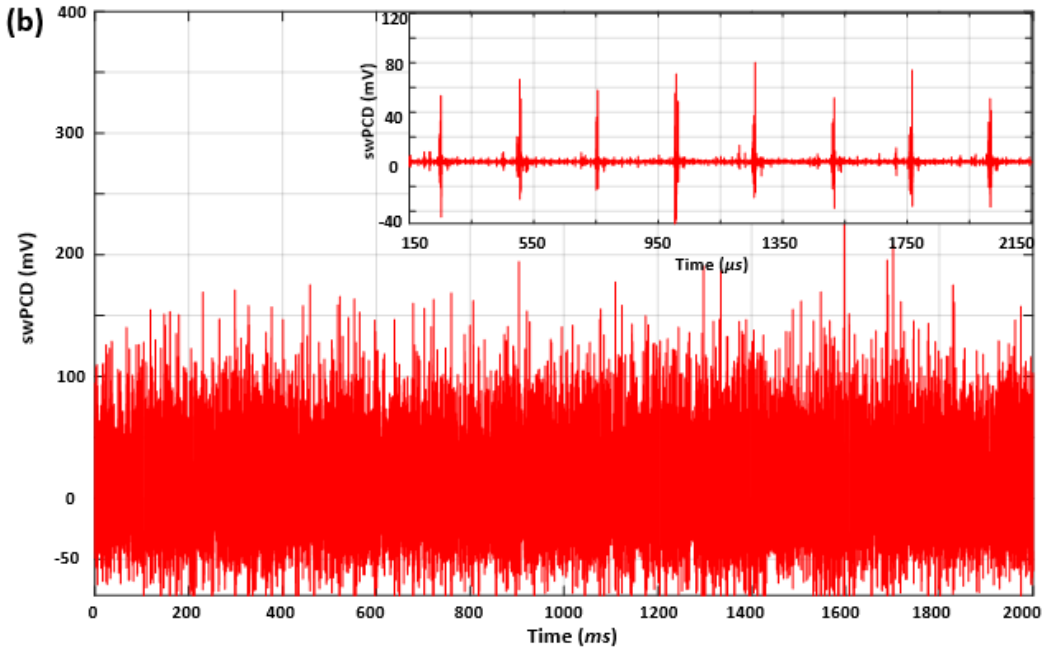
(b)
swPCD (mV)
Time (ms)
Time (µs)

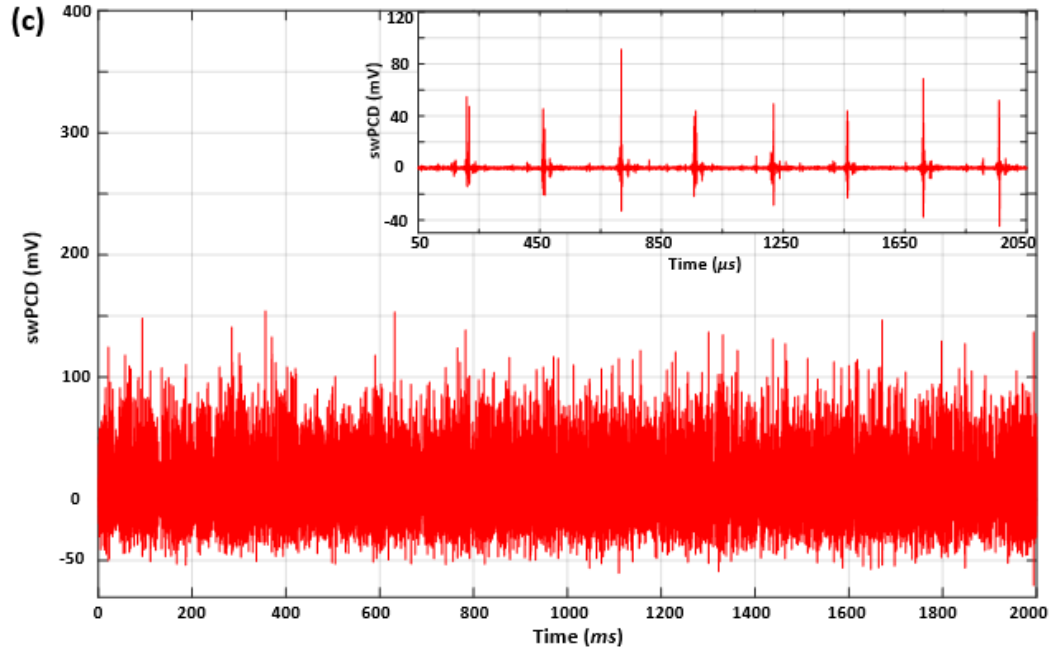
(c)
swPCD (mV)
Time (ms)
Time (µs)

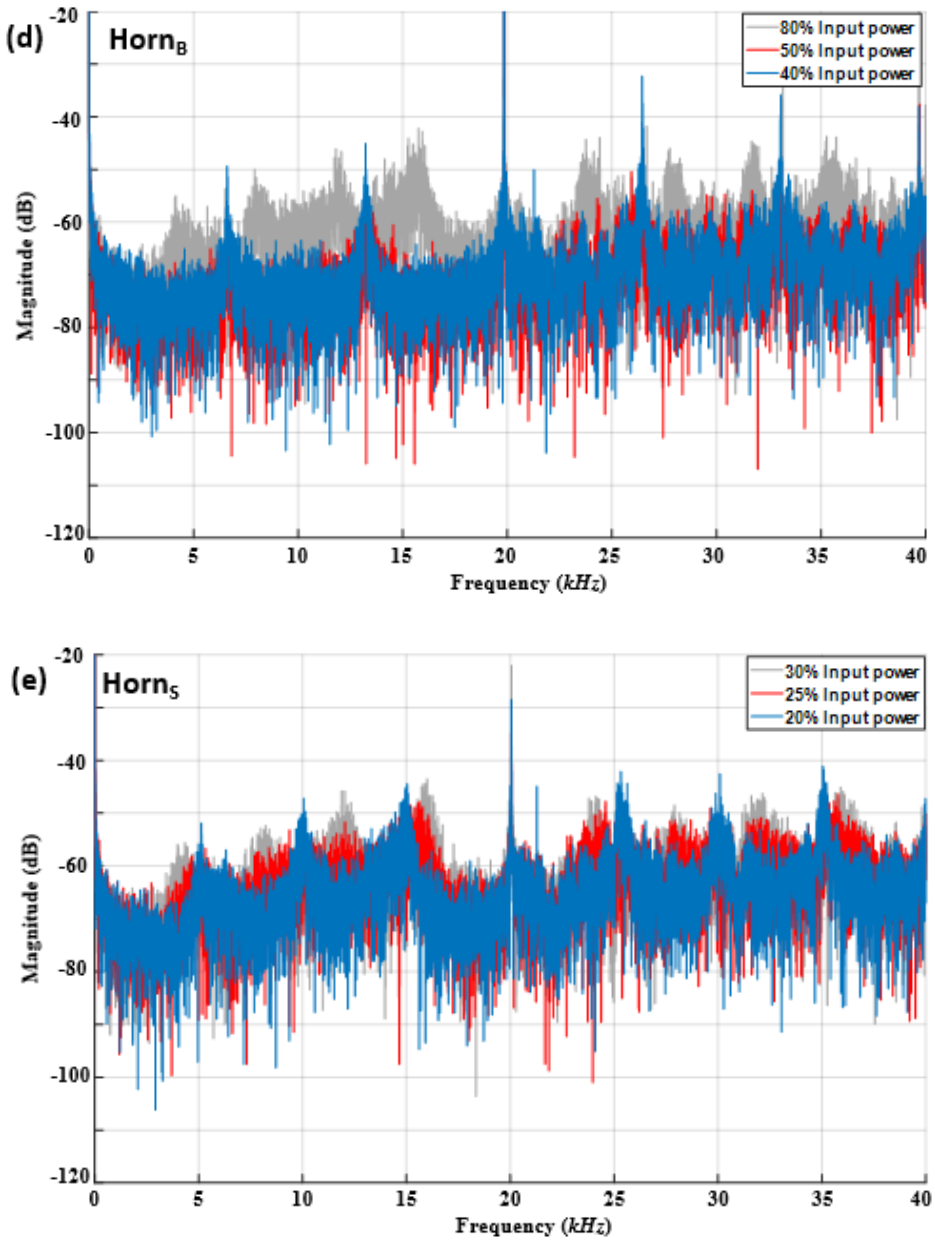

Figure 6.3: Cavitation generated from two horns operated separately: (a) HSI showing the cavitation undergoing $f_0/5$ subharmonic regime at tip-vibration amplitude of ~ 330 µm. Scale is provided by the 6.4 mm-Ø tips. (b) and (c) are the filtered acoustic emission data collected by the swPCD for horn$_B$ and horn$_S$ at tip-vibration amplitude of ~ 330 µm, respectively. Insets show a 2 ms section of swPCD data showing periodic shock waves emission at $5T_0$. (d) Cavitation emission noise spectra for the 2 s sonication period at the selected tip-vibration amplitudes of 40 (blue), 50 (red), and 80% (grey) from horn$_B$. (e) Cavitation emission noise spectra for the 2 s sonication period at the selected tip-vibration amplitudes of 20 (blue), 25 (red), and 30% (grey) from horn$_S$.

Also, the spectra from fig. 6.3 (e) reveal that the primary cluster of horn$_S$ generates cavitation in the $f_0/4$ and $f_0/5$ subharmonic regimes at input powers (tip-vibration amplitudes) of 20% (~ 240 µm), and 30% (~ 330 µm), respectively. The spectrum at 25% (~ 270 µm) does not show any clear subharmonic peaks, indicating a *transitionary tip-vibration* amplitude consistent with those identified in Chapter 4 for the Branson horn. By comparing the spectra feature in fig. 6.3 (d) and fig. 6.3 (e), we can infer that 30% power input for horn$_S$ generates cavitation responding in a similar subharmonic regime to that generated by horn$_B$ operating at 80% power, specifically the $f_0/5$ regime.

Moreover, the spectra of figs 6.3 (d) and (e) reveal that the operating frequency for the two horns is not exactly 20 kHz, but 19.83 kHz and 20.01 kHz for horn$_B$ and horn$_S$, respectively. This slight difference in frequency raises the possibility of a beat phenomenon[15] due to interference between the fields generated.

Table 6.1 summarises the swPCD measurements of the cavitation emissions from the individual operation of the two ultrasonic horns, in terms of $\overline{V}_{rms}$ and the subharmonic spectral features, at some selected input powers. It should be noted here that where the horn is operated separately, the other horn is not present in the tank, just as seen in the HSI in fig. 6.3 (a). The V_{rms} swPCD output obtained here is lower than that from the single horn experiment in Chapter 4 because of the position and distance of swPCD in relation to the tip of the horn.

[15] Beat is a phenomenon associated with the interference of two marginally different frequencies, propagating in the same medium, resulting in a variation of the resultant wave amplitude, with time. In acoustics, beats can be experienced through the interference of the sound fields generated by two tuning forks of slightly different fundamental frequencies (commonly through the addition of a small added mass to one of the tuning forks), such that the loudness/intensity of the resultant sound varies at a frequency much lower than the frequency of the component waves. [207].

The 'beat' frequency ($f_b = \frac{1}{T_B}$) may, to a first approximation, be expressed as difference in the frequencies of the two component waves. In this case, we would therefore anticipate any beat phenomena to manifest at $f_b = f_S - f_B \Rightarrow 20.01 - 19.83 = 0.18\,kHz$. f_S and f_B are the respective frequencies of horn$_S$ and horn$_B$, with $T_b \approx 5.6$ ms (~ 100 T_0 of the ultrasonic horns).

Table 6.1. V_{rms} of the swPCD output for independent operation of the horns, in the position for the two-horn configuration, at some selected input powers.

Input power [%]	Tip-vibration [μm]	Horn$_S$ $\bar{V}_{rms}$ [mV]	Horn$_B$ $\bar{V}_{rms}$ [mV]	Subharmonic regime-Horn$_B$	Subharmonic regime-Horn$_S$
20	125 ± 25	1.85 ± 0.07	—	—	f_0/4
25	180 ± 25	1.98 ± 0.06	—	—	Transition
30	330 ± 25	2.30 ± 0.05	—	—	f_0/5
40	175 ± 25		2.10 ± 0.04	f_0/3	—
50	219 ± 25	—	2.03 ± 0.08	Transition	
80	325 ± 25	—	3.24 ± 0.04	f_0/5	

The mean and standard deviation from the five separate measurements of V_{rms} of swPCD output ($\bar{V}_{rms}$) were used to quantify time average shock wave content within the acoustic data generated from the ultrasonic horns. Next, an investigation of the interaction between cavitation generated from the two horns at selected input powers through HSI observation and parallel acoustic data collection is presented.

6.4.2 Cavitation activity generated during two-horn sonication at tip-vibration amplitude ~330 μm

The spectra of the cavitation emissions generated by each of the two horns, operated individually with tip-vibration amplitudes ~ 330 μm indicate cavitation activity responding in the f_0/5 subharmonic regime. It implies that the primary cluster undergoes periodic collapse, generating periodic shock waves at $5T_0$ as seen from the HSI in fig. 6.3 (a), and the swPCD data in fig. 6.3 (b) and (c). We investigate the behaviour of the cavitation generated when the two horn tips are separated by distances of approximately λ/20 (~ 3.8 ± 0.1 mm) and λ/10 (~7.5 ± 0.1 mm), (assuming ultrasonic propagation in non-cavitating water, determined by f_0 of the ultrasonic horns).

6.4.2.1 Tip separation distance of ~ λ/20

Fig. 6.4 (a) and (b) are selected high-speed images representing the cavitation activity between the tips, during a two-horn operation with a tip-vibration amplitude ~ 330 µm, for the case of the tips vibrating out-of-phase and in-phase, respectively, over approximately 2 cycles. The relative phase of vibration is represented in fig. 6.4 (c) and (d), respectively, where 0 µm is the equilibrium position for each tip (its position when the horn is not operating), a tip 'thrust' (toward the centre-point between the tips) is designated as a positive displacement and a retraction, negative. The yellow and red arrows in fig. 6.4 (a), (b) represent the flow of the acoustic 'streamer' generated during the combined operation of $horn_B$ and $horn_S$. The downward component of the flow seems likely to be due to the angle (~ 15^o to the horizontal) at which the horns are dipped into the tank, fig. 6.2 (a). The tendency for the streaming to flow under the tip of $horn_B$ may suggest that despite the effort made to equalise the contribution from each horn, $horn_S$ is slightly dominant.

For the out-of-phase vibrations (where both tips are moving towards the right or left of the image, approximately simultaneously), fig 6.4 (a), the primary cluster dynamics appear to be in contact with the surface of each tip throughout. Despite the proximity of the tips and the high power sonications from each of the horns, there is no obvious sign of interaction between the primary clusters. The liquid between the tips contains cavitation activity comparable to the 'satellite' or 'distal' clusters and small bubble cloud, identified in the single horn observations of §4.5.1 Data registration and cavitation characterisation.

Within the temporal resolution of the HSI, the tip-vibrations of $horn_B$ and $horn_S$ in fig. 6.4 (b) appear to be perfectly in-phase, as shown in fig. 6.4 (d). This two-horn sonication thus represents an ideal candidate for the enhanced cavitation hypothesis motivating this work. Again, the primary clusters associated with each tip, and their oscillations, are reasonably distinct. The liquid between the tips, however, appears to be more densely populated and includes a cavitating structure within the small bubble cloud (within the green box of fig. 6.4 (b) at 400.10 ms), the morphology of which may in part be explained by the angle at which the horns are dipped into the tank. The HSI of this structure indicates strong collapses, where those at 400.08 ms of fig. 6.4 (b), for example, is reminiscent of the satellite cluster

collapse of the single horn observation captured in fig 4.7 of Chapter 4, except that the cavitating structure of the two-horn sonication is much larger. Although dynamic and evolving, the structure is sustained for the duration of the two-horn sonication. The CBS structure that was observed for single horn investigation is also observed in this configuration, as shown from the HSIs in fig. 6.4 (a, b). Though, the length of the CBS is shorter in this configuration as compared with those observed during single horn operation in chapter 4. This could be due to the buoyancy effect of the column height of the water below the tip of the horns.

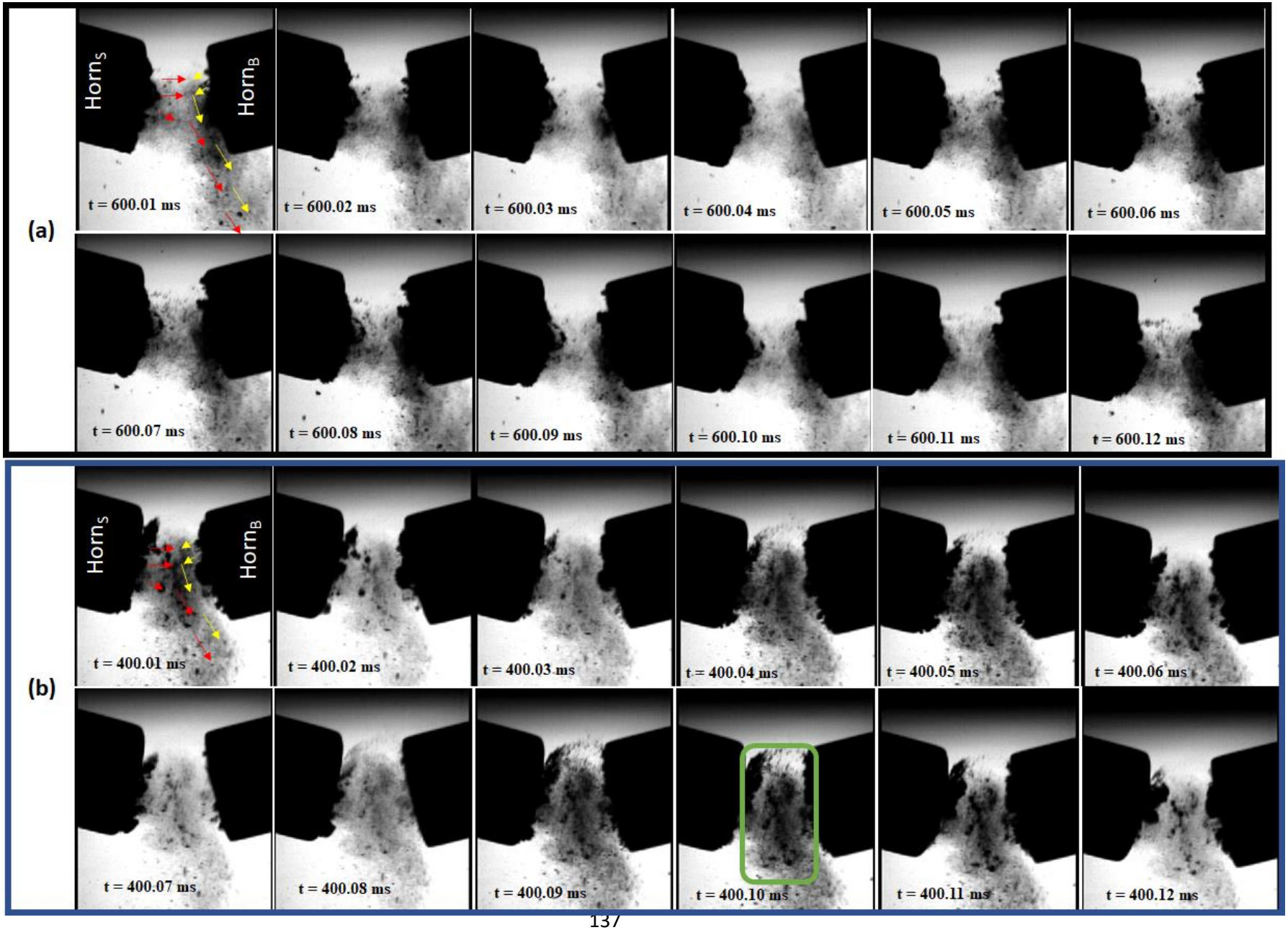
(a)
Horn$_S$
Horn$_B$
t = 600.01 ms
t = 600.02 ms
t = 600.03 ms
t = 600.04 ms
t = 600.05 ms
t = 600.06 ms
t = 600.07 ms
t = 600.08 ms
t = 600.09 ms
t = 600.10 ms
t = 600.11 ms
t = 600.12 ms
(b)
Horn$_S$
Horn$_B$
t = 400.01 ms
t = 400.02 ms
t = 400.03 ms
t = 400.04 ms
t = 400.05 ms
t = 400.06 ms
t = 400.07 ms
t = 400.08 ms
t = 400.09 ms
t = 400.10 ms
t = 400.11 ms
t = 400.12 ms

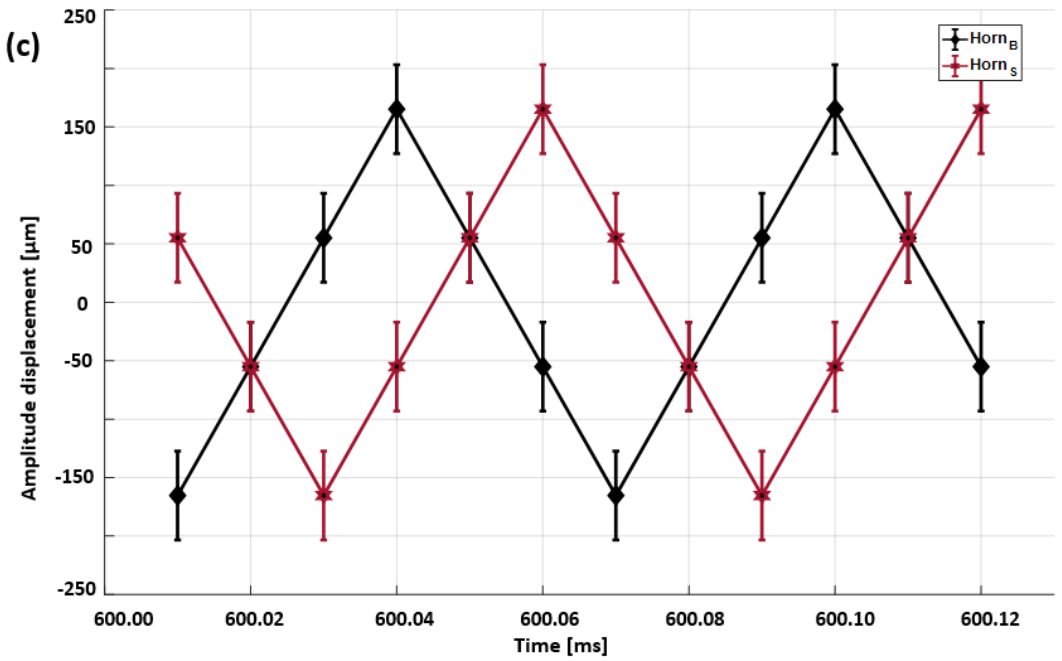
(c)
Horn B
Horn S
Amplitude displacement [µm]
250
150
50
0
-50
-150
-250
600.00
600.02
600.04
600.06
600.08
600.10
600.12
Time [ms]

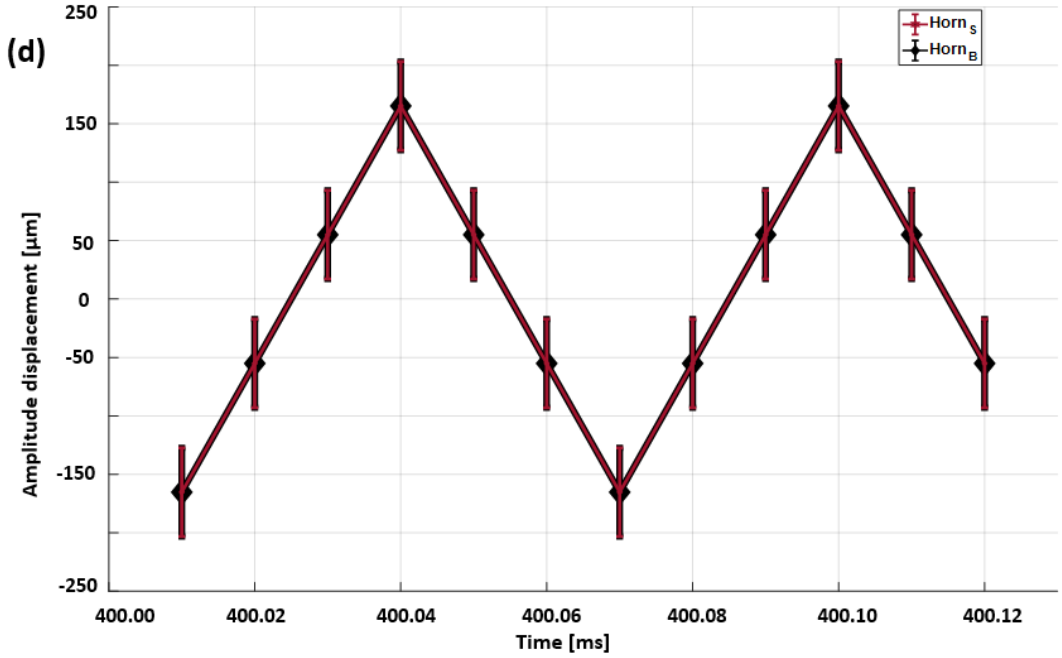
(d)
Horn S
Horn B
Amplitude displacement [µm]
250
150
50
0
-50
-150
-250
400.00
400.02
400.04
400.06
400.08
400.10
400.12
Time [ms]

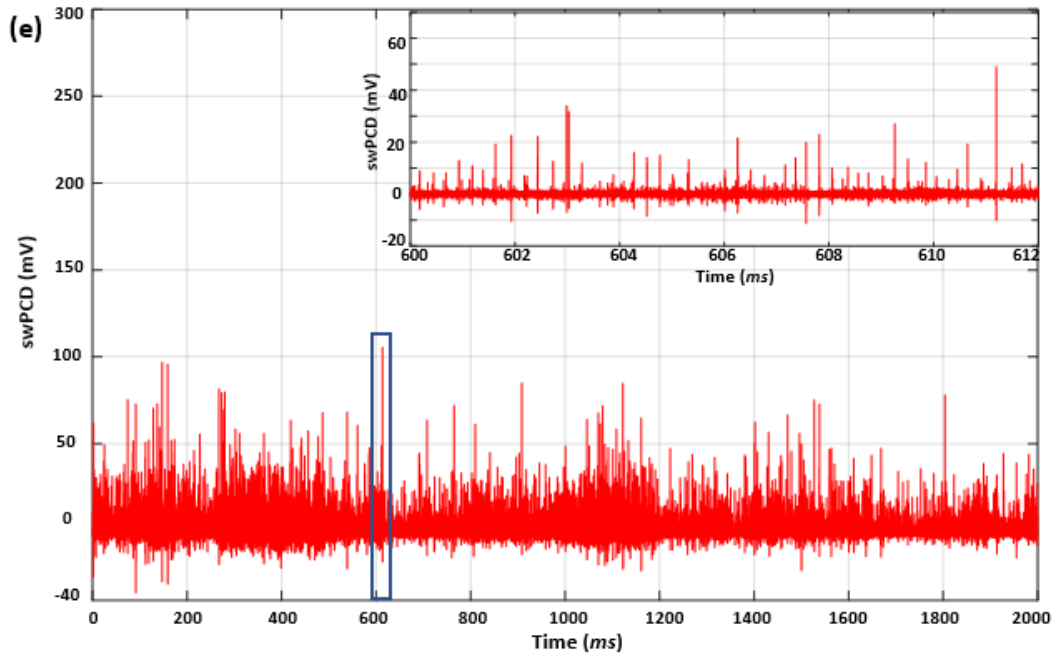
(e)
swPCD (mV)
Time (ms)
swPCD (mV)
Time (ms)

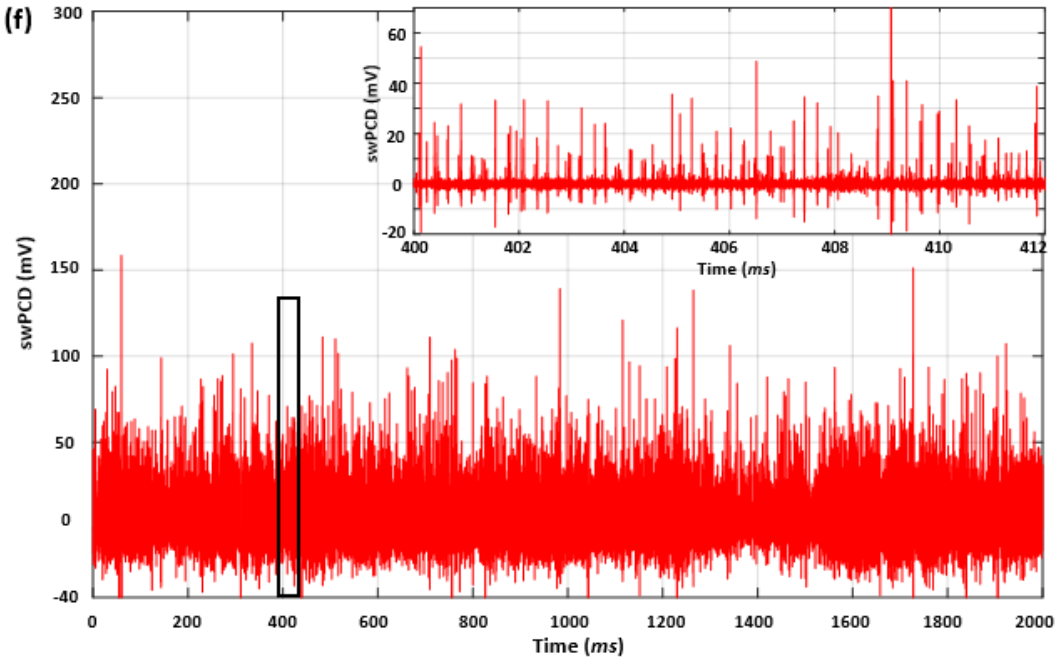
(f)
swPCD (mV)
Time (ms)
swPCD (mV)
Time (ms)

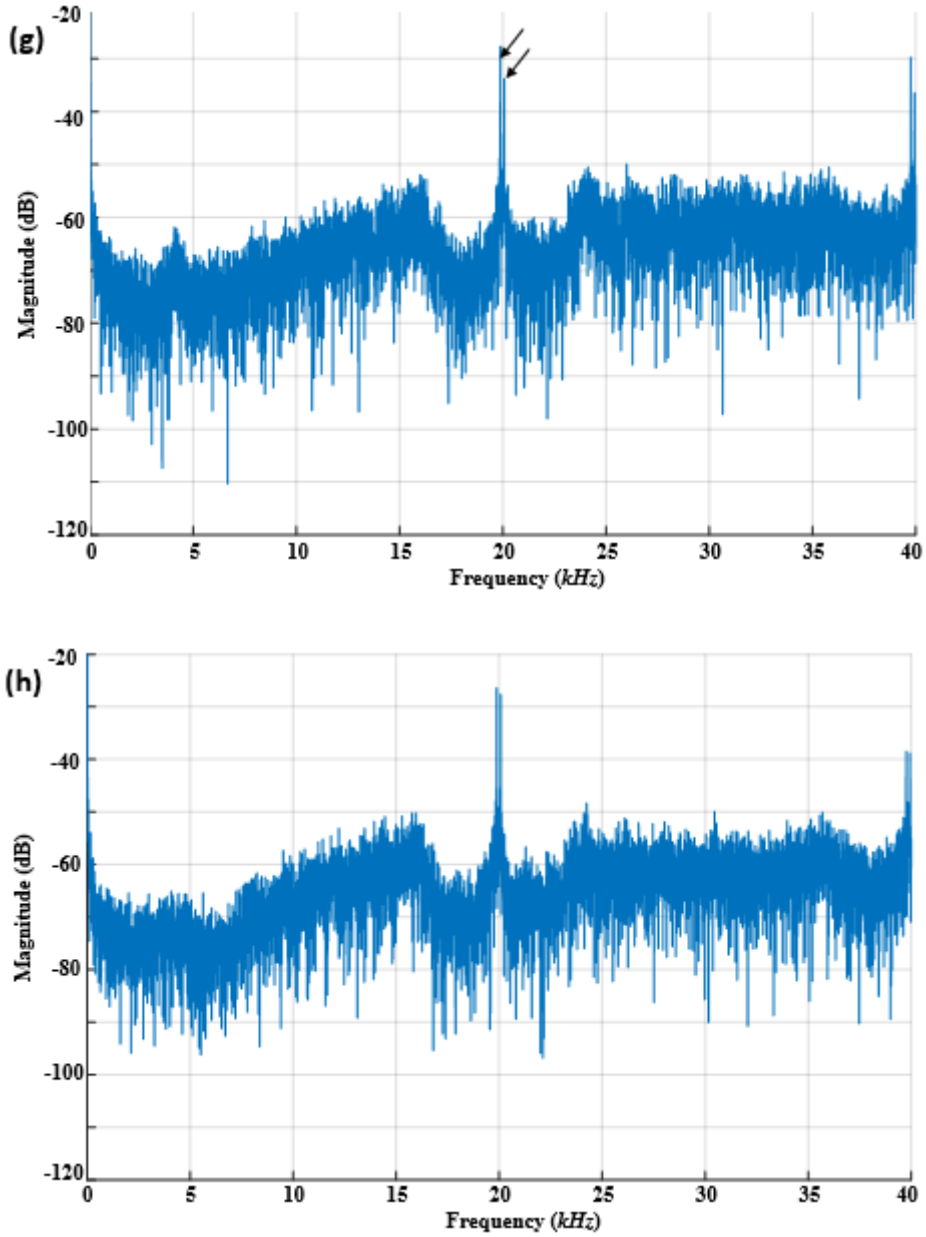

Figure 6.4: Selected frames from Photron high-speed image sequences of two-horn sonications at a tip-separation of λ/2 (~ 3.8 mm), collected at 1 × 10^5 fps, for input powers corresponding to tip-vibration amplitude ~ 330 µm, (a) when the two horns almost oscillating out-of-phase, and (b) in-phase. Scale is provided by the 6.4 mm-Ø tips. (c) and (d) depict the relative phase of vibration for (a) and (b), respectively, obtained via the estimation of tip-displacement from the HSI. (e) and (f) are the filtered acoustic emission data collected by the swPCD for the out-of-phase and in-phase two-horn sonications, respectively. Insets show emission data around the duration for which HSI is presented. (g) and (h) are the corresponding acoustic spectra for (e) and (f), respectively.

Fig. 6.4 (e) and (f) present filtered swPCD data for a 2 s duration of the out-of-phase and in-phase operation of two horns, respectively; data collected at approximately 1 s following initiation. This data can, to some extent, be compared to the acoustic emission data collected from the individual horn$_B$ experiments of Chapter 4, fig 4.6, with the caveats, that the swPCD is located both further away from the cavitation activity and in a position orthogonal to the horn, rather than directly below the tip. This configuration leads to the much lower value of the V_{rms} observed when compared with that observed in chapter 4. The inset in the figures shows emission data around the duration for which the HSI is presented. The 12 ms section is presented to investigate the possible occurrence of the beat[2] phenomenon. The inset is long enough to illustrate the presence or absence of beat phenomenon since the 12 ms is longer than the two-times expected T_b (i.e., 12 ms > $2T_b$). Detailed examination of this 12 ms section of the swPCD data revealed no beat-related features, since there was no consecutive occurrence of high/low voltage whose period is typical of ~ 5.6 ms (expected beat period).

The spectra from both out-of-phase and in-phase operations of the two ultrasonic horns are shown in fig. 6.4 (g) and (h), respectively. From the spectra, it is clearly shown that the subharmonic regimes of $f_0/5$ observed when the ultrasonic horns operate separately (fig. 6.3 (d) and (e)) disappear, which implies that the acoustic field of one ultrasonic horn influences the other, thus affecting the subharmonic regime of the cavitating bubbles. The two parallel arrows (black) in fig. 6.4 (g) indicate the fundamental frequencies (f_0) of the two ultrasonic horns.

Table 6.2 shows the mean and standard deviation from the three sets of data when the tips of the two horns oscillate in-phase or out-of-phase at a tip separation distance of ~ 3.8 ± 0.1 mm. The third column of the table shows the V_{rms} from the individual operation of the ultrasonic horns while the position of the other nonoperating is maintained. It was observed that the standard deviation is minimal when the two horns oscillate in-phase compared with when they oscillate out-of-phase. Also, the $\bar{V}_{rms}$ of the swPCD outputs observed when the two-horns oscillate in-phase is higher than when the two-horns are oscillating out-of-phase as there is more cavitation activity during the former than the latter, as observed in HSI shown in fig. 6.4 (a) and (b), and the acoustic data in fig. 6.4 (e) and (f).

Table 6.2. V_{rms} of the swPCD output for independent and simultaneous operation of the horns, in the two-horn configuration for a tip separation distance of ~3.8 mm and with each horn operating at vibration amplitudes that generate cavitation responding in the $f_0/5$ regime.

Horn type	Input power [%]	$\bar{V}_{rms}$ [mV] from individual horn	$\bar{V}_{rms}$ [mV]	
			In-phase	Out-of-phase
$Horn_B$	80	2.16 ± 0.01	—	—
$Horn_S$	30	1.72 ± 0.04	—	—
$Horn_B$ and $Horn_S$	80 and 30	—	1.45 ± 0.07	1.03 ± 0.22

6.4.2.2 Tip separation distance of ~ λ/10

The simultaneous operation of the two horns, when the distance between the tips is increased to ~7.5 ± 0.1 mm, is now investigated. The observation from the HSI, in fig. 6.5 (a) reveals a sustained oscillating bubble cluster formed almost midway between the two tips beyond the primary cluster associated with each. The bubble cluster moves within the separation of the horn tips, oscillating in size and shape as indicated with a red circle in fig. 6.5 (a). This sustained oscillation bubble cluster phenomenon was not observed in all the data collected when the separation between the tips of the two horns is approximately half of the wavelength. The sustained bubble cluster appears to be trapped in acoustic equilibrium forces from the two horns, which might have been caused by balanced net acoustic forces from the two horns and the force associated with the size of the bubble cluster that makes the bubble cluster of only such size to levitate. The corresponding relative phases of vibration of the two horns is shown in fig. 6.5 (b) obtained in a similar way as fig. 6.4 (a) and (b). The filtered swPCD output for the two-horn sonications is shown in fig. 6.5 (c). The 12 ms section of the swPCD around the duration for which HSI is presented is shown as the inset. The beat phenomenon is examined using this 12 ms portion of the swPCD data, just as in the case presented in fig. 6.4 (e) and (f). The spectra feature (fig. 6.5 (d)) obtained in this case is similar to those in fig. 6.4 (g) and (h).

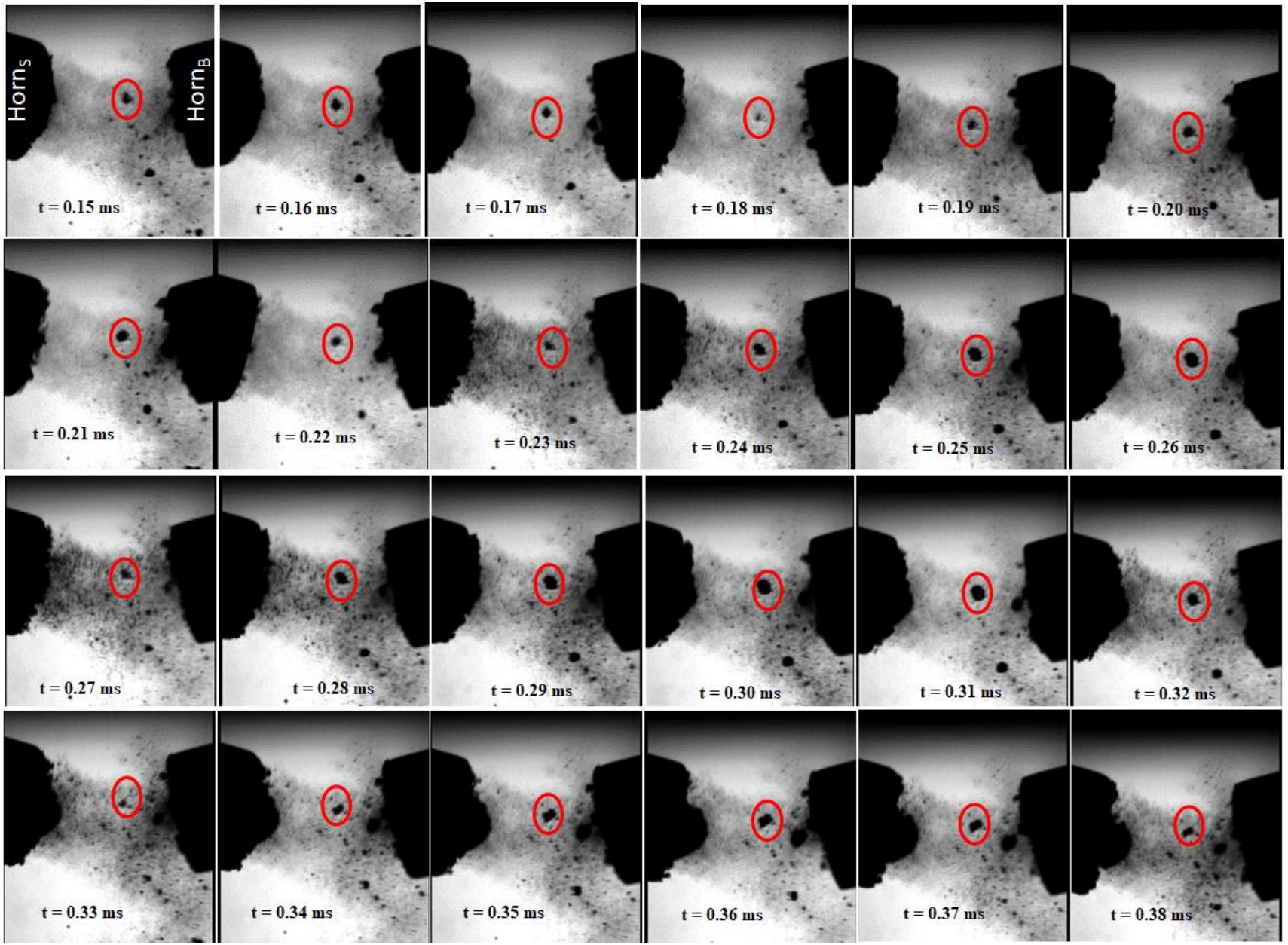
Horn$_S$
Horn$_B$
t = 0.15 ms
t = 0.16 ms
t = 0.17 ms
t = 0.18 ms
t = 0.19 ms
t = 0.20 ms
t = 0.21 ms
t = 0.22 ms
t = 0.23 ms
t = 0.24 ms
t = 0.25 ms
t = 0.26 ms
t = 0.27 ms
t = 0.28 ms
t = 0.29 ms
t = 0.30 ms
t = 0.31 ms
t = 0.32 ms
t = 0.33 ms
t = 0.34 ms
t = 0.35 ms
t = 0.36 ms
t = 0.37 ms
t = 0.38 ms

(a)

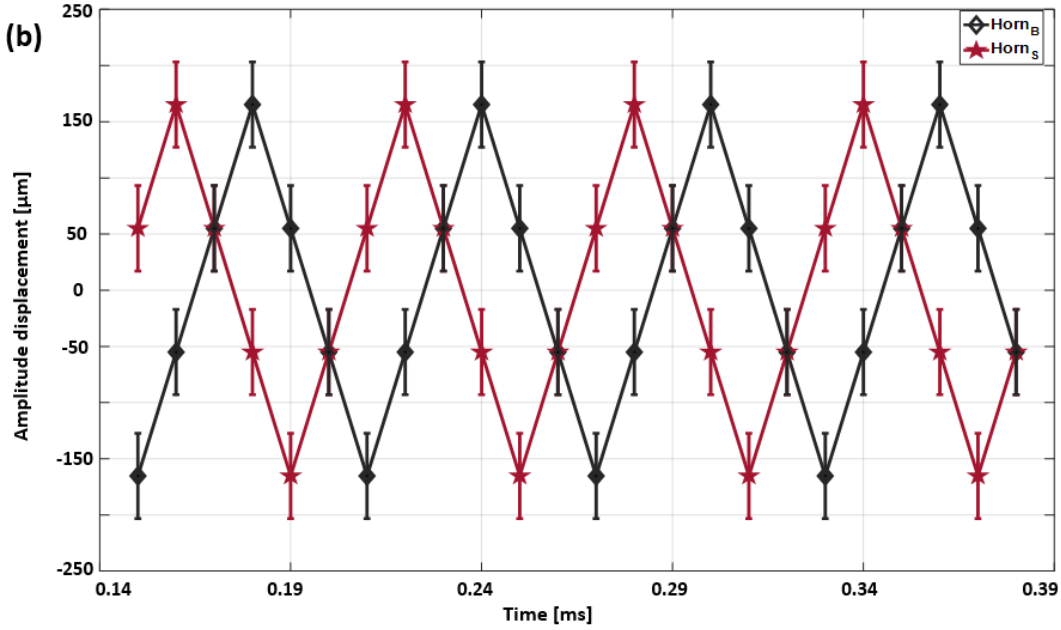
(b)
Horn$_B$
Horn$_S$
Amplitude displacement [µm]
250
150
50
0
-50
-150
-250
0.14
0.19
0.24
0.29
0.34
0.39
Time [ms]

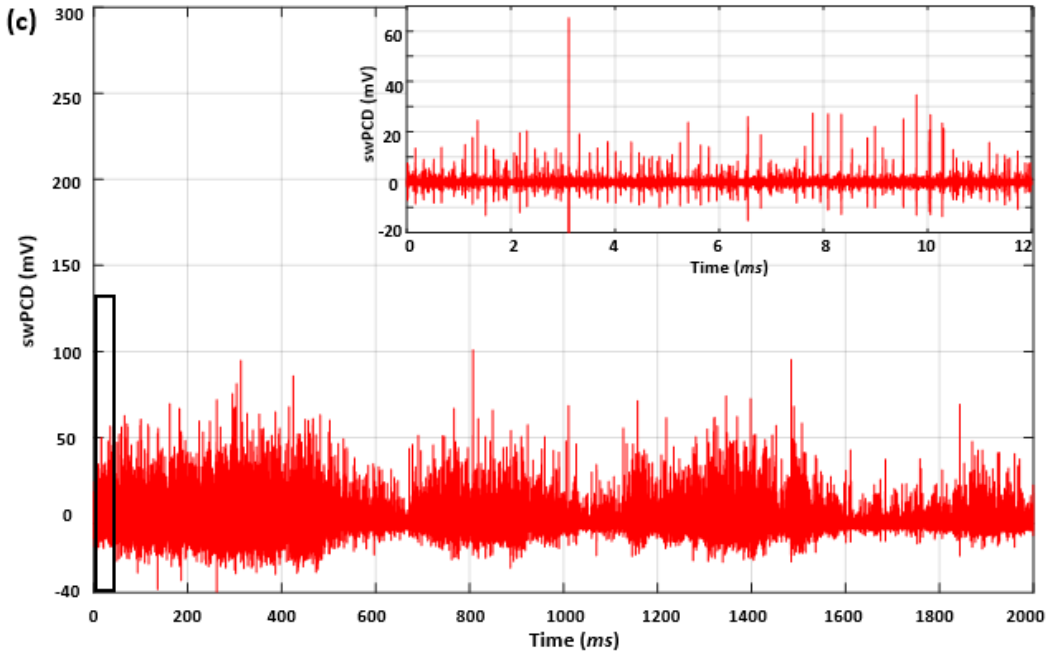
(c)
swPCD (mV)
300
250
200
150
100
50
0
-40
0
200
400
600
800
1000
1200
1400
1600
1800
2000
Time (*ms*)
swPCD (mV)
60
40
20
0
-20
0
2
4
6
8
10
12
Time (*ms*)

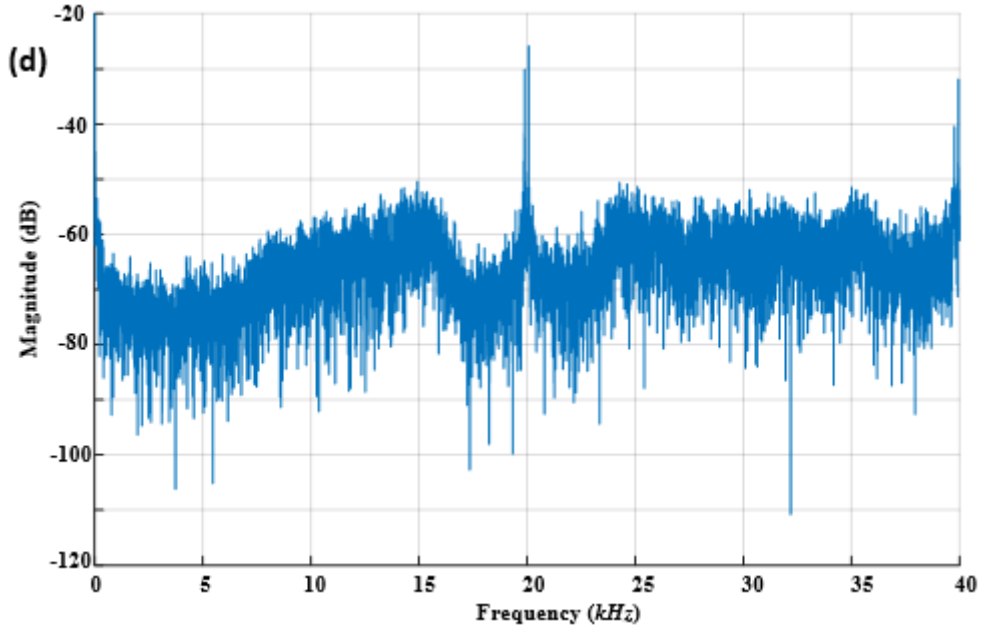

Figure 6.5: Selected frames from Photron high-speed image sequences of two-horn sonications at a tip-separation of λ/10 (~ 7.5 mm), collected at 1 × 10^5 fps, for input powers corresponding to tip-vibration amplitude ~ 330 µm. Scale is provided by the 6.4 mm-Ø tip. (b) depicts the relative phase of vibration for (a) which was obtained via the estimation of tip-displacement from the HSI. (c) the filtered acoustic emission data collected by the swPCD for the two-horn sonications. Insets show emission data around the duration for which HSI is presented. (d) the corresponding acoustic spectra for (c).

The swPCD data, in this case, is similar to that at ~λ/20 tip separation, only that the $\bar{V}_{rms}$ of the swPCD outputs decreased both in-phase and out-of-phase scenarios as seen from Table 6.3. The standard deviation for this set of observations at this separation (~ λ/10) is also lower compared to those when the separation is ~ λ/20. The third column of the table shows the $\bar{V}_{rms}$ from individual operation of the ultrasonic horns while the position of the other nonoperating is maintained. The close values in $\bar{V}_{rms}$ obtained from the individual operation of the horn in Table 6.2 and 6.3 indicates that the effect of the surface of the second horn is negligible. Also, the impact of the phase oscillation relationship between the tips of the two horns on $\bar{V}_{rms}$ of the swPCD outputs is reduced. The lower value of V_{rms} from the swPCD output observed at this separation may be due to the lower interaction between the

cavitation field caused by the decay of this field as the distance from the tips of the horns is increased.

Table 6.3. V_{rms} of the swPCD output for independent and simultaneous operation of the horns, in the two-horn configuration for a tip separation distance of ~7.5 mm and with each horn operating at vibration amplitudes that generate cavitation responding in the $f_0/5$ regime.

Horn type	**Input power [%]**	$\bar{V}_{rms}$ **[mV] from individual horn**	$\bar{V}_{rms}$ **[mV]**	
			In-phase	**Out-of-phase**
$Horn_B$	80	2.12 ± 0.05	—	—
$Horn_S$	30	1.61 ± 0.03	—	—
$Horn_B$ and $Horn_S$	80 and 30	—	1.07 ± 0.02	0.94 ± 0.06

6.5 Discussion

The results presented so far indicate that the simultaneous operation of two ultrasonic horns whose rating (frequency and power) is not the same results in the generation of acoustic cavitation whose time average shock wave content (V_{rms}) depends on both the relative phase vibration between the two-horns and the separation distance between the tips of the horns. The V_{rms} is low when the relative phase oscillation between the horn is out-of-phase, and it is high when the two horns oscillate in-phase, as seen from the results presented in fig. 6.4. This is because the two horns, while operating in phase, create enhanced tensile stress (i.e., both thrusting and retracting simultaneously) within the host medium, resulting in improved cavitation, especially when the separating distance between the two-horns is less than a λ/10. This enhanced cavitation decreased with an increase in separation distance between the tips of the horn since the cavitation field produced from the ultrasonic horn decreased with distance away from the horn's tip, [172] [173], resulting in lower constructive interference between the acoustic field created from the two horns. The low value of V_{rms} when the two horns oscillate out-of-

phase may be due to the mismatch in timing between the tensile strength transmitted to the host medium from both horns; one horn is thrusting while the other is retracting. This leads to net lower tensile stress being transmitted, reducing cavitation activities within the cavitation zone. Tables 6.2 and 6.3 show that the $\bar{V}_{rms}$ values obtained from simultaneous operation of the two horns were lower than those obtained from each horn's separate individual operation (whilst the position of the other non-operating horn is maintained). This observation could be due to the shielding effect from the crowded bubble clusters in the cavitation zone. It could also be due to the limitation of temporal resolution of the swPCD, that is, the inability of the swPCD to resolve some detected SWs whose time difference is in the nano or picosecond range.

Detailed investigation of a section of swPCD data (12 ms) longer than the expected $2T_b$ (i.e., 12 ms > $2T_b$) shows no evidence of the beat phenomenon, which may be present due to a slight difference in the operating frequencies of the two ultrasonic horns. This is possible because the acoustic emission is dominated by the shockwaves generated due to bubble collapse consisting of frequencies broadband rather than a direct sound field.

HSI from figure 6.5 (a) revealed a bubble cluster is trapped or formed almost midway between the two tips beyond the primary cluster associated with each horn. The bubble cluster levitates and undergoes continuous and sustained oscillation in size and shape. This may be due to some forms of acoustic field balancing from both horns, which is associated with the bubble cluster's size since others whose sizes are not of a similar range did not show similar behaviour.

Also, HSI reveals that the acoustic streamers generated from both ultrasonic horns increase with the tip vibration amplitude. This phenomenon can be adequately observed from the attached movies. The net acoustic streamer's direction of the bubbles moves from the ultrasonic horn with a higher power rating ($horn_S$) to the one with a lower power rating ($horn_B$) irrespective of the tip-vibration amplitude.

Further investigation at different tip-vibration amplitude is also carried out at varying tip separation distances. The observation is similar to what is demonstrated in the result presented above. The resultant V_{rms} of the swPCD output

from the simultaneous operation of the two horns decreases as the tip separation distance increase. The result is presented in Supplementary double-horn results

6.6 Conclusion

From all the results reported so far on the parallel observation of the swPCD output and HSI during the simultaneous excitation of two horns, we can conclude with the following remarks:

- The $\bar{V}_{rms}$ of the swPCD output from the resulting simultaneous operation of the two horns depends on the separation between the horn tips and the relative phase oscillation between the two horns. The $\bar{V}_{rms}$ of the swPCD output increases when the relative phase oscillation of the horns is the same (i.e., in-phase), and decreases when out-of-phase.
- At appropriate tip vibration amplitudes and tip separation distance, the bubble cluster may be made to levitate and undergo sustained oscillation in both size and shape within the separation area between the horn, as shown in Fig. 6.5 (a).

This research may serve as a foundation for future upscaling of applications involving the simultaneous operation of two or more ultrasonic horns. The configuration considered here eliminates the complex design associated with the multi-transducers vessel approach. Hence, this approach could be helpful in applications such as ultrasonic melt treatment and sonochemistry, where both higher acoustic streaming and enhanced cavitation is required for optimum yield. Also, this configuration may be helpful in waste-water treatment if it can be adapted such that the waste-water is allowed to pass between the tip separations.

Chapter 7

Ultrasonic fixation of Nitrogen

Nitrogen (N_2) in the form of nitrite and nitrate (NO_x^-) is very important for plant growth and development. Most plants, however, cannot synthesise the required NO_x^- directly from atmospheric nitrogen. They obtain it via the addition of fertilizer. In addition, it plays an important role in protecting the cardiovascular system and gastric mucosa and in metabolic diseases in humans [174]. NO_x^- also serve as food additives where they function as a preservative by inhibiting the growth of microorganisms like Clostridium botulinum [175]. Therefore, research should be encouraged to synthesise these compounds industrially using nonthermal approaches. As discussed in Chapter 2, the sonochemistry technique can also be used to fix N_2 to NO_x^-. The temperature in the hotspot created as a result of bubble collapse joint with the corresponding high pressure can break molecular bonds to generate free radicals that can readily combine to form more radicals or chemical compounds [176]. Fixation of N_2 to NO_x^- requires a high amount of energy (941.4 $kJmol^{-1}$) to break the triple bond in the N_2 to generate nitrogen radicals which may react with other species like oxygen and hydroxide to give stable products [59][177]. The conventional thermal method (Haber-Bosch) of fixing N_2 to NO_x^- requires very high temperature (400 to 500 ^oC) [178] [179], and enormous resources such as capital and efforts are put into realising a suitable reactor that can withstand the expected high temperature [47] [180] [181]. An alternative method which should be encouraged is to generate NO_x^- at much lower temperature. One of such way is through sonochemistry that often takes place at an ambient temperature. This is in line with the famous quotation from Richard Feynman ("There's Plenty of Room at the Bottom").

Despite the advantages offered by the sonochemical approach in the generation of several inorganic and organic compounds, the process still seeks improvement. The focus should be on improving the acoustic cavitation generation

with minimum input resources. Therefore, this chapter considers the optimisation of the process in terms of acoustic power administration and sonochemical yield of NO_x^-. This research was carried out in collaboration with the research group of Dr Mark Symes of the School of Chemistry, University of Glasgow. Dr Symes's group had initially used an ultrasonic horn as the source of ultrasound in fixing N_2 but generated a concentration of NO_x^- below the detectable limit. Therefore, we shall be using a focused transducer, typical of those used for therapeutic ultrasound, as the ultrasound source.

The work described in this chapter was undertaken as a collaborative effort with the group of Dr Mark Symes at the School of Chemistry, University of Glasgow. Their contribution[16] was the quantification of the sonochemical yield of NO_x^- after each sonication.

7.1. Introduction

The first report on the formation of nitrate (NO_3^-) was made by Schultes and Gohr in 1936 [182], where an ultrasound of frequency 300 kHz was irradiated to water saturated with different gases via a radiating surface diameter of 42 mm-Ø. During the sonication, both hydrogen gas (H_2) and N_2 were sparged into the water at the rate of 1 *L/min*, while carbon monoxide (CO) was sparged at 0.41 *L/min*. All the investigations were carried out in the presence of oxygen gas (O_2). They observed that N_2 fixation does not depend on the H_2 so long as the sparging rate of N_2 is fixed. They also observed that the formation of hydrogen peroxide (H_2O_2) was reduced at a pH value below 4, and that of NO_x^- was increased for a pH value below 4. Moreover, it was found that both H_2 and CO inhibit the formation of NO_x^- due to competition for the available O_2. Virtanen *et al* [183], in 1950, used the same ultrasound conditions to investigate the effect of pH variation on the production of NO_x^-. The ultrasound was generated at ~ 300 kHz employing a piezo-quartz (ultrasound transducer) whose radiating surface was noted as ~ 42 mm-Ø in

[16] Special thanks to Mr. Patrick McHugh for his tireless efforts towards concentration quantification

diameter resulting in an ultrasound intensity of 10 W/cm^2. The transducer was completely immersed in a cylindrical oil bath (64 mm -Ø) that served as the host medium, into which the ultrasound was irradiated, as shown in fig 7.1.

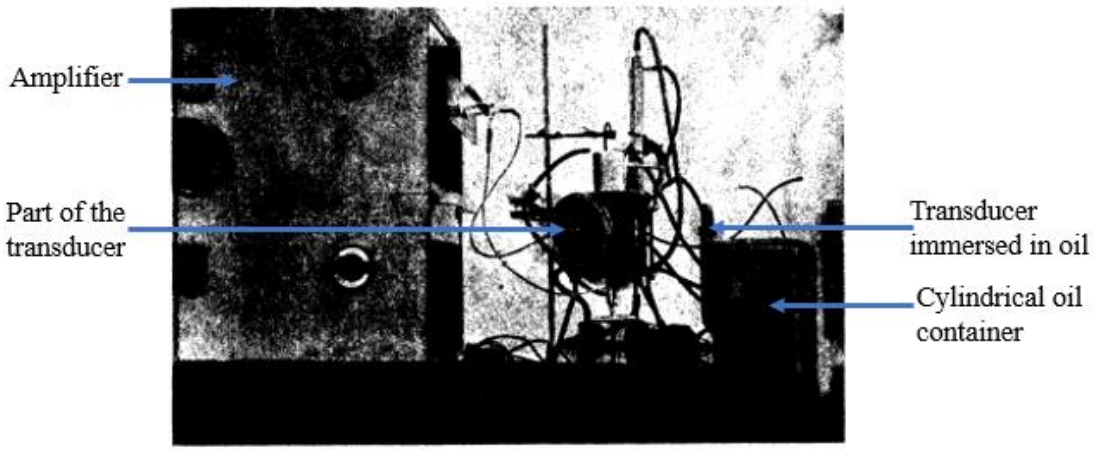

Figure 7.1: Ultrasonic apparatus used in [183], 1950

NO_2^- was detected and quantified photometrically via a sensitive colour indicator when it reacted with both naphthylamine and sulphanilic acid. The presence of NO_2^- creates a reddish colouration of the resulting solution after 30 minutes, which was estimated with a Klett-Summerson photometer at filter S50. Similarly, the concentration of NO_3^- was determined photometrically by the phenol disulphonic acid, which produces a yellow colouration in the presence of NO_3^-. The concentration of both NO_2^- and NO_3^- in their resulting solutions was read from a standard concentration curve. The pH value of the sample was varied from 1.25 to 11.8 using a different acidic solution. The results showed that the pH value does not affect the production rate of NO_x^- but the ratio of NO_3^- to NO_2^- increased with an increase in the pH value. Moreover, the sparged CO inhibits the production of NO_x^- due to competition for the available O_2, a similar finding to that reported in [184]. Mead *et al* [185] in 1976 investigated the effect of ultrasound irradiated into water-saturated with different gases (O_2, N_2, Air, & Argon (Ar)). A 50 W planar cobalt barium titanate transducer was used to generate ultrasound at a frequency of

447 kHz. The ultrasound was irradiated into a 50 mL of water sample maintained at a temperature of 25 *C*. The water sample was sparged with the gases for 10 minutes before and during the sonication. Products such as H_2O_2, nitrous acid (from NO_2^-), and nitric acid (from NO_3^-) were all detected depending on the type of the sparged gas used. The concentration of H_2O_2 found was directly proportional to both the sonication period and the nature of the sparged gas, i.e., the concentration yield follows this particular order O_2 > Air > Ar > N_2. The concentration of the combined acid (NO_2^- and NO_3^-) follows the order Air > N_2 > Ar > O_2. The concentration of NO_2^- and NO_3^- found are 22 x 10^{-6} and 6 x 10^{-6} $molmin^{-1}W^{-1}$ respectively. They suggested that the observed N_2 fixation when the sparged gases were O_2 and Ar may be due to the contamination of N_2 in the dissolved gases or the residual air from incompletely degassed water that was used.

Wakeford *et al* [177] in 1999 investigated the effect of the ionic strength in water solution (i.e., water containing a sodium solution) on the production rate of NO_x^- and H_2. A Kerry ultrasonics PUL 125 cleaning bath equipped with a transducer operating at 35 kHz was used, and a 1000 cm^3 flat-bottomed reaction vessel fitted with a glass sinter was placed inside the bath. 650 cm^3 of the sample solution was placed into the reaction vessel and pre-saturated with different gases (air, N_2 or Ar) at the rate of 1500 cm^3/min for 30 minutes and maintained throughout the sonication period. The effect of these sparged gases on the sonochemical yield was evaluated at a constant experimental temperature of 20°C. At the end of the sonication, the presence of H_2O_2, NO_2^- and NO_3^- were all detected. The concentration of NO_3^- was estimated using a modified Greiss-Isvlay reaction method. This method is based on a colourimetric procedure. A diazonium salt is produced when NO_3^- reacts with an acidic solution of sulphanilamide. The diazonium salt was then treated with complex salt (N-(1-naphthy1)-ethylenediamine dihydrochloride) to form an azo dye. The azo dye (absorbent) was measured spectrophotometrically at a wavelength of 540 nm using a Diode Array Spectrometer. The concentration of NO_3^- evaluated via this method is accurate to ± 3%. The concentration of NO_2^- was determined by reducing NO_3^- to NO_2^- using cadmium granules amalgamated with mercury. The resulting NO_2^- concentration

was then determined using the Greiss method. The ultrasound irradiation of water saturated with O_2 or Ar generates H_2O_2 but neither NO_2^- nor NO_3^-. The ultrasound irradiation of water saturated with either N_2 or air produces NO_2^-, NO_3^- and H_2O_2. The production rate of NO_2^- was twice that of NO_3^-, and the concentrations of both NO_2^- and NO_3^- when N_2 was used as the saturated gas were only 10-15% of the conecentration obtained when air was the saturated gas (see fig. 7.2). They observed improvement in the concentration yield of both NO_2^- and NO_3^- in ionic solution (0.3×10^{-6} M min^{-1}) compared to when ordinary water (1.8×10^{-6} M min^{-1}) was used. The yield of NO_2^- in the ionic solution was approximately four times the yield when ordinary water was used, although the concentration ratio of NO_2^- to NO_3^- formation in both cases remains fairly constant, i.e., between 2-2.5.

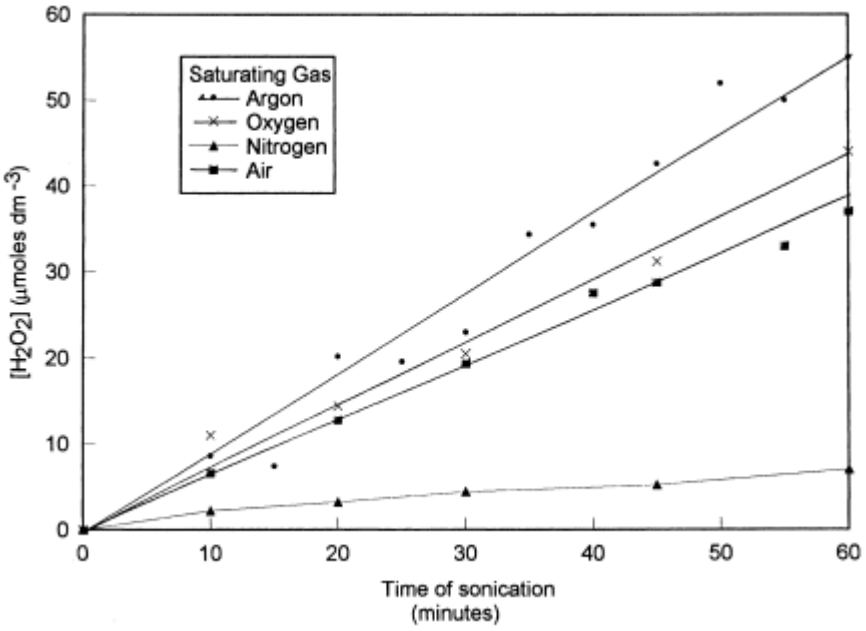

Figure 7.2: Formation of nitrite and nitrate in water saturated with nitrogen or air when exposed to ultrasound at a frequency of 35 kHz [177]

Supeno [186] in 2000 reported the formation of ammonia gas when a water sample pre-saturated with a mixture of N_2 and H_2 was exposed to an ultrasound at a frequency of 900 kHz from a planar transducer. The ammonia yield was maximum

when the mixing ratio of the sparged gases was 3:2 for N_2 and H_2, respectively. However, no formation of NO_x^- was observed in the absence of oxygen gas. This implies that O_2 is very necessary for the formation of both NO_2^- and NO_3^-. Supeno *et al* [187], in 2000, carried out sonolysis of water at 900 kHz at varying sonication time, the mixing ratio of sparged gases (O_2 and N_2), and the experimental temperature. The ultrasound source was a specially constructed apparatus whose acoustic power delivered to the water was estimated to be 27 W, determined via the calorimetric method. A 100 mL of water is sparged at a constant rate of 2.9 mLs^{-1} with either air or a mixture of O_2 and N_2 for 15 minutes before the commencement of sonication. The concentration of the NO_3^- generated was determined with an Orion nitrate-specific ion electrode. The NO_2^- concentration was estimated from the difference between the initial NO_3^- and the oxidized NO_3^- from nitrite. For an average sonication period of 20 minutes, the concentrations of both NO_2^- and NO_3^- were found to be approximately the same, which is not in agreement with findings from [177]. The authors suggested the sonication period as the factor responsible for this difference, where NO_2^- was initially favourably formed at an early stage of the reaction. The concentration of NO_x^- was not detectable in the absence of O_2. However, with a mixture of N_2 and O_2, the maximum concentration of the combined NO_x^- formed was 16×10^{-5} M over a sonication period of 20 minutes equivalent to 30 x 10^{-9} $molmin^{-1}W^{-1}$. An inverse relationship between temperature and the sonochemical yield was observed.

Yao *et al* [75] considered the generation of NO_x^- using an ultrasound source from a 100 W transducer. 200 mL of pure water contained in a cylindrical stainless steel reactor (internal diameter 100 mm (20), and volume 600 mL) was irradiated with ultrasound at varying frequencies (200 to 800 kHz). The water was sparged with O_2 and N_2 for 30 minutes before the start of sonication and continued throughout sonication. At some intervals, part of the sample was collected for concentration analysis using ion chromatography (ICS1000, Dionex companies in the US) equipped with an anion chromatographic column and a suppressed EDC detector. The effects of the sparged gas, bulk temperature, and acoustic intensity on the sonochemical yield of both NO_2^- and NO_3^- were investigated. The kinetic

model[17] describing the rate of radicals generation of both NO_2^- and NO_3^- was derived as respectively given in equation (7.1) and (7.2). This model was solved for the reaction rate constants using the Runge-Kutta Fehlberg method. They found that the concentration of both NO_2^- and NO_3^- increases as the sonication period increases. This was in agreement with their experimental results shown in fig. 7.3. At a constant intensity, the optimum sonochemical yield of both NO_2^- and NO_3^- was found at the frequencies of 200 kHz and 600 kHz, respectively. In addition, the maximum concentration of NO_2^- (1.45 x 10^{-9} molmin^{-1}W^{-1}) and NO_3^- (1.67 x 10^{-9} molmin^{-1}W^{-1}), at 200 kHz after 60 minutes of sonication was found when the mixing ratio of sparged gases was 1:3 for O_2 and N_2, respectively.

$$\frac{d\left[NO_2^-\right]}{dt} = k_1\left[N_2\right]^{1/2}\left[O_2\right]^{1/2}\left[H_2O\right] - \left\{k_3\left[H_2O_2\right] + k_4\left[\bullet O\bullet\right] + k_5\left[\bullet OH\right]^2 + k_6\left[O_2\right]^{1/2}\right\}\left[NO_2^-\right]$$

$$= k_1' - k_3\left[H_2O_2\right]\left[NO_2^-\right] - k_4'\left[NO_2^-\right] \qquad (7.1)$$

$$\frac{d\left[NO_3^-\right]}{dt} = k_2\left[N_2\right]^{1/2}\left[O_2\right]\left[H_2O\right] + \left\{k_3\left[H_2O_2\right] + k_4\left[\bullet O\bullet\right] + k_5\left[\bullet OH\right]^2 + k_6\left[O_2\right]^{1/2}\right\}\left[NO_2^-\right]$$

$$= k_2' + k_3\left[H_2O_2\right]\left[NO_2^-\right] + k_4'\left[NO_2^-\right] \qquad (7.2)$$

Where $k_1' = k_1\left[N_2\right]^{1/2}\left[O_2\right]^{1/2}\left[H_2O\right]$, and $k_2' = k_2\left[N_2\right]^{1/2}\left[O_2\right]\left[H_2O\right]$ are the apparent rate constants representing the primary generation rate of NO_2^- and NO_3^- respectively within the cavitation bubble from direct ultrasound exposure. $k_4' = k_4\left[\bullet O\bullet\right] + k_5\left[\bullet OH\right]^2 + k_6\left[O_2\right]^{1/2}$ is the secondary oxidation rate constant of NO_2^- by oxidation reaction of $\bullet O\bullet$, $\bullet OH$, and O_2 in the bulk solution.

[17] A Kinetic model is a chemical-based mathematical model describing the ionic relationships between two or more chemical species. The details regarding such models are outside the scope of the thesis, but the reader may refer to[75] for further information.

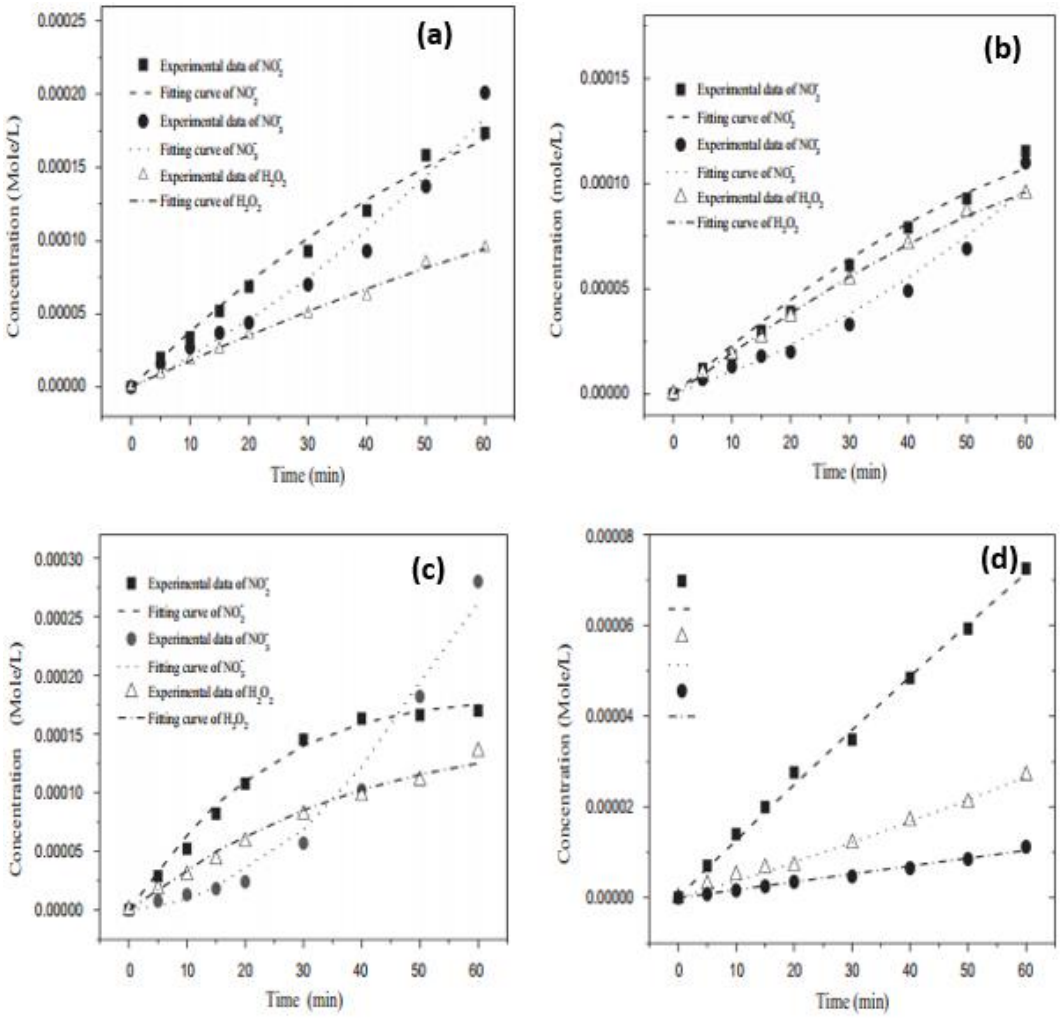

Figure 7.3: Kinetic model fits of the nitrite, nitrate, and hydrogen peroxide with the applied ultrasonic intensity of 0.69 W cm^{-2}, (a) 200 kHz, (b) 400 kHz, (c) 600 kHz, (d) 800 kHz [75].

From the literature reviewed above, the following points can be inferred:

- To generate NO_x^- the host medium (water) must be sparged with N_2, air or a mixture of N_2 and O_2. The yield is higher when air is used as the sparging gas, as seen in Table 7.1.
- Both NO_2^- and NO_3^- are simultaneously formed during sonication, with air or N_2 used as the sparging gas, as also seen in the summarised Table 7.1.

- The concentration for both NO_2^- and NO_3^- depends on the sonication period. The production of NO_2^- is favoured during the early stage of the sonication than NO_3^-. It implies there is a continued oxidation/reduction reaction going on between NO_2^- and NO_3^-.
- The production rate of NO_2^- is optimum at an ultrasound frequency of 200 kHz.
- The sonication mode used has predominantly been the continuous form, i.e., the transducer is energised from a continuous wave (CW) throughout the sonication period.

Table 7.1. Summary of the literature.

Author(s)	Transducer types/frequency used	Acoustic power /Intensity	Saturated gas used	Products formed
Schultes, *et al* (1936) [182]	Planar/300 kHz	—	H_2, N_2, & CO	NO_x^- & H_2O_2
Virtanen , *et al* (1950) [183]	Planar/300 kHz	10 W/cm^2	H_2, N_2, & CO	NO_x^-
Mead *et al* (1976) [185]	Planar/447 kHz	50 W	O_2, N_2, Air, & Ar	NO_x^-
Wakeford *et al* (1999) [177]	Ultrasonics bath/35 kHz	—	air, N_2, & Ar	NO_x^-
Supeno *et al* (2000) [186]	Planar/900 kHz	—	Mixture of N_2 & H_2	NH_3
Supeno *et al* (2000) [187]	Planar/900 kHz	27 W	Mixture of O_2 & N_2	NO_x^-
Yao *et al* (2018) [75]	Planar/200-800 kHz	100 W	Mixture of O_2 & N_2	NO_x^-

Based on this information, we shall be looking at optimising the production yield of NO_x^- at an ultrasound frequency of 200 kHz generated by a focused transducer, using air as the sparged gas. High-speed imaging will be used to monitor and record the cavitation generated during ultrasound exposure. The acoustic detection will be collected by swPCD and used to quantify the time average shock waves (V_{rms}) generated during cavitation after the driving f_0 signal is removed. The sonochemical yield will be measured using the Griess method.

7.2. Pulse width modulation technique

The efficiency of sonochemical processes can be improved through the efficient administration of the acoustic energy generated by an ultrasonic transducer. It will ensure that the acoustic energy is used effectively to generate the cavitations required for sonochemistry to proceed. One way to achieve this is through the controlled electrical excitation of the transducer. The controlled excitation of the transducer is the systematic modification of the electrical input signal so that different electrical excitation protocols other than the continuous protocol can be passed to it. One of the most commonly used methods of controlled excitation is the pulse width modulation method[18] (PWM) which can be achieved through different ways that include but are not limited to the following: If t_{on} represents the time duration for which the transducer is energised, and t_{off} the time duration for which the transducer is not excited.

- Variable frequency modulation: This is achieved by keeping either the t_{on} or t_{off} of the pulse train constant but varying the period (T), as illustrated in fig.7.4. In this case, the energy to the system is the same since the t_{on} is the same.

[18] PWM method is a control excitation technique by which the length of the pulse is varied in a pulse train.

- Constant frequency modulation: In this method, the frequency is maintained constant while both t_{on} and t_{off} are varied, as shown in fig. 7.5. Therefore, the energy to the system is not the same.

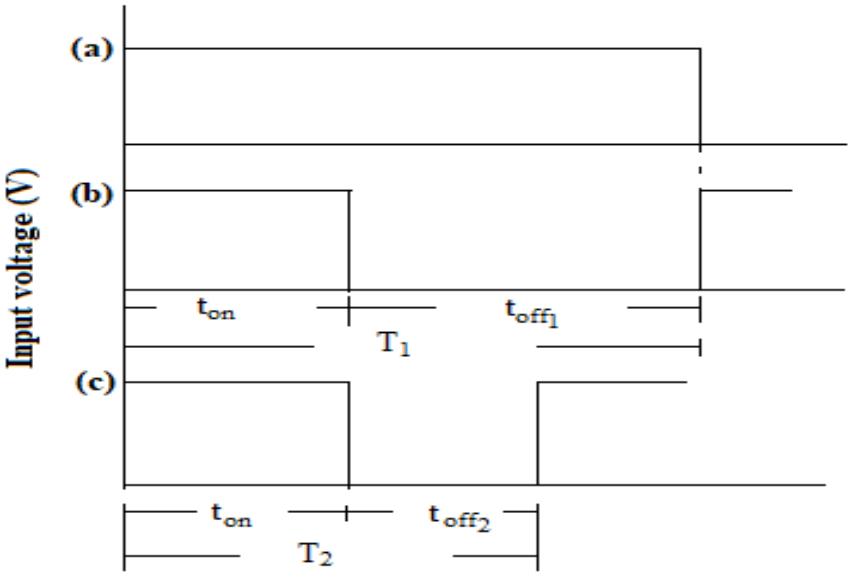

Figure 7.4: PWM method using variable frequency control scheme: (a) CW method; (b) and (c) PWM methods where the t_{on} is constant but the $t_{off1} > t_{off2}$ hence, the period $T_1 > T_2$ therefore, frequency ($f = 1/T$) is varied.

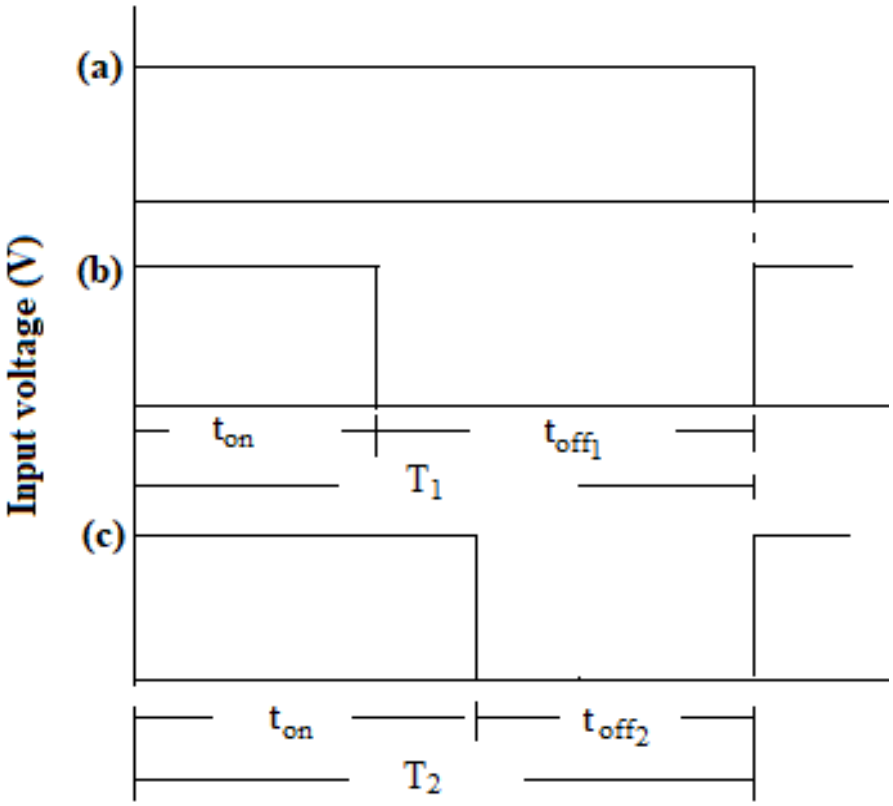

Figure 7.5: PWM method using constant frequency control scheme: (a) CW method; (b) and (c) PWM methods where both the t_{on} and t_{off} are both varied at constant period *T*.

The t_{on} is the period when the transducer is excited with the help of an appropriate input signal, while the t_{off} is the period where the transducer is not excited. Note that the excitation signal can be of different forms depending on the compatibility with a particular transducer. In either of the two methods stated above, the t_{on} and t_{off} are the variables. Therefore, the duty cycle (*K*) is defined as the ratio of t_{on} and t_{off} [188]. For a finite value of *K*, we have pulse control modulation, see equation (7.3).

$$K = \frac{t_{on}}{t_{off}} \qquad (7.3)$$

Understanding the dependency of the chemical activity induced during pulsed irradiation is very important and may serve as a guide in formulating

appropriate input protocols for the generation of effective cavitation for sonochemical activities. Henglein *et al* [189], proposed a theory that described the chemical activity as a function of the t_{on}, K, using a square wave pulse train in terms of activation (τ_1) and deactivation (τ_2) time of 'chemically active' bubbles. τ_1 is the time required for chemically active bubbles to be generated and grow, whereas τ_2 is the duration for which the chemically active vapour bubbles become completely inactive. The theory was formulated based on the following assumptions:

- The bubble is not immediately active after a single pulse but requires some time τ_1 before it starts to contribute actively to the chemical effect, at the period defined as $t_{on} - \tau_1$.
- The bubble starts to deactivate chemically during the interval between consecutive pulses (t_{off}).
- The τ_1 and τ_2 are independent of the t_{on}.
- The chemical reaction does not occur until a certain activation level is reached.

They explain the theory using four different scenarios considered in fig. 7.6.

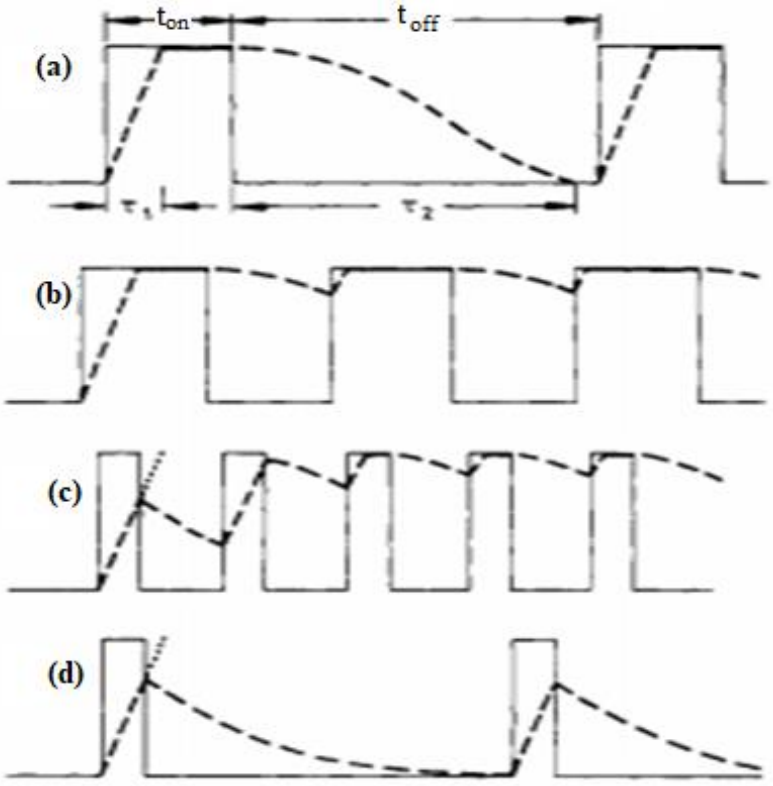

Figure 7.6: Various pulse train (full line) and system activation (dash lines) [189].

As shown in fig 7.6, the full and dash lines represent the pulse train and system activation, respectively. In the first case of fig 7.6 (a), τ_2 is less than t_{on} such that the remaining period defined as $t_{on} - \tau_1$ is used by the chemically active bubble to generate radicals. During the period of t_{off}, the deactivation of the active bubbles begins and reaches zero before the arrival of the next pulse. It implies that the next pulse has to activate the bubble again from the start. The case in fig 7.6 (b) is similar to that in fig 7.6 (a) during the period t_{on}, but the next pulse comes earlier ($\tau_2 > t_{off}$), i.e., before the active bubble is completely deactivated as in the case with fig 7.6 (a). Therefore, the protocol in figure fig 7.6 (b) is more efficient than that in fig 7.6 (a). For the case shown in fig 7.6 (c), the t_{on} is too short (i.e., $\tau_1 > t_{on}$) for the active bubble to be completely developed. Therefore, more pulses are needed before they can actively contribute chemically to radical formation. The last case shown in fig

7.6 (d) is the least efficient, where $\tau_1 > t_{on}$ and $\tau_2 > t_{off}$. It implies that the chemical reaction may not occur at all no matter the number of pulses sent [189].

Following this development, several reports have studied the effect of PWM techniques on sonochemical yield. Sun *et al*, [190] found that the sonochemical yield depends on the t_{on} as well as *K* of the applied pulse train. The efficiency of both the PWM and the CW methods were investigated on the oxidation rate of KI using an ultrasonic horn operated at 20 kHz. The authors revealed that when $K < 50\%$, with $t_{on} = 0.1$ s, there was no difference in the concentration value of the KI obtained from both PWM and CW methods. However, when the t_{on} was increased from 0.1 s to 1 s, the sonochemical yield of KI was higher with PWM compared with that obtained from the CW method. However, the yield was comparably lower than that obtained from the CW method when the t_{on} was increased from 1s to 9s. Finally, the sonochemical yield of KI has no clear performance pattern (lower or higher) in relation to that observed from the CW method for $K > 50\%$. Gutiérrez *et al* [191], claimed that the same sonochemical yield of oxidised KI was found from both PWM and CW methods at low intensity (1.3 W/cm^2) when ultrasound of 1 MHz was used. A 3 dm^3 of an aqueous solution of 0.1 M KI was irradiated with a 152 kHz ultrasound. The sonochemical yield was found to be independent of both t_{on} and K. They suggested that the successive input pulses always find the bubbles within the host in an "activated state" caused by the previous pulses irrespective of the length of the t_{off}. An efficiency improvement of up to 5 times in the sonochemical yield of I_3 under PWM was achieved compared to the CW method in [192]. The low efficiency of the CW exposure was attributed to sound propagation prevented by the degassed bubbles, which attenuated the sound pressure amplitude. The efficiency of the PWM method was found to depend on the t_{off}, at constant *K* ($t_{on} = t_{off}$ for each of the cases considered). The sonochemical yield decreased with length of t_{off}, specifically in this order $0.66 > 6.60 > 66.0$ *ms*. They opined that at a lower value of t_{off}, the sound pressure was not reaching zero (i.e., there is 'residual acoustic pressure' during shorter t_{off}).

Casadonte *et al* [193] proposed that for an equal amount of excitation time to be used for both PWM and CW methods, the peak power in the PWM method

must be modulated according to the equation (7.4). They suggested that the power modulated pulse (PMP) is the only condition for the PWM method's sonochemical yield to be higher than the CW method. The authors used an ultrasound frequency of 400 kHz, in 75 mL of potassium iodide solution (KI), operated at K = 100%, such that the peak power (P_{pulse}) under the PWM technique was twice the peak power (P_{CW}) under the CW method, see equation (7.4). The solution was sparged with Ar for 30 minutes before the initiation of sonication. The concentration of oxidised iodide was measured spectrophotometrically under both PMP and CW methods. The result obtained indicated that the sonochemical yield of oxidised KI was three times higher under PMP than the CW method.

$$P_{pulse} = P_{CW}(1+1/K) \qquad (7.4)$$

A similar PMP approach was used in [188], where 490 kHz ultrasound was generated from two transducers (50 mm-Ø) fixed at the bottom and side of a reactor (120 x 120 x 350 mm^3) for wastewater treatment. An improvement in the degradation of the wastewater pollutant and oxidation of KI (up to 15% higher at $t_{on} = t_{off} = 0.24$ s) was achieved with PWM over CW method for both separate and simultaneous excitation of the transducers. The authors attributed this improvement to residual sound pressure and the removal of 'large bubbles' that do not collapse inertially during t_{off}. The number of the large bubbles removed from within the host medium depends on the length of the t_{off}. The number of large bubbles removed increases as the t_{off} becomes longer. Large bubbles that remain without imploding disturb the sonochemical reaction. The concentration of KI obtained was higher when the side transducer was excited than when the bottom transducer was excited. They attributed this observation to the expansion in the region of a standing wave caused by the reflections from opposite sides of the reactor when the side transducer was excited. The sonochemical reaction proceeded more effectively in the ultrasonic field, forming a standing wave [194]. Recently, Patience *et al* [195] claimed that they achieved an almost equal quantity of extracted pectin during ultrasound exposure using an ultrasonic horn, which was excited from CW and PWM at K = 50%. At this value of K, the authors claimed that the PWM method consumed less than half of the total energy consumed with the CW method. They

observed many non-collapsing large bubbles (degassing bubbles) which do not contribute to the chemical effect during the CW method. Such bubbles limit the spatial region for the chemically active bubbles and reduce the ultrasound intensity by scattering and absorbing the ultrasound wave [192] [196].

The literature describes reports on performance improvement using PWM over CW technique. Therefore, there are more prospects in using the PWM method of transducer excitation. This chapter presents optimisation of the sonochemical yield of NO_x^- using the PWM method based on '*same energy criteria'*.

7.3. Same energy criteria

Energy is the physical quantity used as a medium for cost estimation of work done by an electrical device. It is also easy to monitor and quantify. The efficiency of sonochemical yield and the up-scaling issues have to be addressed to gain industrial attention. For this reason, we aim to explore the possibility of optimising the production quantity of NO_x^- with different PWM input protocols at constant input energy. Consider a sample of input protocol in fig. 7.7, showing the pulse amplitude (PA), pulse duration (PD) and pulse interval (PI) equivalent to the t_{on} and $t_{off,}$ respectively, of fig 7.6.

Following equation (7.5) [197], a constant energy scheme based on active sonication period can be formulated as follows:

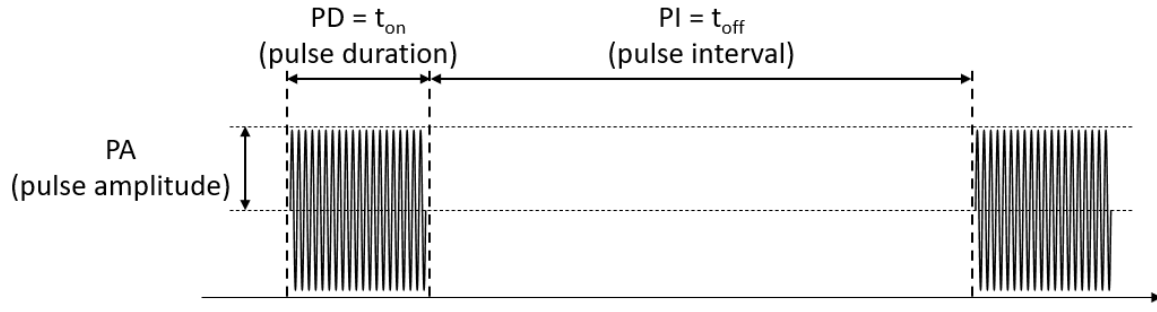

Figure 7.7: Sample of input protocol.

$$I_{spta} = f_p \int_0^{PD} p(t)^2/\rho c \, dt \qquad (7.5)$$

Where f_p is the pulse repetition frequency; p(t) is the acoustic pressure and I_{spta} is the spatial-peak temporal average intensity[19]. Although it is recognised that the I_{spta} is mostly applicable to medical ultrasound and measurements of the acoustic output of scanners. It is used here to illustrate the relationship between pressure amplitudes and acoustic intensity.

- The active sonication time is the sum of all PDs in any protocol as expressed in equation (7.6) under the PWM method.
- At the same PA, the active sonication period is the same for any protocol employed. For example, if the active sonication time is 1 s for the CW method, the 1 s under the PWM method can be chopped into *n* number of bursts such that:

  $$\sum_i^n PD_i = Active\ sonication\ period \qquad (7.6)$$

  Where *n* is the number of times, the pulse is repeated, referred to as the number of bursts.

- The pressure can be scaled to different values at a constant energy value via a corresponding scaling of the active sonication period. For example, if the pressure amplitude is doubled, the sonication period is divided by four.

For example, Table 7.2 consists of six random input protocols at constant PA and active sonication period (5 s). The input energy is the same based on the proposed scheme.

[19] I_{spta} is the highest intensity measured at any point within the ultrasound beam, averaged over the pulse repetition period.

Table 7.2. A random sample of input protocols based on the same energy criteria.

Input protocol	PA [mV]	PD [ms]	PI [ms]	Bursts
1	500	10	10	500
2	500	10	25	500
3	500	20	50	250
4	500	20	75	250
5	500	5	25	1000
6	500	5	75	1000

The underpinning hypothesis of this research is that the higher number of cavitating bubbles that are observed within the HSIs, and detected with swPCD, the higher should be the sonochemical yield of NO_x^-.

7.3. Materials and Methods

7.3.1 Acoustic characterisation of a sonochemical reactor

This section presents both finite element simulation and experimental evaluation of acoustic characterisation of the glass (SiO_2) reactor used for the sonochemical synthesis of NO_x^-. It is recognised that this is not an ideal reactor commonly used for sonochemistry or ultrasound transmission since its characteristic acoustic information is not available, as may be the case with a commercial sonoreactor. We have, however, acoustically characterised the reactor via simulation and proceeded to demonstrate exposure parameter optimisation for sonochemistry.

The ultrasound source is the focused transducer (H-149, Sonic Concepts, Bothwell, WA), driven at f_0 = 200 kHz through a 500 W power amplifier (Electronics & Innovation, Model 1040L). The experimental arrangement for the acoustic characterisation is shown in fig. 7.8.

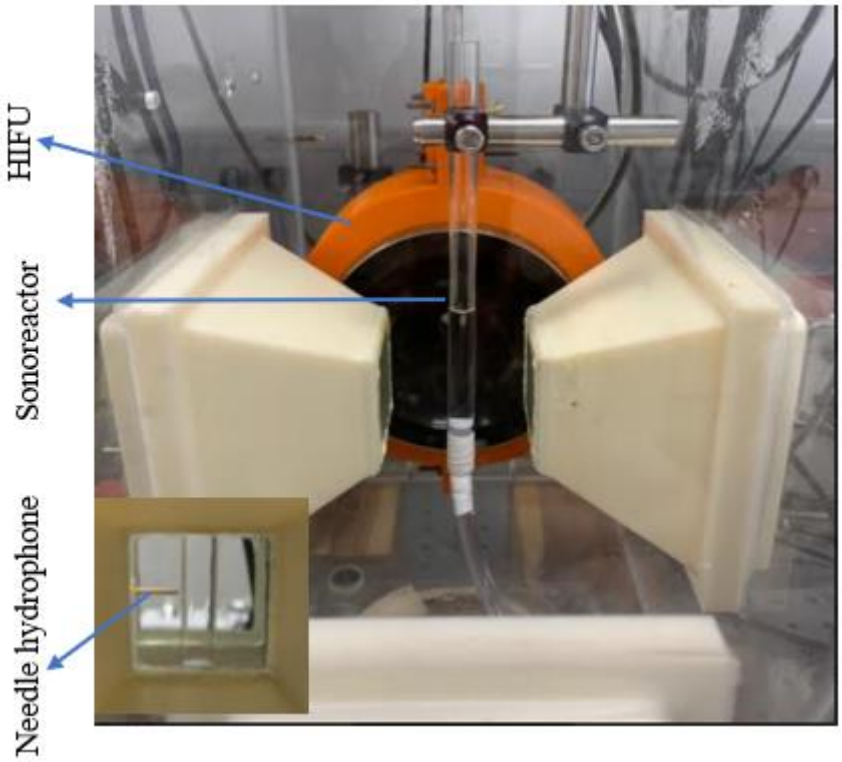

Figure 7.8: Experiment setup: showing the focused transducer (HIFU), the sonoreactor placed at the focus. The needle hydrophone is placed directly opposite the focused transducer, at ~ 5mm behind the sonoreactor. The inset illustrates the position of the hydrophone with respect to the sonoreactor.

7.3.2 The experimental arrangement

The results described here were obtained with the focused transducer arranged within a customised tank measuring 420 × 438 × 220 mm^3 as shown in fig. 7.8. The tank was ¾ filled with deionised, degassed water. A 0.2 mm PVdF needle hydrophone (NH) from Precision Acoustics Ltd was positioned directly opposite the focused transducer and used to measure the focused ultrasound (with and without the sonoreactor in place). The needle hydrophone was calibrated by the National Physics Laboratory (NPL), where magnitude sensitivity and uncertainty at 200 kHz are 32 nV/Pa and 9%, respectively. The output from the NH was connected to a DC coupler (DCPS663) with data collected at a sampling rate of

3.125 GS/s on an oscilloscope (Tektronix 5 series, Berkshire UK). Before the hydrophone undertook the acoustic measurement, the transducer's focus was found by manually performing 3-D scanning of its field with a hydrophone using an x, y, z manipulator fitted on the Sonoptic tank described in §3.1. The Sonoptic tank. The voltage amplitude of sinusoidal waveform output from a signal generator (RIGOL DG 4102) was varied from 50-1100 mV_{pp} and passed to a power amplifier during acoustic measurements. The first acoustic measurement set was undertaken to measure the acoustic pressure generated by the transducer at the focus. The second acoustic measurements were done when the sonoreactor was placed at the focus, and the hydrophone was placed at ~ 5 mm behind the sonoreactor (inset of fig. 7.8), in the far-field beyond the focus. The last set of acoustic measurements was undertaken when the sonoreactor was carefully removed while maintaining the far-field position of the hydrophone. Note that care should be taken while using the hydrophone to collect acoustic data to avoid cavitation damage. Therefore, we ensured the water used was well degassed so that there was no cavitation at the investigated amplitudes during this calibration experiment.

The setup in fig. 7.8 was used for the sonochemical fixation of N_2 only that the NH was replaced with the swPCD (described in §3.3 Shock wave passive cavitation detector). The liquid in the sonoreactor was sparged with air from a 100 kg cylinder (BOC, Linde Group) throughout an experiment, at a constant rate of 34.9 mL/min monitored with an in-line flow meter (Masterflex PMR1-010531), via the attached delivery tube connected to the base of the sonoreactor, fig 7.8. The base of the sonoreactor is fitted with multi-orifice splitters, which ensure the sparged air is split within the reactor. For each experiment round, 6 mL of deionised water was placed in the sonoreactor and pre-sparged with air for 20 minutes before sonication. The acoustic data was undertaken with swPCD for each experiment at a sampling rate of 12.5 MS/s.

The investigation of the effect of PI, at separate values of PD, on the sonochemical yield of NO_2^- was first carried out to obtain the optimum PI value. We then applied the optimum value of PI in investigating the effect of PD on the sonochemical yield of NO_2^-.

High-speed imaging of the sonication process was undertaken with the FASTCAM SA-Z 2100 K (Photron, Bucks UK, 128 GB of RAM) recorded at 20000 fps, with a 159 ns shutter time, through a macro-lens (EX DG, 24-70 mm 1:2.8, Sigma, Hertfordshire UK) and a 36 mm extension tube. At this frame rate, imaging was achieved over 768 × 768 pixels with a resolution of 20 μmpixel^{-1}. Both the HSC and the oscilloscope were systematically triggered simultaneously with the help of the delay generator (DG535, Stanford Research Systems, Sunnyvale USA). At the end of each sonication period, the amount of NO_2^- produced was analysed using the Griess method briefly described in §7.3.4 Griess test.

7.3.3. Simulation using OnScale finite element analysis software

The finite element method (FEM) is a numerical method for solving engineering, mathematics, and physics problems associated with complicated geometries, loadings, and material properties where analytical solutions cannot be obtained [198]. OnScale software is used here because of its efficiency in solving wave propagation and piezoelectric problems. The current task involves; the simulation of the focused transducer based on the available information and the simulation of the focused transducer with the sonoreactor placed in situ. The following steps were taken to realise the OnScale simulation:

- As shown in fig. 7.9, a 3-D model is created to specification in computer-aided design (CAD) using Autodesk Fusion 360. Note that the 3-D model takes longer simulation time and large memory. Therefore, the model was constructed in quarter mode, which is symmetrical about the x- and y-axis, to reduce the simulation time.
- Importing the designed model into OnScale.
- Assigning the selected project materials to the model.
- Adding suitable input function.
- Configuring the mesh for the model.
- Setting the domain boundaries.

The specifications of the focused transducer as obtained from its catalogue are an internal diameter of 20 mm-Ø, an outside diameter of 110 mm-Ø, a focus at 68 mm, and its radius of curvature is 70 mm. The active material used was not stated in the catalogue; however, lead zirconate titanate (PZT4) was used for the simulation.

After the successful simulation of the focused transducer to achieve both the pressure field distribution and pressure value at the focus, we then modified the model by placing the sonoreactor at the focus field of the transducer. The length and thickness of the sonoreactor are 130 and 1 mm, respectively. At the same time, its diameter was changed between 10 mm-Ø and 20 mm-Ø to assess the effect of sonoreactor diameter on the transmission of ultrasound to the host medium within. The model is shown in fig. 7.9, including surrounding water, was simulated to capture the acoustic pressure field and values. We also examined the effect of moving the sonoreactor ± 2mm from the focus point (68 mm) along the z-axis. See (B.2 Onscale simulation codes) for the simulation codes.

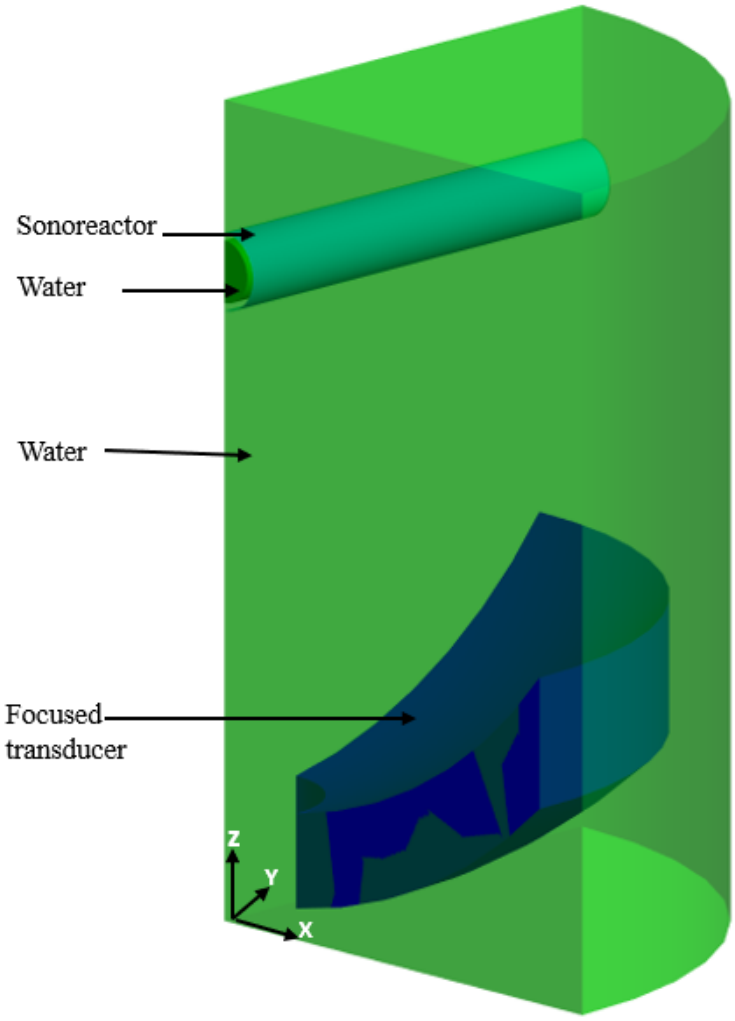

Figure 7.9: Showing 3-D quarter model symmetry about x and y-axis readying for simulation in OnScale software, scale provided by 10 mm-Ø Sonoreactor.

The result from pressure distribution around the focal region of the focused transducer when excited from a sine wave of 200 V_{pp}, 200 kHz, and 30 cycles are presented in this section. Fig. 7.10 (a) was obtained from the OnScale simulation of the model described in fig. 7.9. From this figure, the focal length, focal width, and the peak focal point within the pressure distribution of ~ 22.5 mm, ~ 5 mm, and ~ 68 mm, respectively, were found. A movie showing the build-up process of the pressure field is attached as supplementary material for this thesis. Fig. 7.10 (b) is the independent 3-D scanning of the acoustic field from the focused transducer

carried out by a member of CavLab research group. The scanning was done with a sinusoidal source at 225 kHz, 10 mV, 50 cycles, via a 500 W power amplifier (Model 1040L). The focal length and width of the pressure distribution around the focal region from the 3-D scanning were observed as ~ 24 mm, and ~ 4 mm, respectively.

The results from both the simulation and 3-D scanning of the acoustic pressure field of the transducer are comparable in terms of focal length and focal width. These values compare well to the manufacturer specified for focal length and width of 22.36 mm and 4.87 mm, respectively [199].

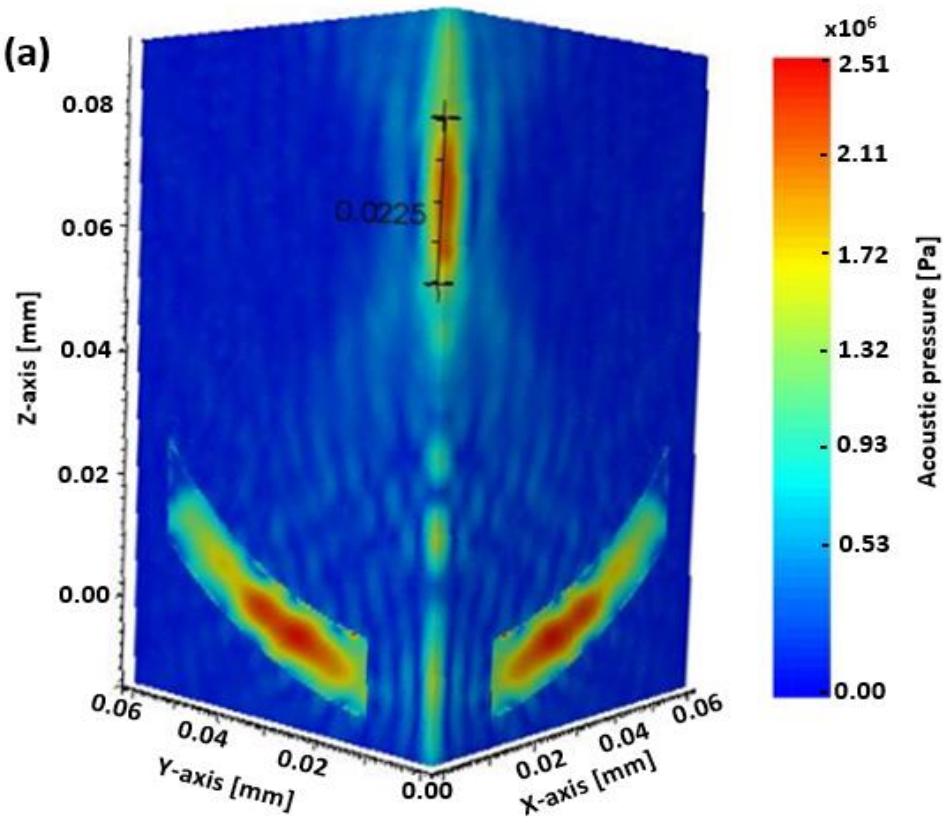

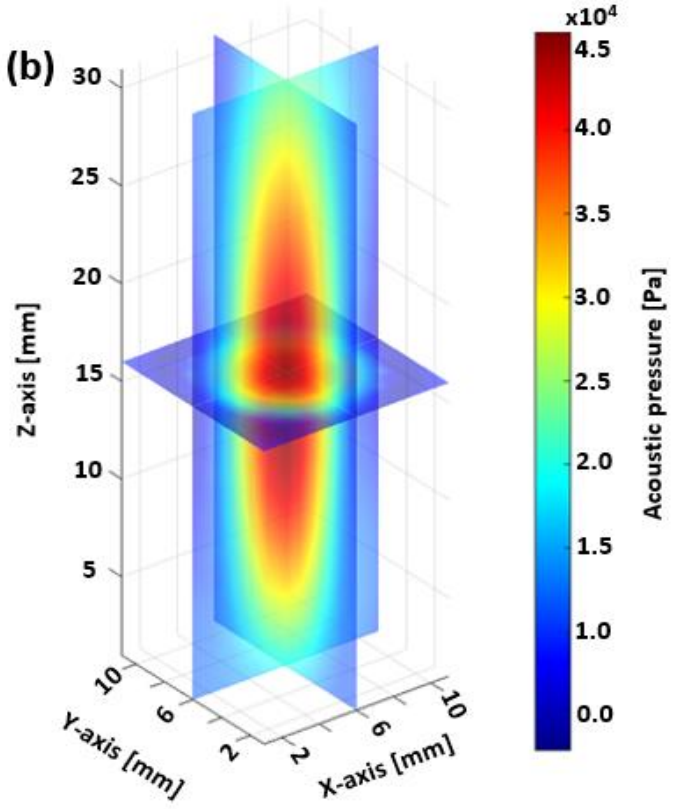

Figure 7.10: Field map of HIFU (H-149) from (a) simulation using OnScale at 200 kHz, 200 Vpp, 30 cycles, and (b) 3-D scanning using 0.2 mm hydrophone at 225 kHz, 10 mV_{pp}, 50 cycles.

7.3.4 Griess test

Detection of NO_2^- was carried out through the Griess method. The sample after sonication was added to a mixture of 0.0116 M sulfanilamide and 6 M of hydrochloric acid (HCL). A 3.86 mM coupling agent (n-(1-naphthyl)ethylenediamine) was added after 2 minutes. The mixture was left for an additional 20 minutes, after which a UV/Vis spectrum was collected over a range of 700 – 400 nm, as shown in fig 7.11. The λ_{MAx} for the UV/Vis active compound is 540 nm. A calibration curve was constructed by performing this test on NO_2^- solutions of known concentrations. Thus, by comparing the recorded absorbances

of the test solutions with the calibration curve, the NO_2 concentrations could be obtained [200].

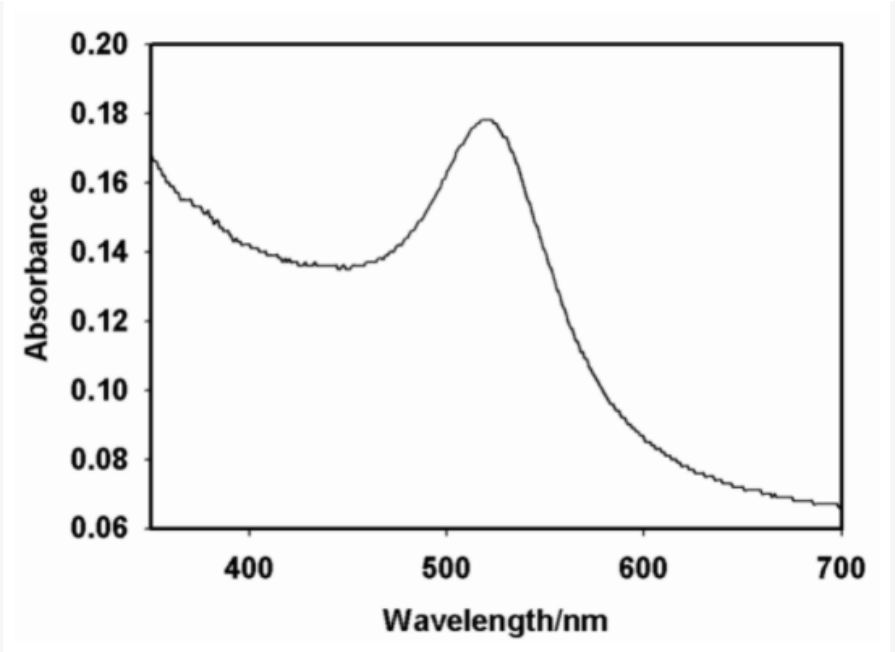

Figure 7.11: Showing UV/Vis spectrum for NO_2^-, the peak of the spectrum is read and compared with the standard curve for concentration estimation.

7.3.5 Estimation of acoustic energy

To obtain the acoustic energy in the sonoreactor, we first obtained the spatial peak pulse average intensity (I_{SPPA}) using the expression in equation (7.6). I_{SPPA} is the highest intensity measured at any point in an ultrasound beam average over the temporal duration [201].

$$I_{SPPA} = \sum (p(t)^2/\rho c)\ x\ {}^{1}/_{f_s} \qquad (7.6)$$

Where p(t) is the measure peak pressure, obtained via the NH described in §7.3.3.1; ρ, c are the density of host and speed of the sound in the host respectively; f_s is the sampling frequency. The acoustic energy (E) is obtained using equation (7.7) [202].

$$E = I_{SPPA}\ x\ Beam\ area \quad (7.7)$$

The beam area of the acoustic field is the area within the focus of the transducer where the sonoreactor was placed. The approximate beam area was obtained using OnScale simulation.

7.4. Results

7.4.1 Acoustic pressure with and without sonoreactor

Fig. 7.12(a) and (b) are the acoustic pressure waveforms obtained from the experimental measurement and OnScale simulation, respectively. They both show a similar attenuation effect of the sonoreactor taken at the approximately same position (i.e., z = 78 mm).

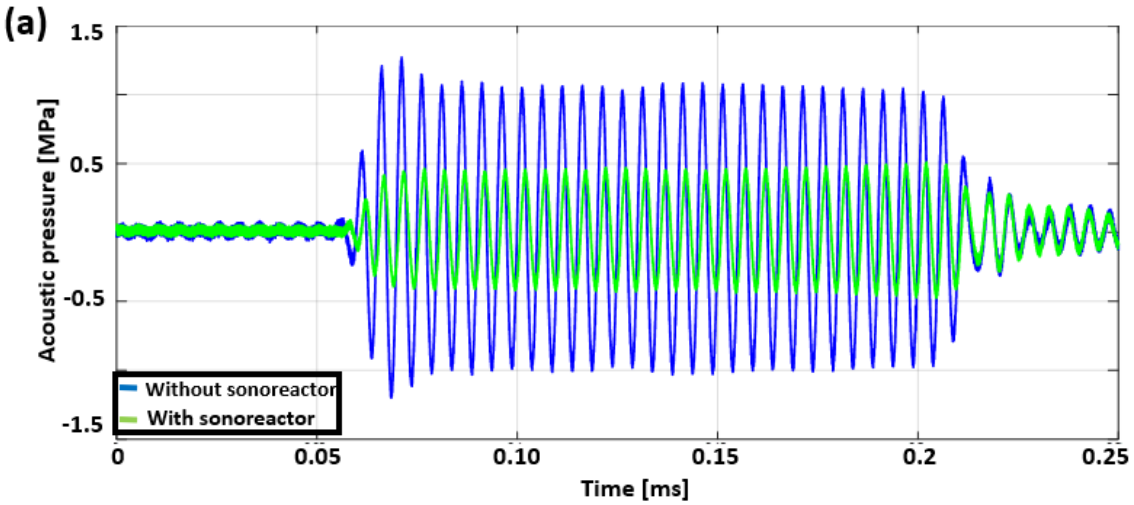

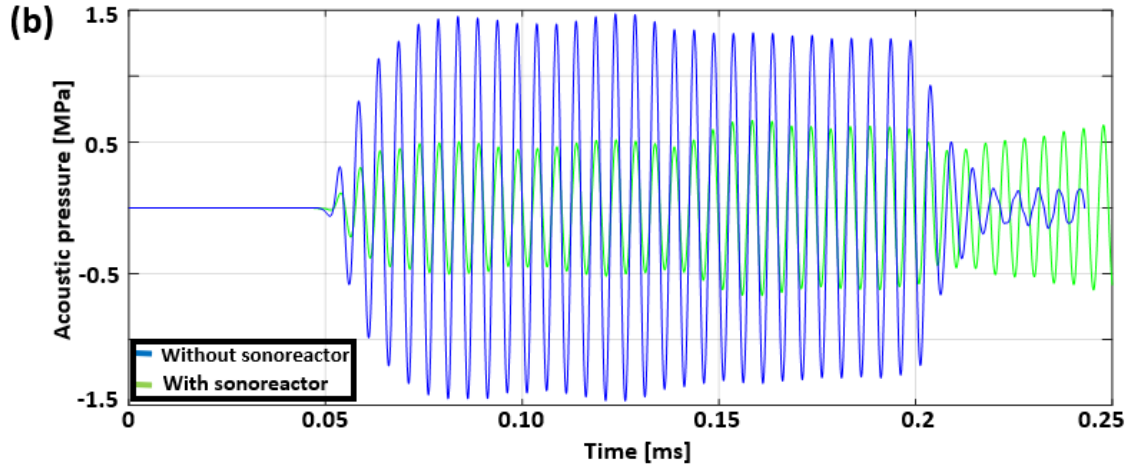
(b)
Acoustic pressure [MPa]
1.5
0.5
-0.5
-1.5
0
0.05
0.10
0.15
0.2
0.25
Time [ms]
Without sonoreactor
With sonoreactor

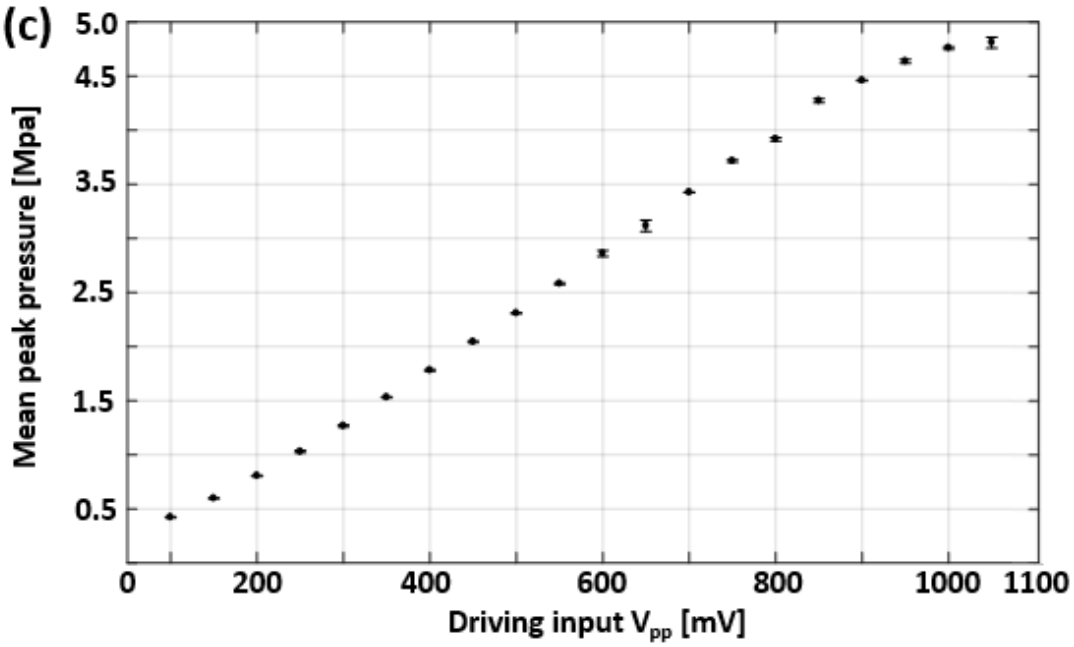
(c)
Mean peak pressure [Mpa]
5.0
4.5
3.5
2.5
1.5
0.5
0
200
400
600
800
1000
1100
Driving input V_{pp} [mV]

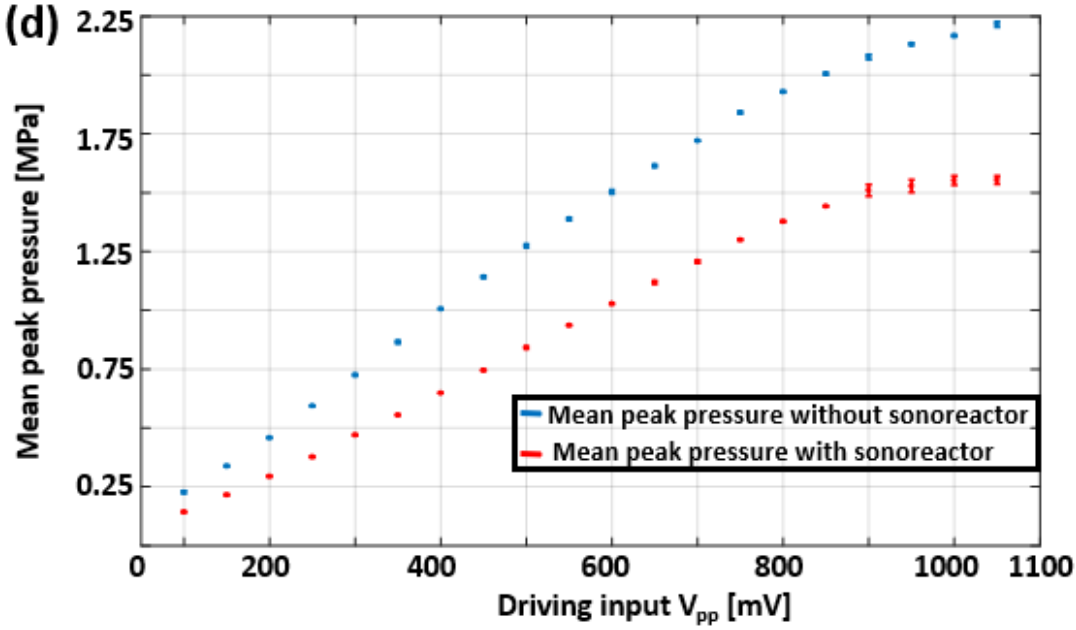

Figure 7.12: Showing (a) Measured mean acoustic pressure waveform with and without sonoreactor at 400 mV_{pp} 200 kHz, and 30 cycles using hydrophone placed at ~ 5 mm behind the sonoreactor (b) Acoustic pressure waveform obtained from the simulation at z = 78 mm, with an input voltage of 200 V_{pp}, 200 kHz, and 30 cycles. (c) Measured mean acoustic pressure at the focus of the transducer; (d) Measured mean acoustic pressure with and without sonoreactor at ~ 78 mm (i.e., ~ 5 mm behind the sonoreactor) as the input voltage varied from 100-1100 mV_{pp}, at 200 kHz, and 30 cycles with 0.2 mm hydrophone.

The mean ± standard deviation of measured peak positive pressure from five sets of acoustic data taken at the same setting was obtained and plotted against the voltage amplitude of the driving input for all the data shown in fig. 7.12 (c) and (d). From fig. 7.12 (c), the mean peak positive acoustic pressure measured at input voltage amplitude of 1000 mV_{pp} is 4.69 ± 0.42 MPa. Also, fig. 7.12 (d) was obtained in the same manner but at a far-field from the focused transducer with and without the sonoreactor. It can be seen from fig. 7.12 (d) that the acoustic attenuation offered by the sonoreactor used in this experiment at voltage amplitude of 1000 mV_{pp} is ~

0.3 MPa. It is the expected attenuation at the centre of the sonoreactor, as estimated from fig. 7.12 (d).

7.4.2 Sonochemical yield of NO_2^-

The literature reviewed in §7.1 revealed that fixing N_2 using air as the sparging gas results in the simultaneous formation of both NO_2^- and NO_3^-. It implies that the cavitation generated from each input protocol is used to produce NO_x^-, and not just NO_2^-. However, we only present the concentration of the NO_2^- despite efforts to gain access to the equipment required to quantify the concentration of the NO_3^-.

The results sections below are organised as follows: §**7.4.2.1** presents the dependence of $\bar{V}_{rms}$/ NO_2^- concentration on the variation of PA at constant PI, PD and bursts number. §**7.4.2.2** presents the variation of $\bar{V}_{rms}/NO_2^-$ concentration against PI at a different PD value under the same energy criteria. Finally, the effect of varying the PD at constant PI on the $\bar{V}_{rms}/NO_2^-$ concentration is presented in §**7.4.2.3**.

7.4.2.1 Effect of varying pulse amplitude at constant PD, PI and Burst on the yield of NO_2^-

In this section, we present the effect of varying PA at constant values of PD = 4 ms equivalent to 800 cycles at 200 kHz, PI = 80 ms, and the number of bursts = 1000. Since both the PD and the number of bursts of the input protocol are constant, the increase in the PA would lead to an increase in the input energy to the transducer.

The cavitation emission signals collected by the swPCD for each input protocol were processed by filtering off the f_0 (200 kHz) component. The mean ± the standard deviation (represented with the error bars) of the V_{rms}, ($\bar{V}_{rms}$), over five

sonications at the same protocol were obtained. The results in fig. 7.13 show that the higher the value of PA of the electrical signal, the higher the cavitation generated, as seen in both numbers of cavitating bubbles shown from the two bursts in HSIs of fig. 7.13 (a) and the obtained swPCD $\bar{V}_{rms}$ values in fig. 7.13 (b). Hence, the corresponding effect of changing the values of PA on the sonochemical yield of NO_2^- is shown in fig. 7.13 (c). This shows that the higher the number of cavitation which can be visibly observed via HSI, the higher the sonochemical yield of NO_2^- generated. For the rest of this investigation, constant PA of 1000 mV_{pp} was used.

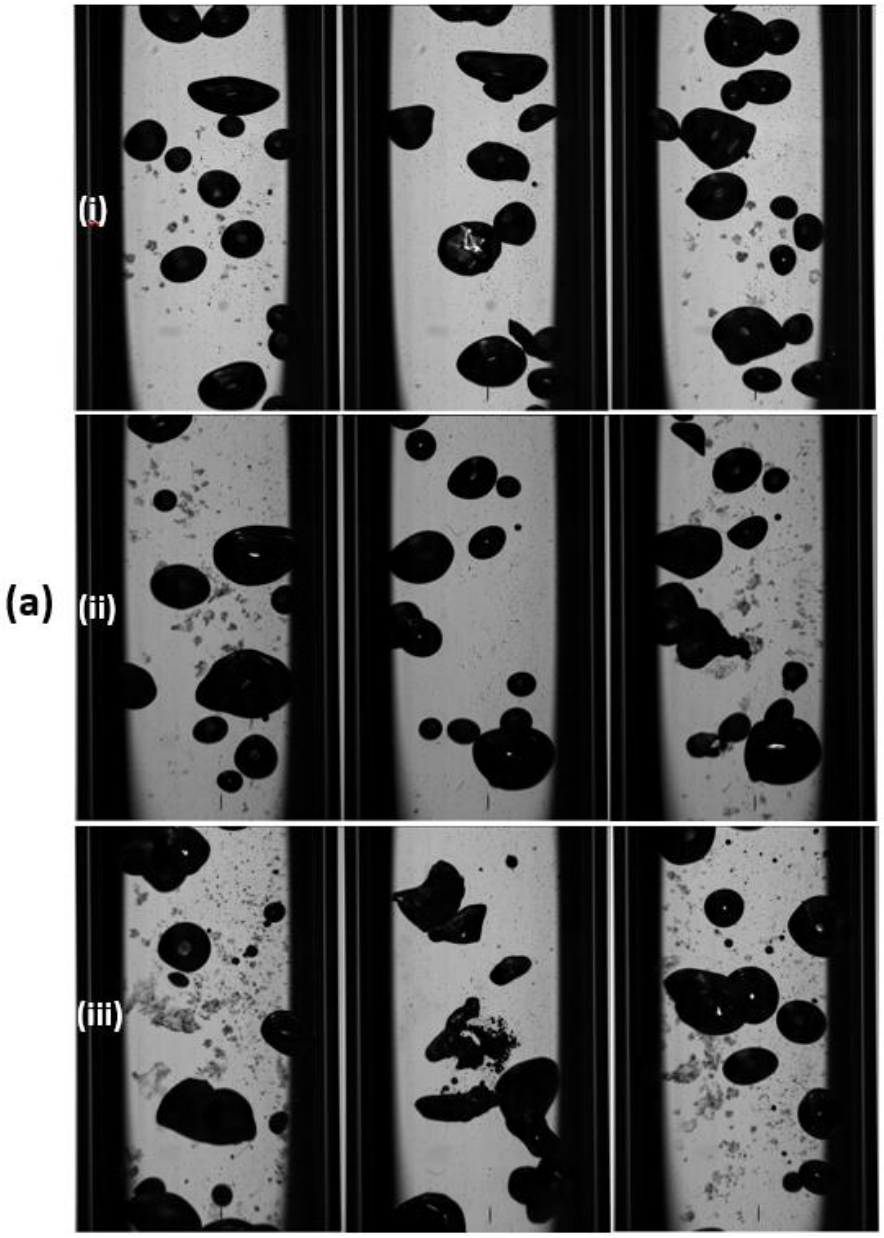

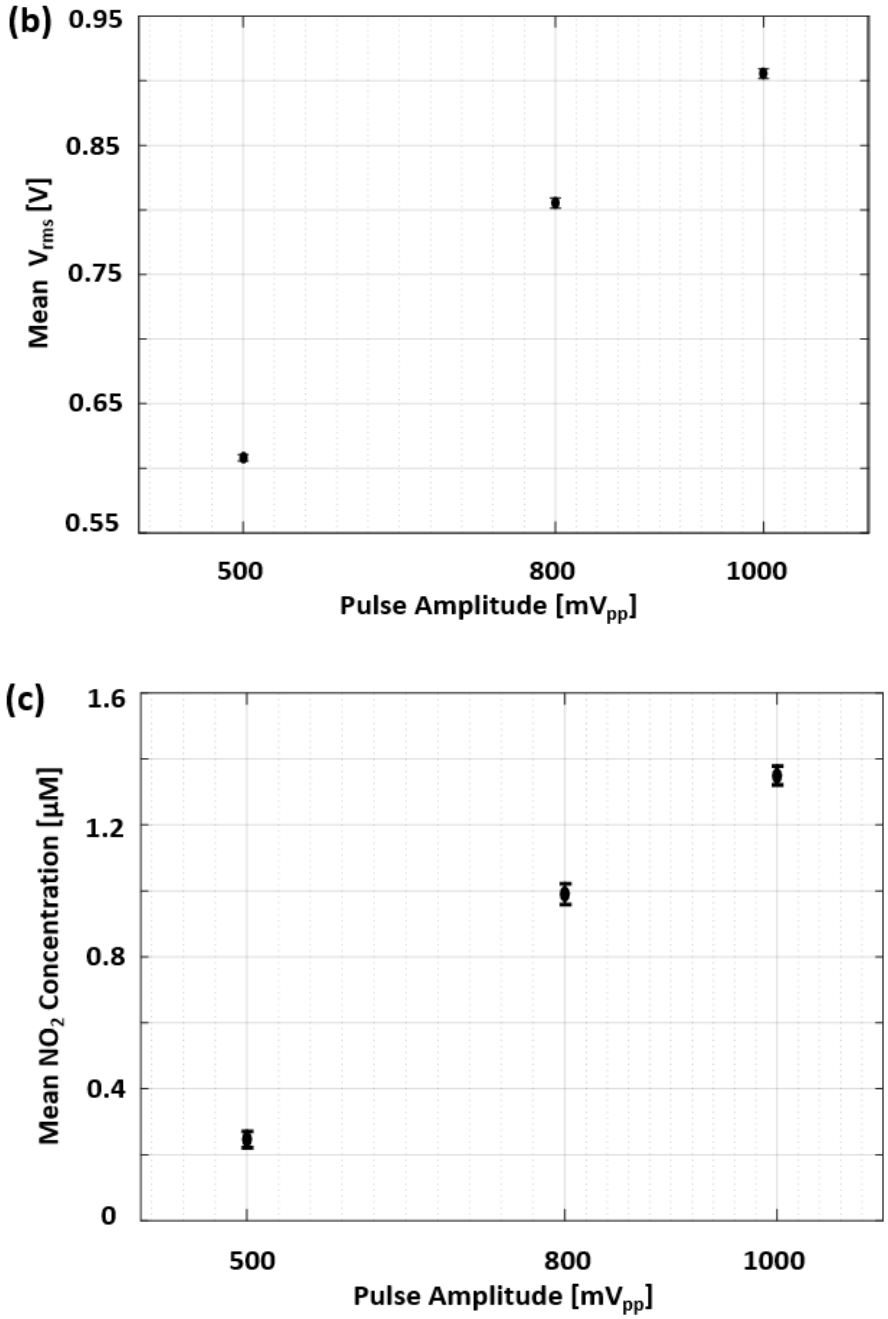

Figure 7.13: Effect of varying pulse amplitude (a) High-speed imaging from two bursts separated by PI collected at 20,000 fps, showing the cavitating bubbles (smaller) and the sparged air (bigger) inside the 10 mm-Ø sonoreactor; the scale is provided by the size of sonoreactor, (i) at PA of 500 mV_{pp}, (ii) at PA of 800 mV_{pp}, and (iii) at PA of 1000 mV_{pp}; (b) on the mean time average shock wave content $\bar{V}_{rms}$ (c) on the mean NO_2^-

concentration; at constant values of PD = 4 ms, PI = 80 ms, and number of bursts = 1000.

7.4.2.2 Effect of varying PI at separate values of PD on the yield of NO_2^-.

This section presents the effect of PI variation at different constant PD values (i.e., when PD = 2, 3, 4, and 5 ms) under the same energy criteria. The PA was maintained at 1000 mV_{pp}, the number of bursts was modified at different separate values of PD to deliver equal sonication energies for each exposure, as shown in Table 7.3.

Table 7.3 Input protocols at constant energy for varying PI

Input voltage [ms]	PD [ms]	Bursts
1000	2	2000
1000	3	1333
1000	4	1000
1000	5	800

Based on the set of input protocols shown in Table 7.3, the results in fig. 7.14 (a) and (b) were obtained. Fig. 7.14 (a) represents the plot of $\bar{V}_{rms}$, against the PI. Fig. 7.14 (b) are the corresponding plot of the mean NO_2^- concentration against PI, for values of PD = 2, 3, 4, and 5 ms.

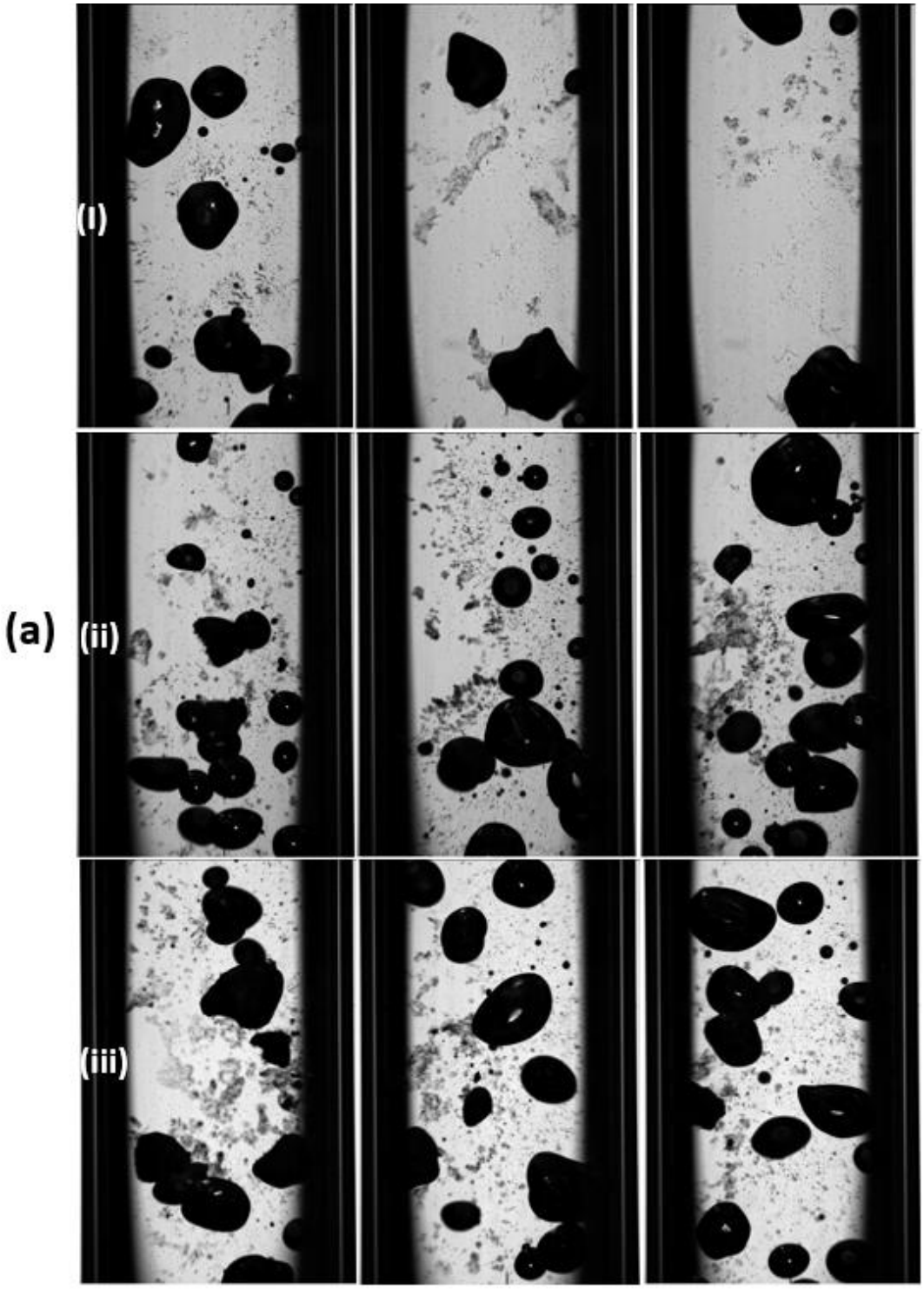
(a)
(i)
(ii)
(iii)

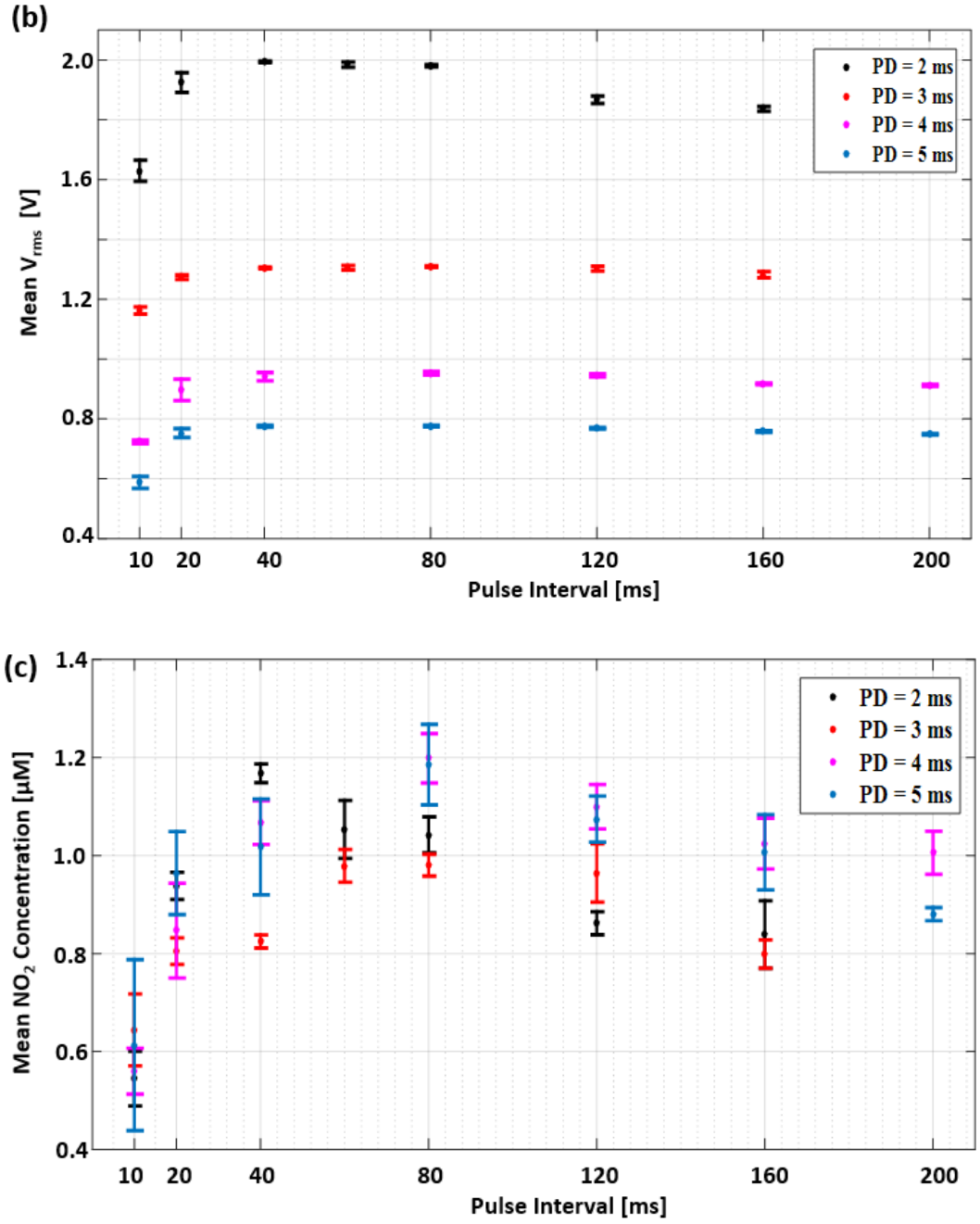

Figure 7.14: Effect of variation of pulse interval (PI) at constant pulse duration (PD) of 4 ms, and peak-to-peak pulse amplitude (PA) of 1000 mV_{pp}; (a) High-speed imaging from three bursts collected at 20,000 fps, showing the cavitating bubbles (smaller) and the sparged air (bigger) placed in the 10 mm-Ø sonoreactor (i) PI = 10 ms, (ii) PI = 40 ms (iii) PI = 80 ms, (b) on the mean time average shock wave content, $\bar{V}_{rms}$ (b) on the mean NO_2^- concentration.

The HSIs in fig. 7.14 (a) (i) show that at a low value of PI, the sparged air could not saturate the sample in the sonoreactor before the arrival of the next pulse. Because the sparging gas bubbles cannot pass the transducer's focus, there is a resultant large, trapped bubble inside the sonoreactor, preventing effective cavitation. This large bubble was not observed when the PI was 40 ms fig. 7.14 (a) (ii), and 80 ms fig. 7.14 (a) (iii). The results in fig. 7.14 (b) and (c) show the same overall trend in the optimum value of PI for different constant values of PD in terms of swPCD $\bar{V}_{rms}$ and NO_2^- concentration. At a constant PD = 2 ms, the optimum value of PI for both $\bar{V}_{rms}$ and NO_2^- concentration is 40 ms, whereas it is 80 ms for the rest of the PD values (i.e., 3, 4, and 5 ms) used. Fig. 7.14 (b) shows that the $\bar{V}_{rms}$ increases with the decrease in the value of PD. However, the production of NO_2^- is favoured at a longer value of PD, as shown in fig. 7.14 (c).

7.4.2.3 Effect of varying PD at constant PI on the yield of NO_2^-

This section presents the effect of varying PD at the constant optimum value of PI = 80 ms. The PA was maintained at 1000 mV_{pp}, the number of bursts was modified based on Table 7.3 for the same energy criteria.

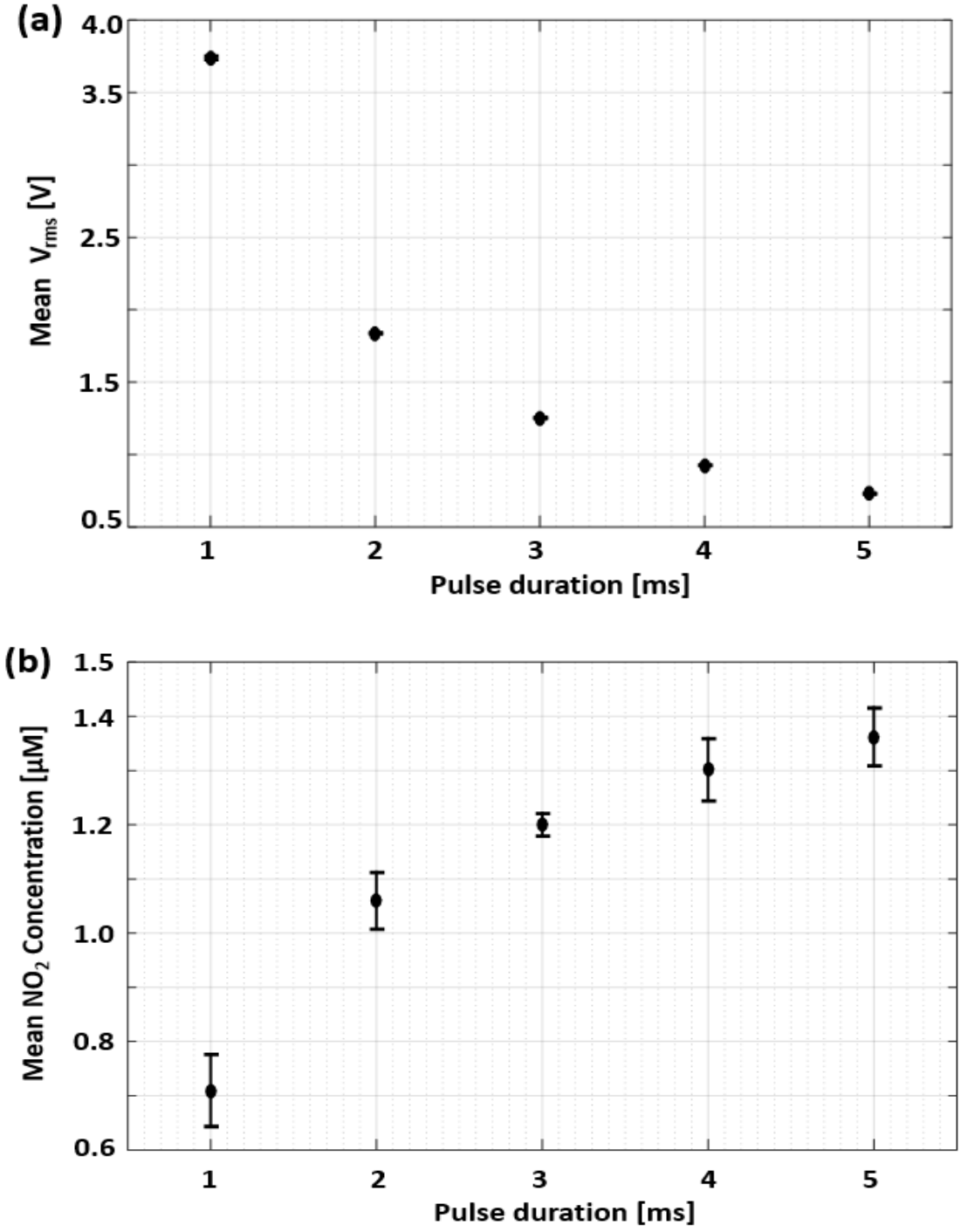

Figure 7.15: Effect of variation of PD on (a) mean time average shock wave content, $\bar{V}_{rms}$, and (b) mean NO_2^- concentration; at same energy criteria (PA 1000 mV_{pp}) and constant PI of 80 ms.

The results presented in fig. 7.15 (a) show that the $\bar{V}_{rms}$ increases as the PD decreases, having a maximum when the PD is 1 ms and minimum at PD equal to 5 ms. However, the reverse was the case for the sonochemical yield of NO_2^-, which increased with increasing PD. This result does not support our hypothesis; possible reasons why it is so are given in the next section.

7.5. Discussion

The result in fig. 7.13 shows that the higher the value of PA of the electrical input signal to the transducer, the higher the number of cavitating bubbles, as seen from the HSI in fig. 7.15 (a) (i-iii). Increasing the PA of the electrical input signal leads to the increase in the acoustic pressure generated by the HIFU, as shown in fig. 7.13 (a) and (b). Higher acoustic pressure produces more active cavitation from numerous nucleating sites within the water sample in the sonoreactor. The increase in the number and size of active cavitating bubbles led to generations of more shock waves which were detected and quantified, as shown in fig. 7.15 (b). The corresponding sonochemical yield of NO_2^- also increased with the increase in the cavitation generated, as shown in fig. 7.15 (c). Islam *et al* [203], observed an increment in the production of H_2 as the acoustic intensity was increasing. They attributed it to the increase in the expansion and compression size of the bubbles with increasing acoustic power. This leads to a higher bubble temperature at this highly compressed state. It was also suggested that the amount of water vapour that diffused inside the cavitating bubbles is higher at a higher expansion state due to high acoustic pressure. These two phenomena promote the formation of more free radicals inside the bubble at higher intensity [204].

Fig. 7.14 (b) and (c) show the effect of variation of length of PI on both the mean sonochemical yield of NO_2^- and the $\bar{V}_{rms}$ of the acoustic emission. The $\bar{V}_{rms}$ depends on both the PI and PD, as different peaks of $\bar{V}_{rms}$ were observed at the different optimum values of PI, depending on the value of PD. From fig. 7.14 (b), the peak of $\bar{V}_{rms}$ was observed at PI of 40 ms when the PD was 2 ms. An optimum PI of 80 ms was observed for the PD values of 3, 4, and 5 ms. The $\bar{V}_{rms}$ was lowest

at the shortest length of PI = 10 ms for all the PD considered. It is because the sparged air could not saturate the sample (host medium) before the next pulse train. The formation of a large bubble resulting from the accumulation of the sparged air gas was observed in the HSI, as shown in fig. 7.14 (a) (i). Therefore, there is a reduction in the number of active cavitating bubbles leading to a reduction in the $\bar{V}_{rms}$. The observed low value of $\bar{V}_{rms}$ at longer PIs of 120, 160, and 200 ms was due to the reduction in the number of active cavitating bubbles at these PIs. So, each pulse train has to start the activation process from the beginning [189]. It implies that the number of sonochemical active cavitation bubbles decreases with an increase in the length of PI. It is, therefore, necessary to find an optimum PI to keep the cavitating bubbles in an active state for sufficient nuclei-replenishment in the host medium. The sonochemical yield of NO_2^- shows a similar trend with the $\bar{V}_{rms}$ in respect to the optimum PI values at the same PD, as shown in fig. 7.14 (c). Gutiérrez *et al* [191], found that the sonochemical yield of oxidised KI decreased with t_{off} (PD) in this order 0.66 > 6.60 > 66.0 ms, which was attributed to sound pressure not reaching zero (i.e., 'residual acoustic pressure') during a shorter duration of a t_{off}. Xu *et al* [188], also opined that short PI allows the remnant of active bubbles to be present before the arrival of the next pulse. The removal of inactive bubbles (larger) takes place during PI.

The results in fig. 7.15 (a) and (b) show the variation of PD on both the $\bar{V}_{rms}$ and the mean sonochemical yield of NO_2^- at a constant PI of 80 ms. The observations in fig. 7.15 (a) show that the lower the value of PD, the higher the $\bar{V}_{rms}$ obtained from the acoustic emission. This observation could be explained as; at a lower PD value, the sample contains mostly active cavitating bubbles that collapse violently (inertially). The short PD value does not support inactive bubbles since the excitation pressure was off during the PI. It implies that each pulse train with a shorter PD value generates mostly active cavitating bubbles leading to more SWs. Hence, there is an increase in the $\bar{V}_{rms}$ value obtained from the acoustic emission. On the other hand, inactive bubbles that do not collapse violently are supported at a longer PD value, generating low-peak SWs [188].

Conversely, the sonochemical yield of NO_2^- was found to increase with an increase in the value of PD, as shown in fig. 7.15 (b). This observation could be due to the lack of an assay for the NO_3^- concentration, which is expected to be simultaneously generated together with NO_2^- during sonication [177][187]. Another way to explain this observation is by using the sono-mechanism involved in the generation of NO_x^- during sonication. Though, the actual mechanism remains unclear [177]. Some researchers opined that several reactions that lead to the formation of (HNO_2, NO_2, HNO_3, NO_x H_2O_2, etc.) occur in the gas phase of the cavitating bubbles [177][187][83][12][69].

Mišík *et al* [59] found that approximately 45% of NO_2^- formation occurs in the liquid host; the remaining was likely formed either in the gas-phase of the cavitation bubbles or from the reaction of the intermediates formed inside the cavitating bubble. A chemical reaction can take place at the liquid region, interface region, or inside the cavitation bubble, during cavitation depending on radicals lifetime [205]. Overall, the observation in fig. 7.15 (b) indicates that the PD has a significant impact on the sonochemical yield of NO_2^-. It possibly suggests that the formation of NO_2^- occurs inside the cavitating bubbles since the bubble lifetime increases with PD.

The maximum NO_2^- obtained was ~1.81 x 10^{-6} mol min^{-1} W^{-1}, observed at the PD of 5 ms. However, this observation seeks more clarification on the actual sono-mechanism involved in N_2 fixation and the anomaly result relationship observed between the $\bar{V}_{rms}$ and the mean NO_2^- concentration.

7.6 Conclusion

The sonochemical generation of NO_2^- using ultrasound generated from the focused transducer has been considered. The transducer was excited by different electrical input protocols based on PWM for both optimum cavitation generation and sonochemical yield of NO_2^-. Our investigations reveal that the higher the acoustic energy, the higher the cavitation observed more so, how this energy is

administered is equally important. We observed the optimum generation of NO_2^- to be ~ 1.81 x 10^{-6} mol min^{-1} W^{-1} at PD, PI of 5 ms, 80 ms respectively under constant energy scheme. Also, it was observed that at constant PD, the same optimum values of PIs were found for both the $\bar{V}_{rms}$ and sonochemical yield of NO_2^-. However, more investigation is still required on the variation of PD at constant PI to clarify the inverse relationship observed with $\bar{V}_{rms}$ and sonochemical yield of NO_2^-. We hypothesise that the lack of accountability on sonochemical yield of NO_3^- was responsible for the inverse relationship observed in fig. 7.15 (a) and (b). Several efforts which were made to access an ion chromatography (IC) machine that can be used to quantify NO_3^- were unsuccessful.

Chapter 8

Conclusion and Future Work

The following points summarise the key results from the research presented in this thesis. This is followed by a brief discussion, linking the experimental results to the industrial implication and potential future work.

- The ultrasonic horn is one of the industrial sources of ultrasound and should be operated efficiently for any cavitation mediated applications. The primary bubble cluster generated at the tip of the horn collapses subharmonically at f_0/m (m is an integer); the value *m* increases as input power to the horn increases. *Transition power amplitudes* (tip-vibration amplitudes) were identified for which *m* is indistinct. The mean time-average shock wave content ($\bar{V}_{rms}$) measured with swPCD reveals a local minimum value at these amplitudes. These observations are significant for the process efficiency in applications mediated by bubble-collapse phenomena, such as sonochemistry, food processing.
- The HSI observation of the role of SWs in the sono-fragmentation of floating intermetallic crystals was identified. The HSIs revealed that the SWs from the primary bubble cluster were responsible for the cracking and breakage of the floating intermetallic crystals. This finding helps to shed more light on the mechanism of the sono-fragmentation process in floating water, which may be crucial in implementing the scaling-up process of UST for industrial applications.
- Most industrial applications would require more than one ultrasound source for cavitation enhancement purposes. The experimental results (both HSIs and $\bar{V}_{rms}$) from the simultaneous operation of two horns revealed that for the two horns to generate enhanced cavitation within the host medium, the

phase oscillation of the horn tips should be approximately the same. More so, the separation distance of the tips should be less than a wavelength for the particular configuration used in this thesis.

- The identification of the key role played by the active cavitation bubble generated via ultrasound in the sonochemical process is a very important consideration for the scaling-up process. It was shown via the HSIs and $\bar{V}_{rms}$ that the higher number of cavitation bubbles generated, the higher the NO_2^- concentration parallelly observed. The enhancement of cavitation was achieved using the PWM method of transducer excitation at the same input energy via the variation of input parameters (PD and PI). An optimum NO_2^- concentration was found to be ~1.81 x 10^{-6} mol min^{-1} W^{-1} at PD, PI of 5 ms, 80 ms, respectively. This finding illustrates that the sonochemical efficiency can be improved through systematic excitation of the ultrasound source (focused transducer) without increasing the input energy. This is relevant towards the up-scaling of the process for industrial application.

In **Chapter 4**, several papers that considered the investigations of the intensity of the cavitation generated at the tip of an ultrasonic horn as a function of varying tip-vibration amplitudes were reviewed. Tzanakis *et al.* [129] considered the variation of tip-vibration amplitude from 0-45 µm in a step of 5 µm. A local minimum was observed at an ~18 µm tip-vibration amplitude. Hodnett *et al.* [130] determined the effect of output setting (equivalent to the input power used in our investigation) in 10% increment on the broadband in the observed acoustic spectra. A single local minimum was observed at 80% and none at lower amplitudes. This is most likely due to a high sample interval used. Both authors attributed the observed local minima to the acoustic shielding at the tip-vibration amplitudes at which they occurred. This thesis has presented the most thorough study of the dependence of hon-tip cavitation on the input power to date. Our finding reveals that the local minimum was due to the *summed duration of the non-shocking activity,* ΣdNSA (*ms*), at these vibration amplitudes, as shown in Table 4.1. These amplitudes should be avoided for applications mediated for bubble collapse phenomena.

The investigation of the mechanism of sono-fragmentation during the UST was reviewed in **Chapter 5** of this thesis. It was revealed that the actual mechanism involved during fragmentation of the floating intermetallic is still not well understood. It became more difficult to investigate the real melt due to the high temperature of the melt system. Therefore water is mostly used for the investigation due to its transparent nature and some shared acoustic properties of liquid Al [206]. Therefore, many researchers have deployed water and transparent liquid for studying the sono-fragmentation process during ultrasound treatment [5][26][27]. These investigations were done when the intermetallic crystal was fixed at positions relative to the ultrasound source. We have reported in this thesis the role of shock waves on the fragmentation process of a floating intermetallic which is close to scenarios taking place in UST of real melt. More investigation is still required, especially in the real melt system, to verify the obtained results.

The operation of two or more transducers is common practice for cavitation enhancement during sonochemistry investigation, as reviewed in **Chapter 6**. Even though literature that considered the simultaneous operation of two or more ultrasonic horns is not found. Therefore, the results presented in **Chapter 6** could serve as a foundation and guidance for future studies involving the simultaneous operation of two ultrasonic horns.

In **Chapter 7**, several papers on the N_2 fixation have been extensively reviewed. The ultrasonic fixation of N_2 to NO_x requires O_2 to be sparged to generate a reasonable concentration of NO_x. The observed NO_x is maximum when air is used as the sparged gas [177][75][185]. Before now, the investigations on ultrasonic fixation of N_2 using air as the sparged gas have employed planar transducers excited from a continuous electrical supply (i.e., CW), and no account for the energy usage was made. Also, they have reported the simultaneous formation of NO_2^- and NO_3^- (NO_x). This thesis uses a focused transducer excited from pulsed control electrical supply (i.e., PWM) at constant input energy. Unfortunately, we can only report the concentration of NO_2^- formed as we could not access the equipment required to quantify the concentration of the NO_3^-. This however, reflected in the anomaly of the results presented in figs. 7.14 and 7.15. Therefore, obtaining the concentration

of the NO_3^- generated is recommended for future work to allow further improvement towards upscaling of the process. The development of a customised sonoreactor fitted with multiple focused transducers (with their foci distributed within the reactor) and multiple channels through which gas can be sparged for the creation of adequate nucleation sites for cavitation should be considered.

For reasonable translation of sonochemistry experiments to industrial application, the cavitation activity in the 'reactor' for any sonochemical experiment needs to be characterised. For this reason, cavitation should be assessed against all variables such as sonication parameters, flowrates of sparging gas, vessel geometry, and the volume of the sample used. Of course, a high-speed camera can be very beneficial for achieving this. With an understanding, however, of the cavitation that a particular ultrasonic source will generate, a simple, cheap but suitable acoustic detector can help optimise processing efficiency significantly. As well as the spectrum of the acoustic data, V_{rms} is also useful for adequate correlation of cavitation activity with sonochemical efficiency and may have been misinterpreted until now. The importance of V_{rms} was evidently shown in Chapters 4, 6 and 7. **Chapter 5** points to the utility of the SWs in sono-fragmentation of metallic alloy that can be directly assessed by V_{rms}.

Upscaling acoustic cavitation for some industrial processes like sonochemistry remains a significant challenge that requires an understanding of the role played by the cavitation and subsequently proceeding with the option of enhancing it (i.e., developing it to industrial standard). It is hoped that the findings presented in this thesis might contribute to the development and characterisation of effective and efficient bench-top experiments that might ultimately benefit industrial applications such as food processing, UST, sonochemistry, and wastewater treatment.

Appendix A

Matlab Scripts

This section presents the Matlab scripts used in this thesis. The Matlab script for filtering the acoustic data obtained with the swPCD, the Matlab scripts used for obtaining the acoustic spectra from the swPCD data, and the Matlab scripts for the dark-pixel algorithm used to observe the variation of the cavitating bubble generated at the tip of the horn are all presented at the appropriate section.

A.1 Matlab filtering and frequency codes

The filtering Matlab codes used are described in § 3.3.1 Filters used for acoustically detected data. Comments are added to the codes for easy understanding.

```
clear all; close all; clc;

fname = 'file name';% The acosutic data store with extension wfm

%% load data
   [y, t, info, ind_over, ind_under, frames] = wfm2read_js(fname);

   dt = t(2,1)-t(1,1);
   fs = 1/dt;

   y = y * 1000; % coverting to mV


Fcut1   =  fb;    % Lower frequency value
Fcut2   = 4000e3;  % Upper sensitivity limit of swPCD

%% low-pass filter at 10 MHz and decimation to removed noise
   h_lpf = fir1(2^9, 10e6/(fs/2));
   slpf1 = convn(y, h_lpf', 'same');
```

```
    FS = fs;

%% high-pass filter at 50 Hz and decimation
    h_hpf = fir1(2^9, 50/(fs/2), 'high');
    slpf1y = convn(slpf1, h_hpf', 'same');
%     %% high-pass filter at f0 Hz and decimation
h_hpf = fir1(2^9, f0/(fs/2), 'high');

slpf1y = convn(slpf1y, h_hpf', 'same');

    %% Bandpass filter
    h_bpf = fir1(2^9, [Fcut1 Fcut2]/(FS/2), 'bandpass');
    sig1  = convn(slpf1y, h_bpf', 'same');

figure();
%hold on
plot(t*1e3, sig1, 'r');
title('Filtered Acoustic data ');


%% frequency spectrum

[SLPF1   w1] = freqz(sig1.*blackman(length(rms(sig1))), 1, 2^21, fs);
figure('unit', 'normalized', 'position', [0.1 0.1 0.8 0.8]);
subplot(2,1,1); hold on;
plot(w1/1e6, db(abs (SLPF1)  /max(abs(SLPF1))),  'LineWidth', 1);
grid on;
xlabel('Frequency [MHz]');
ylabel('Magnitude [dB]');
title('Frequency response of filtered acoustic emission');
```

A.2 Dark-pixel Algorithm codes

```
% clear all;
% close all;

v=VideoReader('filr namee.avi');
x=0;
Z3=0;
J2=0;
%rect=0;
k1=1; % defined the frame number
rect = read(v,k1);
figure
```

```
imshow(rect);
% impixelinfo
% rect1=getrect;
%  title('select');
%rect1=[14,137,244,106]
B=rect1(1,3);
%B1=rect1(1,4);
%B2=B*B1;
Begin=54291;
Endd=54399;

for k=Begin:1:Endd


video = read(v,k);
IY=imcrop(video,rect1);
%I=rgb2gray(video);
J=double(IY);
%T = read(v,k-1);
%I1=rgb2gray(T);
%J1=double(T);

%Z = imsubtract(J,J1);

Z1=abs(J);
%Bin=Z1>20&Z1<130;
Bin=Z1<2;
Area(k,1)=bwarea(Bin);



imshow(Bin)
impixelinfo

end

x=Begin:Endd;

for k=Begin:1:Endd

 if Area(k,1)== minimu
    indexmin=k+Begin;
 end
 if Area(k,1)== maximu
    indexmax=k+Begin;
 end
```

```
end
x=Begin:Endd;
Y=Area(x,1);
z=(x)*t; % depending on frame rate
figure('unit', 'normalized', 'position', [0.1 0.1 0.8 0.8]);
subplot(3,1,1); hold on;
plot(x,Y);
xlabel('Frame Number');
ylabel('Area of the bubble');
title('Variation of bubble size in an acoustic horn (40%)');
grid on;
axis tight
subplot(3,1,2); hold on;
plot(z,Y);
xlabel('Time in us');
ylabel('Area of the bubble');
title('Variation of bubble size in an acoustic horn');
grid on;
axis tight
subplot(3,1,3); hold on;
plot(t*1e3,y,'r');
xlabel('Time in us')
ylabel('Voltage in mV');
title('Time domain signal of acoustic emission for 40%');
grid on;
```

Appendix B

OnScale Simulation

B.1 Preparation for simulation

This section presents 3-D model symmetry about x, y axes of the focused transducer with and without sonoreactor placed in situ as shown in fig B.1 and B.2.

The focused transducer model is surrounded by water elements (fig. B.10) and simulated using the codes in § B.2 to achieve the pressure distribution field at the focal region.

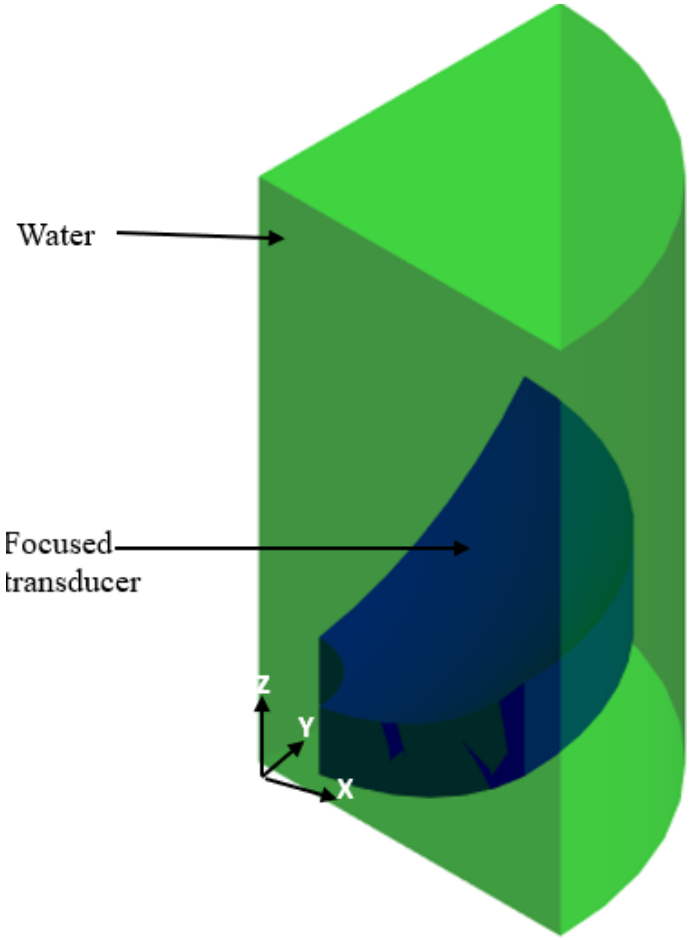

Figure B.1: Showing 3-D quarter model of CAD model symmetry about x and y-axis in OnScale readying for simulation.

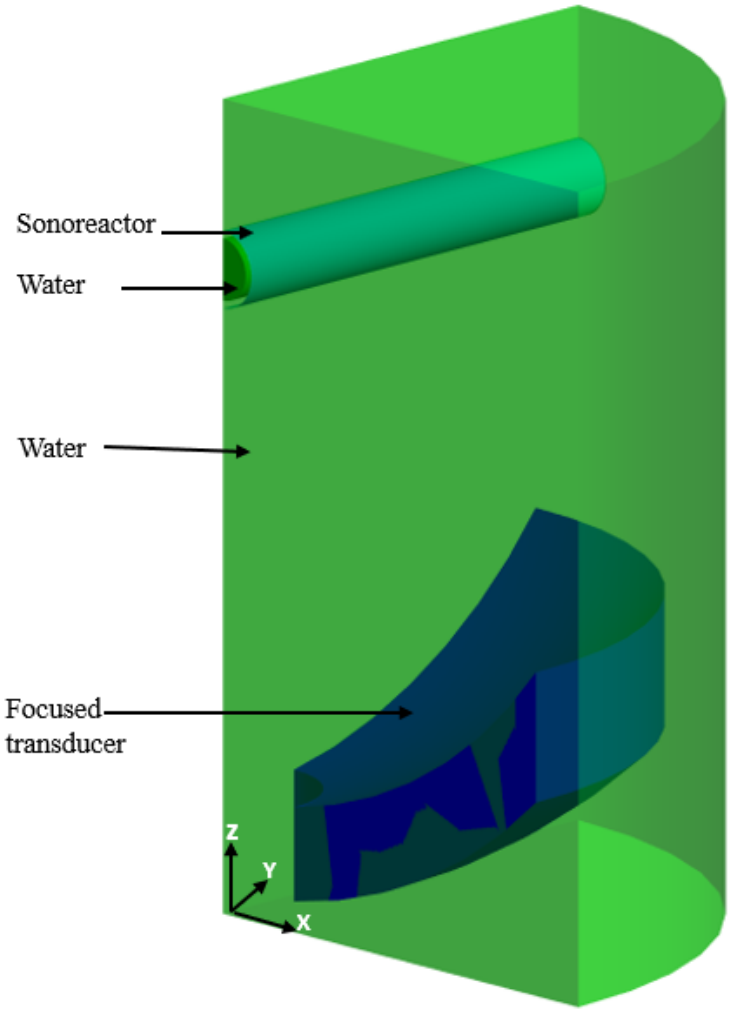

Figure B.2: Showing 3-D quarter model symmetry about x and y-axis readying for simulation in OnScale software.

Fig. B.2 is the combined 3-D model of the sonoreactor placed at the focus of the transducer for characterisation of the acoustic characterisation of the sono reactor. The corresponding simulated code is presented in § **B.2**.

B.2 Onscale simulation codes

c DESIGNER :OnScale - Designer Generated

```
c       MODEL DESCRIPTION  :
c       DATE CREATED                :28 Oct 2020
c       VERSION                             :1.0
c
*********************************************************************************
mp
        omp * *                 /* Number of CPUs to be used in the execution.
        end
titl LY5umSep
c These variables have been set by the user through the interface.
symb coordFactor = 1.0          /* Coordinate conversion factor
symb timeFactor = 1.0           /* Time conversion factor
symb dMassFactor = 1.0          /* Mass conversion factor
text geom_filename = 'LY_0.005mmSeperation_NoVessel.step'                /* The source file
for the model
symb geom_units_scale = 0.001           /* Conversion from file units to meters
symb geom_scaleFactor = 1.0 * $geom_units_scale * $coordFactor
symb freqint = 200000.0         /* Determined Drive Frequency (Hz)


c
*********************************************************************************
*******************
c                       Define Meshing
*********************************************************************************
*******************
symb freqdamp = $freqint
symb wavevel = 1496.0           /* Longitudinal wave velocity in material (m/s)
symb wavelgth = $wavevel / $freqint             /* Wavelength of sound in material (m)
symb nmesh = 20         /* Elements per wavelength
symb box = $wavelgth / $nmesh


c
*********************************************************************************
*******************
c                       CAD Geometry Allocation
*********************************************************************************
*******************
cad
```

```
        defn cad_1
        file 'LY_0.005mmSeperation_NoVessel.step'
        scal $geom_scaleFactor
        mesh struct *
        dout * * 0 0 0
        end

********************************************************************************
c                           Geometry Locations (XYZ)
********************************************************************************
c Scale Parameters
symb xmin = 0.0 * $coordFactor
symb xmax = 0.0625 * $coordFactor
symb ymin = 0.0 * $coordFactor
symb ymax = 0.0625 * $coordFactor
symb zmin = -0.015 * $coordFactor
symb zmax = 0.09 * $coordFactor
c Determine lengths of the model
symb xlen = ( $xmax - $xmin )
symb ylen = ( $ymax - $ymin )
symb zlen = ( $zmax - $zmin )
c ***************************************************
c                           Keypoints in the X-Direction
c ***************************************************
symb #keycord x 1 $xmin $xlen
symb #get { idx } rootmax x
c ***************************************************
c                           Keypoints in the Y-Direction
c c ***************************************************
symb #keycord y 1 $ymin $ylen
symb #get { jdx } rootmax y
c ***************************************************
c                           Keypoints in the Z-Direction
c c ***************************************************
symb #keycord z 1 $zmin $zlen
```

```
symb #get { kdx } rootmax z
*******************************************************************************
c                       Indices Locations (IJK)
*******************************************************************************
c Grid in I direction, using approximately element size of 'box' and at least 1 element
symb #keyindx i 1 $idx 1 $box 1
symb indgrd = $i$idx
c Grid in J direction, using approximately element size of 'box' and at least 1 element
symb #keyindx j 1 $jdx 1 $box 1
symb jndgrd = $j$jdx
c Grid in K direction, using approximately element size of 'box' and at least 1 element
symb #keyindx k 1 $kdx 1 $box 1
symb kndgrd = $k$kdx
c
*******************************************************************************
c                       GCON Grid & Geometry Allocation
*******************************************************************************
grid $i$idx $j$jdx $k$kdx
geom
        keypnt $idx $jdx $kdx
        end
c*******************************************************************************
c                       Driving Conditions
*******************************************************************************
c c                     A number of predefined waveform functions can be accessed in
OnScale. The DATA
c                       HIST option is used below, other examples include wavelets, gaussians
and step
c                       functions. The manual details the function entries
*******************************************************************************
symb freqtimefunc_1 = 200000.0
func
        name timefunc_1
        sine $freqtimefunc_1 200.0 0. 30.0 0. 0.0
        end
 c -------------------------------------------------------------
c               Project Material List
c ------------------------------------------------------------  ------------------------------------------------
-------------------
```

```
c Global variables used in all the material definitions
c -------------------------------------------------------------------------
symb epvacm = 8.854e-12              /* dielectric constant for vacumn
symb freqdamp = 1.e6 if noexist      /* specified frequency for damping model
symb rmu0 = 1.2566e-6
 -------------------------------------------------------------------------
c    Now define the axis transformation - only posx used in this file
c -------------------------------------------------------------------------
axis
    form vctr
    defn posx car2 0. 0. 0.    1.  0.  0.   0. 1. 0.
    defn negx car2 0. 0. 0.   -1.  0.  0.   0. 1. 0.
    defn posy car2 0. 0. 0.    0.  1.  0.   0. 0. 1.
    defn negy car2 0. 0. 0.    0. -1.  0.   0. 0. 1.
    defn posz car2 0. 0. 0.    0.  0.  1.   1. 0. 0.
    defn negz car2 0. 0. 0.    0.  0. -1.   1. 0. 0.
    end
c -------------------------------------------------------------------------
c    Input material properties to program
c -------------------------------------------------------------------------

matr
c ---------------------------------------------------------------
c type : FLUID :
c name : watr :
c desc : Water at 25C :
c ---------------------------------------------------------------
            wvsp on
            type elas
            prop watr 1000.00 1496.00 0.00000 0.
            vdmp watr $freqdamp db 0.002 0 1e+06 2 0.01 *
            thrm watr 4181 0.61 0.61 0.61 1.0 0 0 27
c           define baseline dielectric coefficients
```

```
            symb epxx = 3
            symb epyy = 3
            symb epzz = 3
c           scale material properties as specified above
            symb aepxx = $epvacm * $epxx
            symb aepyy = $epvacm * $epyy
            symb aepzz = $epvacm * $epzz
            elec watr $aepxx $aepyy $aepzz
c -------------------------------------------------------------
c type : FLUID :
c name : watr_2 :
c desc : Water at 25C (Copy of watr material) :
c -------------------------------------------------------------
  copy watr watr_2
c -------------------------------------------------------------
c type : PIEZO :
c name : pzt4 :
c desc : PZT4 Generic :
c -------------------------------------------------------------
            symb rho  = 7500.00              /* density
            wvsp off
            type lean

c    define baseline stiffness coefficients (Constant electric field)
            symb c11 = 1.47e+11
            symb c12 = 8.11e+10
            symb c13 = 8.11e+10
            symb c14 = 0
            symb c15 = 0
            symb c16 = 0
            symb c22 = 1.47e+11
            symb c23 = 8.11e+10
            symb c24 = 0
            symb c25 = 0
```

```
symb c26 = 0
symb c33 = 1.32e+11
symb c34 = 0
symb c35 = 0
symb c36 = 0
symb c44 = 3.13e+10
symb c45 = 0
symb c46 = 0
symb c55 = 3.13e+10
symb c56 = 0
symb c66 = 3.06e+10
prop pzt4 $rho
$c11   $c12   $c13   $c14   $c15   $c16   $c22
$c23   $c24   $c25   $c26   $c33   $c34   $c35
$c36   $c44   $c45   $c46   $c55   $c56   $c66
c       define baseline dielectric coefficients
symb epxx = 730
symb epyy = 730
symb epzz = 635
c       scale material properties as specified above
symb aepxx = $epvacm * $epxx
symb aepyy = $epvacm * $epyy
symb aepzz = $epvacm * $epzz
elec pzt4 $aepxx $aepyy $aepzz
c   define baseline piezoelectric coupling coefficients
symb ex1 = 0                    /* coupling constant
symb ex2 = 0                    /* coupling constant
symb ex3 = 0                    /* coupling constant
symb ex4 = 0                    /* coupling constant
symb ex5 = 11.4                 /* coupling constant
symb ex6 = 0                    /* coupling constant
symb ey1 = 0                    /* coupling constant
symb ey2 = 0                    /* coupling constant
symb ey3 = 0                    /* coupling constant
```

```
        symb ey4 = 11.4                 /* coupling constant
        symb ey5 = 0                    /* coupling constant
        symb ey6 = 0                    /* coupling constant
        symb ez1 = -3                   /* coupling constant
        symb ez2 = -3                   /* coupling constant
        symb ez3 = 16.7                 /* coupling constant
        symb ez4 = 0                    /* coupling constant
        symb ez5 = 0                    /* coupling constant
        symb ez6 = 0                    /* coupling constant

        piez pzt4 1 1 $ex1 1 2 $ex2 1 3 $ex3 1 4 $ex4 1 5 $ex5 1 6 $ex6 &
                        2 1 $ey1 2 2 $ey2 2 3 $ey3 2 4 $ey4 2 5 $ey5 2 6 $ey6 &
                        3 1 $ez1 3 2 $ez2 3 3 $ez3 3 4 $ez4 3 5 $ez5 3 6 $ez6

        rdmp pzt4 $freqdamp q 500 500 1e+06 * * *
        axis pzt4 posz   /* relate materials local system to global system
c -------------------------------------------------------------
c type : FLUID :
c name : watr_topE :
c desc : Water at 25C :
c -------------------------------------------------------------
        wvsp on
        type elas
        prop watr_topE 1000.00 1496.00 0.00000 0.
        vdmp watr_topE $freqdamp db 0.002 0 1e+06 2 0.01 *
        thrm watr_topE 4181 0.61 0.61 0.61 1.0 0 0 27
c       define baseline dielectric coefficients
        symb epxx = 3
        symb epyy = 3
        symb epzz = 3
c       scale material properties as specified above
        symb aepxx = $epvacm * $epxx
        symb aepyy = $epvacm * $epyy
        symb aepzz = $epvacm * $epzz
```

```
        elec watr_topE $aepxx $aepyy $aepzz
c -------------------------------------------------------------
c type : FLUID :
c name : watr_bottomE :
c desc : Water at 25C :
c -------------------------------------------------------------
        wvsp on
        type elas
        prop watr_bottomE 1000.00 1496.00 0.00000 0.
        vdmp watr_bottomE $freqdamp db 0.002 0 1e+06 2 0.01 *
        thrm watr_bottomE 4181 0.61 0.61 0.61 1.0 0 0 27
c       define baseline dielectric coefficients
        symb epxx = 3
        symb epyy = 3
        symb epzz = 3
c       scale material properties as specified above
        symb aepxx = $epvacm * $epxx
        symb aepyy = $epvacm * $epyy
        symb aepzz = $epvacm * $epzz
        elec watr_bottomE $aepxx $aepyy $aepzz
        elec void $epvacm
        end
c
*******************************************************************************
c                           Primitive Definitionsc
*******************************************************************************
site
        regn void
        cadmap cad_1 * * * * * * * stnd *
        end
c
*******************************************************************************
c                           Boundary Definitions
*******************************************************************************
bound
        side xmin symm
```

```
        side xmax absr
        side ymin symm
        side ymax absr
        side zmin absr
        side zmax absr
        end
************************************************************************
c                       Calculated Properties
c************************************************************************
c                       By default, Flex only calculates the minimum required data set,
typically this
c                       means only velocities. This is done for memory efficiency. Should
other
c                       properites be required (e.g. displacements, stresses, strains, pressure),
then
c                       these must be requested by the CALC command. The manual lists all
these options
c************************************************************************
calc
        pres acoustic           /* calculate acoustic pressure
        max aprs apmn apmx              /* calculate min/max acoustic pressure
        loss
        end
c
************************************************************************
c                       Piezoelectric Load Definitions
************************************************************************piez
        wndo auto piez
        defn load_1 0.0
        nod2 pzt4 watr_topE
        bc load_1 volt functimefunc_1 1.0 0.0
        defn load_2 0.0
        nod2 pzt4 watr_bottomE
        bc load_2 grnd
        slvr dcgd
        end
time * * 0.8
```

```
c
**********************************************************************************
**********c                    Process Model
c**********************************************************************************
c                    Issue process (PRCS) command. Checks model integrity, and calculates
stable
c                    time step. NOTE: Process command must always be issued
**********************************************************************************
prcs
grph
        colr user size 4
        colr user 1 0.0 1.0 1.0
        colr user 2 0.576471 0.576471 0.576471
        colr user 3 0.333333 1.0 1.0
        colr user 4 0.333333 1.0 1.0
        colr tabl matr 7
        map watr 1
        map watr_2 1
        map pzt4 2
        map watr_topE 3
        map watr_bottomE 4
        end
grph
        line off
        nvew 2 1
        arrow pole
        plot piez
        plot matr piez
        arrow off
        end

term

c
**********************************************************************************
c                    Choose Time Histories To Store
```

```
c*******************************************************************************
*c                    Save field (such as displacement or pressure) from a node or element
for all
c                    time steps with POUT command. Histories are referenced by order of
c                    specification. Histories will be saved in the Flex History file (flxhst).
*******************************************************************************
pout
        rate 1
        symb xloc = 0.0 * $coordFactor
        symb yloc = 0.0 * $coordFactor
        symb zloc = 0.068 * $coordFactor
        hist xyz aprs $xloc * * $yloc * * $zloc * *
        symb xloc = 0.0 * $coordFactor
        symb yloc = 0.0 * $coordFactor
        symb zloc = 0.06 * $coordFactor
        hist xyz aprs $xloc * * $yloc * * $zloc * *
        symb xloc = 0.0 * $coordFactor
        symb yloc = 0.0 * $coordFactor
        symb zloc = 0.076 * $coordFactor
        hist xyz aprs $xloc * * $yloc * * $zloc * *
        hist functimefunc_1
        histname electrode vq all
        end


pout
  form matlab h1            /* Write Time Histories to Matlab file (.mat)
  histname electrode vq all      /* Time History 1 & 2
  end
*******************************************************************************
c                    Run the Model
c*******************************************************************************
c                    Specify the number of time steps to be run. Can be set to auto by using
c                    'Ringdown'.
*******************************************************************************
c User defined runtime for the model
symb #get { step } timestep
```

```
symb ttime = 0.0003
symb nexec = $ttime / $step
symb nloops = 1000
symb nexec2 = $nexec / $nloops
c Set up Plotting
grph
        set imag avi
        line no
        arrow off
        vpnt 0 -0.5 0
        eye 0 -1 0
        end
c Create run plot procedure
proc plot save
c Run some timesteps
exec $nexec2
c Plot model
grph
        nvew 1 1
        view 1
        vpnt 0 -0.5 0
        eye 0 -1 0
        mirr x symm
        plot apmx
        imag
        view 2
c       plot 4
        end

end$ proc

c Run model then wait
proc plot $nloops
```

```
data
        file out 'improvedTransducer.flxdato'
        out modl
        out apmx
        out apmn
        out loss
        end
data
        file out 'fieldData.mat'
        form out matlab d1
        out modl
        out apmx
        out apmn
        out loss
        end
 data
        file out 'LY_0_01mmSep.flxdato'
        out modl
        end
*************************************************************************
c                       Save symbol variables to file for later use
c*************************************************************************
*****************************
symb #get { labl } jobname
symb #save '$labl.symb'
stop            /* return to command prompt
```

B.3 Supplementary simulation results

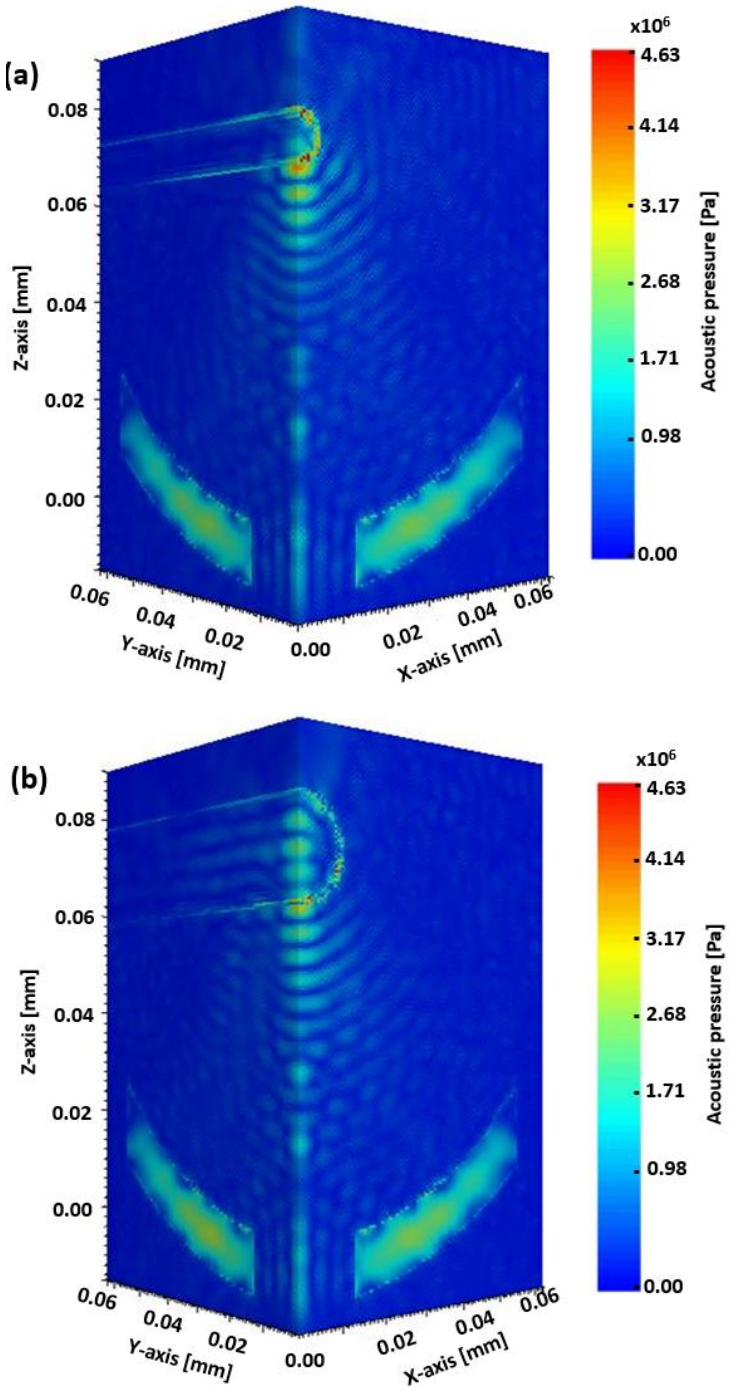

Figure B.3: Simulation ofacosutic field map of HIFU (H-149) (a) with 10 mm-Ø sonoreactor placed at the focus (b) with 20 mm-Ø sonoreactor placed at the focus

Appendix C

Supplementary double-horn results

The result presented in fig. C.1 is the HSIs obtained from the simultaneous operation of two ultrasonic horns operating with different tip-vibration amplitudes, $horn_S$ operating at 25% (~271 µm), and hornB operating at 50% (~219 µm). Both amplitudes are the respective transition amplitude for the two horns.

Fig. C.1 (a) and (b) indicate the situation when the two horns are operating out-of-phase and in-phase, respectively. The cavitation zone (indicated with a green rectangle) is more crowded with cavitating bubbles shown in fig. C.1 (b) than (a) due to enhanced cavitation. The result is similar to the observation in Chapter 6.

Figure C.1: Selected frames from Photron high-speed image sequences of simultaneous operation of two horns (with ~ λ mm separation) collected at 1×10^5 fps, for input powers (50% $horn_B$, and 25% $horn_S$), (a) when the two

horns oscillate out-of-phase (b) when the oscillation of the two horns in-phase. Scale is provided by the 6.4 mm-Ø tip.

Bibliography

[1] M. López-Pedrouso *et al.*, *Green technologies for food processing: Principal considerations*. Elsevier Inc., 2019.

[2] C. E. Brennen, *Cavitation And Bubble Dynamics*. 2003.

[3] E. -a. Weitendorf, “On the History of Propeller Cavitation and Cavitation Tunnels,” *Proc. Fourth Int. Symp. Cavitation*, no. 189 5, pp. 1–13, 2001.

[4] L. C. Burrill, “Charles Parsons and Cavitation,” *Inst. Mar. Eng. Trans.*, vol. LXIII, no. 8, pp. 148–155, 1951.

[5] K. Johnston, “The cavitation subharmonic signal : mechanistic source and optimised detection,” University of Dundee, 2016.

[6] K. Johansen, “Stable-inertial Cavitation,” 2018.

[7] R. Knapp and A. Hollander, “Laboratory Investigations of the Mechanism of Cavitation,” *Trans. ofthe ASME*, pp. 419–435, 1948.

[8] L. H. Thompson and L. K. Doraiswamy, “Sonochemistry : Science and Engineering,” *Ind. Eng. Chem. Res.*, vol. 38, pp. 1215–1249, 1999.

[9] T. G. Leighton, “Bubble population phenomena in acoustic cavitation,” *Ultrason. - Sonochemistry*, vol. 2, no. 2, pp. 123–136, 1995.

[10] C. C. Church and E. D. L. C. Arstensen, “‘Stable’ Inertial Cavitation,” *Ultrasound Med. Biol.*, vol. 27, no. 10, pp.

1435–1437, 2001.

[11] W. Lauterborn and R. Mettin, “Acoustic cavitation: bubble dynamics in high-power ultrasonic fields,” in *Power Ultrasonics*, Elsevier Ltd., 2015, pp. 37–78.

[12] S. K. Bhangu and M. Ashokkumar, *Theory of Sonochemistry*, vol. 374, no. 4. Springer International Publishing, 2016.

[13] G. Eskin and D. Eskin, *Ultrasonic treatment of light alloy melts*, Second Edi. Boca Raton: CRC Press, 2014.

[14] V.I. Il’ichev, “Acoustic Caviataion,” in *In Proc. Akustichesky Institut Akademii Nauk SSSR (AKIN) 6*, 1969, pp. 16–29.

[15] J. Rooze, “Cavitation in gas-saturated liquids,” 2012.

[16] K. S. Suslick, “Sonochemistry,” in *Sonochemistry*, no. March, 1990.

[17] R. Pflieger, C. Cairós, S. Nikitenko, and R. Mettin, *Characterization of Cavitation Bubbles and Sonoluminescence*. 2017.

[18] S. Niazi, S. H. Hashemabadi, and M. M. Razi, “CFD simulation of acoustic cavitation in a crude oil upgrading sonoreactor and prediction of collapse temperature and pressure of a cavitation bubble,” *Chem. Eng. Res. Des.*, vol. 92, no. 1, pp. 166–173, 2013.

[19] A. Sadatshojaie, D. A. Wood, S. M. Jokar, and M. R. Rahimpour, “Applying ultrasonic fields to separate water

contained in medium-gravity crude oil emulsions and determining crude oil adhesion coefficients," *Ultrason. Sonochem.*, vol. 70, no. August 2020, p. 105303, 2021.

[20] J. Virkutyte, *The use of power ultrasound in biofuel production, bioremediation, and other applications*. Elsevier Ltd., 2015.

[21] B. Rao, T. Sivasankar, M. Sivakumar, and V. S. Moholkar, "Physical facets of ultrasonic cavitational synthesis of zinc ferrite particles," *Ultrason. - Sonochemistry*, vol. 17, no. 2, pp. 416–426, 2010.

[22] P. R. Gogate and A. B. Pandit, *Design and scale-up of sonochemical reactors for food processing and other applications*. Elsevier Ltd., 2015.

[23] E. Ortega-Rivas, "Ultrasound in food preservation," *Food Eng. Ser.*, vol. 5, no. 8, pp. 251–262, 2012.

[24] M. Hodnett, *8 - Measurement techniques in power ultrasonics*. Elsevier Ltd., 2015.

[25] K. S. Suslick and E. B. Flint, "Sonoluminescence from non-aqueous liquids," *Nature*, vol. 2, no. 1, pp. 9–11, 1987.

[26] P. R. Birkin, D. G. Offin, C. J. B. Vian, and T. G. Leighton, "Multiple observations of cavitation cluster dynamics close to an ultrasonic horn tip," *J. Acoust. Soc. Am.*, vol. 130, no. 5, pp. 3379–3388, 2011.

[27] F. R. Young, *Cavitation*. London: Imperial College Press,

1999.

[28] M. Ashokkumar, M. Hodnett, F. B. Zeqiri, and G. J. Grieser, “Acoustic emission spectra from 515 kHz cavitation in aqueous solutions containing surface- active solutes,” *J. Am. Chem. Soc.*, vol. 129, pp. 2250–2258, 2007.

[29] Y. Son, M. Lim, J. Khim, and M. Ashokkumar, “Acoustic emission spectra and sonochemical activity in a 36 kHz sonoreactor,” *Ultrason. - Sonochemistry*, vol. 19, no. 1, pp. 16–21, 2012.

[30] M. Hodnett, R. Chow, and B. Zeqiri, “High-frequency acoustic emissions generated by a 20 kHz sonochemical horn processor detected using a novel broadband acoustic sensor: A preliminary study,” *Ultrason. Sonochem.*, vol. 11, no. 6, pp. 441–454, 2004.

[31] G. J. Price, M. Ashokkumar, M. Hodnett, and B. Zequiri, “Acoustic Emission from Cavitating Solutions : Implications for the Mechanisms of Sonochemical Reactions,” *J. Phys. Chem.*, vol. 109, pp. 17799–17801, 2005.

[32] J. Frohly, S. Labouret, C. Bruneel, I. Looten-Baquet, and R. Torguet, “Ultrasonic cavitation monitoring by acoustic noise power measurement,” *J. Acoust. Soc. Am.*, vol. 108, no. 5, pp. 2012–2020, 2000.

[33] E. A. Brujan, T. Ikeda, and Y. Matsumoto, “Shock wave emission from a cloud of bubbles,” *Soft Matter*, vol. 8, no.

21, 2012.

[34] J. R. McLaughlan, S. Harput, R. H. Abou-Saleh, S. A. Peyman, S. Evans, and S. Freear, “Characterisation of liposome-loaded microbubble populations for subharmonic imaging,” *Ultrasound Med. Biol.*, vol. 1, no. 11, 2016.

[35] U. Sonic Concepts Bothell, WA, “Datasheet Y-107 and Y-102 Hydrophones.” Sonic Concepts, USA.

[36] K. Johansen, J. H. Song, and P. Prentice, “Performance characterisation of a passive cavitation detector optimised for subharmonic periodic shock waves from acoustic cavitation in MHz and sub-MHz ultrasound,” *Ultrason. Sonochem.*, vol. 43, pp. 146–155, 2018.

[37] I. Tzanakis, M. Hodnett, G. S. B. Lebon, N. Dezhkunov, and D. G. Eskin, “Sensors and Actuators A : Physical Calibration and performance assessment of an innovative high-temperature cavitometer,” *Sensors Actuators A. Phys.*, vol. 240, pp. 57–69, 2016.

[38] M. A. Oreilly and K. Hynynen, “A PVDF receiver for ultrasound monitoring of transcranial focused ultrasound therapy,” *IEEE Trans. Biomed. Eng.*, vol. 57, no. 9, pp. 2286–2294, 2010.

[39] P. P. B. Gerold, S. Kotopoulis, C. McDougall, D. McGloin, M. Postema, “Laser-nucleated acoustic cavitation in focused ultrasound,” *Rev. Sci. Instrum.*, vol. 82, no. 4, 2011.

[40] C. Caneva, I. M. De Rosa, and F. Sarasini, “Monitoring of impacted aramid-reinforced composites by embedded PVDF acoustic emission sensors,” *‘La Sapienza’, Via Eudossiana*, vol. 18, no. 00184, pp. 308–316, 2008.

[41] I. M. De Rosa and F. Sarasini, “Use of PVDF as acoustic emission sensor for in situ monitoring of mechanical behaviour of glass/epoxy laminates,” *Polym. Test.*, vol. 29, no. 6, pp. 749–758, 2010.

[42] A. S. C. M. Schoellhammer, A. Schroeder, R. Maa, G. Y. Lauwers, D. G. A. M. Zervas, R. Barman, A. M. DiCiccio, W. R. Brugge, and and G. T. D. Blankschtein, R. Langer, “Ultrasound-mediated gastrointestinal drug delivery,” *Sci. Transl. Med.*, vol. 7, pp. 160–168, 2015.

[43] C. Desjouy, A. Poizat, B. Gilles, C. Inserra, and J. C. Bera, “Control of inertial acoustic cavitation in pulsed sonication using a real-time feedback loop system,” *J. Acoust. Soc. Am.*, vol. 134, no. 2, pp. 1640–1646, 2013.

[44] J. H. Song, A. Moldovan, and P. Prentice, “Non-linear Acoustic Emissions from Therapeutically Driven Contrast Agent Microbubbles,” *Ultrasound Med. Biol.*, vol. 45, no. 8, pp. 2188–2204, 2019.

[45] J. H. Song, K. Johansen, and P. Prentice, “An analysis of the acoustic cavitation noise spectrum: The role of periodic shock waves,” *J. Acoust. Soc. Am.*, vol. 140, no. 4, pp. 2494–2505, 2016.

[46] E. A. Neppiras, “Acoustic cavitation,” *Phys. Rep.*, vol. 61, no. 3, pp. 159–251, 1980.

[47] G. Ondrey, I. Kim, and G. Parkinson, “Reactors for the 21st Century,” *Chem. Eng.*, pp. 39–45, 1996.

[48] S. Brohult, “Splitting of the hæmocyanin molecule by ultrasonic waves,” *Nature*, vol. 140, no. 3549. p. 805, 1937.

[49] B. Gerold, “Cavitation in focused ultrasound,” p. 183, 2013.

[50] S. Pilli, P. Bhunia, S. Yan, R. J. LeBlanc, R. D. Tyagii, and R. Y. Surampalli, “Ultrasonic pretreatment of sludge: a review,” *Ultrason. Sonochem.*, vol. 18, pp. 1-18., 2011.

[51] M. Zupanc, Ž. Pandur, T. Stepišnik Perdih, D. Stopar, M. Petkovšek, and M. Dular, “Effects of cavitation on different microorganisms: The current understanding of the mechanisms taking place behind the phenomenon. A review and proposals for further research,” *Ultrason. Sonochem.*, vol. 57, no. May, pp. 147–165, 2019.

[52] A. Moghtada and R. Ashiri, “Superiority of sonochemical processing method for the synthesis of barium titanate nanocrystals in contrast to the mechanochemical approach,” *Ultrason. Sonochem.*, vol. 41, no. September 2017, pp. 127–133, 2018.

[53] G. L. Sharipov, B. M. Gareev, K. S. Vasilyuk, D. I. Galimov, and A. M. Abdrakhmanov, “New sonochemiluminescence involving solvated electron in

Ce(III)/Ce(IV) solutions," *Ultrason. Sonochem.*, no. Iii, p. 105313, 2020.

[54] K. S. Suslick, "Applications of Ultrasound to Materials Chemistry," *MRS Bull.*, vol. 20, no. 4, pp. 29–34, 1995.

[55] M. A. Dheyab, A. A. Aziz, M. S. Jameel, P. M. Khaniabadi, and B. Mehrdel, "Mechanisms of Effective Gold Shell on Fe3O 4 Core Nanoparticles Formation using Sonochemistry Method," *Ultrason. Sonochem.*, p. 104865, 2019.

[56] F. G. G.J. Price, M. Ashokkumar, M. Hodnett, B. Zequiri, "Acoustic emission from cavitating solutions: implications for the mechanisms of sonochemical reactions," *J. Phys. Chem. B*, vol. 109, pp. 17799–17801, 2005.

[57] B. Avvaru and A. B. Pandit, "Oscillating bubble concentration and its size distribution using acoustic emission spectra," *Ultrason. Sonochemistry J.*, vol. 16, pp. 105–115, 2009.

[58] K. Johnston *et al.*, "Periodic shock-emission from acoustically driven cavitation clouds: A source of the subharmonic signal," *Ultrasonics*, vol. 54, no. 8, pp. 2151–2158, 2014.

[59] V. Mišík and P. Riesz, "Nitric oxide formation by ultrasound in aqueous solutions," *J. Phys. Chem.*, vol. 100, no. 45, pp. 17986–17994, 1996.

[60] G. Mark *et al.*, "OH-radical formation by ultrasound in

aqueous solution - Part II: Terephthalate and Fricke dosimetry and the influence of various conditions on the sonolytic yield," *Ultrason. Sonochem.*, vol. 5, no. 2, pp. 41–52, 1998.

[61] K. S. Suslick *et al.*, "Acoustic cavitation and its chemical consequences," *Phil. Trans. R. Soc. Lond.*, vol. 357, pp. 335–353, 1999.

[62] J. J. Yao *et al.*, "Sonolytic degradation of parathion and the formation of byproducts," *Ultrason. Sonochem.*, vol. 17, no. 5, pp. 802–809, 2010.

[63] J. Zhang, P. Yu, L. Fan, and Y. Sun, "Effects of ultrasound treatment on the starch properties and oil absorption of potato chips," *Ultrason. Sonochem.*, vol. 70, no. August 2020, p. 105347, 2021.

[64] M. H. Islam, H. Mehrabi, R. H. Coridan, O. S. Burheim, J. Y. Hihn, and B. G. Pollet, "The effects of power ultrasound (24 kHz) on the electrochemical reduction of CO2 on polycrystalline copper electrodes," *Ultrason. Sonochem.*, vol. 72, no. November 2020, p. 105401, 2021.

[65] Q. Shu, H. Lou, T. Wei, X. Zhang, and Q. Chen, "Synergistic antibacterial and antibiofilm effects of ultrasound and MEL-A against methicillin-resistant Staphylococcus aureus," *Ultrason. Sonochem.*, vol. 72, p. 105452, 2021.

[66] T. J. Mason, J. P. Lorimer, and D. M. Bates, "Quantifying

sonochemistry: on a ‘black art,’” *Ultrasonics*, vol. 30, no. 1, pp. 40–42, 1992.

[67] S. Koda, T. Kimura, T. Kondo, and H. Mitome, “A standard method to calibrate sonochemical efficiency of an individual reaction system,” *Ultrason. Sonochem.*, vol. 10, pp. 149–156, 2003.

[68] J. Choi, J. Khim, B. Neppolian, and Y. Son, “Enhancement of sonochemical oxidation reactions using air sparging in a 36 kHz sonoreactor,” *Ultrason. - Sonochemistry*, vol. 51, no. July 2018, pp. 412–418, 2019.

[69] M. E. Fitzgerald, V. Griffing, J. Sullivan, M. E. Fitzgerald, V. Griffing, and J. Sullivan, “Chemical Effects of Ultrasonics — ’ ’ Hot Spot ’ ’ Chemistry,” *J. Chem. Phys.*, vol. 25, no. 5, pp. 926–933, 1954.

[70] M. Vinatoru and T. J. Mason, “Can sonochemistry take place in the absence of cavitation ? – A complementary view of how ultrasound can interact with materials,” *Ultrason. - Sonochemistry*, vol. 52, no. 313, pp. 2–5, 2019.

[71] S. Suslick and M. Fang, “Acoustic cavitation and its chemical consequences,” *Phil. Trans. R. Soc. Lond. A*, vol. 357, no. 1927, pp. 335–353, 1999.

[72] S. I. Nikitenko, “Plasma Formation during Acoustic Cavitation: Toward a New Paradigm for Sonochemistry,” *Hindawi Publ. Corp. Adv. Phys. Chem.*, vol. 2014, 2014.

[73] J. Frenkel, “On electrical phenomena associated with

cavita- tion due to ultrasonic vibrations in liquids," *Acta Physicochim. USSR*, vol. 12, p. 317, 1940.

[74] T. Lepoint and F. Mullie, "What exactly is cavitation chemistry?," *Ultrason. - Sonochemistry*, vol. 1, no. 1, pp. 13–22, 1994.

[75] J. Yao, L. Chen, X. Chen, L. Zhou, W. Liu, and Z. Zhang, "Formation of inorganic nitrogenous byproducts in aqueous solution under ultrasound irradiation," *Ultrason. - Sonochemistry*, vol. 42, pp. 42–47, 2018.

[76] M. W. S. Xu, Y. Zong, W. Li, S. Zhang, "Bubble size distribution in acoustic droplet vaporization via dissolution using an ultrasound wide-beam method," *Ultrasonics-Sonochemistry*, vol. 21, pp. 975–983, 2014.

[77] O. Louisnard and J. González-garcía, *Acoustic Cavitation*. 2011.

[78] I. Tzanakis, G. S. B. Lebon, D. G. Eskin, and K. A. Pericleous, "Characterizing the cavitation development and acoustic spectrum in various liquids," *Ultrason. Sonochem.*, vol. 34, pp. 651–662, 2017.

[79] T. J. Mason, A. J. Cobley, J. E. Graves, and D. Morgan, "New evidence for the inverse dependence of mechanical and chemical effects on the frequency of ultrasound," *Ultrasonics-Sonochemistry*, vol. 18, pp. 226–230, 2011.

[80] M. H. Entezari and P. Kruus, "Effect of Frequency on Sonochemical Reactions: Oxidation of Iodide.," *Ultrason.*

Sonochem., vol. 1, no. 2, pp. 75–79, 1994.

[81] D. G. Wayment and D. J. Casadonte, “Frequency effect on the sonochemical remediation of alachlor,” *Ultrason. Sonochem.*, vol. 9, no. 5, pp. 251–257, 2002.

[82] G. Petrier, C.; Jeunet, A.; Luche, J. L.; Reverdy, “Unexpected Frequency Effects on the Rate of Oxidative Processes Induced by Ultrasound.,” *J. Am. Chem. Soc.*, vol. 114, no. 8, pp. 3148-3150., 1992.

[83] S. Merouani, H. Ferkous, O. Hamdaoui, Y. Rezgui, and M. Guemini, “A method for predicting the number of active bubbles in sonochemical reactors,” *Ultrason. - Sonochemistry*, vol. 22, pp. 51–58, 2015.

[84] I. H. M.A. Beckett, “Impact of Ultrasonic Frequency on Aqueous Sonoluminescence and Sonochemistry,” *J. Phys. Chem.*, vol. 3796, 2001.

[85] H. M. S Koda, T Kimura, T Kondo, “A standard method to calibrate sonochemical efficiency of an individual reaction system,” *Ultrason. Sonochem.*, vol. 10, 2003.

[86] S. Merouani and O. Hamdaoui, “Computer simulation of chemical reactions occurring in collapsing acoustical bubble : dependence of free radicals production on operational conditions,” *Res Chem Intermed*, vol. 41, pp. 881–897, 2015.

[87] A. Brotchie, F. Grieser, and M. Ashokkumar, “Effect of Power and Frequency on Bubble-Size Distributions in

Acoustic Cavitation,” *Phys. Rev. Lett.*, vol. 084302, no. February, pp. 1–4, 2009.

[88] and S. J. P. Bradley P. Barber, C. C. Wu, Ritva Löfstedt, Paul H. Roberts, “Sensitivity of sonoluminescence to experimental parameters,” *Phys. Rev. Lett.*, vol. 72, no. 1380, 1994.

[89] A. Gutierrez, M.; Henglein, “Chemical Action of Pulsed Ultrasound: Observation of an Unprecedented Intensity Effect,” *J. Phys. Chem.*, vol. 94, no. 9, pp. 3625-3628., 1990.

[90] M. A. Mark G, Tauber A, Laupert R, Schuchmann HP, Schulz D and von S. C, “OH-radical formation by ultrasound in aqueous solution--Part II: Terephthalate and Fricke dosimetry and the influence of various conditions on the sonolytic yield,” *Ultrason. - Sonochemistry*, vol. 5, no. 2, pp. 41–52, 1998.

[91] S. Merouani, O. Hamdaoui, F. Saoudi, and M. Chiha, “Influence of experimental parameters on sonochemistry dosimetries : KI oxidation , Fricke reaction and hydrogen perioxide production,” *J. Hazard. Mater.*, vol. 178, no. 1–3, pp. 1007–1014, 2010.

[92] G. Cioncoloni, “Towards an anthropogenic nitrogen cycle based on nitrite,” 2018.

[93] M. A. Beckett and I. Hua, “Impact of Ultrasonic Frequency on Aqueous Sonoluminescence and Sonochemistry,” *J.*

Phys. Chem, vol. 105, no. 15, pp. 3796–3802, 2001.

[94] G. J. Price, “Sonochemistry and Sonoluminescence in Aqueous Systems,” in *Proceedings of 20th International Congress on Acoustics ICA*, 2010, no. August, pp. 23–27.

[95] Weissler, A., H. W. Cooper, and S. Snyder, “Chemical effect of ultrasonic waves: oxidation of potassium iodide solution by carbon tetrachloride,” *J. Am. Chem. Soc.*, vol. 72, pp. 1769–1775, 1950.

[96] H. Hasanzadeh, M. Mokhtari-Dizaji, S. Z. Bathaie, and Z. M. Hassan, “Evaluation of correlation between chemical dosimetry and subharmonic spectrum analysis to examine the acoustic cavitation,” *Ultrason. Sonochem.*, vol. 17, no. 5, pp. 863–869, 2010.

[97] H. Ratoarinoro, N.; Contamine, F.; Wilhelm, A. M.; Berlan, J.; Delmas, “Power Measurement in Sonochemistry,” *Ultrason. Sonochem*, vol. 2, no. 1, pp. 43-47.

[98] I. Thormählen, J. Straub, and U. Grigull, “Refractive Index of Water and Its Dependence on Wavelength, Temperature, and Density,” *J. Phys. Chem. Ref. Data*, vol. 14, no. 4, pp. 933–945, 1985.

[99] Shimadzu, “HyperVision Shimadzu Camera HPV,” *Shimadzu Europa GmbH Analytical and Measuring Instruments*, 2021. [Online]. Available: https://www.shimadzu.eu/hypervision-hpv-x. [Accessed: 13-Nov-2021].

[100] Photron, “PHOTRON FASTCAM SA-Z,” *EMEC Motion Engineering*, 2021. [Online]. Available: https://www.highspeedimaging.com/photron-fastcam-sa-z/. [Accessed: 12-Nov-2021].

[101] S. Concepts, “Y (PCD)-Series Passive Cavitation Detectors,” *Techincal Doc. Sonic Concepts*, vol. 1, no. 425, pp. 1–4, 2019.

[102] R. Oshana, “Overview of DSP Algorithms,” in *DSP for Embedded and Real-Time Systems*, Elsevier Inc., 2012, pp. 113–131.

[103] E. Digital Signal Processing Committee of the IEEE Acoustics, Speech, and Signal Processing Society, *Programs for Digital Signal Processing*. New York: IEEE Press, 1979.

[104] P. R. Gogate, P. A. Tatake, P. M. Kanthale, and A. B. Pandit, “Mapping of sonochemical reactors: Review, analysis, and experimental verification,” *AIChE J.*, vol. 48, no. 7, pp. 1542–1560, 2002.

[105] A. M. Hurrell and S. Rajagopal, “The Practicalities of Obtaining and Using Hydrophone Calibration Data to Derive Pressure Waveforms,” *IEEE Trans. Ultrason. Ferroelectr. Freq. Control*, vol. 64, no. 1, pp. 126–140, 2017.

[106] B. U. Corporation, “Digital Sonifier ® Models 250 & 450 User’s Manual Manual Change Information Patents and

Copyright," no. 203, 2001.

[107] and E. B.-F. A. U. Kapturowska, I. A. Angieszka, J. Krzyczkowska, "Studies on the lipolytic activity of sonicated enzymes from Yarrowi lipolytica," *Ultrason. Sonochem.*, vol. 19, pp. 186-191., 2012.

[108] Z. H. D. Liu, X. A. Zeng, D. W. Sun, "Disruption and protein release by ultrasonification of yeast cells," *Innov. Food Sci. Emerg. Technol.*, vol. 18, pp. 132-137., 2013.

[109] A. S. Peshkovsky, S. L. Peshkovsky, S. Bystryak, "Scalable high-power ultrasonic technology for the production of translucent nanoemulsions," *Chem. Eng. Process. Process Intensif.*, vol. 69, pp. 77-82., 2013.

[110] and A. K. S. B. Bittmann, F. Haupert, "Preparation of TiO2/epoxy nanocomposites by ultrasonic dispersion and their structure property relationship," *Ultrason. Sonochem*, vol. 18, pp. 120–126, 2011.

[111] M. D. Luque de Castro and F. Priego-Capote, "Ultrasound-assisted crystallization (sonocrystallization)," *Ultrason. Sonochem.*, vol. 14, pp. 717-724., 2007.

[112] S. M. Hingu, P. R. Cogate, and V. K. Rathod, "Synthesis of biodiesel from waste cooking oil using sonochemical reactors," *Ultrason. Sonochem.*, vol. 17, pp. 827–832, 2010.

[113] K. Kezia *et al.*, "Crystallisation of minerals from concentrated saline dairy effluent," *Water Res.*, vol. 101,

pp. 300-308., 2016.

[114] B. J. O'Daly, E. Morris, G. P. Gavin, J. M. O'Byrne, and G. B. McGuinness, "High-power low-frequency ultrasound: A review of tissue dissection and ablation in medicine and surgery," *J. Mater. Process. Technol.*, vol. 200, pp. 38-58., 2008.

[115] T. Terahara, S. Mitragotri, J. Kost, and R. Langer, "Dependence of low-frequency sonophoresis on ultrasound parameters: distance of the horn and intensity," *Int. J. Pharm.*, vol. 235, pp. 35-42., 2002.

[116] M. J. Borrelli *et al.*, "Production of uniformly sized serum albumin and dextrose microbubbles," *Ultrason. Sonochem.*, vol. 19, no. 1, pp. 198–208, 2012.

[117] T. J. Mason and J. P. Lorimer, *Applied Sonochemistry*. Weinheim: Wiley VCH, 2002.

[118] I. Tzanakis, G. S. B. Lebon, D. G. Eskin, and K. A. Pericleous, "Characterizing the cavitation development and acoustic spectrum in various liquids," *Ultrason. - Sonochemistry*, vol. 34, pp. 651–662, 2017.

[119] A. Moussatov, C. Granger, and B. Dubus, "Cone-like bubble formation in ultrasonic cavitation field," *Ultrason. Sonochem.*, vol. 10, no. 4–5, pp. 191–195, 2003.

[120] L. Bai, W. Xu, J. Deng, C. Li, D. Xu, and Y. Gao, "Generation and control of acoustic cavitation structure.," *Ultrason. Sonochem.*, vol. 21, no. 5, pp. 1696–1706, 2014.

[121] H. N. McMurray and B. P. Wilson, “Mechanistic and spatial study of ultrasonically induced luminol chemiluminescence,” *J. Phys. Chem. A*, vol. 103, no. 20, pp. 3955–3962, 1999.

[122] A. Žnidarčič, R. Mettin, C. Cairós, and M. Dular, “Attached cavitation at a small diameter ultrasonic horn tip,” *Phys. Fluids*, vol. 26, no. 2, pp. 023-304., 2014.

[123] K. L. Tan and S. H. Yeo, “Bubble dynamics and cavitation intensity in milli-scale channels under an ultrasonic horn,” *Ultrason. Sonochem.*, vol. 58, p. 104666., 2019.

[124] B. Gerold, I. Rachmilevitch, and P. Prentice, “Bifurcation of ensemble oscillations and acoustic emissions from early stage cavitation clouds in focused ultrasound,” *New J. Phys.*, vol. 15, no. 3, p. 33044, 2013.

[125] P. R. Birkin, D. G. Offin, C. J. B. Vian, T. G. Leighton, and A. O. Maksimov, “Investigation of noninertial cavitation produced by an ultrasonic horn,” *J. Acoust. Soc. Am.*, vol. 130, no. 5, pp. 3297–3308, 2011.

[126] and P. P. J. H. Song, A. Moldovan, “Non-linear acoustic emissions from therapeutically driven contrast agent microbubbles,” *Ultrasound Med. Biol.*, vol. 45, no. 8, pp. 2188-2204., 2019.

[127] J. T. Tervo, R. Mettin, and W. Lauterborn, “Bubble cluster dynamics in acoustic cavitation,” *Acta Acust. united with Acust.*, vol. 92, no. 1, pp. 178–180, 2006.

[128] W. Lauterborn and E. Cramer, “Subharmonic route to chaos observed in acoustics,” *Phys. Rev. Lett.*, vol. 47, no. 20, pp. 1445–1448, 1981.

[129] I. Tzanakis, M. Hodnett, G. S. B. Lebon, N. Dezhkunov, and D. G. Eskin, “Calibration and performance assessment of an innovative high-temperature cavitometer,” *Sensors Actuators, A Phys.*, vol. 240, pp. 57–69, 2016.

[130] M. Hodnett, R. Chow, and B. Zeqiri, “High-frequency acoustic emissions generated by a 20 kHz sonochemical horn processor detected using a novel broadband acoustic sensor: A preliminary study,” *Ultrason. Sonochem.*, vol. 11, no. 6, pp. 441–454, 2004.

[131] B. Zeqiri, P. N. Gélat, M. Hodnett, and N. D. Lee, “A novel sensor for monitoring acoustic cavitation. Part I: Concept, theory, and prototype development,” *IEEE Trans. Ultrason. Ferroelectr. Freq. Control*, vol. 50, no. 10, pp. 1342–1350, 2003.

[132] B. Zeqiri, N. D. Lee, M. Hodnett, and P. N. Gélat, “A novel sensor for monitoring acoustic cavitation. Part II: Prototype performance evaluation,” *IEEE Trans. Ultrason. Ferroelectr. Freq. Control*, vol. 50, no. 10, pp. 1351–1362, 2003.

[133] K. S. Suslick, “Sonochemistry,” *Science (80-.).*, vol. 247, pp. 1439-1445., 1990.

[134] G. B. Daware and P. R. Gogate, “Sonochemical Degradation of 3-Methylpyridine (3MP) intensified using combination with various oxidants,” *Ultrason. Sonochem.*, vol. 67, p. 105120, 2020.

[135] W. Hongyu, G. J. Hulbert, and J. R. Mount, “Effects of ultrasound on milk homogenization and fermentation with yogurt starter,” *Innov. Food Sci. Emerg. Technol.*, vol. 1, no. 3, pp. 211–218, 2000.

[136] G. Wang *et al.*, “Role of ultrasonic treatment, inoculation and solute in the grain refinement of commercial purity aluminium,” *Sci. Rep.*, vol. 7, no. 1, pp. 2–10, 2017.

[137] D. G. Eskin *et al.*, “Fundamental studies of ultrasonic melt processing,” *Ultrason. Sonochem.*, vol. 52, no. December 2018, pp. 455–467, 2019.

[138] W. W. Xu *et al.*, “Synchrotron quantification of ultrasound cavitation and bubble dynamics in Al-10Cu melts,” *Ultrason. Sonochem.*, vol. 31, pp. 355–361, 2016.

[139] I. Tzanakis, M. Hodnett, G. S. B. Lebon, N. Dezhkunov, and D. G. Eskin, “Calibration and performance assessment of an innovative high-temperature cavitometer,” *Sensors Actuators A. Phys.*, no. January, 2016.

[140] A. Priyadarshi *et al.*, “On the governing fragmentation mechanism of primary intermetallics by induced cavitation,” *Ultrason. Sonochem.*, vol. 70, no. July 2020, p.

105260, 2021.

[141] J. Wannasin, R. Canyook, S. Wisutmethangoon, and M. C. Flemings, “Grain refinement behavior of an aluminum alloy by inoculation and dynamic nucleation,” *Acta Mater.*, vol. 61, no. 10, pp. 3897–3903, 2013.

[142] M. A. Easton, M. Qian, and D. H. StJohn, *Grain Refinement in Alloys: Novel Approaches*. 2011.

[143] K. T. Kashyap and T. Chandrashekar, “Effects and mechanisms of grain refinement in aluminium alloys,” *Bull. Mater. Sci.*, vol. 24, no. 4, pp. 345–353, 2001.

[144] M. Easton and D. St John, “An analysis of the relationship between grain size, solute content, and the potency and number density of nucleant particles,” *Metall. Mater. Trans. A Phys. Metall. Mater. Sci.*, vol. 36, no. 7, pp. 1911–1920, 2005.

[145] M. Easton, C. Davidson, and D. St John, “Effect of alloy composition on the dendrite arm spacing of multicomponent aluminum alloys,” *Metall. Mater. Trans. A Phys. Metall. Mater. Sci.*, vol. 41, no. 6, pp. 1528–1538, 2010.

[146] D.G. McCartney, “Grain Refining of Aluminium and Its Alloys Using Inoculants,” *Int. Mater. Rev.*, vol. 34, pp. 247–260, 1989.

[147] S. D. H. Easton M A, “Grain refinement of aluminium alloys. Part 1-The nucleant and solute aradigms -a review

of the literature.," *Met. Mater. Trans*, vol. 30A, pp. 1613–23.

[148] S. V. Komarov, M. Kuwabara, and O. V. Abramov, "High power ultrasonics in pyrometallurgy: Current status and recent development," *ISIJ Int.*, vol. 45, no. 12, pp. 1765–1782, 2005.

[149] H. T. Li, Y. Wang, and Z. Fan, "Mechanisms of enhanced heterogeneous nucleation during solidification in binary Al-Mg alloys," *Acta Mater.*, vol. 60, no. 4, pp. 1528–1537, 2012.

[150] G. I. Eskin and D. G. Eskin, *Ultrasonic Treatment of Light Alloy Melts*. 2014.

[151] D. G. E. G.I. Eskin, *Ultrasonic treatment of light alloy melts*, Second. Boca Raton, Florida, USA: CRC Press, 2017.

[152] G. S. B. Lebon, G. Salloum-Abou-Jaoude, D. Eskin, I. Tzanakis, K. Pericleous, and P. Jarry, "Numerical modelling of acoustic streaming during the ultrasonic melt treatment of direct-chill (DC) casting," *Ultrason. Sonochem.*, vol. 54, no. April 2021, pp. 171–182, 2019.

[153] B. Wang *et al.*, "Ultrafast synchrotron X-ray imaging studies of microstructure fragmentation in solidification under ultrasound," *Acta Mater.*, vol. 144, pp. 505–515, 2018.

[154] S. Bae *et al.*, "Effect of Ultrasonic Melt Treatment on

Solidification Microstructure of Al – 5Ti – 1B Alloy Containing Numerous Inoculant Particles," *Met. Mater. Int.*, no. 0123456789, 2021.

[155] Y. Han, D. Shu, J. Wang, and B. Sun, "Microstructure and grain refining performance of Al-5Ti-1B master alloy prepared under high-intensity ultrasound," *Mater. Sci. Eng. A*, vol. 430, no. 1–2, pp. 326–331, 2006.

[156] B. S. H. Huang , D. Shu , Y. Fu , J. Wang, "Synchrotron radiation X-ray imaging of cavitation bubbles in Al-Cu alloy melt," *Ultrason. Sonochem.*, vol. 21, pp. 1275–1278, 2014.

[157] J. M. T.L. Lee , J.C. Khong , K. Fezzaa, "Ultrafast X-ray imaging and modelling of ultrasonic cavitations in liquid metal," *Mater. Sci. Forum*, vol. 765, pp. 190–194, 2013.

[158] D. Tan, T. L. Lee, J. C. Khong, T. Connolley, K. Fezzaa, and J. Mi, "High-Speed Synchrotron X-ray Imaging Studies of the Ultrasound Shockwave and Enhanced Flow during Metal Solidification Processes," *Metall. Mater. Trans. A Phys. Metall. Mater. Sci.*, vol. 46, no. 7, pp. 2851–2861, 2015.

[159] Z. Zhang, C. Wang, B. Koe, C. M. Schlepütz, S. Irvine, and J. Mi, "Synchrotron X-ray imaging and ultrafast tomography in situ study of the fragmentation and growth dynamics of dendritic microstructures in solidification under ultrasound," *Acta Mater.*, vol. 209, p. 116796, 2021.

[160] I. Tzanakis, W. W. Xu, D. G. Eskin, P. D. Lee, and N.

Kotsovinos, “In situ observation and analysis of ultrasonic capillary effect in molten aluminium,” *Ultrason. Sonochem.*, vol. 27, pp. 72–80, 2015.

[161] R. Chow, R. Blindt, R. Chivers, and M. Povey, “A study on the primary and secondary nucleation of ice by power ultrasound,” *Ultrasonics*, vol. 43, no. 4, pp. 227–230, 2005.

[162] R. Chow, R. Blindt, A. Kamp, P. Grocutt, and R. Chivers, “The microscopic visualisation of the sonocrystallisation of ice using a novel ultrasonic cold stage,” *Ultrason. Sonochem.*, vol. 11, no. 3–4, pp. 245–250, 2004.

[163] C. Beckwith *et al.*, “Multiphysics modelling of ultrasonic melt treatment in the hot-top and launder during direct-chill casting: Path to indirect microstructure simulation,” *Metals (Basel).*, vol. 11, no. 5, 2021.

[164] B. W. Zeiger and K. Suslick, “Sonofragmentation of molecular crystals: Observations and Modeling,” *J. Am. Chem. Soc.*, vol. 19, pp. 14530–14533, 2011.

[165] H. N. Kim and K. S. Suslick, “Sonofragmentation of Ionic Crystals,” *Chem. - A Eur. J.*, vol. 23, no. 12, pp. 2778–2782, 2017.

[166] Yoshiyuki Asakura, K. Yasuda, D. Kato, Y. Kojima, and S. Koda, “Development of a large sonochemical reactor at a high frequency,” *Chem. Eng. J.*, vol. 139, no. 2, pp. 339–343, 2008.

[167] E. Gonze, Y. Gonthier, P. Boldo, and A. Bernis, “Standing

waves in a high frequency sonoreactor: Visualization and effects,” *Chem. Eng. Sci.*, vol. 53, no. 3, pp. 523–532, 1998.

[168] H. Destaillats, T. M. Lesko, M. Knowlton, H. Wallace, and M. R. Hoffmann, “Scale-up of sonochemical reactors for water treatment,” *Ind. Eng. Chem. Res.*, vol. 40, no. 18, pp. 3855–3860, 2001.

[169] F. F. John, “Ultrasonic Cleaning: Fundamental Theory and Application.” 2008.

[170] M. Hodnett, M. J. Choi, and B. Zeqiri, “Towards a reference ultrasonic cavitation vessel. Part 1: Preliminary investigation of the acoustic field distribution in a 25 kHz cylindrical cell,” *Ultrason. Sonochem.*, vol. 14, no. 1, pp. 29–40, 2007.

[171] L. Yusuf, M. D. Symes, and P. Prentice, “Characterising the cavitation activity generated by an ultrasonic horn at varying tip-vibration amplitudes,” *Ultrason. Sonochem.*, vol. 70, no. August 2020, p. 105273, 2021.

[172] A. B. Chivate, M.M., Pandit, “Quantification of cavitation intensity in fluid bulk,” *Ultrason. Sonochem*, vol. 2, pp. 19-25., 1995.

[173] L. Sutkar, V.S., Gogate, P.R., Csoka, “Theoretical prediction of cavitational activity distribution in sonochemical reactors.,” *Chem. Eng. J.*, vol. 158, pp. 290–295., 2010.

[174] L. Ma, L. Hu, X. Feng, and S. Wang, “Nitrate and nitrite in health and disease,” *Aging Dis.*, vol. 9, no. 5, pp. 938–945, 2018.

[175] N. S. Bryan and J. L. Ivy, “Inorganic nitrite and nitrate: Evidence to support consideration as dietary nutrients,” *Nutr. Res.*, vol. 35, no. 8, pp. 643–654, 2015.

[176] J. Rooze, E. V Rebrov, J. C. Schouten, and J. T. F. Keurentjes, “Ultrasonics Sonochemistry Dissolved gas and ultrasonic cavitation – A review,” *Ultrason. - Sonochemistry*, vol. 20, no. 1, pp. 1–11, 2013.

[177] C. A. Wakeford, R. Blackburn, and P. D. Lickiss, “Effect of ionic strength on the acoustic generation of nitrite, nitrate and hydrogen peroxide,” *Ultrason. Sonochem.*, vol. 6, no. 3, pp. 141–148, 1999.

[178] S. Zhang *et al.*, “Sustainable nitrogen fixation with nanosecond pulsed spark discharges: insights into free-radical-chain reactions,” *Green Chem.*, pp. 1534–1544, 2022.

[179] P. Kruus, “Fixation of nitrogen with cavitation,” *Ultrason. Sonochem.*, vol. 9, pp. 53–59, 2002.

[180] F. Maslan, “Process for Thermal Fixation of Atmospheric Nitrogen,” vol. 2, 1969.

[181] S. Asgharzadehahmadi, A. Aziz, A. Raman, and R. Parthasarathy, “Sonochemical reactors : Review on features , advantages and limitations,” *Renew. Sustain.*

Energy Rev., vol. 63, pp. 302–314, 2016.

[182] H. Schultes and H. Gohr, “Über chemische Wirkungen der Ultraschallwellen,” *Angew. Chem*, vol. 49, no. 420, pp. 420–423, 1936.

[183] A. I. Virtanen, N. Ellfolk, L. G. Sillén, and M. Rottenberg, “Oxidative Nitrogen Fixation in Ultrasonic Field.,” *Acta Chemica Scandinavica*, vol. 4. pp. 93–102, 1950.

[184] G. Rosenkranz, S. Kaufmann, J. Pataki, and C. Djbrassi, “Nitrogen Fixation in an Ultrasonic Field,” 1949.

[185] E. L. Mead *et al.*, “The effect of ultrasound on water in the presence of dissolved gases,” *Can. J. Chem.*, no. 15, 1976.

[186] Supeno, “Sonochemical Fixation of Nitrogen,” 2000.

[187] K. P. Supeno, “Sonochemical formation of nitrate and nitrite in water,” *Ultrason. Sonochem.*, vol. 7, pp. 109–113, 2000.

[188] Z. Xu and K. Yasuda, “Enhancement of sonochemical reaction by dual-pulse ultrasound,” *Jpn. J. Appl. Phys.*, vol. 50, no. 7 PART 2, 2011.

[189] A. Henglein, R. Ulrich, and J. Lilie, “Luminescence and Chemical Action by Pulsed Ultrasound,” *J. Am. Chem. Soc.*, vol. 111, no. 6, pp. 1974–1979, 1989.

[190] Y. Sun and X. Ye, “Enhancement or reduction of sonochemical activity of pulsed ultrasound compared to

continuous ultrasound at 20 kHz?," *Molecules*, vol. 18, no. 5, pp. 4858–4867, 2013.

[191] M. Gutiérrez and A. Henglein, "Chemical action of pulsed ultrasound: Observation of an unprecedented intensity effect," *J. Phys. Chem.*, vol. 94, no. 9, pp. 3625–3628, 1990.

[192] T. Tuziuti, K. Yasui, J. Lee, T. Kozuka, A. Towata, and Y. Iida, "Mechanism of enhancement of sonochemical-reaction efficiency by pulsed ultrasound," *J. Phys. Chem. A*, vol. 112, no. 22, pp. 4875–4878, 2008.

[193] D. J. Casadonte, M. Flores, and C. Petrier, "Enhancing sonochemical activity in aqueous media using power-modulated pulsed ultrasound: An initial study," *Ultrason. Sonochem.*, vol. 12, no. 3, pp. 147–152, 2005.

[194] K. Yasuda *et al.*, "Enhancement of sonochemical reaction of terephthalate ion by superposition of ultrasonic fields of various frequencies," *Ultrason. Sonochem.*, vol. 14, no. 6, pp. 699–704, 2007.

[195] N. A. Patience, D. Schieppati, and D. C. Boffito, "Continuous and Pulsed Ultrasound Pectin Extraction from Navel Orange Peels," *Ultrason. Sonochem.*, p. 105480, 2021.

[196] T. G. Leighton, *The Acoustic Bubble*, First. Academic: London, 1996.

[197] E. L. Carstensen, K. J. Parker, and D. B. Barbee,

“Temporal peak intensity,” *J. Acoust. Soc. Am.*, vol. 74, no. 3, pp. 1057–1058, 1983.

[198] F. Cheli and G. Diana, “Introduction to the Finite Element Method,” 2015.

[199] S. Concept, “Transducer selection guide,” *https://sonicconcepts.com/transducer-selection-guide-single-element/*, 2021. .

[200] M. U. Bowdish Lab, “Griess Assay for nitrite determination,” 2015.

[201] K. Retz, S. Kotopoulis, T. Kiserud, K. Matre, G. E. Eide, and R. Sande, “Measured acoustic intensities for clinical diagnostic ultrasound transducers and correlation with thermal index,” *Ultrasound Obstet. Gynecol.*, vol. 50, no. 2, pp. 236–241, 2017.

[202] R. C. Preston, *Output measurements for medical ultrasound*, vol. 19, no. 5. 1993.

[203] H. Islam, O. S. Burheim, and B. G. Pollet, “Sonochemical and sonoelectrochemical production of hydrogen,” *Ultrason. - Sonochemistry*, vol. 51, no. September 2018, pp. 533–555, 2019.

[204] S. Merouani, O. Hamdaoui, Y. Rezgui, and M. Guemini, “Computational engineering study of hydrogen production via ultrasonic cavitation in water,” *Int. J. Hydrogen Energy*, vol. 41, no. 2, pp. 832–844, 2016.

[205] Pankaj and M. Ashokkumar, *Theoretical and Experimental*

Sonochemistry Involving Inorganic Systems. 2011.

[206] G. S. B. Lebon, I. Tzanakis, K. Pericleous, and D. Eskin, “Experimental and numerical investigation of acoustic pressures in different liquids,” *Ultrason. Sonochem.*, vol. 42, no. December 2017, pp. 411–421, 2018.

[207] H. Georgi, *The Physics of waves*, 5th ed. New Jersey: PRENTICE HALL, 2015.